Errata (corrected in the present version)

page 21 line 20: aluminium → copper

page 174: middle being the expected background track density very low
→ the expected ...being very low

page 179 line 10 : Therefore, the electron and the particles giving...
→ Therefore, the particles giving...

page 179 last line : $\varepsilon_{e\to e}$ is missing in the formula

page 180 last-9: the average pt in hadronic...900 MeV/c
→ the maximum pt ....

page 180 line 14: 78(76)% for DIS(QE)...
→ $\sim$ 70 for both DIS and QE...

page 180 last : Several sets of the D...exist
→ Several sets of these functions exist in the literature

page 186 last-1 6% out of 19.3% of the events....
→ 6% of the events with ...

page 225 line 10: field length of 1.18 cm
→ of 118 cm

Fig. 57: (spacer are made of "Lexan" and not "PVC")

Fig 104 : $\sigma \to \sigma/\sqrt{2}$

Fig 142: corrected slope of the signal curve

Fig 145: horizontal axis

Table 14: 0.587 → 0.74

Table 29: (Upper-Lower)/True → (Upper-Lower)/2 × True

Formulae page 183: $\varepsilon_{fake-e(\mu)} \to 1 - \varepsilon_{fake-e(\mu)}$

CERN/SPSC 2000-028
SPSC/P318
LNGS P25/2000
July 10, 2000

An appearance experiment to search for $\nu_\mu \leftrightarrow \nu_\tau$ oscillations in the CNGS beam

Experiment Proposal

The OPERA Collaboration[1]

M. Guler, M. Serin-Zeyrek, P. Tolun, M.T. Zeyrek
METU, Ankara, Turkey

D. Duchesneau, A. Degré, J. Favier, H. Pessard
LAPP, IN2P3-CNRS and Université de Savoie, Annecy, France

M.T. Muciaccia, P. Righini, S. Simone
Bari University and INFN, Bari, Italy

S.L. Lu, S.J. Zhou
IHEP, Beijing, China PR

K. Winter
Humboldt University, Berlin, Germany

K. Borer, C. Haeberli, M. Hess, R. Klingenberg, U. Moser, K. Pretzl, T. Waelchli, M. Weber
Bern University, Bern, Switzerland

G. Giacomelli, G. Mandrioli, L. Patrizii, P. Serra, M. Sioli, G. Sirri
Bologna University and INFN, Bologna, Italy

G. Van Beek, P. Vilain, G. Wilquet
IIHE (ULB-VUB), Brussels, Belgium

M. Spinetti, L. Votano
LNF, Frascati, Italy

S. Ogawa, H. Shibuya
Toho University, Funabashi, Japan

D. Autiero, L. Camilleri, L. Di Lella, J. Dupraz, J.P. Fabre, R. Petti, P. Schilly
CERN, Geneva, Switzerland

H. Sohlbach, H. Woltersdorf
Märkische Fachhochschule FB Elektrotechnik, Hagen, Germany

J. Goldberg, M. Khalifa
Israeli group c/o Technion, Haifa, Israel

F.W. Buesser, A. Garfagnini, A. Geiser, K. Höpfner, B. Koppitz, B. Naroska, W. Schmidt-Parzefall, R. van Staa
Hamburg University, Hamburg, Germany

K. Kodama, N. Ushida
Aichi University of Education, Kariya, Japan

S. Aoki, T. Hara
Kobe University, Kobe, Japan

L. Chaussard, M. Chemarin, Y. Déclais, P. Jonsson,[2] S. Katsanevas, I. Laktineh, J. Marteau, G. Moret
IPNL, IN2P3-CNRS and Université C. Bernard Lyon I, Villeurbanne, France

N. D'Ambrosio, P. Boschan, D. Frekers, T. Kellmann, J. Kueckmann, J. Schmand, H.J. Wörtche, T. Wolff
Münster University, Münster, Germany

K. Hoshino, M. Komatsu, M. Miyanishi, M. Nakamura, T. Nakano, K. Niwa, O. Sato
Nagoya University, Nagoya, Japan

[1] The participation of the groups is subject to final approval by the respective Institutions.

[2] Post-doctoral stipend from STINT, The Swedish Found. for Int. Cooper. in Research and Higher Education.

N. Bruski, S. Buontempo, F. Carbonara, A. G. Cocco, G. De Lellis, G. De Rosa, A. Ereditato, G. Fiorillo, T. Kawamura, M. Messina, P. Migliozzi, L. Saggese, P. Strolin,[3] V. Tioukov
"Federico II" University and INFN, Naples, Italy

J. Boucrot, J.E. Campagne, B. Merkel, J.P. Repellin, J.J. Veillet
LAL, IN2P3-CNRS and Université Paris-Sud, Orsay, France

R. Brugnera, F. Dal Corso, S. Dusini, C. Fanin, L. Stanco
Padova University and INFN, Padova, Italy

G. Rosa
"La Sapienza" University and INFN, Rome, Italy

M. Beyer, H. Schroeder, R. Waldi
Fachbereich Physik der Universitaet Rostock, Rostock, Germany

E. Barbuto, C. Bozza, G. Grella, G. Romano, S. Sorrentino
Salerno University and INFN, Salerno, Italy

R. Arnold, E. Baussan, M. Dracos, J.L. Guyonnet, R. Strub
IReS, IN2P3-CNRS and Université Louis Pasteur, Strasbourg, France

M. He, J.Y. Li, C.F. Feng, Y. Fu, L. Xue
Shandong University, Tsinan (Shandong), China PR

Y. Sato, I. Tezuka
Utsunomiya University, Utsunomiya, Japan

M. Stipcevic, A. Ljubicic, K. Jakovcic
Rudjer Boskovic Institute (IRB), Zagreb, Croatia

We would like to acknowledge the important contributions made to the conceptual design of the experiment by the group of ITEP Moscow (A. Artamonov, V. Epshteyn, P. Gorbounov, V. Khovansky, M. Ryabinine, P. Shatalov and V. Zaitsev). This group has also built prototypes of scintillator strip modules, measured their performance in test beams and carried out measurements for background estimates. The ITEP group maintains its interest in the OPERA experiment.

[3] Presently CERN Scientific Associate.

ABSTRACT

The OPERA[4] experiment is proposed for an appearance search of $\nu_\mu \leftrightarrow \nu_\tau$ oscillations in the parameter region indicated by Super-Kamiokande as the explanation of the zenith dependence of the atmospheric neutrino deficit. OPERA is a long baseline experiment to be located at the Gran Sasso Laboratory in the CNGS[5] neutrino beam from the CERN SPS. The detector design is based on a massive lead/nuclear emulsion target. Nuclear emulsions are used as high resolution tracking devices, for the direct observation of the decay of the τ leptons produced in ν_τ charged current interactions. Electronic detectors locate the events in the emulsions. Magnetised iron spectrometers measure charge and momentum of muons. The discovery potential of OPERA originates from the observation of a ν_τ signal with very low background level. The direct observation of $\nu_\mu \leftrightarrow \nu_\tau$ appearance will constitute a milestone in the study of neutrino oscillations.

[4] Oscillation Project with Emulsion-tRacking Apparatus.
[5] Cern Neutrino beam to Gran Sasso.

Contents

1 Introduction

In this document we propose an experiment (OPERA) for the direct observation of ν_τ appearance from $\nu_\mu \leftrightarrow \nu_\tau$ oscillations in the CNGS long baseline beam [1] from the CERN SPS to the Gran Sasso Laboratory. OPERA aims at high sensitivity in the parameter region indicated by the deficit of atmospheric muon neutrinos and by its zenith angle dependence as observed by the Super-Kamiokande experiment. The experiment exploits nuclear emulsions as very high resolution tracking devices for the direct detection of the decay of the τ produced in the charged current (CC) interaction of the ν_τ with the target. Preliminary ideas and designs of the experiment can be found in [2–5] and in the Progress Report presented to the Scientific Committees in 1999 [6].

The technique of nuclear emulsion has found a large scale application in the target of the CHORUS experiment [7] in which the automatic scanning of a large sample of events has first been applied. This technique can be further improved and lead to the much larger scale of the OPERA target. Its mass is made of lead plates, with emulsion films used as high precision trackers, unlike in CHORUS in which emulsions constitute the bulk of the target mass.

The experiment design is based on the Emulsion Cloud Chamber (ECC) detector, a modular structure made of a sandwich of passive material plates interspaced with emulsion layers (Fig. 1). By assembling a large quantity of such modules, it is possible to conceive and realise a $\sim 2000\ ton$ fine-grained vertex detector optimised for the study of ν_τ appearance.

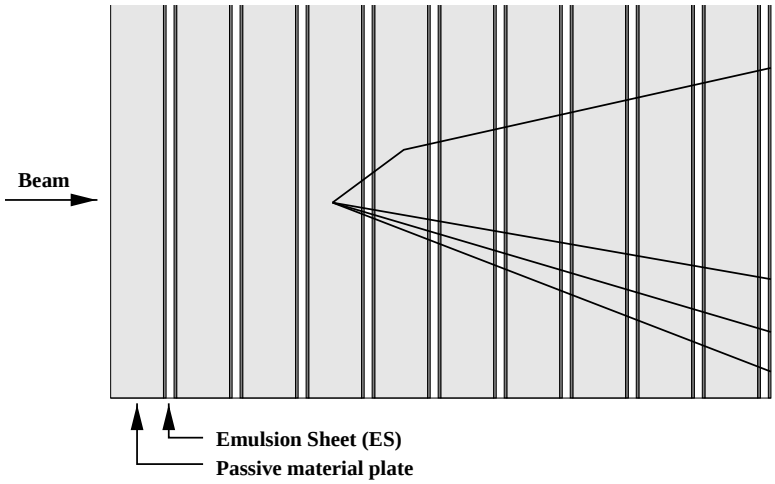

Figure 1: Schematic structure of an Emulsion Cloud Chamber (ECC).

This target is complemented by arrays of electronic trackers for the real time determination of the event position and by magnetised iron spectrometers for muon identification and for the reconstruction of their charge and momentum.

The feasibility of OPERA is linked to the production of emulsion films on an industrial scale and to the impressive progress in the field of computer controlled microscopes read out by CCD cameras, with automatic pattern recognition and track reconstruction [8, 9]. Nowadays, nuclear emulsion can be considered as a data storage device readout by automatic scanning systems which reconstruct 3D vectors of particle tracks. Further improvements are expected from the intense R&D programme underway within several groups of the Collaboration.

This document gives the design and the expected performance of OPERA according to the choice of detector baseline options. It describes results from tests on prototypes of detector elements and the programme of further studies. The construction, installation and operation of the detector are discussed. We present the cost estimate of the experiment and the areas where the groups expect to contribute.

1.1 Physics motivations

The possibility of a non-vanishing mass for the neutrino is one of the most intriguing questions of particle physics. On the one hand, there is no fundamental principle for the neutrino to be massless; on the other hand, a neutrino mass implies physics beyond the Standard Model of elementary particles, representing a fundamental milestone in particle physics, astrophysics and cosmology.

Most likely, the neutrino mass is too small and therefore out of reach of precision studies of the kinematics of decays involving neutrinos [10, 11]. The search for a process which can only occur if the neutrino has non vanishing mass, even if very low, is crucial to asses this issue. Neutrino oscillations are such a process. They were originally postulated by Pontecorvo [12, 13] in terms of $\nu \leftrightarrow \bar{\nu}$ oscillation, before the discovery of distinct neutrino flavours. Maki et al. [14] introduced the possibility of neutrino flavour transitions with a mixing matrix. The present description of the phenomenon in terms of weak and mass eigenstates was provided by Gribov and Pontecorvo [15].

For a massive neutrino, according to the oscillation mechanism, a given weak interaction eigenstate (ν_e, ν_μ or ν_τ) may be seen as a different eigenstate at some distance from the source. The corresponding probability has an oscillatory behaviour (hence *oscillation*) with parameters which can be determined by experiments. In the simplified scheme in which oscillations occur dominantly between a pair of neutrino flavours, they are described by two quantities: the mixing parameter $\sin^2 2\theta$ (related to the oscillation amplitude) and the mass squared difference Δm^2 between the two mass eigenstates (related to the oscillation frequency). The sensitivity of the experimental searches to the above parameters depends on the neutrino energy E and on the distance L of the detector from the neutrino source. In some cases, the electron density of the traversed medium may also play a non negligible role through the so-called MSW effect [16].

Several review papers exist in the literature [17] describing the neutrino oscillation phenomenology and signals or limits obtained in solar, atmospheric, reactor and accelerator experiments. The first indication came from the deficit in the detected ν_e flux from the Sun. However, its interpretation in terms of neutrino oscillation, to a certain extent, depends on the solar model. The SNO experiment [18] has started and a new generation of experiments (BOREXINO [19], ICARUS [20], ...) are being prepared or foreseen to disentangle the possible solutions compatible with the existing data [21]. Long baseline

reactor experiments (KAMLAND [22], BOREXINO) aim at testing the Δm^2 range of $10^{-4} - 10^{-5}\ eV^2$ relevant for the MSW large mixing angle solution of the solar neutrino problem.

Another indication, the $\nu_\mu \leftrightarrow \nu_e$ oscillation signal observed in LSND [23], is still to be confirmed and a conclusive check will probably have to wait for the results of the MiniBoone experiment at Fermilab [24].

The strongest evidence for the existence of neutrino oscillations comes from recent results on the so-called atmospheric neutrino anomaly. We shall briefly review these results since they are directly related to the motivation of the OPERA experiment.

The Kamiokande Collaboration [25] suggested neutrino oscillations as an explanation of the anomalous ratio of atmospheric muon neutrinos to electron neutrinos and of its zenith angle dependence. The best fit to their data, in terms of $\nu_\mu \leftrightarrow \nu_\tau$ oscillations, gives $\Delta m^2 = 1.6 \times 10^{-2}\ eV^2$ and $\sin^2 2\theta = 1$. The CHOOZ reactor experiment excluded to a large extent the possibility of $\nu_\mu \leftrightarrow \nu_e$ oscillations [26] leaving open the case for $\nu_\mu \leftrightarrow \nu_\tau$ oscillations. The introduction of a fourth sterile neutrino would allow to explain all experimental results, including LSND.

The Super-Kamiokande experiment has confirmed the Kamiokande result with a statistics several times larger [27–30], making a strong claim for the observation of neutrino oscillations. The interpretation of the observed ν_μ disappearance in terms of $\nu_\mu \leftrightarrow \nu_{sterile}$ is disfavoured with respect to the $\nu_\mu \leftrightarrow \nu_\tau$ hypothesis. The data also disfavour the possibility of $\nu_\mu \leftrightarrow \nu_e$ oscillation. The above results have been confirmed by data on upward muons produced by neutrinos interacting in the rock below the detector.

A combined analysis of all the Super-Kamiokande measurements (*sub-GeV*, *multi-GeV* and upward-going muons) has been reported [28]. The best fit result is $\Delta m^2 = 3.5 \times 10^{-3}\ eV^2$ and $\sin^2 2\theta = 1$. At the 90% confidence level (CL) the oscillation parameters are constrained in the region of $\sin^2 2\theta > 0.8$ and $\Delta m^2 = (2 - 6) \times 10^{-3}\ eV^2$.

Recently, the Super-Kamiokande Collaboration has presented preliminary new results [30]; they confirm the previous measurements with higher statistics and improved analyses. A global fit to the data yields $\Delta m^2 = 3.2 \times 10^{-3}\ eV^2$ and $\sin^2 2\theta = 1$. Δm^2 is constrained at the 90% CL within the interval $1.5 - 5 \times 10^{-3}\ eV^2$.

The Soudan2 experiment, exploiting a fine-grained tracking calorimeter, also observed a smaller than expected yield of ν_μ, although with a less pronounced zenith angle dependence [31]. Soudan2 has a better angular resolution than Super-Kamiokande but lower statistics. The MACRO experiment at Gran Sasso [32], based on a massive tracking calorimeter, detected a statistically significant deficit of upward-going muons consistent with the Super-Kamiokande observations on the disappearance of muon neutrinos. To observe the L/E pattern characteristic of the oscillations, atmospheric neutrino detectors with better energy and angular resolutions are required [33].

To summarise, the disappearance of atmospheric ν_μ is well established. The conclusive test of the $\nu_\mu \leftrightarrow \nu_\tau$ hypothesis will be the direct observation of ν_τ appearance in an initially pure ν_μ beam, as proposed by OPERA.

The OPERA sensitivity covers the Δm^2 region allowed by the present atmospheric data. In the case of a positive signal, the observation of even a few ν_τ events will be significant, because of the very low expected background. The number of observed ν_τ events will provide a measurement of the product of

the two oscillation parameters $\sin^2 2\theta$ and Δm^2 in the two flavour mixing scheme. Given the already known constraint of nearly maximum mixing [30], OPERA can improve the determination of Δm^2.

Because of its capability of identifying electrons and to the small ν_e contamination in the CNGS beam, OPERA is also suited for a $\nu_\mu \leftrightarrow \nu_e$ oscillation search. The sensitivity to oscillations of a NC/CC measurement (where CC and NC represent the rates of events with and without a muon in the final state) is being investigated in view of a three-flavour analysis.

1.2 Oscillation searches with long baseline beams

Recently, new neutrino beams and detectors have been designed to provide an E/L spectrum suitable to probe the parameter space region pointed to by atmospheric-neutrino experiments. Compared to natural sources, an accelerator-based neutrino beam offers the advantages of a higher flux and of a good purity in ν_μ with known and small contaminations of other flavours.

The K2K experiment [34, 35] has been commissioned in 1999. It is searching for ν_μ disappearance by using the long baseline neutrino beam from KEK to Super-Kamiokande (250 km away) [36]. Given the low beam energy, which is below the kinematical threshold for τ production, K2K is not able to perform a ν_τ appearance search. A significant difference between the ν_μ CC rates measured in the Super-Kamiokande detector and the predictions based on extrapolations of near detector rates can be observed provided the effective Δm^2 value is larger than about 2×10^{-3} eV^2. Preliminary results have been recently presented [37], consistent with the oscillation parameters determined by Super-Kamiokande with atmospheric neutrinos.

At Fermilab the MINOS experiment [38] will use the NuMI beam [39] from Fermilab to the Soudan Mine, 730 km away. The high repetition rate of the 120 GeV/c Main Injector and the presence of a near detector make it suitable to perform a ν_μ disappearance experiment. The granularity of the detector is too coarse to allow the flavour tagging of ν_τ CC interactions but the excellent muon identification efficiency will be used to exploit the measurement of the NC/CC ratio as an indirect probe of ν_τ appearance.

The CNGS facility from the CERN SPS to the Gran Sasso Laboratory is planned to deliver a ν_μ beam from 2005 onwards. In its present design, the beam is optimised for a ν_τ appearance search, as proposed by both experiments ICANOE [40] and OPERA.

The full understanding of neutrino masses and mixings is a long term programme and will certainly require the combination of many experimental efforts, as is still the case for quarks. The difficulty of the experiments require approaches from different points of view, in order to firmly assess the experimental scenario. In a more distant future, the next steps towards the precise determination of all oscillation parameters will require the availability of very intense neutrino beams and of massive detectors placed at even larger distances from the neutrino sources. Along these lines, studies for the use of muon storage rings as powerful and very pure neutrino sources are pursued [41].

1.3 ν_τ detection by the ECC technique

So far only the DONUT experiment [42] has succeeded in detecting ν_τ interactions, as illustrated in Fig. 2. They are identified in an ECC detector conceptually similar to that planned for OPERA; one

difference being the nature of the passive material, iron plates for DONUT and lead plates for OPERA. The DONUT ECC detectors were exposed to a prompt neutrino beam created by 800 GeV/c protons in the beam dump experiment E872 at FNAL.

The high position resolution of nuclear emulsions, the existence of automatic readout systems (Track Selector) and the availability of fast data processing (Net Scan) are the essential ingredients of the present ECC detection technique. These advances have largely profited from the experience in the CHORUS and DONUT physics analyses.

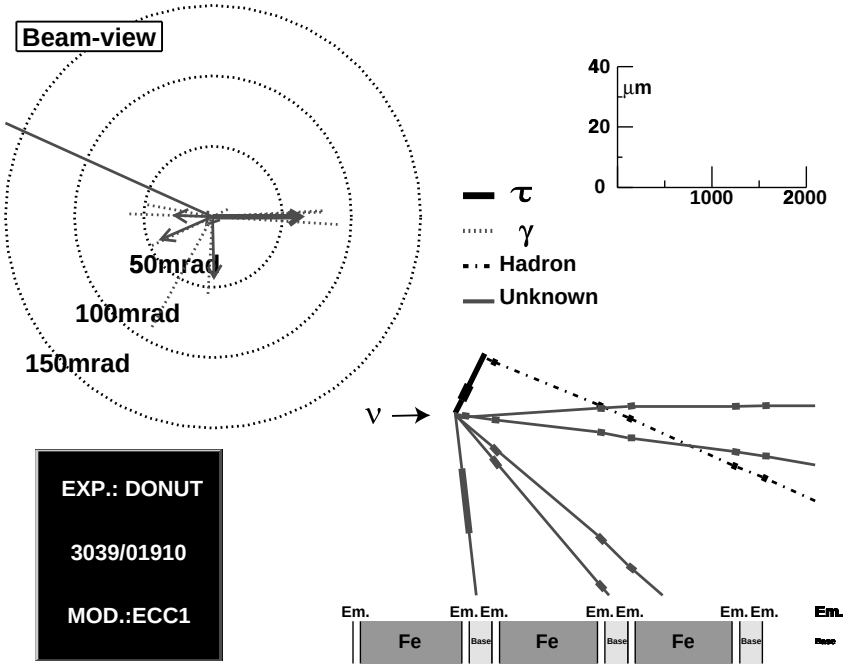

Figure 2: Detected τ event in DONUT [43]. One track, which is isolated and opposite in direction to the other charged particles, shows a *kink* topology after a short flight of 280 μm. The kink angle is measured to be 90 $mrad$. The momentum of the kink daughter is $4.6 \pm^{1.6}_{0.9}$ GeV/c ($p_t = 414 \pm^{144}_{81}$ MeV/c), as evaluated by multiple scattering.

Nuclear emulsions are made of micro-crystals of silver halides (AgBr) as sensitive devices dispersed in a thin gelatin layer. The size of the micro crystal is ~ 0.2 μm and is well controlled by the current industrial technologies developed for photographic films.

Emulsion films have nuclear emulsion layers on both sides of a transparent plastic base. In the DONUT ECC, 100 μm thick emulsion layers are coated on both sides of a 200 μm (or 800 μm) thick plastic base. For OPERA we use 50 μm thick emulsion layers on both sides of a 200 μm thick base. This structure of the film allows to connect track segments (micro tracks) on both sides of the base. The positions and angles of the connected tracks (base tracks) are thus free from distortions in the emulsion layers.

Table 1: Steps in the development of the Track Selector systems. The scanning speed is expressed in views per second (a view corresponds to an area of $\sim 0.018\ mm^2$).

Name	Year	Scanning speed (Specified angle)	Scanning speed (All angles)	Experiment
TS	1982	0.2	not tried	Test for CERN WA75/ FNAL E653
TS2	1994	0.4	0.008	CHORUS
NTS	1996	3	0.25	CHORUS
UTS	1998	3	3	DONUT/CHORUS
Super UTS	2001	30	30	OPERA/DONUT/CHORUS

After emulsion processing ionising particles are recognised by the microscope as the alignment of silver grains of about 0.6 μm diameter. For very high energy particles, the RMS deviation of the central coordinate of each grain from a straight line is measured to be $\sim 0.06\ \mu m$. This is the intrinsic resolution of nuclear emulsions.

The effort in developing automatic systems for the analysis of nuclear emulsions was initiated by Niwa in the late 70's [44]. The concept proposed at that time of fully automatic track recognition is still the basic algorithm used in the current systems. In order to recognise the presence of tracks penetrating almost perpendicularly the emulsion layer, a series of digitised tomographic images are recorded through the emulsion depth. For example, 16 views are taken to scan a 100 μm thick layer. The correlation of grains in the different layers identifies the track segments.

Table 1 gives a short summary of the R&D progress for the Track Selector in Nagoya. In the 80's a prototype Track Selector was devised, but its first application was for the CHORUS analysis, a real cradle for present and future achievements. The improvements have been closely following the development of the digital technologies like clock-up, parallel processing and pipeline processing. As described in Section 6, the Super UTS (S-UTS) development is now in progress in order to cope with the scanning power required for OPERA. New systems are being developed also in Europe.

For each emulsion layer positions and angles of the detected tracks are recorded as micro tracks. Then, the micro tracks on the two sides of the base are connected to form base tracks, whose positions and angles are not affected by distortion. After collecting these base tracks in a series of emulsion films, track reconstruction (*i.e.* connection between films) is performed. In DONUT the deviation of the measured micro track positions from the reconstructed straight line is $\sim 0.3\ \mu m$. This resolution, mainly determined by the precision of the readout system, is perfectly adequate for the detection of τ decays. The corresponding angular resolution from the measurements in two consecutive films (1.3 mm apart in OPERA) is $\sim 0.2\ mrad$ (Section 6.3.2). This can be compared with the expected angular distribution of the τ decay products (see Fig. 5).

The ECC structure is well suited for the measurement of charged particle momenta and for particle identification. The momentum is measured from the multiple scattering. Electrons can be identified by detecting cascade electromagnetic showers. γ rays are detected by their conversion into electron pairs.

The total energy of electrons and γ's can be evaluated by the analysis of the shower development. Details of the methods and results from test measurements are given in Section 6.

The above features have been exploited in the DONUT analysis, although with limited efficiency due to the longer radiation length of the passive material. In OPERA, lead plates allow a better performance.

In addition, the use of the ECC technique makes it possible to design the OPERA target in a cost effective way. The required mass of $\sim 2\ kton$, about 2000 times larger than in CHORUS, rules out a detector entirely made of emulsion. The emulsion weight to be used in OPERA is about $40\ ton$, a quantity which can be realistically produced in the form of thin emulsion films. The total film surface is about 176000 m^2, ~ 350 times more than for CHORUS. However, the film manufacture will be made industrially by using production lines of commercial photographic or X-ray films and can be achieved in less than two years.

The ECC technique has a long history. The main technological developments and applications to experiments were accomplished in Japan. The first notable physics result obtained with an ECC was in 1956 the measurement of the transverse momentum of multi particle production in high-energy hadron interactions [45].

After this success the ECC technique developed in two different directions. One consisted in building large size detectors at high altitudes, such as for the experiments on Mt. Norikura [46], Mt. Chacaltaya [47], Mt. Pamir [48], Mt. Fuji [49] and Mt. Kanbala [50], which took advantage of the cost effectiveness of the ECC structure. The physics motivation was the observation of rare events at extremely high energies. The intention was to use the atmosphere as a target and the ECC as an analyser. Those ECCs consisted of a sandwich of thick material plates ($5\ mm$ lead or $1\ cm$ iron) and shielded packages of emulsion plates and X-ray films. The area of the exposures extended up to $100 - 1000\ m^2$ for a corresponding weight of $100 - 1000\ ton$.

The other direction consisted in carrying out detailed observations of special events with compact ECCs by profiting from the high spatial resolution of the emulsions. An example of this is the discovery of charmed particles in cosmic ray interactions by Niu et al. [51, 52] in 1971, three years before the J/Ψ discovery. In that application, the analysing layer was used not only for the energy measurement of electromagnetic showers, but also for the momentum measurement of charged particles by multiple scattering. Until the end of '75, Niu and coworkers also observed the difference in lifetime between charged and neutral charmed particles by analysing the event samples accumulated in several cosmic-ray experiments [53]. This result was confirmed by experiments employing compact ECC detectors at Fermilab [54] [55] and at CERN [56] about five years later.

The design of the OPERA target can be considered as a unification of the above two approaches, by using the mass of a large size ECC while keeping the precision of a compact ECC.

2 General features of the experiment

In this Section we illustrate the main features of the experiment design and present an overview of the detector layout as well as of its operation scheme. The expected experimental performance are summarised, anticipating the detailed evaluations given in Section 7.

2.1 Conceptual design

The OPERA experiment is designed starting from the ECC concept, which combines in one *cell* the high precision tracking capabilities of nuclear emulsions and the large target mass given by the lead plates. By piling-up a series of cells in a sandwich-like structure one obtains a *brick*, which constitutes the detector element appropriate for the assembly of more massive planar structures (*walls*). A wall and its related electronic tracker planes constitute a *module*. A *supermodule* is made of a *target* section, which is a sequence of *modules*, and of a downstream *muon spectrometer*. The detector consists of a sequence of supermodules.

The so-called *compact cell* is shown in Fig. 3. It is composed of a 1 mm thick lead plate followed by a thin film made up of a pair of emulsion layers 50 μm thick on either side of a 200 μm plastic base. A charged particle produces two track segments in each film. The number of grain hits in 50 μm (15-20) is adequate for reconstruction of track segments by means of automatic scanning devices and ensures redundancy in the measurement of particle trajectories.

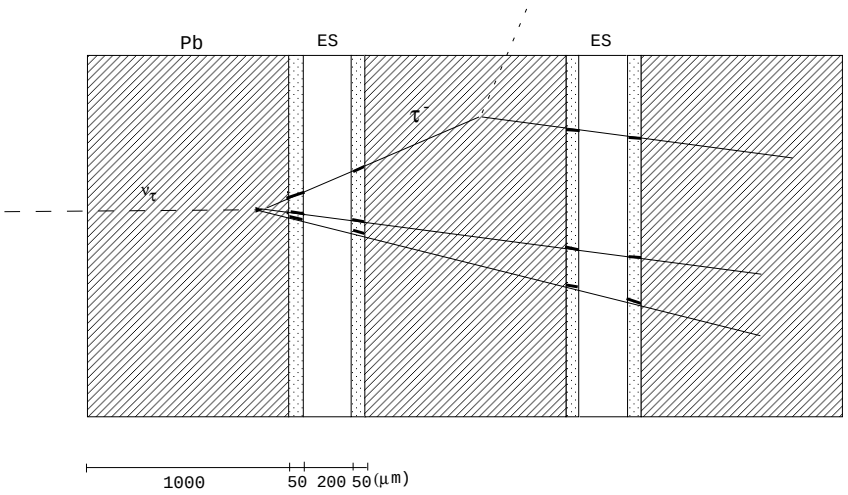

Figure 3: Schematic structure of an ECC cell. The τ decay kink is reconstructed in space by using four track segments in the emulsion films.

2.1.1 τ detection

The signal of the occurrence of $\nu_\mu \leftrightarrow \nu_\tau$ oscillations is the CC interaction of τ neutrinos in the detector target: $\nu_\tau N \rightarrow \tau^- X$. The reaction is identified by the detection of the τ lepton in the final state

through the decay topology and its decay modes into an electron, a muon and a single charged hadron

$$\tau^- \to e^- \nu_\tau \overline{\nu}_e, \qquad \tau^- \to \mu^- \nu_\tau \overline{\nu}_\mu, \qquad \tau^- \to h^- \nu_\tau (n\pi^0)$$

Despite its distinctive topology the multi-prong channel of the τ has not been considered for the present estimate of the OPERA sensitivity, due to the less favourable signal to noise ratio.

Measurements of the branching ratio (BR) of the three single-prong decay modes give 17.8%, 17.7% and 49.5% for the electronic, muonic and hadronic channel, respectively. For the typical τ energies expected with the CNGS one obtains the decay length distribution shown in Fig. 4, evaluated for the oscillation parameter values indicated by the Super-Kamiokande results.

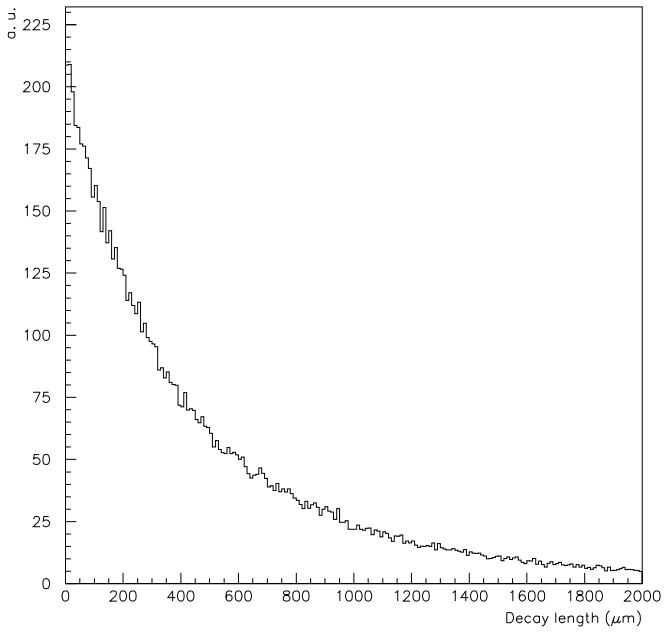

Figure 4: τ decay length distribution.

If a τ is produced in a lead plate it will decay either in the same plate (*short decays*) or further downstream (*long decays*). For long decays, the τ is detected by measuring the angle between the charged decay daughter and the parent direction. For example, Fig. 5 shows the distribution of the τ decay kink angle for the electron channel. For this measurement the directions of the tracks before and after the kink are reconstructed (in space) by means of the pair of emulsion films sandwiching the lead plate where the decay vertex occurred (Fig. 3). The τ can also decay in one of the films downstream of the vertex plate (*e.g.* in its plastic base). Even then, the kink angle can be reconstructed, albeit with a lower angular resolution, from the track segments in the emulsion layers on either side of the base. A fraction

of the short decays is detectable by measuring a significant impact parameter (IP) of the daughter track with respect to the tracks originating from the primary vertex.

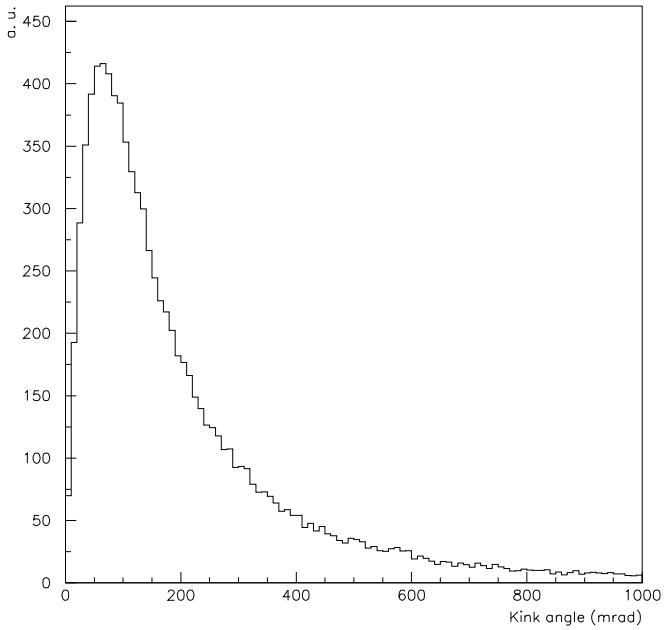

Figure 5: τ kink angle distribution for the $\tau \rightarrow e$ decay mode.

The detection of the τ decay into an electron benefits from the dense brick structure given by the compact cell design, which allows the electron identification through its showering in the downstream cells (Fig. 6).

For the muonic decay mode the presence of the penetrating (often isolated) muon track allows an easier event vertex finding. The potential background from large angle scattering of muons produced in ν_μ CC interactions can be reduced to a tolerable level by applying cuts on the kink angle and on the transverse muon momentum at the decay vertex.

Hadronic decay modes have the largest branching ratio but are affected by background due to hadron reinteractions. One of the primary hadrons, in fact, can interact in the first lead plates and, if the other products of this interaction are not detected in the emulsion, it may simulate the charged single-prong decay of the τ. Strong kinematical cuts can be used to reduce this background.

An important tool for background rejection is the determination of the transverse momentum of the daughter particle with respect to the direction of the τ track candidate. For electronic τ decays the ECC technique is well suited to identify electrons and to determine their energy by measuring the density of track segments associated to their showering in the brick. For charged hadrons and muons, the

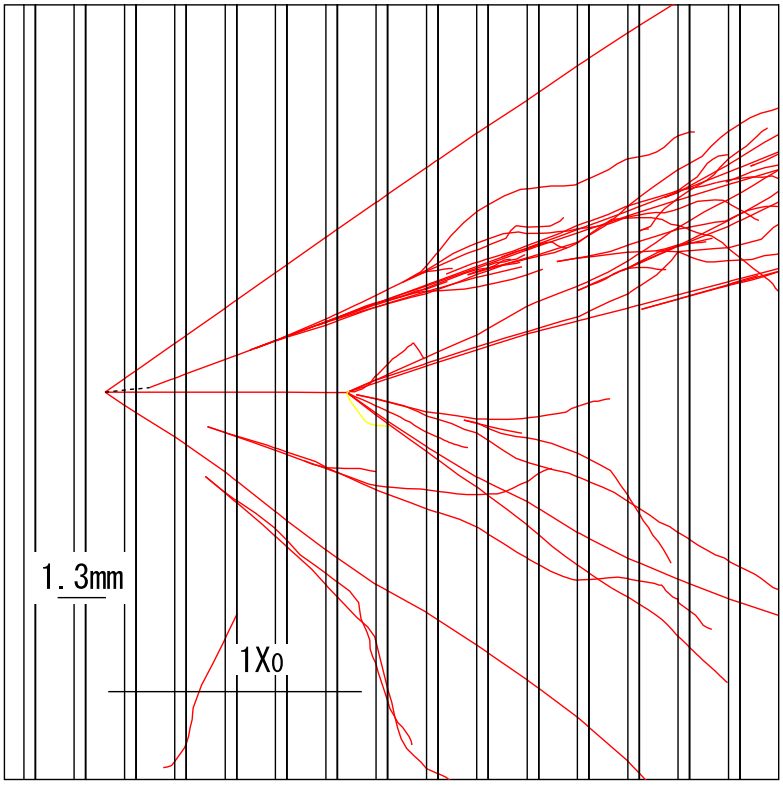

Figure 6: Simulated ν_τ event with τ decaying into electron.

momentum is deduced from the measurement of the multiple scattering in the lead plates. As discussed above, the muon momentum is also measured by the electronic detectors in a large fraction of the cases.

2.1.2 Event reconstruction with electronic detectors

Electronic detectors placed downstream of each emulsion brick wall are used to select the brick (to be removed for analysis) where the neutrino interaction took place and to guide the scanning, by defining the region of the films to be scanned. Fast and efficient scanning of the emulsion films, as by the Net Scan method described in Section 6, removes the need for a precise reconstruction of individual tracks by the electronic trackers. Therefore, a moderate spatial resolution can be tolerated, which allows to reduce the cost of the electronic trackers covering a large surface.

The target electronic detectors are also used to sample the energy of hadronic showers and to contribute to the identification and reconstruction of penetrating tracks.

The selection of the brick containing the neutrino interaction vertex is performed by combining different algorithms based on the observed transverse and longitudinal event profiles as well as on the presence of individual reconstructed tracks. As an illustration, Fig. 7 shows a simulated ν_τ event with a muonic decay for one of the two projections transverse to the beam direction. The transverse granularity of the trackers is assumed to be $2.5\ cm$.

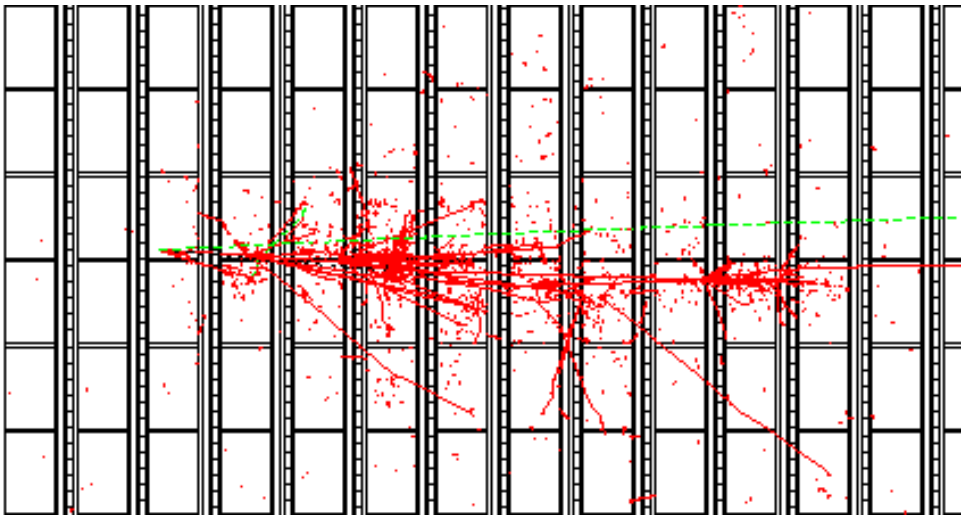

Figure 7: Display of a simulated $\tau \rightarrow \mu$ event in the OPERA target. The beam comes from the left of the figure. The primary vertex occurs in the third brick wall. Each wall of bricks is followed by the target tracker planes. These planes are oriented along the X and Y directions, perpendicular to the beam. The muon track corresponds to the longest track escaping on the right of the figure.

Fig. 8 shows the multiplicity distributions of particles traversing the tracker planes downstream of the vertex brick and downstream of the following brick wall. The simulated sample corresponds to ν_μ CC interactions. In the simulations, electron and photons have an energy above $1\ MeV$, charged

particles above 10 MeV. One can see that due the thickness of the brick ($\sim 10\ X_0$) the charged particle multiplicity significantly decreases already after the second wall.

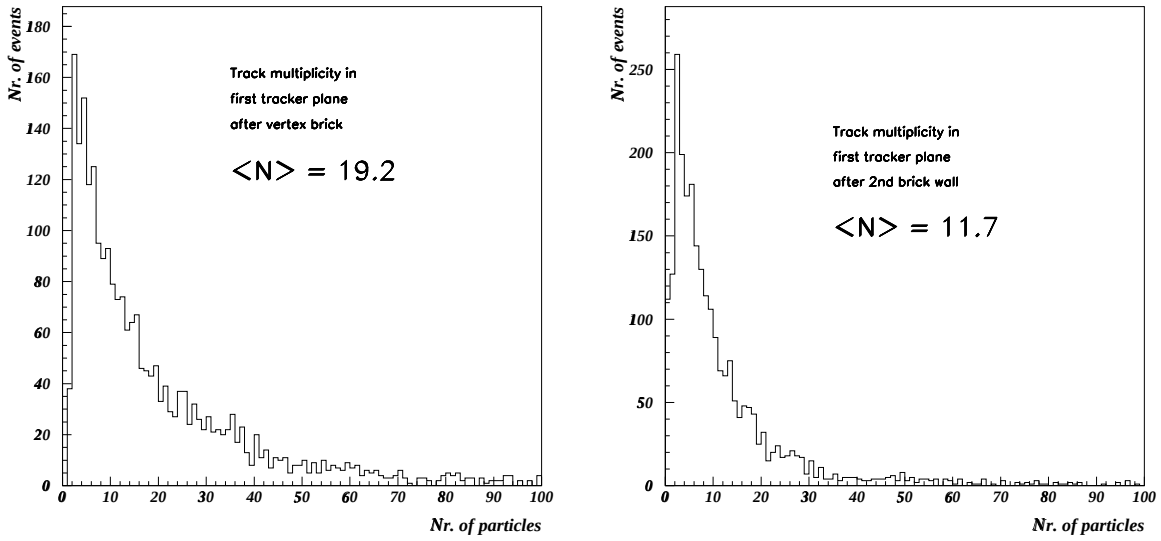

Figure 8: Left: particle multiplicity in the tracker plane immediately downstream of the vertex brick wall. Right: particle multiplicity in the tracker plane downstream of the following brick wall.

A muon spectrometer constitutes the downstream part of each detector supermodule. Its purpose is to identify muons and to measure the sign of their charge, for background rejection.

For given muon identification criteria the background on the ν_τ signal from single or associated charm production in ν_μ CC interactions is proportional to the inefficiency of identifying the primary muon (Section 7.4). The design goal is to keep this inefficiency below $\sim 5\%$, while retaining high purity for the reconstructed muon sample.

For muonic τ decay candidates the residual background from charmed particles produced in ν_μ CC interactions and decaying into muons is further reduced by the measurement of the charge of the secondary muon. The charge measurement is practically impossible for the other decay modes. The measurement of the muon momentum in the spectrometer, either by range or by curvature, complements the momentum measurement performed with the emulsion films by the evaluation of the multiple scattering in the lead/emulsion sandwich structure of the brick.

Through the measurement of the muon charge and momentum in ν_μ CC interactions, the muon spectrometers provide information on the beam, such as the total flux, the energy spectrum and the $\overline{\nu}_\mu$ contamination. Furthermore, the neutrino interactions occurring in the instrumented mass of the spectrometers contribute to the measurement of the NC/CC ratio. The sensitivity to oscillations, however, is not comparable to that obtainable by dedicated experiments (Section 7.7.2).

2.2 Detector structure and operation

A key feature of the target structure is its design which allows the prompt removal of the bricks selected on the basis of the electronic detector information and the analysis of their emulsion films during the run. A total mass of about 2000 ton is needed to meet the physics goal of the experiment. This can be obtained with three supermodules. A schematic view of the OPERA detector is shown in Fig. 9.

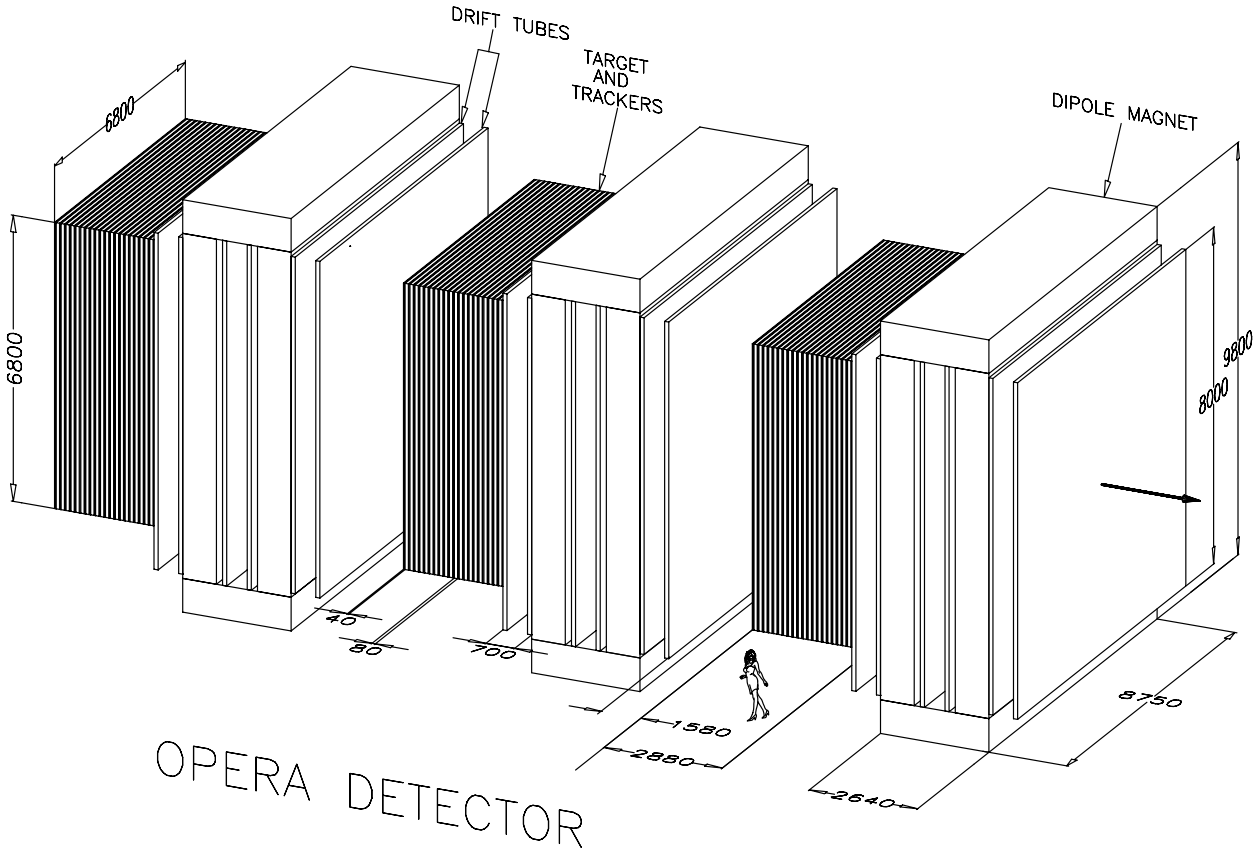

Figure 9: Schematic view of the OPERA detector.

2.2.1 Target

Each brick has transverse dimensions of $10.2 \times 12.7\ cm^2$ ($4 \times 5\ in$ squared). It consists of 56 cells with a total thickness of about 7.5 cm (10 X_0) and a weight of 8.3 kg. The dimensions of the bricks are determined by conflicting requirements. On the one hand, the integrated mass of the bricks selected and removed for analysis should represent a small fraction of the total target mass, which favours a small brick size; in addition, bricks have to be light enough for easy handling by automatic machines. On the other hand, the brick transverse dimensions should be substantially larger than the uncertainties on the

vertex position as predicted by the downstream electronic trackers. Also, losses due to edge effects are reduced with larger brick cross section.

The brick thickness in units of radiation lengths should be large enough to allow electron identification through their electromagnetic showering and momentum measurement by multiple scattering following tracks in consecutive cells. An efficient electron identification requires about $3-4\ X_0$ (see Section 6.7) and the multiple scattering requires $\sim 5\ X_0$. With a $10\ X_0$ brick thickness, for half of the events such measurements can be done within the same brick where the interaction took place, without the need to follow tracks into downstream bricks.

The brick support structure has to be sufficiently light in order to limit the number of neutrino interactions in the uninstrumented material, thereby reducing the rate of removal and scanning of *empty* bricks.

When located close to the brick edges tracks from τ candidate events might need to be followed in downstream or adjacent bricks to perform a complete kinematical analysis of the event. This requirement imposes mechanical constraints on the way bricks are assembled and installed on their support structure. The distance between consecutive walls has to be minimised, just to allow the insertion of electronic trackers. The transverse distance between bricks within the wall matrix is also kept as low as possible.

The spatial correlation of tracks in neighbouring bricks is determined by the association of hit patterns in the corresponding emulsion films. To determine these patterns with a sufficient number of connecting tracks, the number of relative brick displacements during the run must be minimised.

The module and supermodule dimensions are governed by the efficient use of the space in the underground hall. The beam size is not an issue, as its RMS value at Gran Sasso is about $800\ m$ [1]. This would justify the maximal transverse dimensions of the modules, compatibly with the need for sufficient lateral space in the underground hall for services and brick handling. One has then to provide large surface electronic detectors and iron magnets. These considerations favour a transverse target dimensions of about $6-7\ m$. The transverse shape of the target is nearly square and matches with the cross section of the muon spectrometer.

The number of modules in a supermodule, and hence its longitudinal dimension, is basically determined by the muon acceptance and thus by the maximum realistic size of the spectrometers. This limits the longitudinal length of the target in a supermodule to about $3\ m$.

According to the above requirements the target structure is foreseen as follows. A target supermodule consists of 24 modules, each made of a wall of 3264 bricks followed by two planes of electronic trackers. The module dimensions are $\sim 12\ cm$ in thickness and $\sim 6.75\ m$ side to side. The number of bricks per wall comes from a practical estimate of the dead space between bricks ($\sim 4\ mm$) which to some extent depends on the support structure. The clearance between consecutive brick walls is $3.6\ cm$, in order to accommodate the electronic trackers. This makes the total length of the supermodule target about $290\ cm$. A supermodule comprises 78336 bricks for a mass of $623\ ton$ of lead. Table 2 lists the features of a target supermodule.

Table 2: Design features of the target section of a supermodule.

Dimensions	$\sim 671\ (H) \times 675\ (V) \times 290\ (L)\ cm^3$
Cell thickness (mm)	1.3
Number of cells/brick	56
Number of emulsion films/brick	58
Brick x-section (cm^2)	10.2×12.7
Brick thickness (cm)	7.5 (packing not included)
Brick thickness (X_0)	10
Brick weight (kg)	7.9 (lead) + 0.4 (films) = 8.3
Module thickness (cm)	12
Bricks/wall	3264
Number of modules/superm.	24
Number of bricks/superm.	78336
Emulsion film surface/supermodule (m^2)	~ 59000
Target supermodule weight (ton)	623 (lead) + 29 (films) = 652

2.2.2 Electronic detectors in the target modules

The required spatial resolution of the Target Trackers is determined by the need of a high brick location efficiency. The requirement of long term reliability and the large total area to be covered (about 3000 m^2 for each transverse coordinate) restrict the choice to cost effective and mature technologies.

The baseline design foresees the use of extruded plastic scintillator strips read out by wavelength-shifting (WLS) fibres coupled to photodetectors at both ends. This technique is used, in particular, for the MINOS experiment [38] for which $\sim 28000\ m^2$ of scintillator strips have to be built. The MINOS R&D experience indicates that the technology is suitable for large scale industrial production.

Each brick wall is followed by two electronic tracker planes (with strips oriented along the X and Y axis, respectively).[6] The planes are squares of $\sim 6.7\ m$ edge-to-edge and contain 256 scintillator strips. Each group of 64 strips constitutes an independent unit read out on each side by a 64-pixel photodetector, such that 8 photodetectors are required for each tracker plane. No multiplexing scheme is foreseen.

The scintillator strip Target Trackers have the following main features

- transverse segmentation: the strips are $2.6\ cm$ wide and $1\ cm$ thick. Simulations have shown that a transverse segmentation below this value does not significantly improve the physics performance, in particular the brick finding efficiency;
- energy resolution: given the calorimetric sampling of the target structure, the expected energy resolution for hadronic showers is $0.65/\sqrt{E} + 0.16$;
- calibration: during the run, muons generated in the interaction of CNGS neutrinos in the cavern rock (rock muons), cosmics, radioactive sources and light injection systems are used;

[6] In this document the detector reference frame has the X axis horizontal and normal to the beam, and the Y axis vertical. The beam axis has a vertical slope of 5.6 $mrad$ with respect to the Z axis.

- stability and maintenance: no problem of aging is expected with scintillators;
- cost and production: the development of large area plastic scintillator detectors has shown that industrial production at relatively low cost and R&D effort is achievable.

2.2.3 Muon spectrometers

Each muon spectrometer consists of a dipolar magnet made of two iron walls interleaved by pairs of high resolution trackers. Each wall is made of 12 iron plates 5 cm thick. The iron is magnetised by a current of about 1200 A circulating in the top and bottom copper coils. The magnetic flux density in the tracking region is 1.55 T with vertical field lines of opposite directions in the two magnet walls. The transverse useful dimensions of the magnets are 8.75 m (horizontal) and 8 m (vertical) providing adequate geometrical acceptance also for muons originating in the upstream target volume.

The high resolution trackers, denoted as Precision Trackers, consist of vertical drift tube planes with an intrinsic resolution of 0.3 mm in the bending direction. Allowing for some misalignment, an overall resolution on each measured coordinate of 0.5 mm has been assumed in the following. The two tracker planes housed between the two magnet walls provide an angular measurement of the track with a 100 cm lever arm. The lever arm for the external trackers is 50 cm (Fig. 10) This design leads to a momentum resolution better than 30% in the relevant kinematical domain. Resistive Plate Chambers (RPC) with inclined strips, called XPC, are combined with the Precision Trackers to provide unambiguous track reconstruction in space.

The so-called Inner Trackers are inserted between the magnet iron plates. They are made of RPC detectors. On each face of the chambers, the induced pulses are collected by 3 cm wide pickup copper strips in the horizontal and vertical directions.

The Inner Trackers allow a coarse tracking inside the magnet to identify muons and ease track matching between the Precision Trackers. They also provide a measurement of the tail of the hadronic energy leaking from the target and of the range of muons which stop in the iron.

Fig. 10 shows a simulated ν_μ CC event occurring in the target section of a supermodule. The reconstruction of the event by the electronic detectors allows the identification of the vertex brick.

2.2.4 Detector operation

A well organised scheduling of all operations during the installation and the running of the experiment is crucial for the experiment. The different phases are briefly presented here and discussed in more detail later on. In particular, Fig. 11 illustrates the various operations to be performed from the brick extraction after the occurrence of a neutrino interaction to the emulsion film development.

Emulsion films are produced by the supplier with the required dimensions and packed into light tight packages for transportation to Gran Sasso. There, an automatic brick assembly-line stacks the lead plates and the emulsion films in a light-tight, vacuum-packed envelope on which a bar code identifies the brick for further book-keeping. The production rate is estimated at about one brick per minute. The latent images of cosmic ray tracks accumulated during production and transportation are erased by temperature and humidity controlled fading.

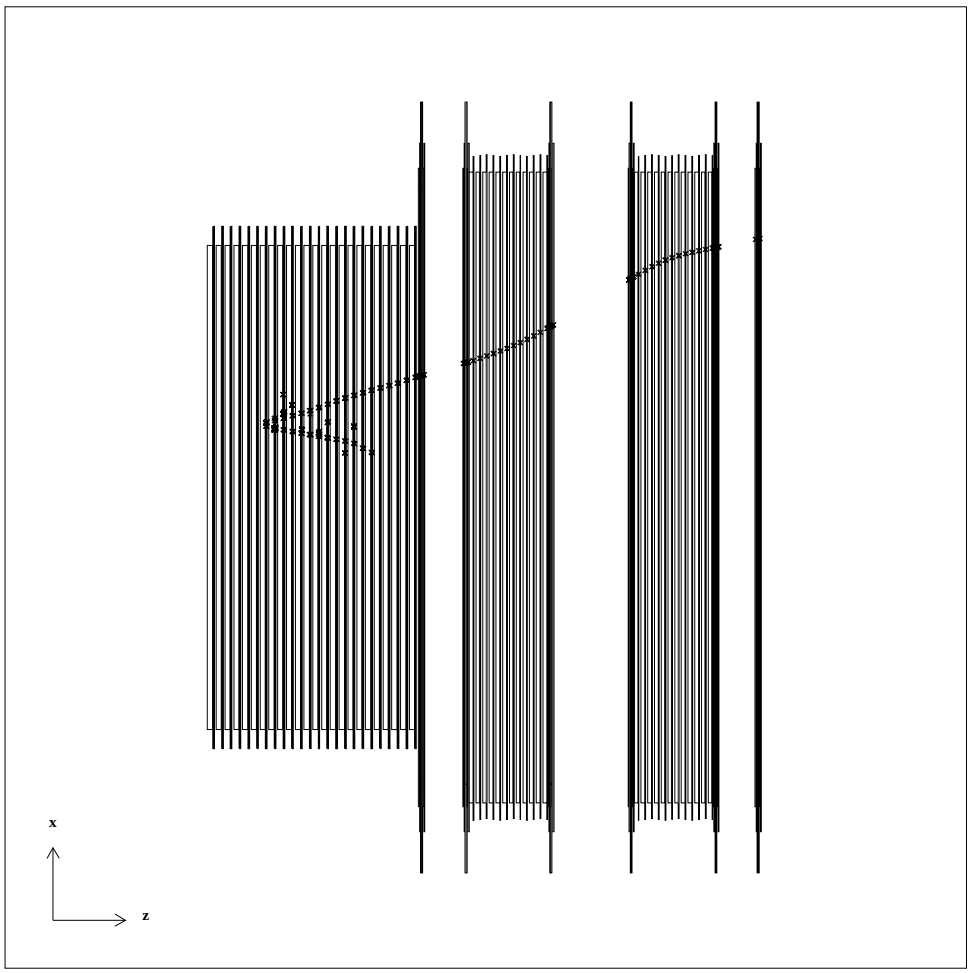

Figure 10: Simulated ν_μ CC event in an OPERA supermodule (top view). The muon is identified by the Target Trackers and by the muon spectrometer Inner and Precision Trackers. Its track is bent in the $X - Z$ plane.

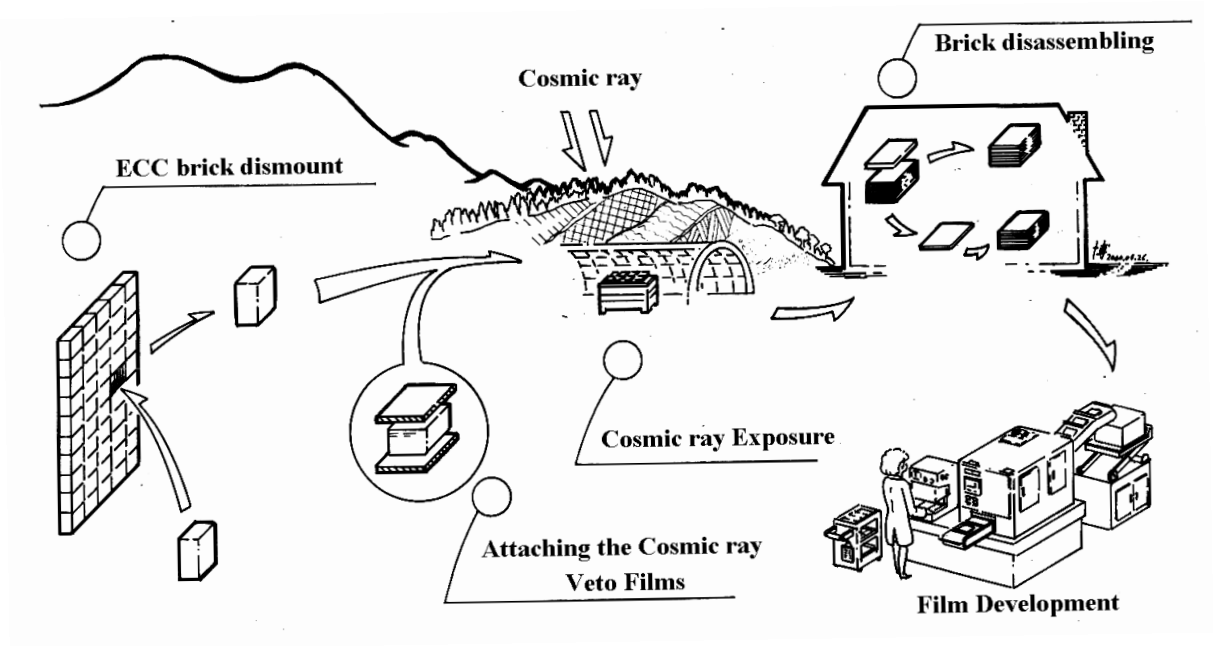

Figure 11: Illustration of the various operations from the brick extraction to the emulsion film development.

Computer controlled robots transport the bricks to their allocated positions in the target wall structure. About one year is needed to complete brick production and installation for the full detector.

During the run data from the electronic detectors are analysed by quasi-online software. The decision on which bricks need to be removed after a neutrino interaction is based on the information of the electronic detectors and is executed by the brick handling machine. About 30 ν_μ interactions per day occur in the OPERA detector (see Section 3.1).

Removed bricks are then brought to a location at a shallow depth outside the underground hall and exposed to the cosmic muon flux in order to produce a track density of about 1 track/mm^2. This provides the required pattern for the accurate alignment of the emulsion films within a brick. The alignment is essential for the momentum measurement in the brick. For this exposure, the brick lays horizontally and is covered on top and bottom by two extra emulsion films (VETO films) to allow the separation between cosmics and neutrino event related tracks. The remnant of electromagnetic showers in cosmic rays have to be suppressed by appropriate shielding.

The bricks are then unpacked and a precise map of fiducial marks together with a numbering code is printed on each film, prior to development. Automatic printing and development machines are installed in a dedicated laboratory with controlled humidity and temperature. After development, each emulsion film is packed in a plastic foil to stabilise the emulsion layer thickness and to protect it during the readout operation.

Emulsion films are then sent from the Gran Sasso Laboratory to the scanning *stations* for the neutrino interaction vertex location and the ν_τ candidate selection. These stations have the task to locate the neutrino interaction registered by the electronic detectors and to select ν_τ candidates. If the event is not found in the extracted brick, a second brick could be extracted. The removal of additional (downstream) bricks may be required for a complete analysis of decay candidate events. Most of the scanning power, *i.e.* S-UTS resources, has to be concentrated in the stations devoted to this operation, which have to be organised as scanning factories.

Events selected as τ decay candidates are then sent to dedicated scanning stations, where extensive measurements to suppress backgrounds and to confirm the τ decay topology are performed. These stations only process a small fraction of the events. Therefore, they can be located in smaller dedicated laboratories.

Since the different stations for ECC brick analysis are spread out over the world, the sharing of informations and of the different tasks have to be well organised and coordinated for an efficient and smooth operation over a long period. This is similar to the large (completely) electronic experiments, with the difference that the emulsion films, instead of DST's, play the role of data storage.

2.3 Performance of the experiment

In this Section, we briefly summarise the expected performance of the experiment, presented in detail in Section 7.

2.3.1 Signal detection efficiency and background

The signal detection efficiency of OPERA has been estimated on the basis of tests and simulations. The latter have been tuned with data obtained in emulsion experiments such as CHORUS and DONUT.

All single-prong τ decay modes are used to search for the so-called long τ decays. These are events in which the τ track is long enough to exit the lead plate where the primary vertex occurs. Short decays (in which the τ track is contained within the vertex plate) are considered for the $\tau \rightarrow e$ channel.

Long decay candidates are selected by detecting a kink topology and short decays by exploiting an impact parameter method. Kinematical cuts are applied to both samples in order to enhance the signal to background ratio.

The $\tau \rightarrow e$ decay mode is identified by the distinctive energy loss of the daughter electron in the lead/emulsion brick structure. The main background to this channel is given by charm production in ν_μ CC interactions undergoing electronic decay and with the primary muon escaping detection.

Muonic τ decays are characterised by an identified muon originating from the τ track kink. For these events the main background is constituted by large angle muon scattering in the lead plates.

Hadronic decay candidates are defined as those events in which the kink daughter particle is not identified either as an electron or a muon. In this case, charm production with subsequent hadronic decay and hadronic reinteractions in lead give a similar contribution to the background.

Table 3: Expected numbers of τ and background events collected by OPERA in five years of data taking ($2.25 \times 10^{20} pot$). Signal events are given for full mixing and for three values of Δm^2: the most recent best fit by Super-Kamiokande [30] and the two 90% CL limits. 22 events would be observed for the previous best fit value ($\Delta m^2 = 3.5 \times 10^{-3}\ eV^2$ [28]).

τ decay mode	Signal ($1.5 \times 10^{-3} eV^2$)	Signal ($3.2 \times 10^{-3} eV^2$)	Signal ($5.0 \times 10^{-3} eV^2$)	BG
e^- long	1.3	5.9	14.2	0.16
μ^- long	1.3	5.7	13.8	0.13
h^- long	1.1	4.9	11.8	0.25
e^- short	0.4	1.8	4.3	0.03
Total	4.1	18.3	44.1	0.57

The different factors determining the efficiency are described in Section 7.3. Weighing each channel by its branching ratio, the total τ decay detection efficiency amounts to 8.7%.

2.3.2 Signal and sensitivity to oscillations

Under the assumption of five years of running in the CNGS beam, operated in shared mode and with nominal beam intensity (see Section 3.1), OPERA will collect the number of signal and background events listed in Table 3 for different Δm^2 values and maximal mixing, according to the most recent Super-Kamiokande results [30]. The signal/background ratio ranges from 7 to about 80.

The OPERA sensitivity at the 90% CL is shown in Fig. 12 together the most recent result of a global fit to the Super-Kamiokande data from atmospheric neutrinos [30]. At the 90% CL the parameter region allowed by Super-Kamiokande covers the Δm^2 range of $1.5 - 5 \times 10^{-3}\ eV^2$, instead of $2 - 6 \times 10^{-3}\ eV^2$ as in the previous fit [28]. The central value of $3.2 \times 10^{-3}\ eV^2$ is a little lower than the previous one, $3.5 \times 10^{-3}\ eV^2$.

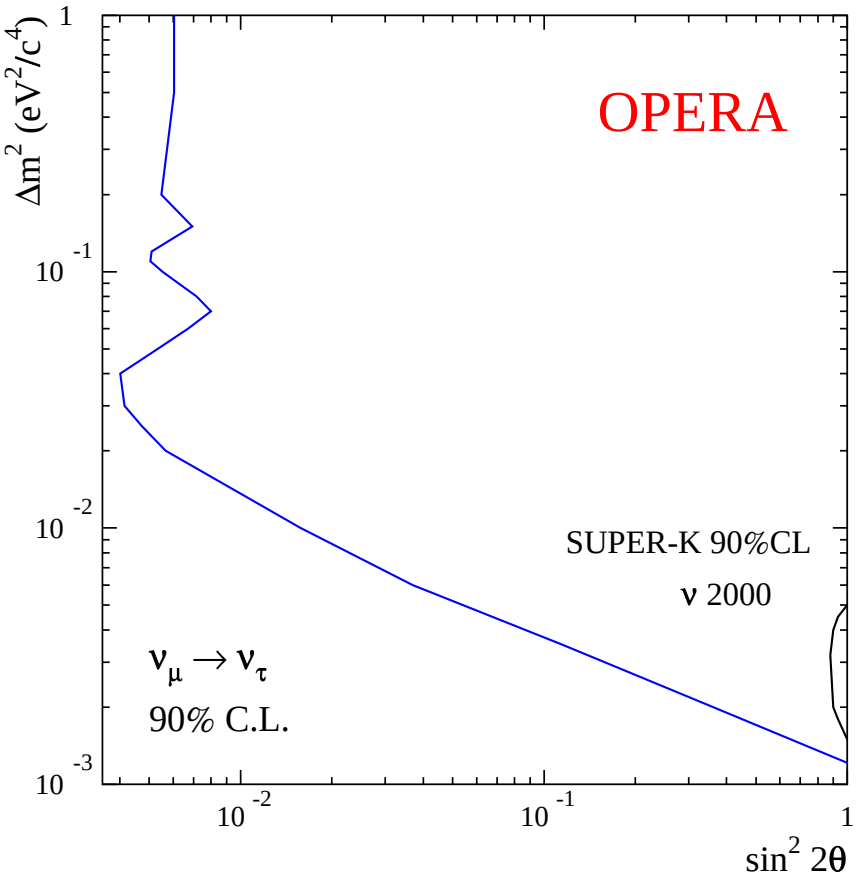

Figure 12: OPERA sensitivity to $\nu_\mu \leftrightarrow \nu_\tau$ oscillations for 5 years CNGS running, defined as the 90% CL upper limit obtained in the case of a negative search. The region allowed by the Super-Kamiokande data [30] is also shown.

3 The CNGS neutrino beam

3.1 The beam layout

The original CNGS *reference* neutrino beam from the CERN SPS to the Gran Sasso is described in [1]. A further optimisation of the ν_τ interaction yield was presented in [57]. It contributed to the new significantly improved CNGS beam design developed by the CERN/INFN Technical Committee [58], to which we refer presenting the OPERA performance.

Compared to [1], the present civil engineering design of the CNGS facility is unchanged. Only the tuning of the focusing elements downstream of the production target is modified.

A schematic overview of the CNGS reference beam is shown in Fig. 13. SPS protons hit a graphite target made of rods, for an overall target length of $2\,m$, producing secondary pions and kaons. The target rod diameter is $4\,mm$ so that the proton beam is well contained within the target. The diameter was $3\,mm$ in the original CNGS design. Such an increase reduces spurious background from residual protons interacting later in the beam line, without significantly affecting the ν_μ flux and energy spectrum. The thermo-mechanical properties of the target rods under shock from the proton beam impact are slightly improved by the increased rod diameter.

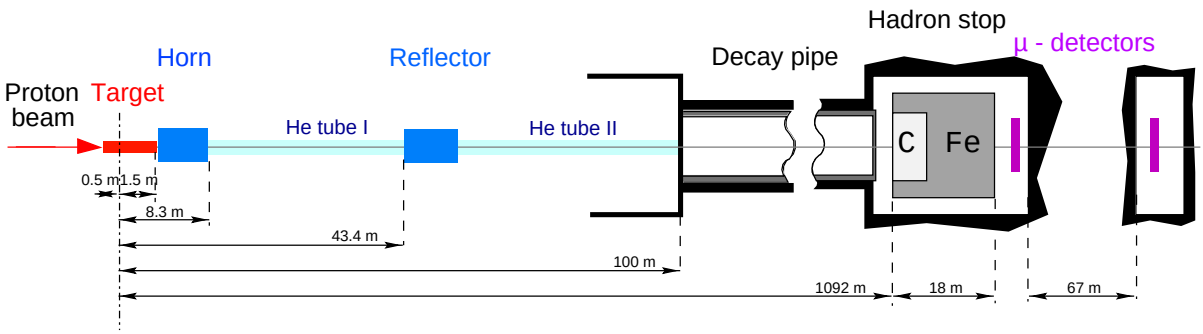

Figure 13: Layout of the CNGS reference beam. The coordinate origin is the focus of the proton beam.

The first coaxial lens, the horn, starts at $1.7\,m$ from the focus of the proton beam. The second one, the reflector, is $43.4\,m$ downstream of the focus. The nominal current for both horn and reflector is $150\ kA$. Prototype tests have demonstrated the feasibility of using electron beam welding to assemble the inner conductor elements of the magnets, rather than the bolted flanges previously used for the West Area Neutrino Facility (WANF).

Helium tubes are placed in the free spaces of the target chamber in order to reduce the interaction probability for secondary hadrons. A first tube is located between the horn and reflector, while a second one fills the gap between the reflector and the decay tunnel. A detailed view of the target/horn region is shown in Fig. 14.

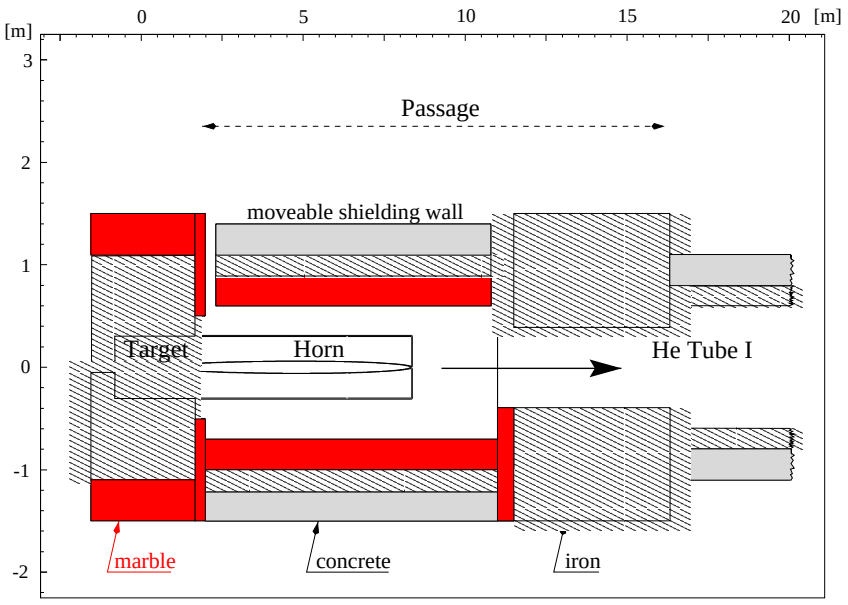

Figure 14: Close-up on the region around target and horn.

Pions and kaons focused by the optics are then directed towards a decay tunnel to produce the neutrino beam. The typical π decay length ($2.2\ km$ at $40\ GeV/c$) makes a long decay tunnel justified. Given the angular distribution of the parent mesons, the longer the decay tunnel the larger must its diameter be. A tunnel of $2.45\ m$ diameter and $1000\ m$ length has been chosen for the CNGS. A massive iron hadron stopper is situated at the exit of the decay tunnel.

The signals induced by muons (from meson decays) in two arrays of silicon detectors placed in the hadron stopper are used for the online monitoring and the tuning of the beam (steering of the proton beam on target, horn and reflector alignment, etc.). The separation of the two arrays, equivalent to $25\ m$ of iron, allows a rough measurement of the muon energy spectrum and of the beam angular distribution.

3.2 SPS operation and proton yield

The SPS proton beam intensity is one of the main ingredients needed to achieve the physics goal of our experiment. However, the CNGS target constraints have to be taken into account. In addition, for a realistic evaluation of the SPS performance, the requests from the LHC operation as well as those from the SPS fixed-target users have to be considered.

The boundary conditions for the SPS running have been analysed in [58] after the publication of the original CNGS Technical Design Report [1]. It was realised that the RF acceleration time could be shortened by $0.2\,s$, allowing to reduce the length of the CNGS cycles with two fast extractions at $400\,GeV/c$ from 6.2 to $6.0\,s$. This brings an appreciable gain in the number of protons on target (pot)

per year of operation because the SPS cycle must be a multiple of the PS cycle time ($1.2\,s$) and so it goes from $7.2\,s$ [1] to $6.0\,s$.

Two possible CNGS running modes are envisaged: i) the *shared mode*, in which both CNGS and fixed-target users are supplied with protons; ii) the *dedicated mode*, in which the CNGS is the only user. By assuming a 400 GeV/c proton beam and 200 days of running per year, the expected number of *pot* is $4.5 \times 10^{19}/year$ in the shared mode and $7.6 \times 10^{19}/year$ in the dedicated mode [58]. These estimates assume the SPS operation performance achieved in the past years of running with the WANF, namely a peak intensity of 4.8×10^{13} protons per cycle with an overall machine efficiency of 55%.

A possible SPS cycle corresponding to the shared operation mode is described in Fig. 15. Fig. 16 shows a cycle for the dedicated mode. Protons for the CNGS are extracted in 10 μs long spills.

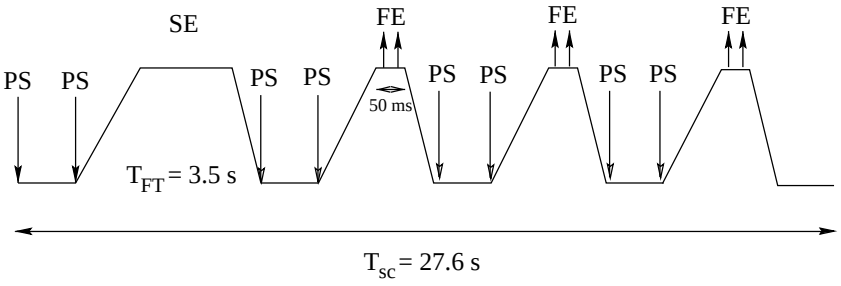

Figure 15: Possible SPS supercycle for shared operation mode. The flat top corresponds to 400 GeV/c.

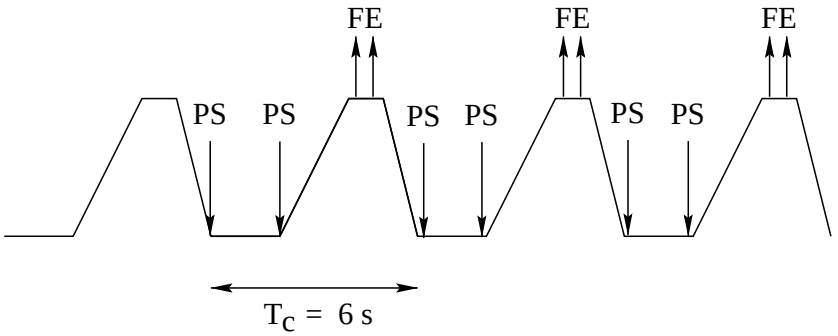

Figure 16: Possible SPS supercycle for dedicated operation mode. The flat top corresponds to 400 GeV/c.

3.3 Neutrino spectrum and interaction rate

The nominal CNGS beam features with the new design given in [58] are summarised in Table 4. The referred to numbers of neutrino CC interactions include deep-inelastics (DIS) and quasi-elastics plus resonances (QE). The expected rate of ν_τ CC interactions for $\sin^2 2\theta = 1$ and three values of Δm^2 are shown in Table 5.

Table 4: Nominal performance of the CNGS reference beam [58].

ν_μ (m^{-2}/pot)	7.45×10^{-9}
ν_μ CC events/pot/kton	5.44×10^{-17}
$\langle E \rangle_{\nu_\mu}$ (GeV)	17
ν_e/ν_μ	0.8 %
$\overline{\nu}_\mu/\nu_\mu$	2.0 %
$\overline{\nu}_e/\nu_\mu$	0.05 %

OPERA expects about 32000 neutrino interactions (including all neutrino flavours and NC events) in a five year run with a ~ 2 $kton$ detector mass. This correponds to about 30 events per day with shared beam operation. The number of interacting ν_τ for $\sin^2 2\theta = 1$ and $\Delta m^2 = 3.2 \times 10^{-3}$ eV^2 is ~ 240.

Fig. 17 shows the ν_μ flux and the ν_μ CC energy spectrum of the CNGS beam. Fig. 18 shows the flux of the other neutrino flavours.

Table 5: Number of ν_τ CC interactions at Gran Sasso per $kton$ and per year (shared mode). The expectation for $\Delta m^2 = 10^{-3}$ eV^2 and $\sin^2(2\theta) = 1$ is given [58] together with the corresponding numbers at higher Δm^2.

Δm^2	ν_τ CC interactions/kton/year
1×10^{-3} eV^2	2.48
3.5×10^{-3} eV^2	30.4
5×10^{-3} eV^2	62.0

A further increase of the the CNGS neutrino flux and fine-tuning of the beam spectra to match the characteristics of the Gran Sasso experiments will certainly be beneficial for the $\nu_\mu \leftrightarrow \nu_\tau$ appearance programme of the CNGS project.

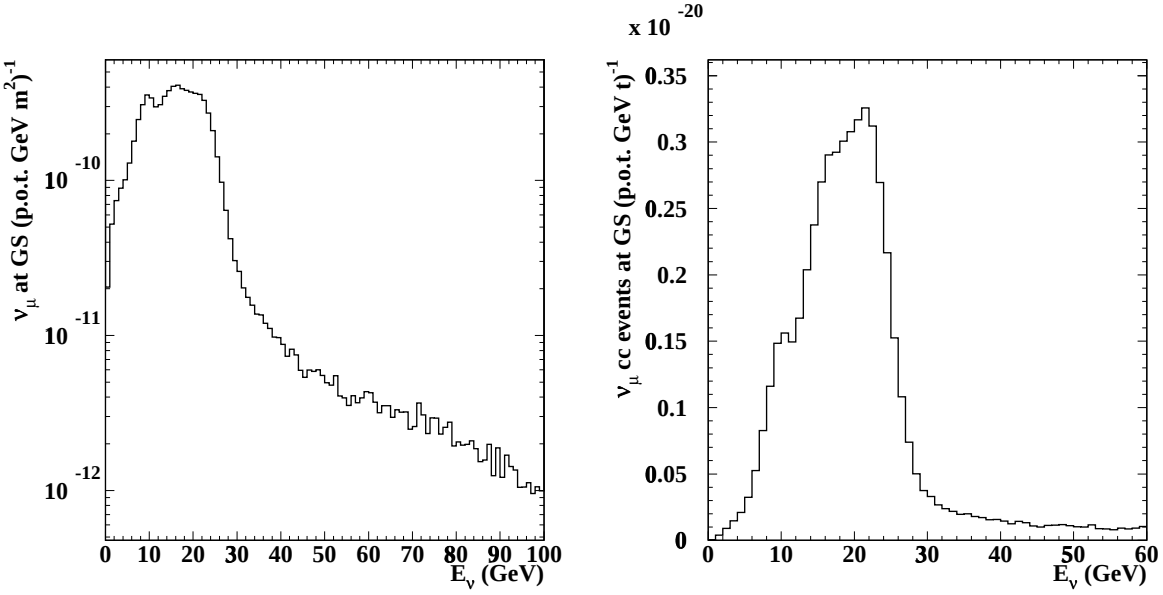

Figure 17: Left: the CNGS ν_μ flux at the Gran Sasso. Right: the ν_μ CC energy spectrum.

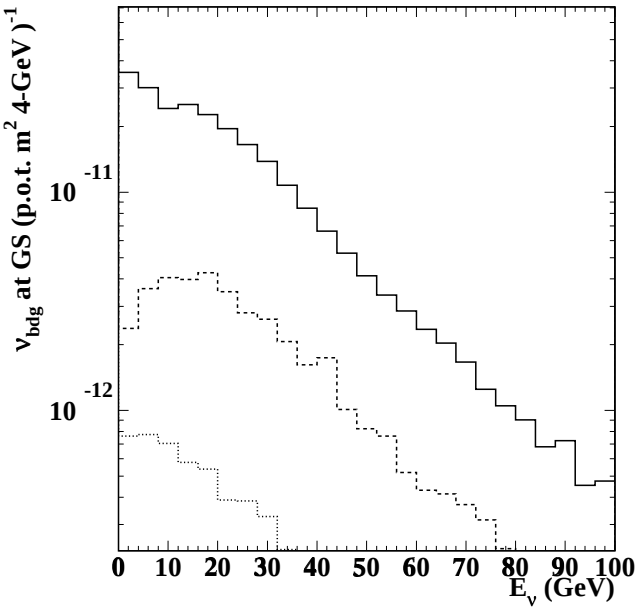

Figure 18: CNGS $\overline{\nu}_\mu$ (continuous line), ν_e (dashed) and $\overline{\nu}_e$ (dotted) fluxes.

3.4 Beam monitoring at Gran Sasso

In Section 5.7 we discuss the capability of the OPERA detector in measuring the hadronic shower produced in neutrino interactions. Together with the muon momentum measurement, this feature allows to infer the energy of the incoming neutrino, which can be used, in particular, to monitor the beam spectrum.

The neutrino energy resolution is different for ν_μ CC and ν_μ NC events. For CC events the muon momentum is measured in the spectrometer with a resolution of $20-30\%$. If the muon is soft enough to be stopped inside the detector, its momentum is deduced from the total range with a resolution of better than 10%. The neutrino energy is obtained by adding the muon energy to that of the hadronic shower produced in the interaction. The comparison of the reconstructed and generated energy for simulated ν_μ CC events shows that the shape of the neutrino energy distribution is well reproduced (Fig. 19). A resolution of $\sim 20\%$ is obtained (Fig. 20).

For ν_μ NC events the escaping neutrino makes the energy measurement of the incoming lepton difficult. A resolution of about 35% is obtained by a parametrisation of the incident neutrino energy as a function of the measurable hadronic energy.

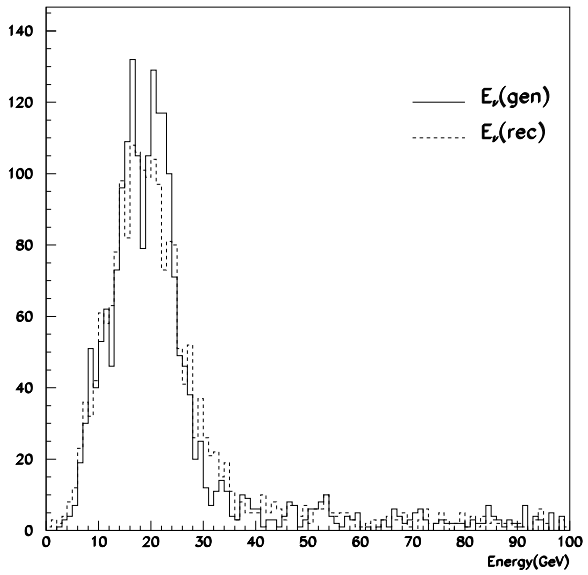

Figure 19: Generated (continuous line) and reconstructed (dashed line) CNGS ν_μ energy spectrum (see text for details).

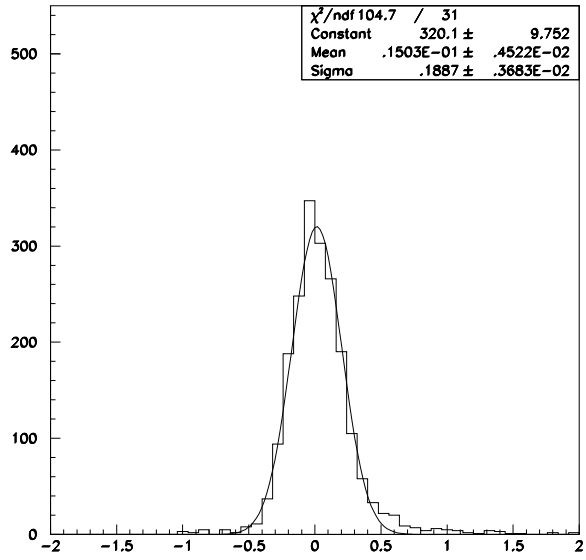

Figure 20: The difference between reconstructed and generated energy for simulated ν_μ CC events.

4 The detector

4.1 Detector configuration and choice of baseline options

The Progress Report [6] submitted in 1999 to the Scientific Committees outlined the design of an experiment sensitive to ν_τ appearance in the parameter region indicated by the atmospheric neutrino signal. Different detector options fulfilling the physics requirements were considered. Our main efforts have since then been devoted to the definition of a baseline experiment design with cost effective solutions and a reduced need for R&D studies.

In particular, two different kinds of brick structures were envisaged in [6]: the so-called *spacer* and *compact* bricks. The main features of spacer bricks can be found in Section 9 and in [3–6]. Their cell structure includes a low density spacer of 3 mm thickness. The low density material minimises the probability of reinteractions allowing to reduce the corresponding backgrounds.

On the other hand, compact bricks have the advantage of a denser brick structure, optimal for the identification of the $\tau \rightarrow e$ decay mode and for the measurement of charged particle momentum by the multiple scattering method. Because of this capability, the hadron reinteraction background in compact bricks can be suppressed by kinematical cuts. For a given emulsion surface, compact bricks also provide a larger target mass and their mechanical rigidity ensures a better parallelism of the emulsion films.

The above arguments, together with the existing experience with similar detectors (DONUT), leads us to propose as a baseline option a setup made up of three compact brick supermodules. A total lead mass of about 2 $kton$ can be obtained with a surface of emulsion films similar to what foreseen in [6].

Baseline options have also been identified for the magnet (dipole), for the spectrometer Inner Trackers (RPC detectors), for the spectrometer Precision Trackers (drift tubes) and for the Target Trackers (scintillator strips). In all cases, the decision has been driven by the physics requirements, by consideration of cost effectiveness and by the needs of large scale production and reliable long term operation.

4.2 The ECC bricks

4.2.1 ECC brick structure

About 235000 ECC bricks compose the OPERA detector. A schematic drawing of a brick is shown in Fig. 21. Its structure is obtained by stacking 56 1 mm thick lead plates interleaved with thin emulsion films. Each film has 50 μm thick emulsion layers on both sides of a 200 μm thick plastic base. An extra emulsion film in front of the first lead plate helps in connecting tracks from the upstream wall. Another film, called Special Sheet (SS) is placed at the most downstream part, separated from the 56^{th} film by a 2 mm thick plastic plate. This allows to preserve the τ decay detection efficiency for events occurring in the last lead plate.

The brick-stack is kept together by the so-called *origami* packing method, a technique used in previous emulsion experiments. A photograph of a prototype brick packed with origami is shown in Fig. 22. The packing material is an aluminium-coated paper closed under vacuum by thermo-sealing. The paper quality is selected in order to avoid chemical contamination which could affect the emulsion sensitivity.

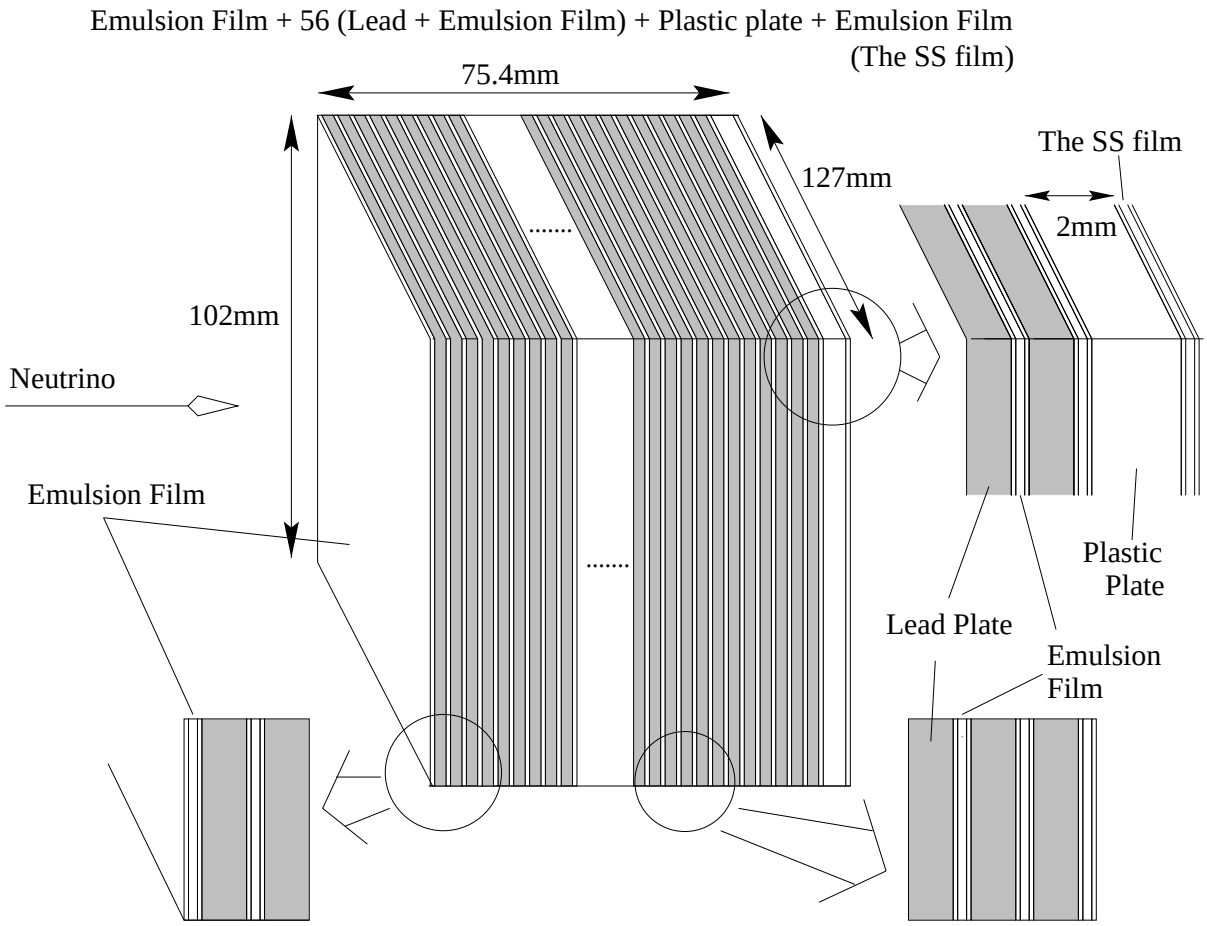

Figure 21: Schematic structure of the OPERA ECC brick.

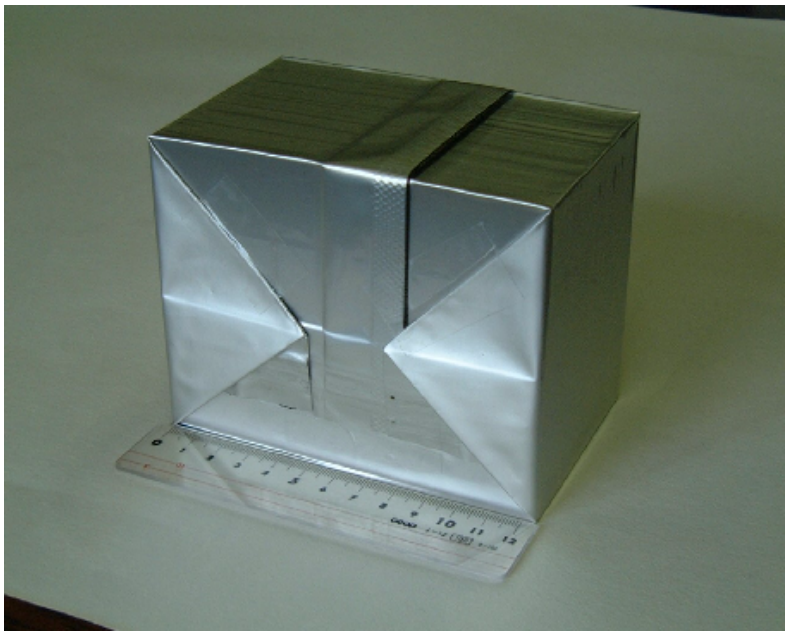

Figure 22: A photograph of an ECC brick with *origami* packing.

Due to the thin aluminium layer and to thermo-sealing, the inner pressure and humidity are kept stable. The inner pressure is less than 0.1 atmosphere. This can be achieved by conventional vacuum packing techniques. The hermeticity of the packing has been checked over long periods, as demonstrated by existing samples packed more than ten years ago.

The vacuum packing also helps maintaining the brick mechanical stability. Under the atmospheric pressure, the sandwich structure can well resist external mechanical constraints, because of the friction between plates. In addition, slipping between plates due to the difference of the thermal expansion coefficients between emulsion films and lead plates is suppressed by the vacuum packing.

The maximum tolerable temperature variation (ΔT) can be expressed as follows

$$\Delta T_{max} = \frac{2 \cdot F}{E \cdot A \cdot \Delta k}$$

where F is the friction force between the lead plate and the film, E is the Young's modulus of the film ($3 \times 10^4\ kgf/cm^2$), A is the thickness of the film and Δk is the difference of the thermal expansion coefficient between the lead plate and the film ($k(lead) \sim 30 \times 10^{-6}$, $k(film) \sim 50 \times 10^{-6}$). Here F is expressed as $\mu \times N$, μ is the friction coefficient and N is the force supplied by the vacuum packing. The friction coefficient is measured to be $0.31 - 0.34$ at $N = 0.2\ kgf/cm^2$ in the case of lead plates and emulsion films.

The mechanical properties of the film are governed by the characteristics of the plastic base (cellulose triacetate). For an inner pressure of 0.1 atm, which corresponds to a force of $\sim 0.9\ kgf/cm^2$, ΔT is estimated to be about 50^oC.

We performed beam tests in order to confirm the above calculations. The results indicate that the plate position can be kept within the emulsion track measurement errors, even for temperature variations as high as 20^oC.

An alternative packing method based on the use of plastic boxes is being studied and is described in Section 9.1.2.

4.2.2 Emulsion films

The total area of emulsion films in the OPERA detector is $\sim 176000\ m^2$. This corresponds to 18 m^3 of dried emulsion gel. For comparison, the amount of emulsion handled for CHORUS is equivalent to a surface of 500 m^2 and to a 0.4 m^3 total volume of dried emulsion.

The emulsions used for CHORUS were poured by hand following standard procedures developed in many years of experience. This operation lasted about six months and involved several skilled persons. The same procedure applied to OPERA would be prohibitively time consuming. To overcome this problem, a R&D project is jointly being carried out by Nagoya University and the Fuji Film company[7] to establish the process of automatic coating of nuclear emulsion films. After several tests, it is confirmed that the OPERA emulsion film can be produced by commercial photographic film production lines. The required amount of films needed for the experiment will be produced within one or two years. Fig. 23 shows the cross sectional view of the newly developed machine-coated emulsion film.

As opposed to hand-made films, the thickness can be precisely controlled as in the case of commercial color films. We measured the film emulsion layer thickness after development, as shown in Fig. 24. The σ of the distribution is $\sim 1.3\ \mu m$. This result can be compared with the Z coordinate measurement error of the scanning system ($\sim 50\ \mu m/16\ layer/\sqrt{12} \sim 0.9\ \mu m$). For comparison, in the case of the CHORUS and DONUT hand-made films with nominal emulsion thickness of 100 μm, variations of up to a factor two were observed.

As shown in Fig. 23, each film has a protective gelatin layer of 1 μm thickness on the sensitive layers. This prevents the occurrence of black or gray patterns on the emulsion surface. Fig. 25 shows a photograph of the surface of a machine-coated film and of a hand-poured emulsion plate after development. The black patterns, frequently emerging in the case of hand-poured plates, are due to silver chemically deposited during the development. The removal of these stains had been the most time-consuming task in the emulsion preprocessing for the experiments performed so far. By means of the protective coating, surface cleaning is not needed anymore and the preprocessing procedure becomes compatible with the daily handling of thousands of emulsion films, as in the case of OPERA.

In addition, the presence of this protective layer allows direct contact with the lead plates. Without this protection, one would have to insert thin insulator sheets in order to avoid chemical reactions between the lead plates and the silver halides contained in the emulsion. We are performing tests on the film/lead

[7]Fuji Film, Minamiashigara, 250-0193, Japan.

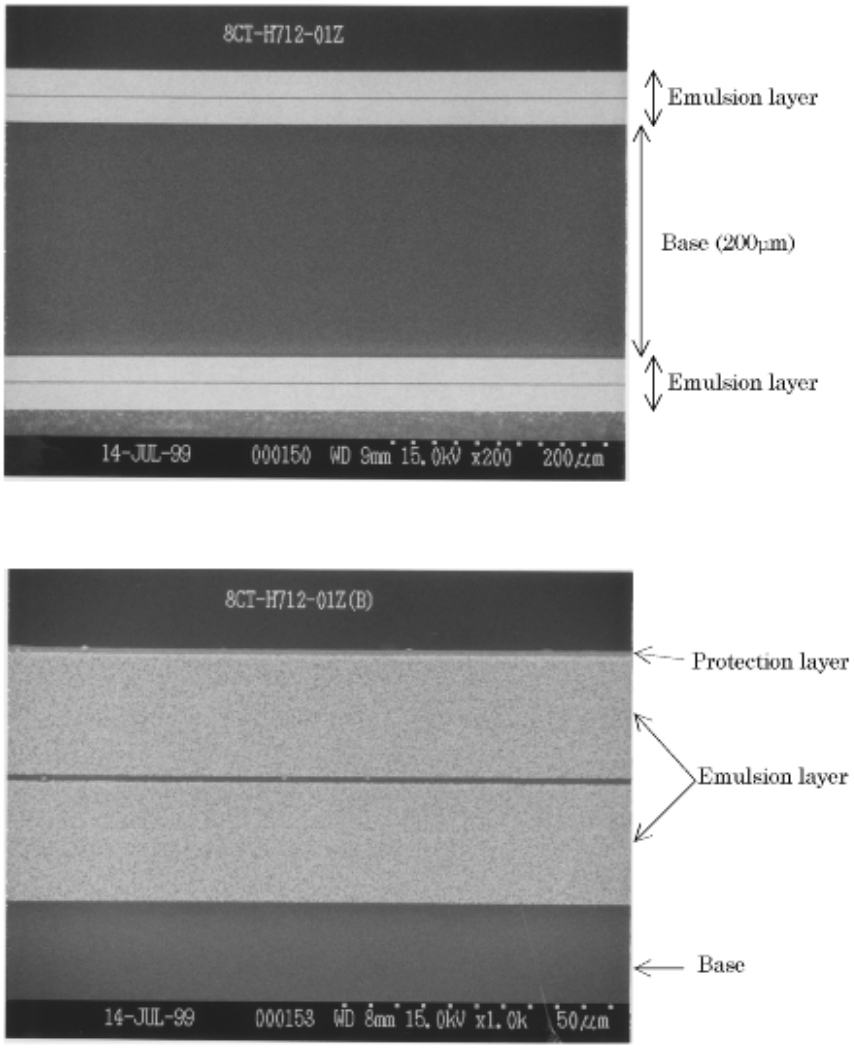

Figure 23: Top: photograph of the cross section of a machine-coated emulsion film. The picture was taken by an electron microscope. Diluted emulsion layers of 50 μm thickness are coated on both sides of a 200 μm thick triacetate base. Bottom: enlarged view of the top emulsion layer. A thin ($\sim$ 1 μm) protective film (gelatin) is placed over the emulsion layer at the same time of coating.

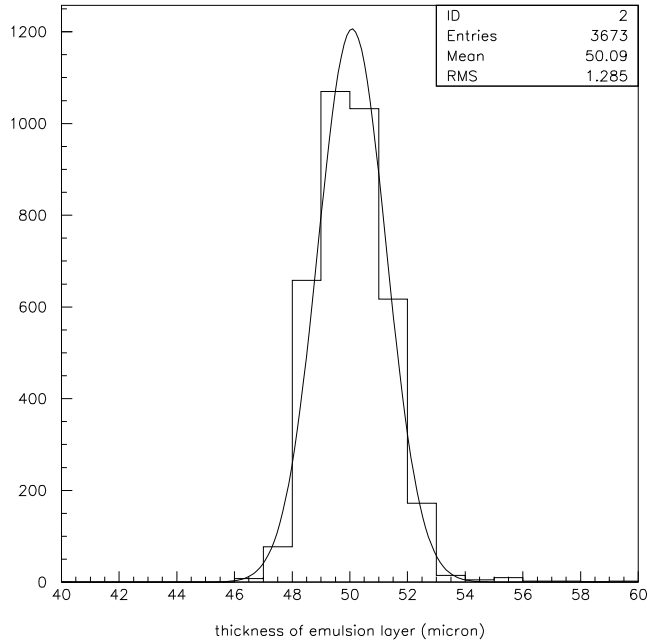

Figure 24: Film thickness distribution after development. Four films have been measured. For each of them, the emulsion layer thickness is measured in 16×15 points over a surface of $3\ cm \times 3\ cm$ (nearly at the film centre).

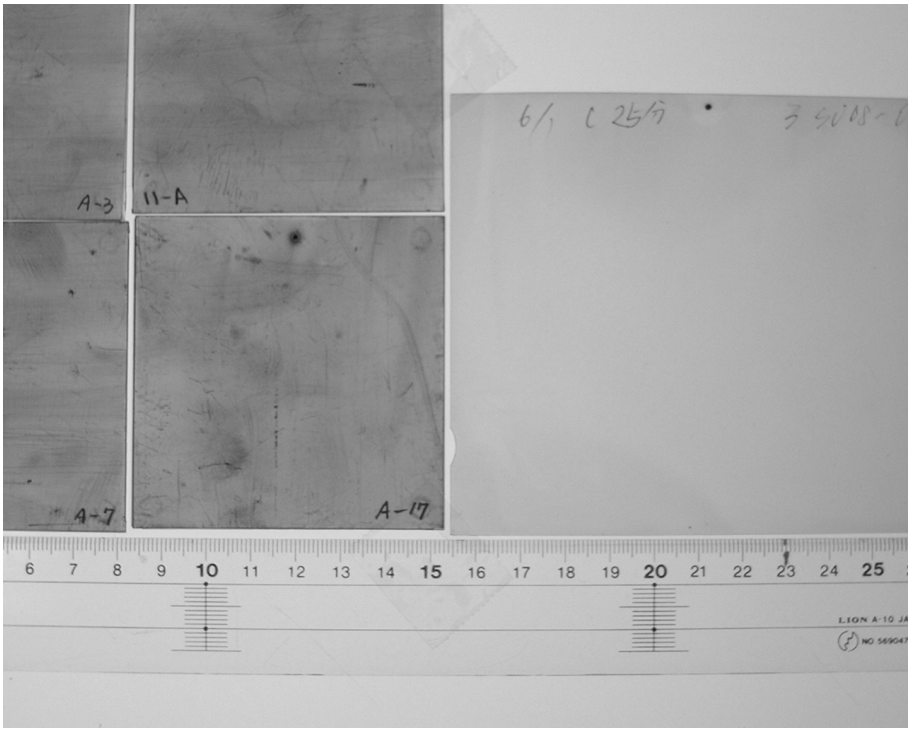

Figure 25: Left: hand-poured emulsion plates after development. The thickness of the emulsion layers is $\sim$ 100 μm on both sides of a 200 μm plastic base. Right: surface of a machine-coated film after development. No surface silver is visible in this case. The small spot marked at the upper side is due to a pressure mark of a clip used during development.

contact at different temperature and humidity conditions. So far, we have not observed any effect on the film surface, such as chemical aggression to the protective layer.

A micro-photograph of the cross section of the machine-coated emulsion layer is shown in Fig. 26. Each individual crystal acts as an independent particle detector. After development the particle trajectory can be recognised as aligned grains, as shown in Fig. 27.

For automatic coating some dilution of the gel is required. Under normal conditions, the grain density, defined as the number of grains per 100 μm along the particle trajectory, decreases almost linearly with the dilution factor although part of the sensitivity loss may be regained in the development phase. This problem has been solved by increasing the sensitivity of each crystal using the technology of crystal growth developed for standard photographic films.

As shown in Fig. 26, the crystal diameter distribution in the emulsion layer is rather uniform around 0.20 μm. The currently achieved grain density of the machine-coated emulsion films is 30 grains/100 μm even in the case of a factor of two dilution. One can compare this feature with the 34 grains/100 μm of the ET7B gel (without dilution) used for CHORUS and with the 28 grains/100 μm of ET7C (without dilution) used for the DONUT experiment.

The so-called emulsion fog is due to accidental grains randomly distributed in the emulsion volume (Fig. 27). They constitute a background which has to be kept at the level of ≤ 5 fog /1000 μm^3. This can be achieved by applying a moderate development to the emulsion films, still keeping a sufficient sensitivity of ~ 30 grains/100 μm, as shown in Fig. 28.

The intrinsic position resolution of the emulsion films can also be investigated by measuring the position residuals of the centre of each grain with respect to a fitted straight line. The result is shown in Fig. 29. The measured resolution of $\sigma \sim 0.06$ μm can be compared with the expected value of 0.058 $\mu m \sim 0.2$ $\mu m/\sqrt{12}$, where 0.2 μm is the diameter of the original crystal. This result implies that the crystal uniformly grows under development up to a grain with diameter of ~ 0.6 μm. This intrinsic resolution can be compared with that of ET7B, $\sigma \sim 0.074$ μm.

The physics properties of the emulsion layer are the following: density $\rho = 2.40$, average atomic number $< A >= 18.2$, average atomic charge $< Z >= 8.9$ ($< Z^2 >= (16)^2$), radiation length $X_0 = 5.5$ cm, $(\frac{dE}{dx})_{mip} = 1.55$ $MeV/g/cm^2$ or 37 $keV/100$ μm, nuclear collision length $\lambda_T = 33$ cm and nuclear interaction length $\lambda_I = 51$ cm.

The measured range of α particles emitted from internal emulsion radioactivity (^{212}Po,$E(\alpha) = 8.785$ MeV) is 74 μm, which is about 1.45 times longer than for ET7B. This value is quite consistent with the ratio

$$\frac{(dE/dx)^{ET7b}_{mip}}{(dE/dX)^{Newgel}_{mip}} \sim 1.47$$

Compared with ET7B, the new gel is better suited for particle tracking purposes because of its lower density.

The base material of the films is cellulose triacetate (TAC), which is one of the commonly used base materials for photographic films. There are other materials available for commercial films, such

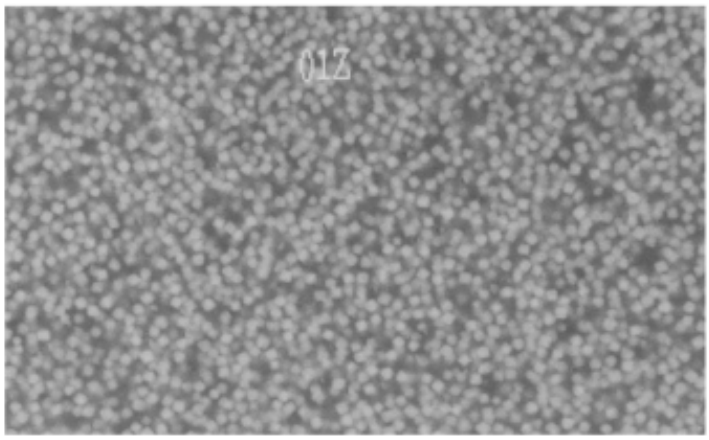

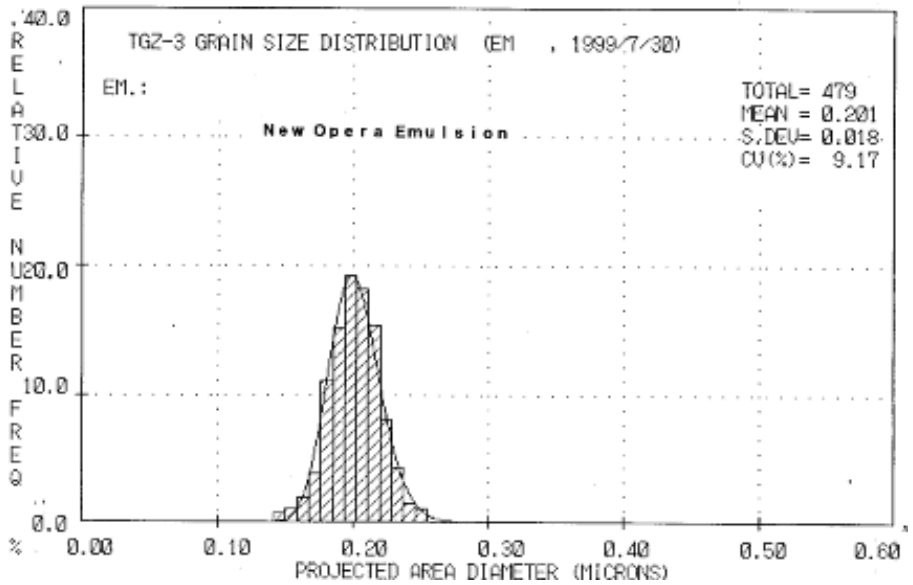

Figure 26: Top: micro-photograph of the crystals distributed in the emulsion layer. Micro crystals can be recognised as white grains. Bottom: crystal diameter distribution.

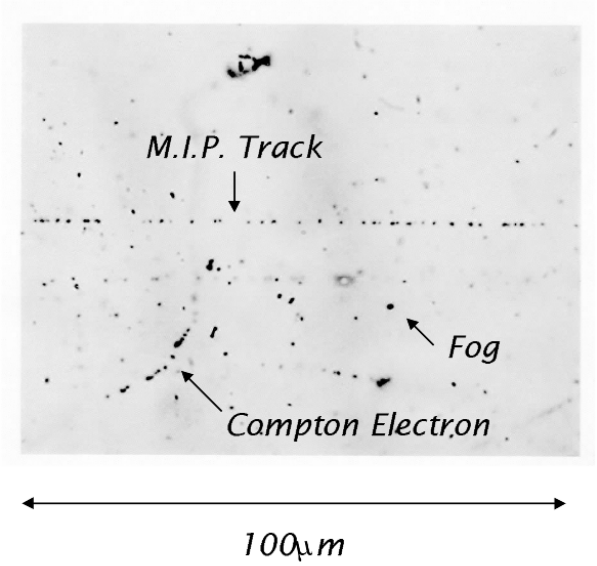

Figure 27: Photograph of a minimum ionising particle (*mip*) recorded in an emulsion layer. The grain density is defined as the number of grains per 100 μm track; the fog density as the number of fog grains per 1000 μm^3.

as poly-ethylene-terephthalate (PET), which has better mechanical properties than TAC. However, the microscopic image observed through a typical PET base may have serious problems caused by disuniformities of the optical features of micro structures in the plastic.

TAC has no special problems. Its physics properties are: density $\rho = 1.28\ g/cm^3$, optical index $n = 1.48$, radiation length $X_0 = 31\ cm$, nuclear collision length $\lambda_T = 47\ cm$ and nuclear interaction length $\lambda_I = 67\ cm$.

Emulsion films distortions have also been investigated. Distortion is a phenomenon which shifts the position of the recorded trajectories in the emulsion layer because of stresses accumulated in the gelatin layer. In hand-made emulsion plates, shifts of several μm are frequently observed, caused by a disuniform drying at the plate production.

The distortion affects the efficiency in connecting two micro tracks in the two emulsion layers of a film. The base tracks constructed with these connected micro tracks have positions and angles not affected by distortion. They are actually used in most of the analyses foreseen for OPERA. The position and angular resolutions obtained by using base tracks are described in Section 6.

Fig. 30 shows the typical distortion pattern in the central part of an emulsion film. The distortion effect is very much suppressed in industrial films down to $\sim 0.4\ \mu m$. This value is almost at the level of the readout accuracy of the present scanning systems ($\sim 0.3\ \mu m$). This result is basically due to the uniform drying process at the production and also to the careful development treatment specially devised for OPERA.

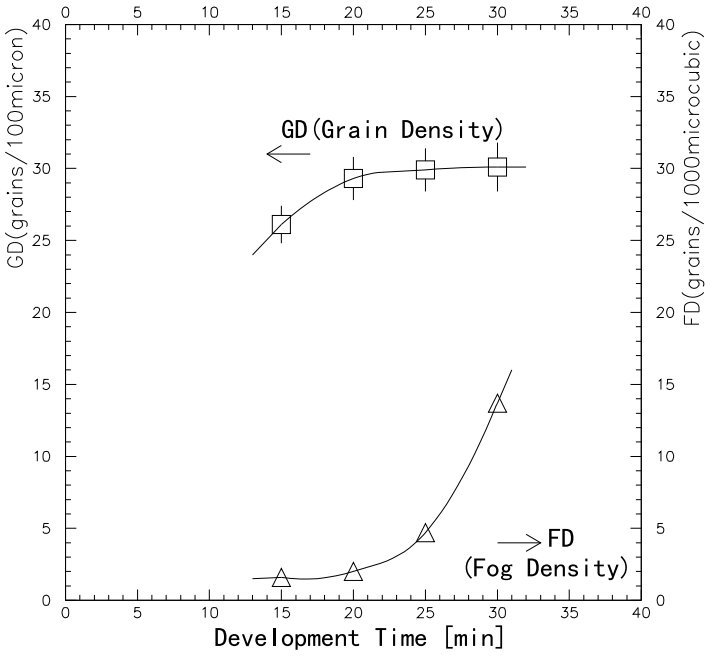

Figure 28: Time dependence of the developed grain density and fog density. Conditions are: amidol developer at 20^{o}C. A development time from 20 to 25 minutes gives satisfactory results.

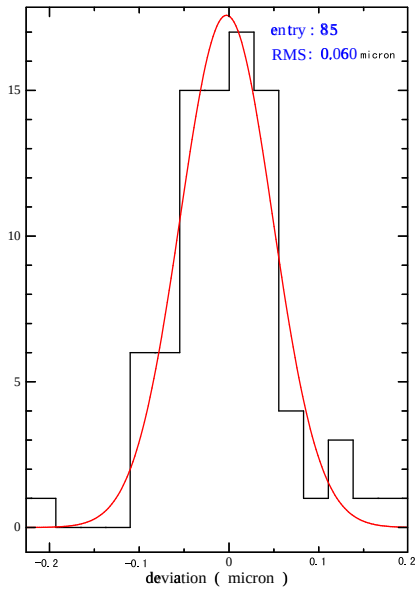

Figure 29: Position residuals of the grain centre with respect to a fitting straight line.

Usually the distortion becomes larger near the edge of the film. In the case of industrial emulsion films, the distortion is lower than $\sim 1\ \mu m$ up to $1\ mm$ from the film edge. At $\leq 500\ \mu m$ from the film border, track recognition by eye is still rather easy. This means that by using a proper distortion correction, tracks can be well recognised by automatic systems even at this position. Only at about $100\ \mu m$ from the edge the film is completely damaged, due to black stripes caused by the pressure applied at the film cutting. Fig. 31 displays some measurements of edge distortions. The data show that these effects are negligible up to $\sim 200\ \mu m$ from the film edge.

The fading and aging features of the industrial emulsion films have been investigated. Fading is the loss of the latent image occurring prior to development. Aging is the degradation of the emulsion sensitivity during the exposure.

Fading is not a severe problem for this experiment, since we plan to extract the selected brick and develop the emulsions within one week after the event occurred. Within about one month, possible extra bricks required for further analysis (candidate events) are extracted and developed. Moreover, one can take advantage of the existence of some fading, which contributes to erase unwanted cosmic ray tracks accumulated during film production and transportation before the run, as described in the next Section. This feature is beneficial to suppress the degradation of the electron identification efficiency and obtain an adequate energy resolution for cascade showers. In principle, the fading time constant depends on the environmental temperature, humidity and on the oxygen density. One example of these properties is shown in Fig. 32. According to the film producer, fading properties are well under control.

In order to check the features of the Fuji emulsion in maintaining their sensitivity with age we have

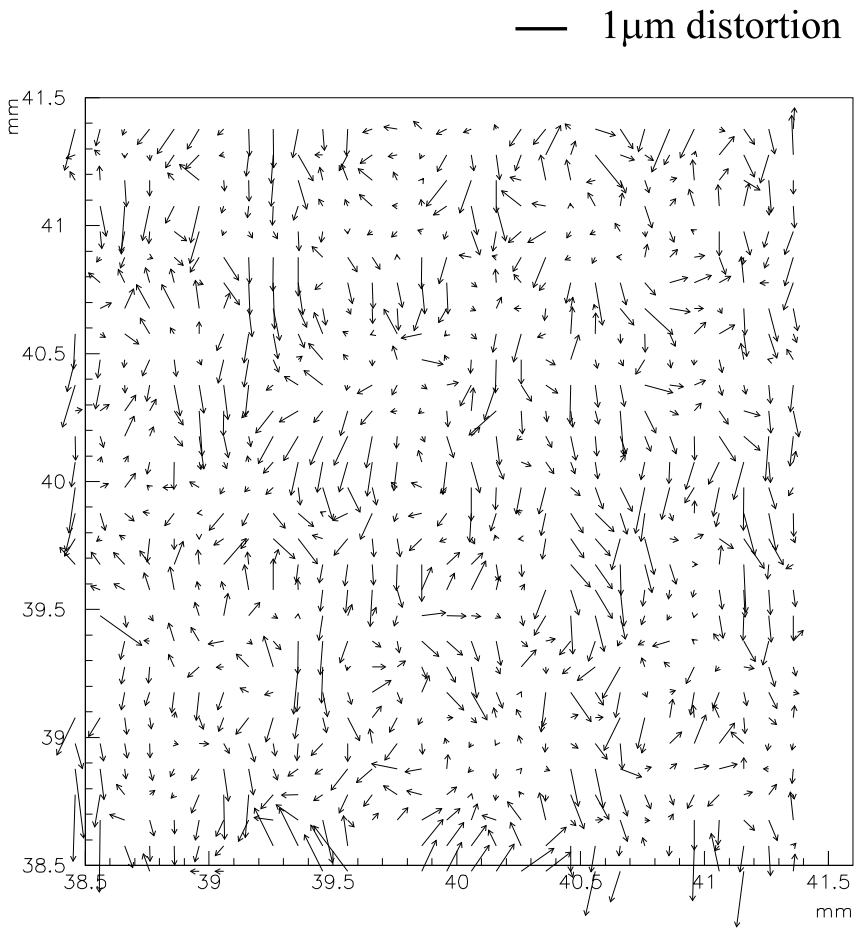

Figure 30: Measurement of the emulsion distortion at the centre of an emulsion film. The scanning area is $\sim 3\ mm \times 3\ mm$. The vectors indicate the distortion direction. The absolute value of the distortion is indicated by the length of the arrow (the unit is given on top of the plot).

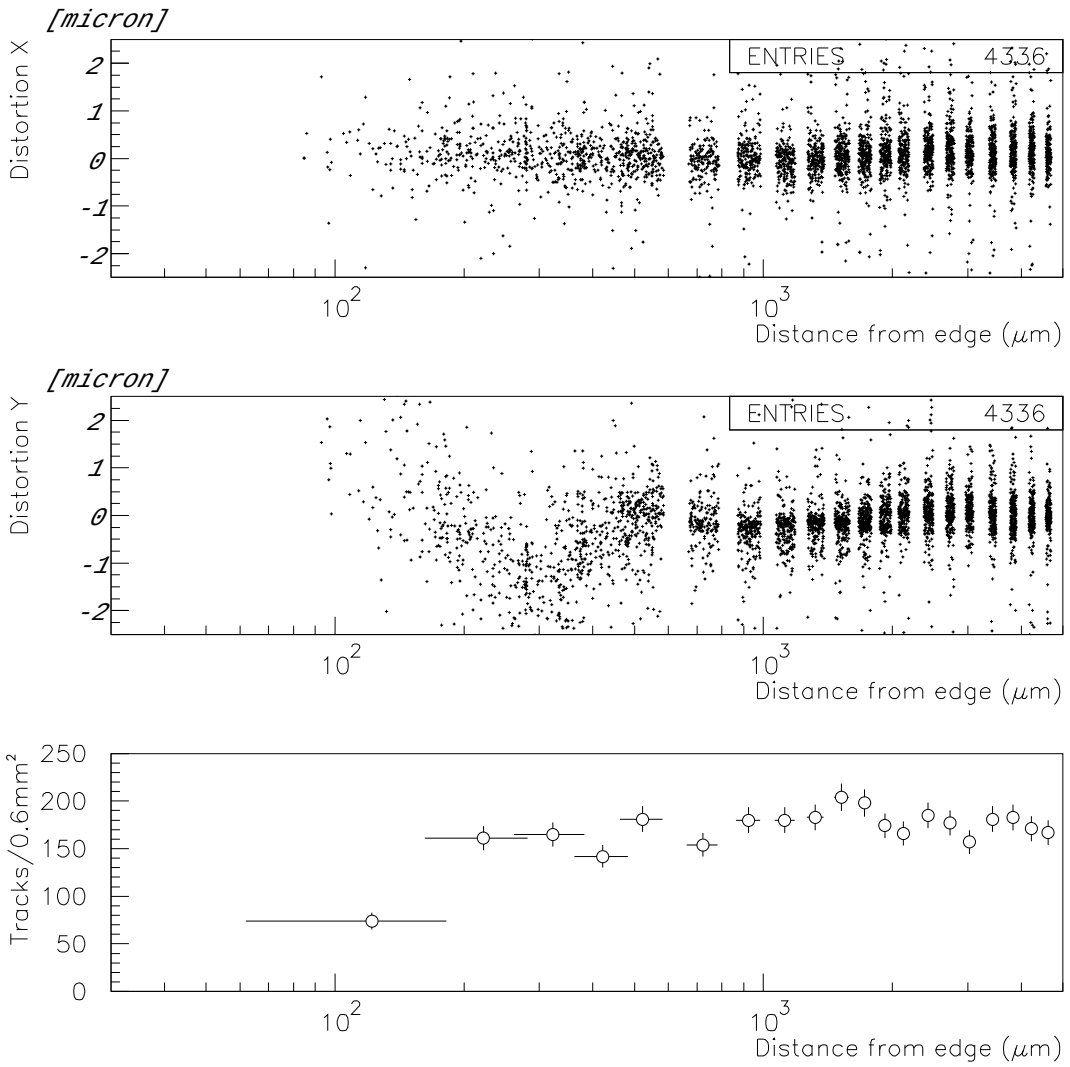

Figure 31: Measurement of emulsion distortion as a function of the distance to the film edge. Top and middle figures: the effect of the distortion along the X and Y directions are measured as the position deviation of the segment reconstructed in the emulsion layer with respect to the undistorted crossing points with the plastic base. The X axis is aligned with the film edge. Bottom figure: the number of tracks found by the automatic system without applying any distortion correction.

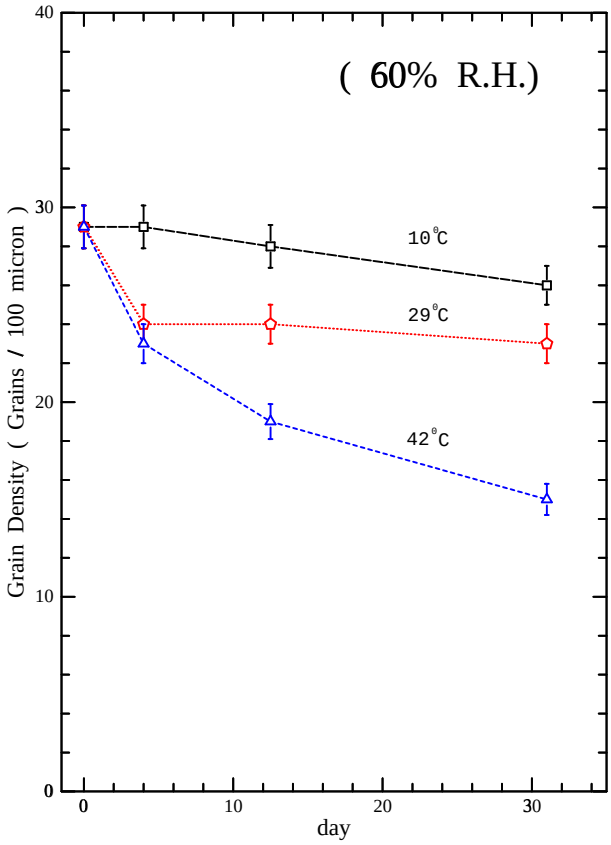

Figure 32: An example of the fading properties of the emulsion films. Each film sample is packed at a humidity of 60% and at a temperature of 20^oC. After beam exposure, the samples have been stored at different temperatures. At 10^oC the time needed to reduce the grain density to 25 grains/100 μm is estimated to 1.5 to 2 months. This lifetime is compatible with the planned brick removal and analysis strategy.

been searching for old emulsion plates in our and Fuji's stock rooms. The present sensitivity of these samples has been determined by exposing the emulsions to an electron beam and by developing them soon after. The results are shown in Table 6. Even the oldest plates still show enough sensitivity, *i.e.* $\geq$ 25grains/100 μm. The situation is even better for OPERA, since the natural temperature of the Gran Sasso hall is appreciably lower. Therefore, we can conclude that the OPERA emulsion sensitivity will be preserved over their (maximum) 7 years lifetime (*i.e.* 2 years for production and 5 years for exposure).

In summary, the performance of industrial emulsion films fulfils the requirements of OPERA and ensures the efficient operation of the automatic scanning systems.

Table 6: Results of an aging test performed with several emulsion plates. The age is defined as the time passed from production to development. The storage temperature varies from 20 to 30^{o}C over one year. Sample 4 includes emulsion films produced in Summer 1999 by the production line of commercial photographic films.

Batch	Production	age [year]	Storage condition 5^{o}C + Room temp.	Initial grains/100μm	after aging grains/100μm
Sample 1	'92 May	7.5 y	2.1 y + 5.4 y	32	27
Sample 2	'94 April	5.5 y	0.1 y + 5.4 y	25	25
Sample 3	'97 July	2.3 y	0 + 2.3 y	31	34
Sample 4	'99 July	1.0 y	0 + 1.0 y	30	30

4.2.3 Emulsion film transportation and erasing procedure

After production emulsion films have to be cut to the desired size and packed into air- and light-tight packages (aluminium-coated paper) at well defined humidity conditions for transportation to the Gran Sasso Laboratory. Each package contains the 58 films needed for one brick. The OPERA emulsion film size has been determined by the considerations described in Section 2.2.1. The actual dimensions of 4×5 *in* squared (10.2×12.7 cm^2) was selected among the existing standards for commercial X-ray films, in order to minimise the extra labour needed for cutting and packing.

Upon arrival the latent image of tracks recorded until that moment is erased by an accelerated fading procedure. This is obtained by rising the temperature and/or the humidity (and/or the oxygen density if needed). The tuning of the operating conditions is presently under study.

For example, one could work with a temperature of $\sim 40^o$C and with a relative humidity of $\sim$ 90%. The grain density becomes $\sim$ 10 grains/100 μm after 24 hours exposure to these conditions. Tests have shown that films processed by such an erasing procedure still have sufficient sensitivity ($>$ 25 grains/100 μm) and show no increase of the fog density.

The currently achieved performance is adequate for the electromagnetic shower analysis. Relaxed conditions with lower temperature ($30 - 40^o$C) and lower relative humidity ($70 - 85\%$) are under investigation in order to minimise the possibility of chemical contaminations from the processing cycle.

We aim at keeping the time needed for erasing within a few weeks, including the re-conditioning of the film at 20^oC and relative humidity of $\sim 60\%$.

During the erasing process the emulsion films must be kept separated from each other, because processing at high temperature and high humidity can make films sticking to each other (the so-called film blocking). For this reason, adequate space is required in the underground laboratory.

The transportation of the emulsions is also an issue to be considered. Ground level (sea) transportation is preferable in order to avoid the hadronic components of cosmic rays, which can create black tracks in the emulsions, difficult to be erased by fading.

4.2.4 Lead plates

Lead is well suited as passive material of the OPERA ECC bricks due to its high density and short radiation length. The former enhances the neutrino interaction rate and the latter the momentum determination by multiple scattering as well as the electron identification and energy measurement.

However, lead has the drawback of being radioactive and creates background tracks in the emulsion films. We performed an extensive search for low radioactivity lead in samples from companies in different countries. Three producers, one in Japan, one in the USA and one in Sweden, were found able to satisfy our requirements. With their samples, background rates of ~ 10 α tracks and ~ 50 β tracks per day per cm^2 were measured (see Section 8.1.2).

The density of fake tracks created by the mismatching of unrelated low energy segments (from lead plates), can be estimated to be $\sim 1/mm^2$ even after seven years, without considering fading. This value is acceptable for the electromagnetic shower analysis described in Section 6.7.

The variation of the thickness of laminated lead plates is within acceptable tolerances. This has been shown, for example, in the case of the liquid argon electromagnetic calorimeter of the ATLAS experiment.[8] This lead was laminated in 800 mm wide sheets with a thickness of 1.13 mm by a continuous production process. A feedback measuring system guarantees the stability of the lead thickness. The plate dimensions are 700 $mm \times 1800$ mm.

Fig. 33 shows how constant the thickness has been kept in the longitudinal direction (along 1800 mm). Fig. 34 shows the two-dimensional distribution profile of one of the plates. The thickness of each plate is measured every 50 mm. Using the measured distribution, the RMS of the thickness distribution can be calculated for each plate. This value is one of the indicators of the plate quality. Fig. 35 shows the distribution of this value over 472 large plates. In the particularly bad case of Fig. 34 the maximum thickness variation over 100 mm is ~ 15 μm.

The above results indicate that for the OPERA plate size one could aim at only 15 $\mu m/102$ $mm \sim 0.15$ $mrad$ slope for a wedge-like shape, much lower than the angular resolution obtained with one emulsion film (~ 1 $mrad$). We can then conclude that the needed mechanical accuracy can be achieved with currently available production lines.

[8] The information and the data on lead plates given in the following have been kindly made available to us by Ph. Schwemling from LPNHE Paris.

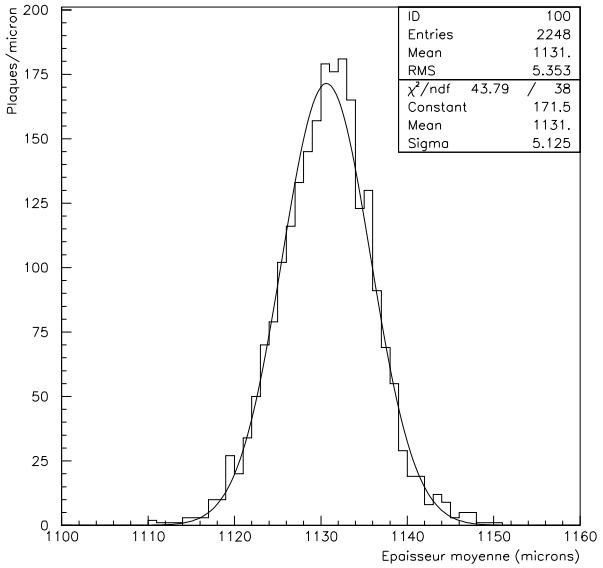

Figure 33: Thickness distribution for the lead plates of the ATLAS calorimeter. The result was obtained by measuring the attenuation of 100 keV X-rays, giving an accuracy of about 4 μm. The measurements have been taken every 150 mm along the 1800 mm plate length, by averaging the measurement of 7 gauges distributed in the transverse direction.

Since emulsion films have a very small distortion even at the edge, the mechanical properties of lead plates at their edges must be accordingly good. These properties depend on the cutting method and post-cutting treatment. Several cutting procedures (shearing, punching, laser or water jet cutting) are under investigation.

The total number of lead plates needed for OPERA is about 13×10^6. In order to produce them in two years, a production rate of about 25000 plates per day is required. The process includes laminating the lead, slicing to rolls, cutting to plates and cleaning. Normally, large smelter companies provide leads in rolls of the requested width and thickness. Cutting and cleaning should not take a long time, since a speed of about 1 plate/s can be achieved by automatic machines.

After machining and cleaning the 56 lead plates of a brick are set in a box (or package) which is the basic unit for transportation and assembly. The storage place can be at a surface laboratory. The required amount of lead needed for assembly are transported to the underground laboratory daily or weekly.

The absence of radioactivity, a lower price and better mechanical properties would make iron a possible option for the brick plates. However, if one wishes to keep the same number of neutrino interactions, about 30% more emulsions are needed to compensate for the difference in density, making the iron option globally more expensive. In addition, iron gives a worse performance for the brick event analysis (momentum measurement and electron identification) and is corroded by water and air, implying the need for adequate surface treatment. Stainless steel could be used, but with a cost about three times

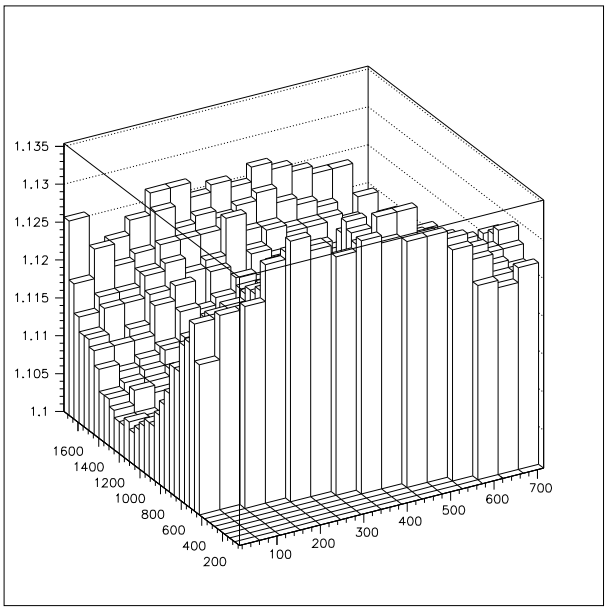

Figure 34: Thickness distribution map of one lead plate with a RMS of 8 μm. Units are mm. The thickness is measured every 50 mm by ultrasonic method. The accuracy of the device is about 1 μm. In the transverse direction (along 700 mm) the deformation of the mandrels can determine an increased thickness in the centre. In the longitudinal direction (along 1800 mm) waves can be observed due to the slight eccentricity of the mandrels.

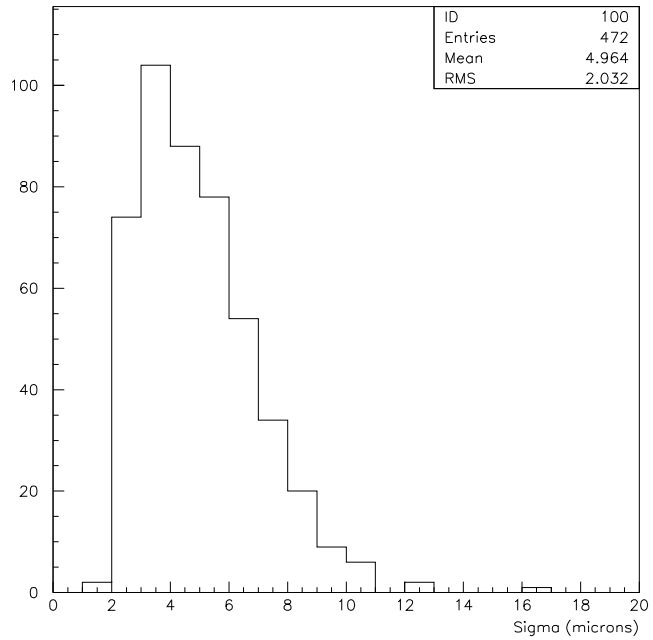

Figure 35: RMS distribution of 472 large lead plates. See the text for details.

higher than normal iron.

4.2.5 ECC brick assembly in the Gran Sasso

In order to suppress the cosmic ray background the brick assembly will be made at the Gran Sasso underground laboratory. An assembly speed of about 1000 ECC bricks per day is required in order to complete the whole procedure within one year. This speed corresponds to ≥ 1 brick/minute. This requires a semiautomatic or automatic assembly line. According to contacts with companies in Europe and Japan, it should be possible to achieve this performance. In particular, there are companies that can build automatic machines for origami packing starting from a roll of coated paper. Vacuum packing is also quite a standard industrial technology.

Fig. 36 shows a schematic view of a possible brick assembling machines (BAM). The brick assembly room must be clean in order to avoid fine dusts (of the size of $\sim 10\ \mu m$) which may disturb the stacking accuracy and degrade the quality of the measurements. The room must be dark with safety lights installed. With such a machine, two ECC bricks can be assembled in about one minute. Before transfer to the next step, each stacked brick is tied using tapes to keep its shape.

Two double arms pickup and pile up different kind of plates like emulsion films or lead plates. Films and lead plates are stacked into bricks as shown in the left most side of Fig. 36. The accuracy of stacking can be within $\sim 0.1\ mm$. The bricks are then fixed by temporary straps in order to fix their relative position prior to vacuum packing. With a belt conveyor the brick is moved to the packing machine. In

order to suck air out, one side is not complete sealed. The packed brick is then pushed into a vacuum vessel equipped by a heat sealer. After a vacuum tightness check, packed bricks are ready for installation in the detector. Each brick is marked for further book-keeping.

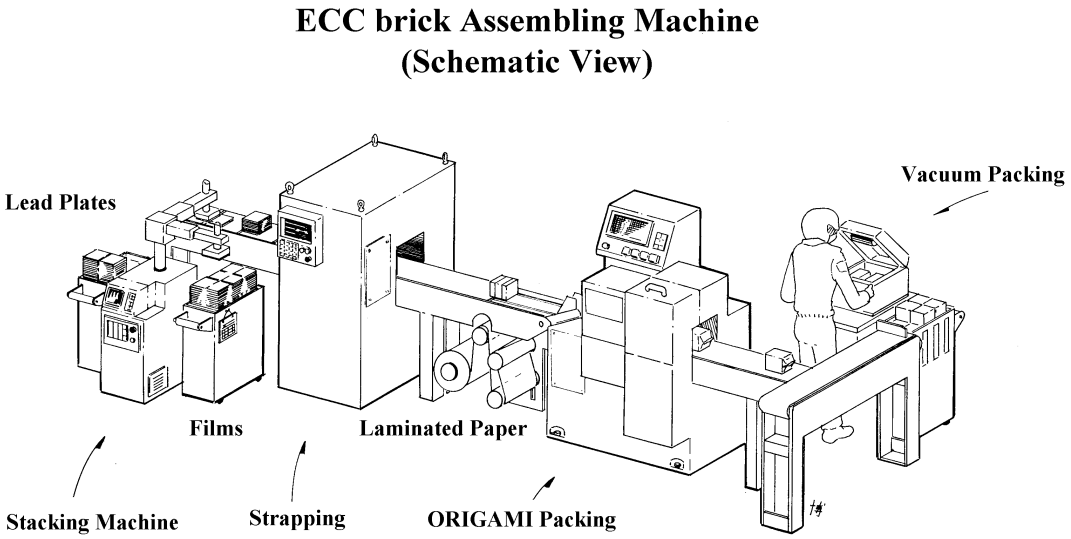

Figure 36: Schematic layout of a brick assembly system. From left to right, ECC brick stacking, temporary strapping, origami packing and vacuum packing machines.

4.3 Target walls

The ECC bricks are assembled in vertical walls perpendicular to the beam direction. Bricks are placed with the 12.7 cm long side of the film along the horizontal direction. The mechanical accuracy in the positioning must be of the order of $1 - 2$ mm (Fig. 83). Each target wall is approximately square and houses 51 bricks horizontally by 64 bricks vertically. Including clearances the total size of the wall amounts to about 6.7×6.7 m^2. The total weight of the 3264 bricks to be supported in a wall is about 27 ton.

The wall support structure is shown in Fig. 37 and Fig. 38. The mechanical structure in which bricks are accommodated is made of thin stainless steel vertical bands linked with light horizontal trays where the bricks are placed. This choice allows a light mechanical design in order to limit as much as possible neutrino interactions in the target area outside the bricks themselves and to permit a small spatial separation between bricks in transverse and longitudinal directions. The brick support structure is suspended from the general wall support and pulled from the bottom.

Apart from the requirement of a minimum amount of dead material the main constraint in the mechanical design of the target walls is to ensure easy and quick removal of bricks. The wall structure

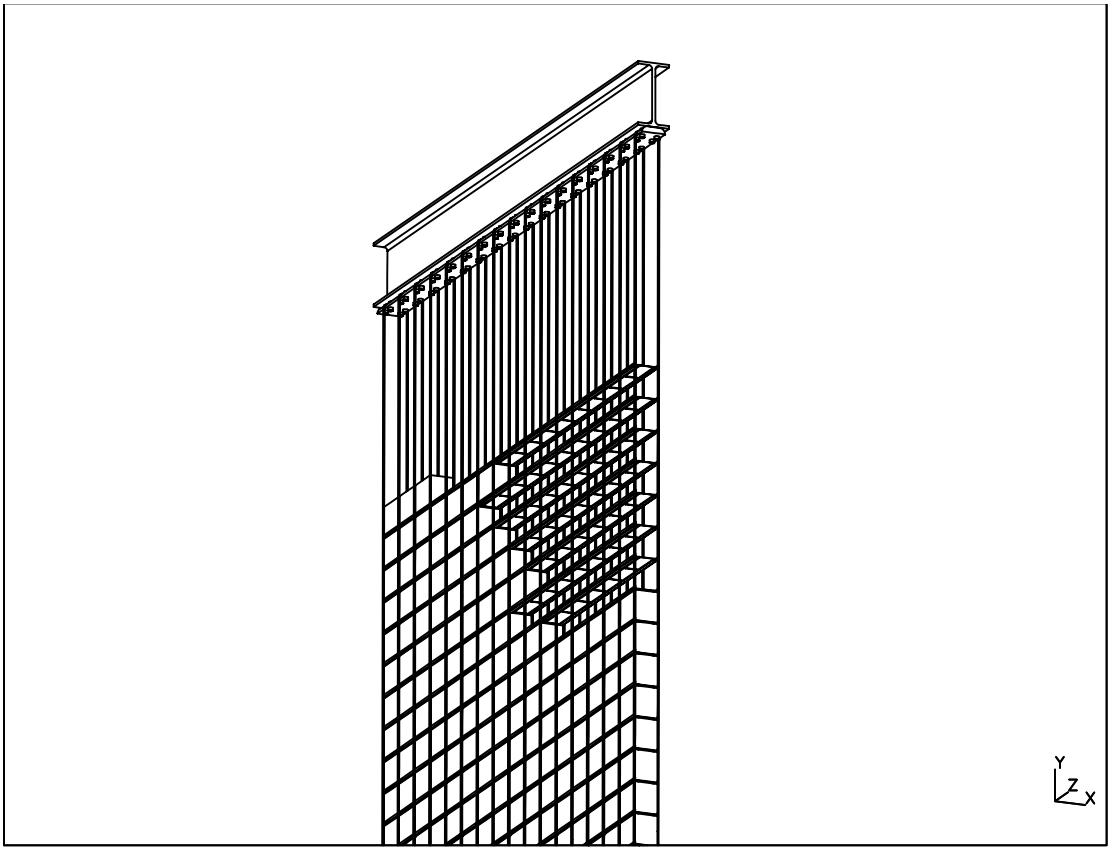

Figure 37: Wall support structure.

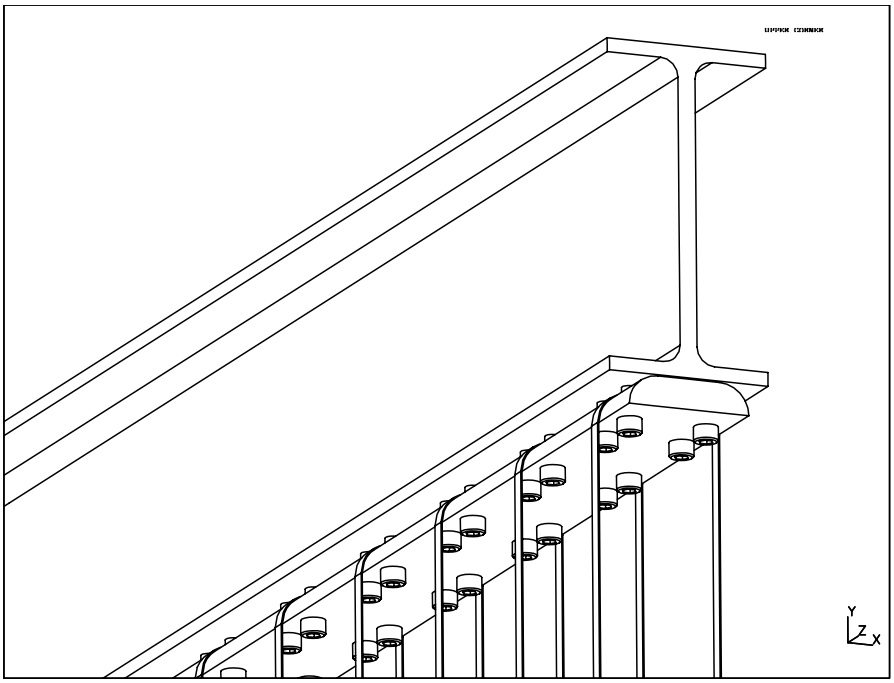

Figure 38: Possible design of the wall suspension.

provides horizontal access to the rows of bricks from the sides and is associated with an automatic system for brick installation and removal.

The wall structure bears collectively the weight of the entire brick wall. Using high resistance stainless steel bands of 0.8 mm thickness, the structure weight represents less than 0.5% of the total weight.

Different ways of attaching the trays can be considered; they can be directly welded to the vertical bands or mounted at the installation stage on transverse bands linking the vertical ones. Solutions in which complete wall parts can be built in advance seem preferable. After being manufactured outside, half-wall structures are introduced in the hall, suspended from an assembly tool and joined together before being put in place.

Each brick wall is coupled to the electronic trackers consisting of two planes of scintillator strips oriented along the X and Y directions, respectively. The wall structure can also be used to support the electronic Target Tracker planes. They could hang directly from the main supporting beams or they could be attached to the wall structure itself. In the latter case, vertical and horizontal tracker plane elements are mounted on the upstream and downstream faces of each brick wall, respectively. Alternatively, vertical scintillator package envelopes are suspended from supporting beams and maintained in place on the wall structure with the help of folded metallic bands. Horizontal scintillator packages are also kept by folded metallic bands. The envisaged solutions provide the required mechanical positioning of the tracker relative to the bricks, compactness and rigidity.

The bricks are moved in and out of their tray being contained within individual plastic holders. This

ensures a well defined brick position relative to the mechanical structure and eases brick handling, while providing an additional mechanical protection. The bricks can be situated on sliding bands (Fig. 39) which are pulled and rolled sideways to bring bricks in and out. Alternatively, they can slide directly on horizontal trays. Each choice has a corresponding automatic system for brick installation and removal.

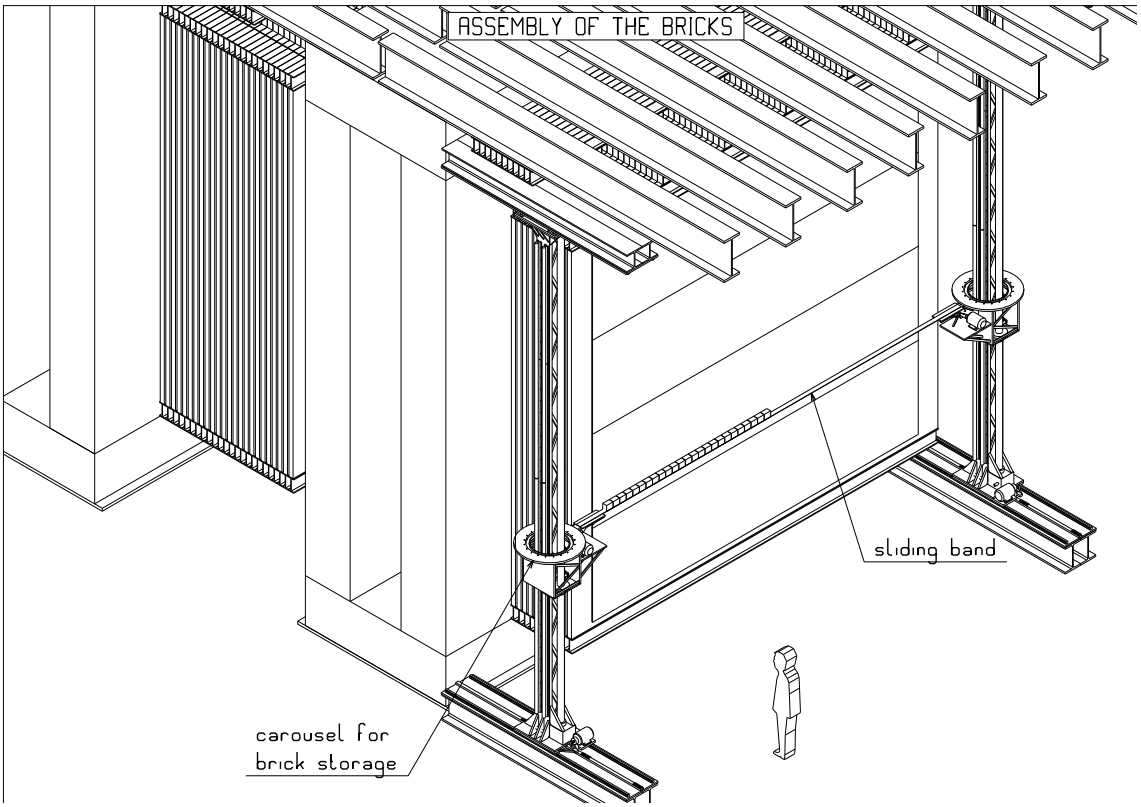

Figure 39: Principle of a brick manipulator system in the case of a target wall structure with sliding bands.

A robot extracts from the target side all the bricks needed to reach the selected brick. They are temporary stored and then put back in place.

Fig. 39 shows a design of the brick manipulator system using a thin sliding band, possibly reinforced by steel wires. The manipulator operates in the following way. Two frames allow the vertical columns to move along the beam direction on each side of a supermodule target (Fig. 39). Two *carousels* can be positioned in front of the brick row containing the brick to be removed.. Each end of the sliding band is automatically connected to a motor-driven roll fixed below the carousel. It can be pulled by the rolls in either direction along the X axis. One can envisage to extend the system in order to cover the sides of all three detector supermodules. During the brick manipulation the detector operation is not affected, apart from the row of bricks which contains the selected brick. Estimating to about 10 minutes the time

needed to complete the removal of a given brick, no appreciable dead time is expected for the experiment.

Another possible system for brick handling, whose design has been carried out in collaboration with industry,[9] is described in Fig. 40 and 41.

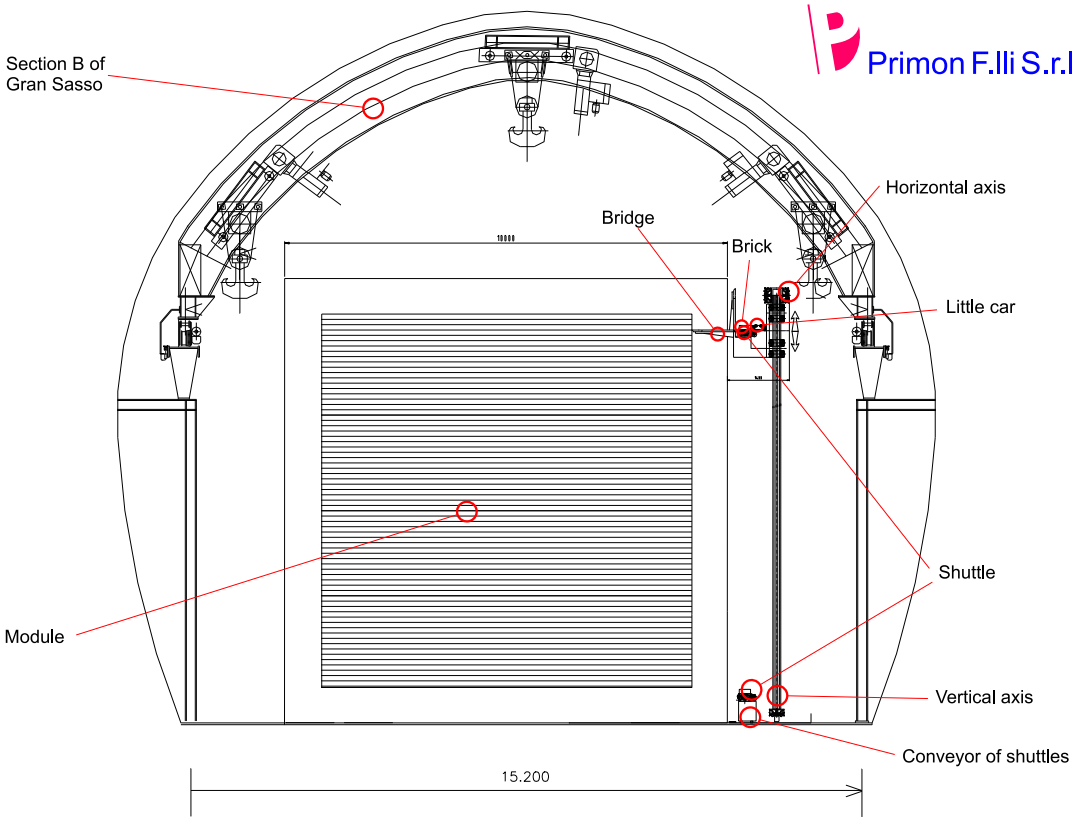

Figure 40: Brick manipulator system employing a self-propelled vehicle.

The envisaged solution consists of a manipulator with two axes of movement (horizontal and vertical) located on one side of the target. The horizontal stroke for the accurate insertion of the bricks on the tray is given by a small self-propelled vehicle (*little car*) which moves on the tray which constitute the brick shelf. The vehicle is fed by a belt conveyor (shuttle), on which the bricks accurately oriented are laid. The shuttle is loaded at floor level and is moved vertically by a single track conveyor. At least two shuttles are used, so that a shuttle is feeding the vehicle while another is (*e.g.* manually) loaded.

The two axes manipulator is composed of an upper track with a rack for the longitudinal stroke (as long as the three supermodules) to which the trolley is hung, on which is bound the vertical axis. In the lower part there is a track to avoid oscillations of the manipulator around the horizontal axis. The vertical axis is made of a linear unit with meshed belt and a geared motor assembled in a high position, which handles the vertical trolley to which the shuttle is connected through an electrical jack. To connect

[9] Primon F.lli S.r.l, Crusinallo di Omegna (VB), Italy.

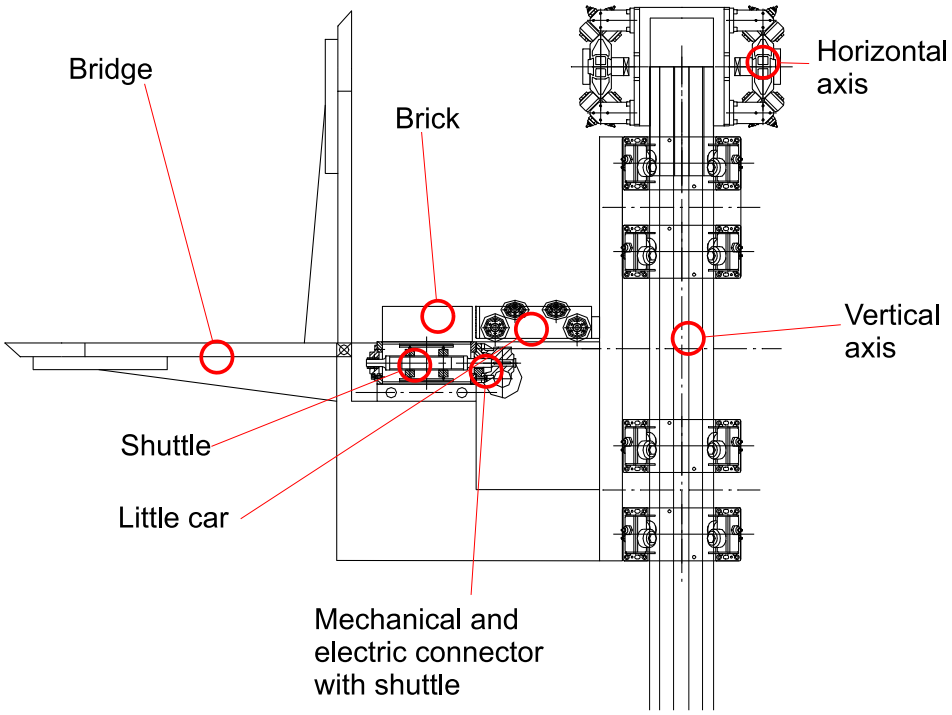

Figure 41: Detail of the brick manipulator system.

the shuttle to the shelf on which the bricks have to be positioned a folding plane is designed which, once stretched, obtains a unique level between shuttle and shelf. To position along the shelf of the module the single brick and at the same time not to hinder on the sides the space close to the supermodule, a small car is designed to push or pull the brick.

During the wall filling operation the small car pushes the brick (present in first position on the shuttle) on the retractable junction plane, then along the shelf until reaching the position required. To obtain a sufficient grip on the shelves the small car has four lower steering wheels and four upper steering wheels with a pre-load spring to increase the weight and consequently traction. A wire encoder controls the position along the shelf. The grip of the brick on the machine is made with a device of vacuum grip or alternatively with a mechanical device of hook on the plastic material container. The power of the small car can be by batteries (directly on the car) or wire.

After positioning the small car returns to its parking slot where it clutches automatically in a connector for recharging the batteries. In this moment the shuttle performs the thread progression of the belt to display a new brick aligned between the small car, the retractable plane and the shelf of the module. An opposite cycle is applied for brick removal during the data taking.

The entire system can be connected to a PC network and consequently to remote PCs via modem or Internet, to check the number of stored bricks and the relative position in the absolute matrix from the shelves of the various walls. Close to the parking slot of the small car there is a bar code reader to register and check the exact correspondence between the brick and the relative position.

An alternative scheme for the wall structure, with bricks held by movable ladders in vertical shafts, is described in Section 9.

The mechanical wall structures described above were preferred to solutions implying longitudinal displacements of entire target walls to access the bricks. This solution would have required longer brick access times as well as dead time for part of detector during brick removal. Such schemes would also need more longitudinal space in the Gran Sasso hall.

4.4 Electronic Target Trackers

4.4.1 Detector elements

The construction of large scintillator strip planes ($6.7 \times 6.7\ m^2$) needs a careful study of the mechanical handling and of the optical couplings. In order to investigate the technical problems, we have constructed prototype detectors.

The baseline design foresees 64 strips read out by WLS fibres coupled to a single 64-pixel photodetector. This constitutes one basic unit. Four such units can be assembled in situ to construct a whole scintillator plane, which is composed of 256 strips. This assembly system has the advantage to allow the parallel production of detectors in several sites.

A unit is made of 4 sub-units each including 16 strips enclosed in a light-tight aluminium case $0.5\ mm$ thick to provide the needed mechanical strength (Fig. 42). A strong requirement for the construction is to keep as small as possible the gaps between individual strips and the gaps between basic units.

The strips are 6.7 m long, 2.6 cm wide and 1 cm thick. They are obtained by extrusion, with a TiO_2 co-extruded reflective coating. A 6.7 m long groove, 1.2 mm deep, in the centre of the scintillator strip houses the WLS fibre which is glued in the groove.

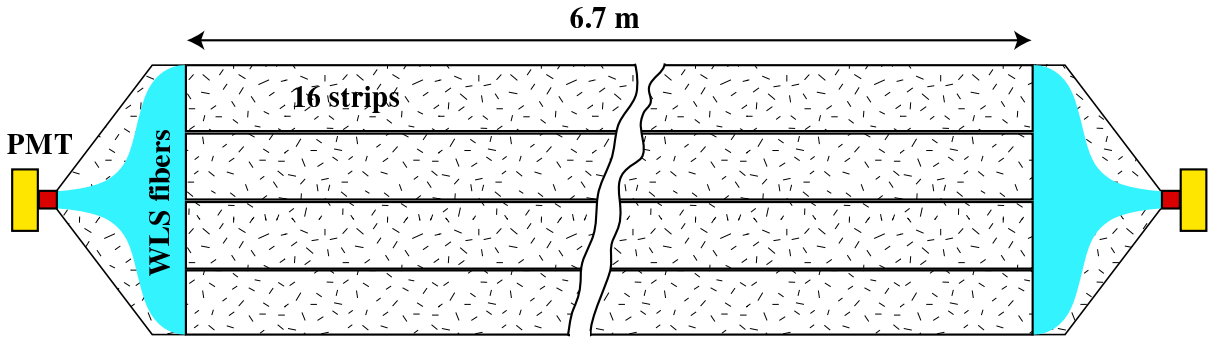

Figure 42: Schematic view of a scintillator strip unit. The dashes indicate the 0.5 cm thick aluminium case.

The fibres are routed at both ends to the photodetectors through the end manifolds (Fig. 43). Care has to be taken to respect the minimum bending radius which is of the order of 12 cm. The end manifold length, including the photodetector and the electronic readout card, does not exceed $35-40$ cm, leaving enough space on the side for the brick manipulator robot. The lengths of the PMT and the readout card are each about 5 cm. The end manifold has a thickness of 1.1 cm near the scintillator strips and 3.1 cm at the level of the photodetector. The high voltage and readout cables can be extracted and routed through a narrow column near the scintillator strips (Fig. 43).

In order to have a detection efficiency for a mip higher than 97%, the number of photoelectrons ($p.e.$) per mip at normal incidence must be at least 4. The light yield depends on the light output of the strips, on the light collection efficiency, on the fibre's transmission and on the photodetector efficiency.

Different types of WLS fibres are under test. The key parameter of WLS fibres is their effective attenuation length. In the range of fibre lengths used in the tracker plane, double clad fibres which are commercially available from Bicron[10] and Kuraray[11] are suitable to meet the requirements. Fig. 44 shows the expected light yield at each side of the plane and the sum of signals from both sides. The calculations are based on the effective attenuation length of Bicron BCF91A fibres as measured by the MINOS experiment [38] (up to 7.5 m). The absolute scale is taken from measurements performed with prototype detectors.

We performed additional tests with 2×1 cm^2 NE110 scintillator strips and 1 mm diameter Bicron 91A fibres read out by Hamamatsu[12] bialcali R6091 tubes. With such a good quality scintillator material, we obtained 5 $p.e.$ at 4.6 m from the PMT with no reflection at the other fibre end (Fig. 45). In OPERA,

[10]Bicron Corp., 12345 Kinsman Road, Newbury, Ohio 44065.
[11]Kuraray Co., Methacrylic Resin Division, 8F, Maruzen Building, 3-10, 2-Chrome, Hihonbashi, Chuo-ku, Tokyo, 103-0027, Japan.
[12]Hamamatsu Photonics K.K., 325/6, Sunayama-CHO, Hamamatsu City, 430, Japan.

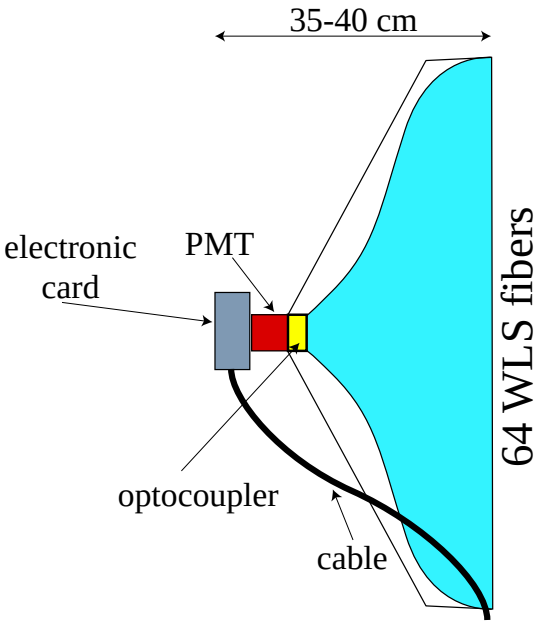

Figure 43: End-manifold of the scintillator strips prototype.

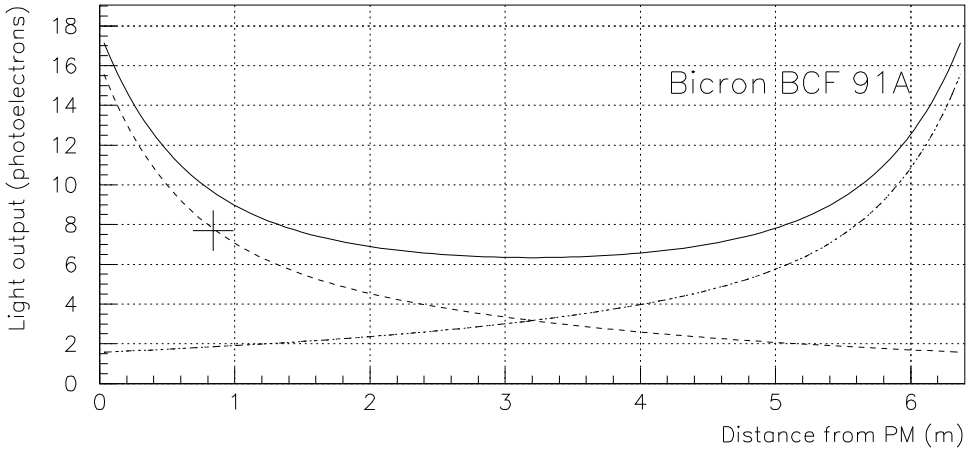

Figure 44: The expected light yield at each side of the plane (dashed lines) and the sum from both sides (continuous line) [38]. The cross correspond to the test beam measurement value.

the effective maximal length (for photons crossing the middle of the scintillator strips) is less than 4.5 m (3.35 m in the scintillator and 1.10 m maximum at the optocoupler).

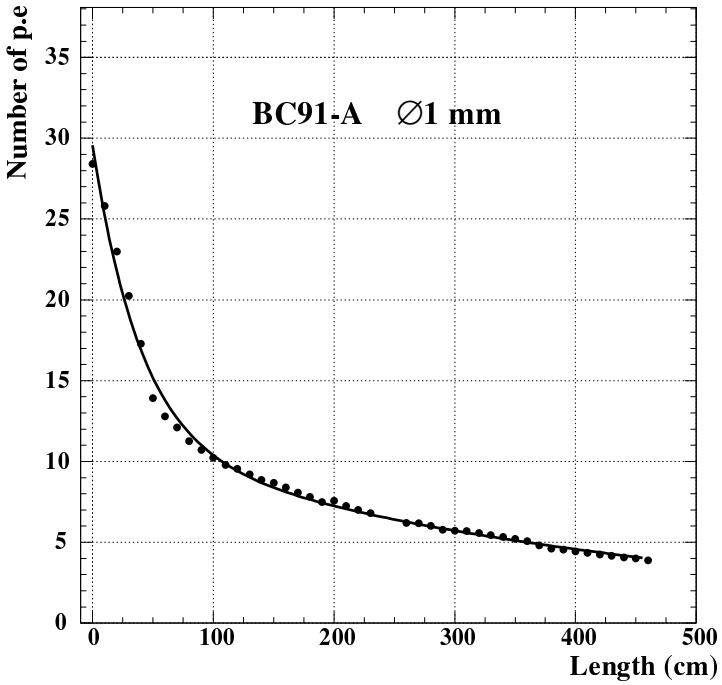

Figure 45: Light yield obtained with 2×1 cm^2 NE110 scintillator strips and 1 mm diameter Bicron 91A fibres.

4.4.2 Detector planes

One target tracker plane contains an array of 256 strips with fibres readout at both ends. Two planes with perpendicular strip orientation are placed downstream of each target wall. No multiplexing scheme is foreseen. A total of 16 64-pixel photodetectors is needed to serve one tracker wall. Fig. 46 shows the layout of a plane with its fibre readout.

The detector planes must be installed as close as possible to the brick walls. Simulations have shown that the space resolution in the determination of the event vertex in the brick depends on the gap between the brick and the tracker walls. In addition, the gap between two brick walls has to be small for an easy matching of the tracks between two consecutive bricks, by minimising the scanning area in the downstream wall. In the present design, a value of 3.6 cm is retained by practical considerations related to the transverse size of the photodetectors. Alternative solutions are under study to minimise the gap thickness.

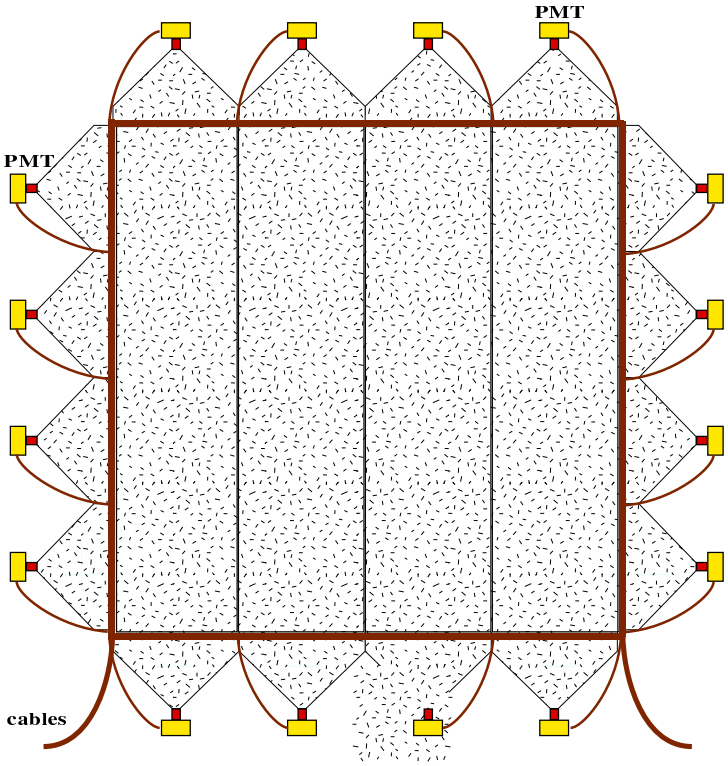

Figure 46: Tracker plane layout.

Table 7: Characteristics of the 64-channel Hamamatsu H7546 PMT.

Photocathode material	bialkali
Window material	borosilicate
Spectral response	300-650 nm
Wavelength of maximum response	420 nm
Number of dynode stages	12
Anode size	2×2 mm^2
Maximum supply voltage between anode and cathode	1000 V
Divider circuit	$3:2:2:1:\cdots:1:2:5$
Divider current at 1 kV	455 μA
Gain at 800 V	3.0×10^5
Cross talk (with 1 mm optical fibre)	2%
Uniformity among all anodes	1:3

4.4.3 Photodetectors

The choice of the photodetector is mainly based on the single photoelectron detection efficiency, the dynamic range and the cost. Other considerations are gain uniformity among channels, linearity, electronic cross talk and integration time. The baseline photodetector for the OPERA Target Trackers is the commercially available 64-channel Hamamatsu H7546 PMT's (Fig. 47). This PMT has also been chosen for the MINOS [38] near detector and has been extensively evaluated.

The characteristics provided by the Hamamatsu PMT are given in Table 7. The PMT provides an output of the last dynode number 12. This signal common to all channels could be used as a FAST-OR to trigger the acquisition system or for timing purposes.

Preliminary tests of the PMT's have been performed. Fig. 48 presents the channel response (normalised to 100) for an anode-cathode voltage of 800 V for one of the tubes under test. The PMT was illuminated by a W-lamp (400 nm). The measured capacitance to ground of each anode, important for the front end electronics, was found to vary from 1.8 pF to 2.8 pF.

A more elaborate test system has been prepared to study in details the M64 PMT performance. This is schematically shown in Fig. 49. A computer guided translation system and the PMT are enclosed in a light-tight box together with a H_2 lamp and focalisation optics. With this system, a fine light spot (< 50 μm) can be produced at any place of the PMT photocathode allowing the scanning of the whole sensitive surface. By removing the focalisation lens near the PMT, the light beam can uniformly illuminate the whole photocathode. This option can be used for massive production tests. The PMT can also be illuminated through a fibre. A passband filter centred at 490 nm chooses the light corresponding to the WLS fibre emission spectrum.

The details on the front end electronics for this test system are given in Section 8.2.3.

Other readout option are considered. One of these is represented by the Hybrid Photo Diode (HPD)

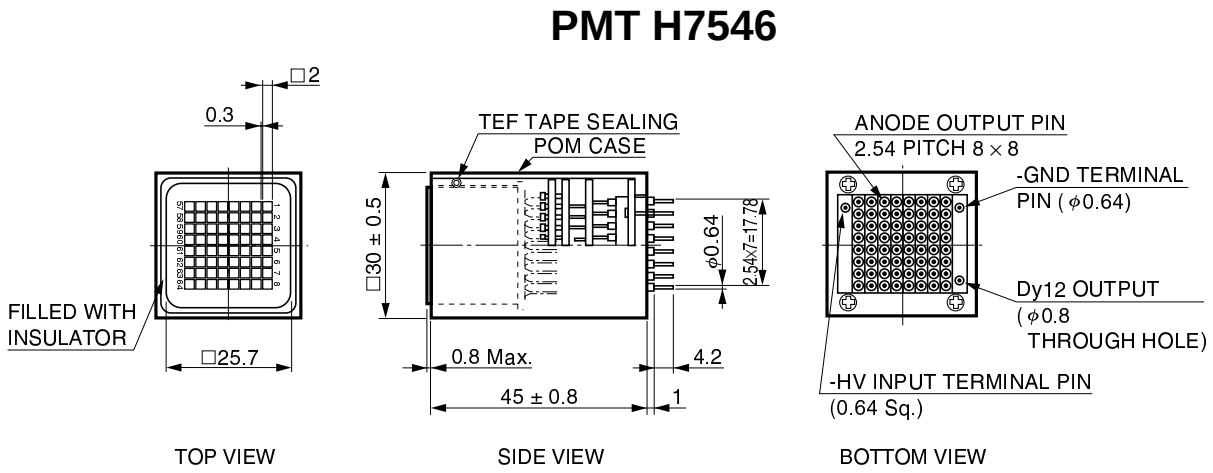

Figure 47: The 64-channel Hamamatsu H7546 PMT.

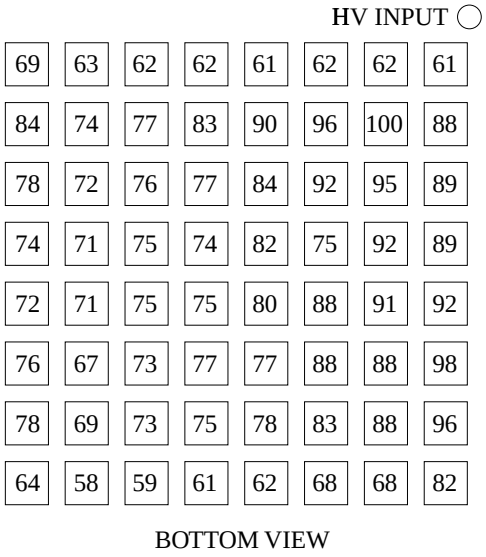

Figure 48: Response of the 64 channels of the Hamamatsu H7546 PMT GA0036 at 800 V. The signal values are normalised to 100.

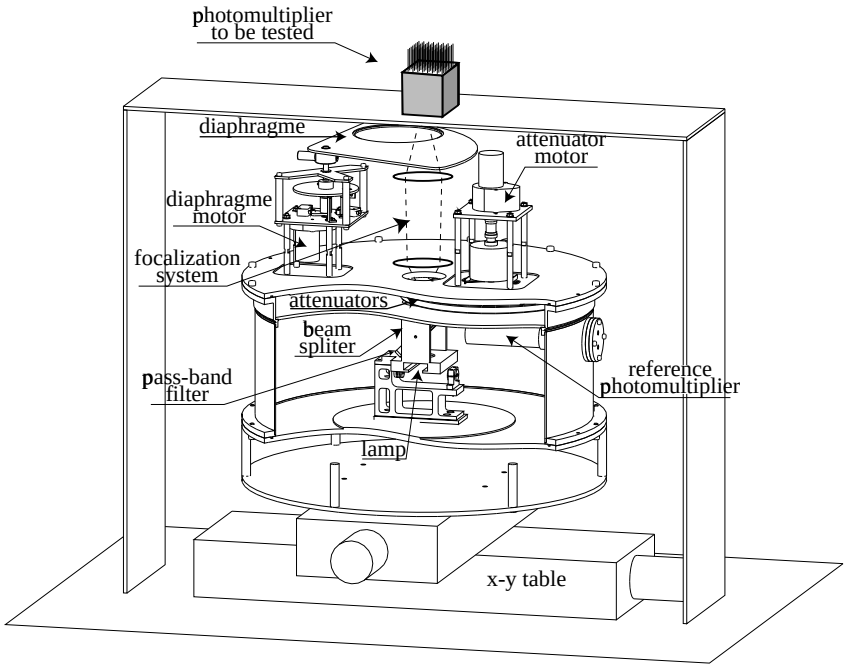

Figure 49: Schematic structure of the PMT test system.

from DEP.[13] The DEP 61-pixel HPD is available with a S20 photocathode. The useful diameter of the photocathode is 18 mm.

The gain of the HPD is defined by the number of electron-hole pairs generated by the photoelectrons in the depleted silicon (the typical depletion voltage is 60 V). When operated at a voltage of 15 kV the typical gain is 3500. This relatively low gain requires a high gain preamplifier and a noise performance suitable to resolve the single photoelectron peak. HPD's can be coupled to VLSI front end chips, which are already available for silicon detector readout.

HPD's provide a good single photoelectron sensitivity (Fig. 50) and a pulse height resolution which allows to clearly distinguish the different photoelectron peaks. HPD's feature a better uniformity and linearity (over five orders of magnitude) than the multianode PMT's. The development of new HPD designs suitable for mass production is in progress.

Due to the recent development of large size Avalanche Photo Diodes (APD), we are evaluating also this solution as an alternative option. Preliminary studies have been performed in a test beam. A signal to noise ratio of about 7 was achieved with a gain of about 50 at a voltage of 390 V. Further studies are underway.

Still another readout option is given by the Electron Bombarded CCD (EBCCD) [59] from Geosphaera.[14] Various gateable EBCCD's with photocathode diameter from 18 to 80 mm are available. They can ac-

[13] DEP Electronic Products BV, P.O. Box 60, NL 9300AB Roden, The Netherlands.
[14] Geosphaera Research Center, Moscow 117261, Russia.

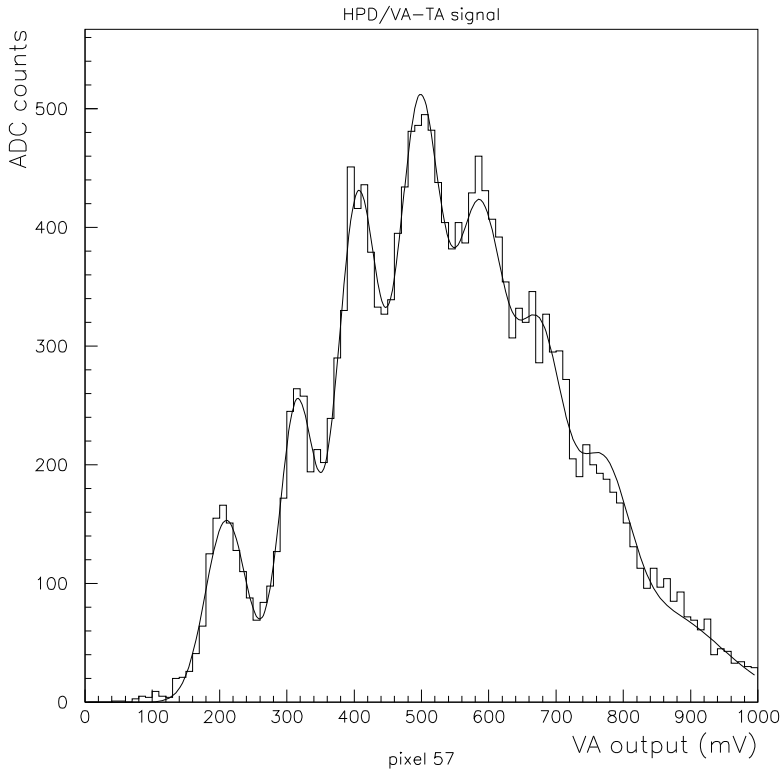

Figure 50: HPD pulse height measurement. The first peak around bin 200 corresponds to the pedestal. The photoelectron peaks are clearly visible (up to the 7^{th} one). A global fit is applied using a Gaussian approximation for the individual peaks. The heights of the photoelectron peaks are fitted by a Poissonian. The mean number of photoelectron is around 3.5.

commodate from 512 up to 5180 fibres. The high spatial resolution allows to resolve individual fibres. The readout time of 100 ms is limited by CCD's. Therefore, no trigger signal can be provided by the EBCCD. Several types of tubes with different CCD's were tested and results are encouraging. At relatively low cost per channel, the EBCCD can provide good gain uniformity, low cross talk and single photoelectron detection capability (see Section 8.2.3).

4.4.4 Readout electronics

Studies have shown that an analog readout is preferred for the brick finding efficiency. A fast trigger has to be implemented in order to start the electronic channel readout and the data acquisition. In order to achieve triggering and charge measurement capabilities, the electronic signals from the photodetectors are amplified and split into two parts. One is sent to a fast discriminator and the other one to a slow shaping and charge measurement device.

Depending on the strip and photodetector modularity, 16 to 64 channels are combined in a chip. In the baseline option we assume the combination of 64 channels, corresponding to the readout of one photodetector. The OR of the discriminators for each chip can trigger the charge sampling. The charge output of the electronic channels is multiplexed and sent to an ADC. It is also possible to send to the ADC's only the signals of the channels above the discriminator threshold (selective readout). In this way, zero suppression is performed in the readout chip.

This general scheme is common for the PMT and the HPD front end electronics. The changes mainly concern the first stage of preamplification because of the different polarities and amplitudes of the signal. A schematic layout of the readout electronics is shown in Fig. 51.

The amplification of the first stage is defined by the sensitivity and the dynamical range to be covered by the whole electronic chain. The scintillator strip detectors aim at a sensitive range from 1 to 200 $p.e.$ For PMT's operated at a gain of 10^6 the range varies from 0.16 pC to 32 pC. In the case of HPD operation with a gain of 3500, the charge range varies from 0.6 fC to 120 fC.

The discriminator thresholds must not exceed a value equivalent to 1 $p.e.$ in order to keep a detector track efficiency higher than 97%. However, thresholds must be high enough to avoid triggering on electronic noise which would increase the counting rate and thus the acquisition dead time. The thresholds can be set to five times the RMS of the electronic noise. This was achieved by the MINOS collaboration using 64-pixel Hamamatsu PMT's with a threshold at 0.3 $p.e.$ This is more constraining for HPD's, which have a relatively small gain and quite broad pedestal. In the following we describe three possible solutions under test for the front end electronics.

A prototype chip based on the scheme described above has been designed with 16-signal channels and two test channels for electrical characterisation. Each signal channel mixes a slow and a fast line to provide the autotrigger. The preamplifier, shared by these two lines, generates a voltage step in response to the signal of the photodetector. For PMT readout the preamplifier is replaced by a switch of adjustable gain. In 1999, a test chip was developed containing only a preamplifier with characteristics fulfilling the following requirements: gain of 3 $mV/p.e$, linearity over 300 $p.e$, ENC of 450 electrons at 10 pF input capacitance and shaping time of 600 ns.

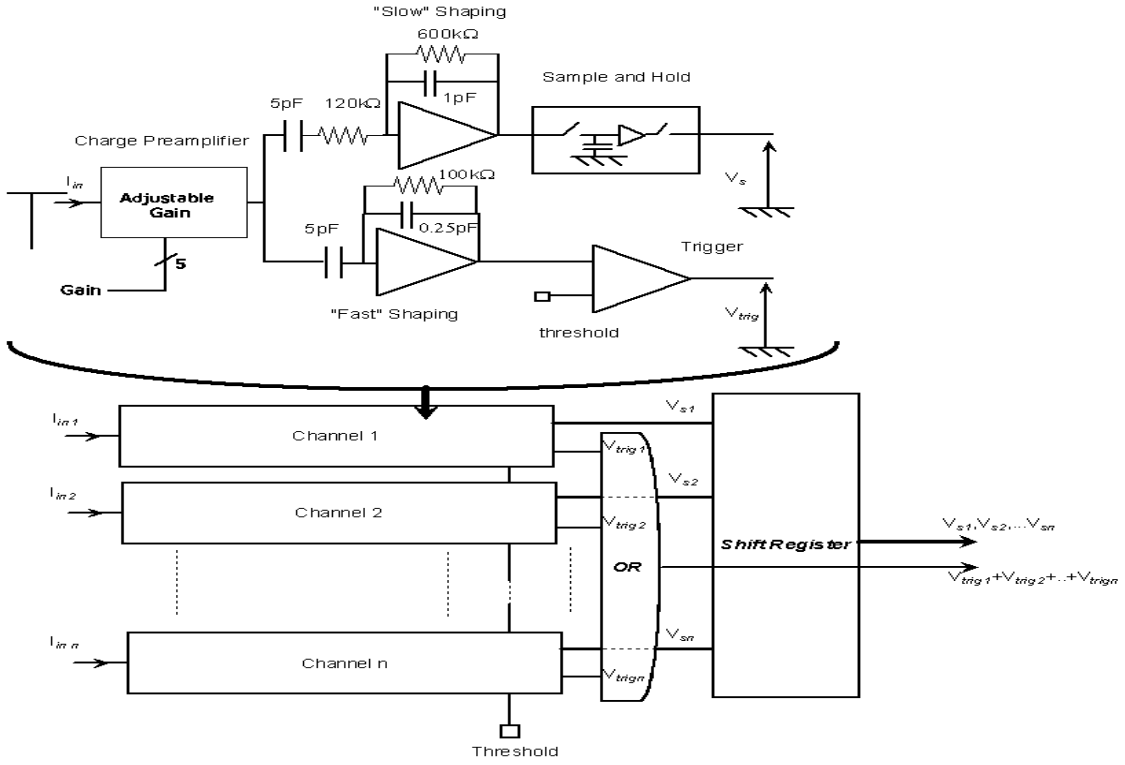

Figure 51: Layout of the front-end electronics.

The fast shaper has a high gain in order to trigger on a single photoelectron and to reduce the spread between different channels when triggering on low levels. This shaper is followed by a comparator with common adjustable voltage threshold. The 16 outputs of the comparator are ORed together to provide a common trigger for all the channels. A mask gives the possibility to disable given channels. Simulations predict a voltage gain of 20 in the fast shaper, 40 ns for the shaping time and the 1 $p.e.$ peak at $4-5$ σ from the pedestal.

The slow shaper line measures the charge of the signal. The maximum is stored on a capacitance cell with a hold command generated by the autotrigger. All 16 channels are then read through a multiplexer implemented on the chip. The following characteristics are expected: shaper gain of 1.2, linearity over 300 $p.e$ (5% non linearity for the whole channel), peaking time of 600 ns, S/N ratio of ~ 10 for 1 $p.e.$ This HPD chip is expected to be soon available. In parallel, a similar chip is being designed for PMT's.

We are also testing commercially available chips for the readout of the HPD's. A large number of front end chips is suitable for the silicon detectors with various gains, peaking times, noise levels. Among them the Viking family [60] of IDE AS,[15] originally developed at CERN, offers adequate performance.

The readout sequence of the slow shaper (called VA) starts with a hold signal depending on the trigger. Each channel holds the signal at the time it received the hold. The delay between trigger and hold matches the peaking time of the VA (~ 2 μs). The chip is then clocked and an ADC sampling is performed until all channels have been read out. The VA chips can host up to 128 channels. We have tested HPD's front end boards with two 32 channels VA (VA32c).

Various types of external triggers can be used for the VA. We adopt the TA chip which is directly bonded to the output of the preamplifier of each VA channel. The TA contains a very fast shaper with peaking time of 75 ns followed by a comparator. A voltage threshold is set for each channel. The working principle and the timing sequence of a VA-TA combination are displayed in Fig. 52.

The nominal gain and noise performance of the VA32c (TA32c) are 150 mV/fC and 450 e^- ENC (15 mV/fC and 750 e^- ENC). These quantities can be measured in a calibration mode. For a typical HPD signal of 3500 $e^-/p.e.$, corresponding to a charge of 0.57 $fC/p.e.$, one obtains a signal/noise ratio of ~ 6 on the charge measurement for a single photoelectron. The details on the test results and performance of the VA-TA are given in Section 8.2.5.

As an ultimate solution for the front end electronics we are designing an Ethernet capable front end card. Indeed, the relatively low data rate (~ 50 Hz in average)[16] allows the direct connection of the sensors to the event building network through a compact, autonomous, low power and low cost front end module.

A general block diagram of such a device is shown in Fig. 53. The card contains an analogue front end, followed by a high speed ADC. A programmable logic device (FPGA) is dedicated to the control of the readout, the time stamping and communication with the Ethernet device. A FIFO is used for data buffering.

[15] IDE AS, Veritasveien 9, 1322 Hovik, Norway.

[16] The exact rate is under evaluation. The Ethernet solution allows a comfortable safety factor of ~ 40.

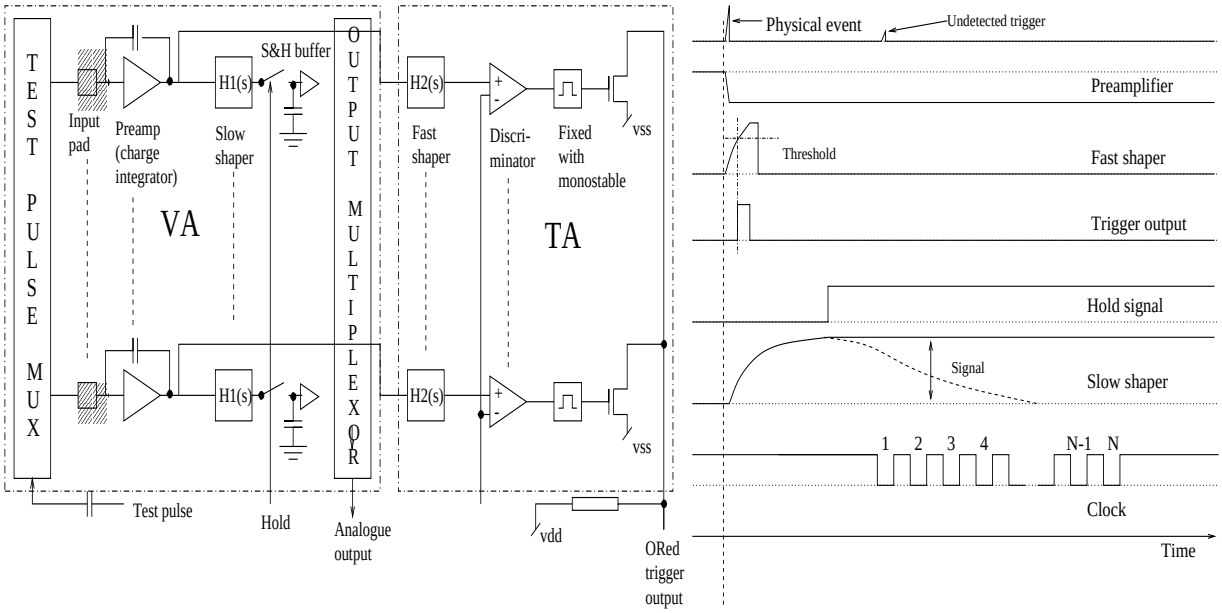

Figure 52: Working principle and timing sequence of the VA-TA.

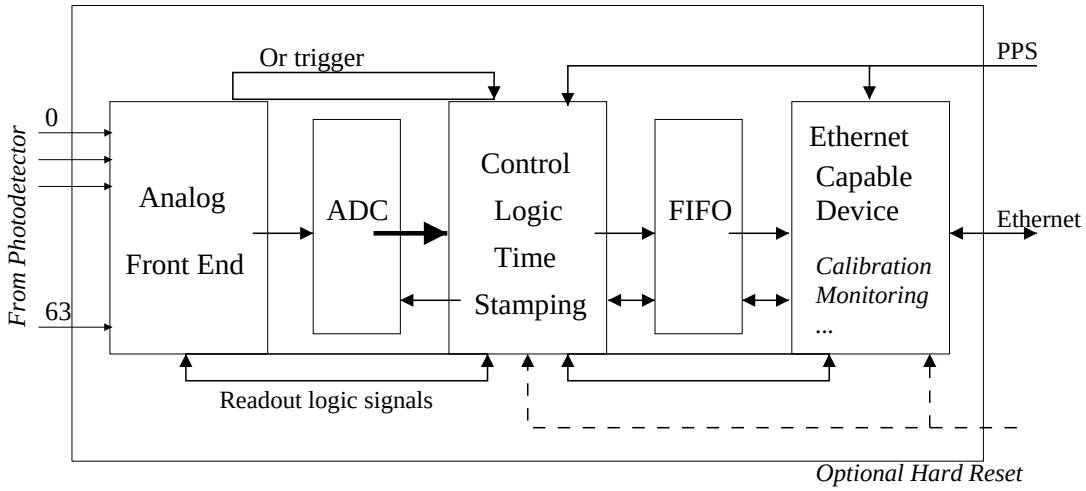

Figure 53: General block diagram of an Ethernet capable front end module.

The Ethernet capable device provides all the functions needed at the front end level: calibration, monitoring, data transmission and communication with the event building computers. This card needs three external connections (receiver for the PPS, Ethernet connection, hardware reset). Direct Java Processors represent excellent candidates for such Ethernet devices and are currently evaluated. With the exploding number of Real time Embedded applications, low power direct Java processors are available at very low cost. The evaluation of the performance in terms of data rates and processor load is underway.

Such Ethernet capable front end modules lead to simplified low cost DAQ systems. A global architecture could be based on a three-level scheme, the first level of which contains 1152 nodes of 64-channel modules. The second level is made of 10/100 $Mbits$ switches which concentrate the front end module outputs of each plane (72 in total). The third stage is a Gigabit switch that allows the connection to the events building PCs and storage devices as described in Section 4.7. An additional PC could be connected via each plane's switch if a local processing is needed ($X-Y$ coincidences for example). The advantage of such an approach is the possibility to use standard, reliable and low cost products. The system can be upgraded and scaled up if more power processing is required.

Although tested with a HPD detector in the scintillator tracker, the system can be extended to other detectors (RPC's and drift tubes) since the bandwidth constraints are quite similar. This global scheme forms a low cost alternative to the more classical DAQ system described in Section 4.7.

4.4.5 Calibration system

The tracker calibration procedure has to fulfil several objectives. One must keep the efficiency of individual strips to mip's above 97% and the brick finding efficiency constant, as well as to ensure the nominal energy resolution of the target calorimetry.

A complete calibration scheme for the scintillator trackers is foreseen, by using muons, light injection system, radioactive sources and direct charge injection in the front end electronics. The light injection tests the response of the photodetectors and of the electronic chain. The muons allow a global normalisation of the energy response for the whole optoelectronics chain, from the scintillator strips to the ADC. The same normalisation is obtained with radioactive sources which in turn allow quick checks and troubleshooting of the optoelectronics chain. The charge injection on the front end electronics, generated close to the front end chips, calibrates the response of the electronics (gain, noise, peaking time, threshold levels), over its full dynamic range. Cross checks between the various calibration methods are used for the overall consistency of the procedure.

The light injection system is well suited for the tracking and the corrections of short-term variations of the detector response. It gives also an information relative to connection problems in the optical chain from the scintillator to the photodetector. The basic element of this light injection system has to be located in the end-manifold area of a scintillator module. The idea is to use light emitters such as ultra-bright blue LEDs to flash the WLS fibres aside. The first prototypes of the light injection box are under study.

The mip efficiency can be kept under control with radioactive sources. The signal rate is indeed very sensitive to the electronics threshold levels. Furthermore, one can monitor the ADC charge spectra showing the single photoelectron peak for PMT's or the first, (or second, or third) photoelectron peak for

HPD's. The design of the radioactive sources calibration system is not yet completed. One could foresee the use of sources attached to the end of a wire and running along tubes, fixed to scintillator planes, perpendicular to the direction of the strips. This system performs a rapid mapping of the scintillator detector response. A similar device is also used during the detector construction and assembly phases before the installation.

Natural radioactivity of the emulsion bricks lead is also used for the calibration. The tracker local trigger can be made very loose for dedicated calibration runs. As discussed above, the calibration can be achieved by the survey of the counting rate for each individual strip and the monitoring of the ADC charge spectra.

Cosmic-ray muons can contribute to the calibration by comparing the muon energy deposition with that of test beam muons in a prototype detector. This can be a scaled version of an OPERA target tracker module including lead walls interleaved with scintillator planes. A full modelisation of the muons rates, path length and energy distribution at the Gran Sasso site is required. The muon calibration can also be checked by bringing the calibration module at Gran Sasso.

4.4.6 Detector production

The large scale production of the electronic trackers requires the collaboration between laboratories and industries. The quantities of the various detector components are reported in Table 8.

Table 8: Summary of the quantities required for the target electronic trackers.

Number of detector components	per module	per supermodule	for the full detector
Scintillator planes	2	48	144
Scintillator strips	512	12288	36864
WLS fibres	512	12288	36864
PMT's	16	384	1152
Aluminium cases	32	768	2304
Scintillator elements	8	192	576

WLS fibres and PMT's can be produced in large quantities by industry. The choice of the WLS fibres has to be driven by considerations of cost and by the performance obtained with full size prototypes equipped with fibres from different producers. The machines for gluing fibres into the grooves of the strips are under study.

The baseline photodetectors are the 64-channel Hamamatsu H7546 PMT's. However, contacts are underway with industries to design HPD's fitting the physics and mechanical constraints with 64 to 128 pixels.

The scintillator procurement requires a specific industrial production. Contacts have been taken with industries to undertake a common R&D effort towards the production of scintillator strips with better performance in terms of light yield and quality of the reflective coating. In this respect, we profit from the

R&D already performed by the MINOS Collaboration. Two years are expected for the total production of the scintillator strips.

We have to specially produce for OPERA the aluminium cases for the 16 scintillator strips sub-detector, the surrounding box which gives the mechanical rigidity to each 64-strip element and the end manifold housing photodetector and readout electronics. The first prototypes are presently being developed in our laboratories.

4.4.7 Detector assembly

Each scintillator plane is composed of four 64-strip elements. This modularity allows the trackers to be mounted at different sites and then be carried to the Gran Sasso experimental hall. A production site has to ensure the following operations

- gluing checks of strips and fibres;
- gluing WLS fibres into scintillator grooves;
- assembly of the 16-strip sub-unit into the aluminium case;
- assembly of 4 sub-units into one unit;
- routing of the fibres through the end manifold to the cookie adapted to the photodetector;
- mounting of the photodetector and of its readout card;
- calibration of the unit using a light injection system with blue LEDs and radioactive sources.

The detector transportation requires careful handling, in order to keep the rigidity of the units. These are then mounted sequentially with the mounting of the brick support structure. Different schemes are under study for the installation of the electronic trackers. In one of them the 64-strip units are hung from the same I-beam as the emulsion bricks. The advantage of this scheme is that no extra mechanical structure is needed which would increase the amount of material between brick walls.

We foresee a construction period of about two years which largely overlaps with the installation at Gran Sasso. The first tests will then begin with cosmics and natural radioactivity for a first calibration.

4.5 Muon spectrometers

4.5.1 Magnets

The baseline option for the spectrometers foresees the use of warm iron dipolar magnets (Fig. 54 and Fig. 55). Each of the magnets consists of two vertical walls of rectangular cross section and of top and bottom flux return paths. In the walls (tracking volume), the magnetic field is essentially uniform, with a flux density of 1.55 T. The field lines are vertical and of opposite orientations in the two magnet walls.

The walls consist of iron layers interleaved with RPC's (Inner Trackers). Drift tubes (Precision Trackers) are located in front and behind the magnet as well as between the two walls, to measure the muon momentum.

Externally, the magnet is 8.75 m wide, 10.0 m high and 2.64 m long. The length is given by the two walls, each of 0.82 m, with a free space of 1.0 m in between allowing the insertion of the Precision Trackers. This free space is defined to optimise the momentum resolution. Each wall is made of 12 iron layers 50 mm thick, with 11 gaps 20 mm thick to house the Inner Trackers. Each iron layer is made of 7 iron plates $50 \times 1250 \times 8200$ mm^3 to be assembled in situ, for a total of 168 plates per spectrometer. The plates are precisely milled along the two short sides (1250 mm). They include holes for bolting and lifting as well as slots for cabling.

The total weight of one magnet is about 950 ton: 270 ton for the top and bottom flux return paths and 680 ton for the walls.

The plates are bolted together with bolts (36 mm in diameter 820 mm long) spaced by about 1 m, resulting in a solid structure which is used as a base for the emulsion target supports. The nuts holding the bolts also serve as 20 mm spacers between the plates. The plates are also bolted at the top and bottom edges to the return flux paths. This design permits a fast and clean magnet assembly, alternately mounting in iron layers and inner tracker planes.

We envisage the use of a spin casted unalloyed quality steel with magnetic properties of the type Fe GM01 UNI 3595. The permeability is 7×10^{-4} Hy/m, for an average magnetic field of 1.55 T, well below saturation. The first tests performed on a sample of this iron indicate magnetic properties about 3% better than nominal.

A field map calculation performed with the ANSYS 5.3 code has shown that the homogeneity of the wall magnetisation is within 5% or better over most of the plates. The fringe field is about 10 G at 10 cm distance from the edge. Fig. 56 shows the distribution of the magnetic field in the 12 iron layers at their centre (left) and at the connection with the top flux return iron (right).

In order to simplify the construction and the operation, the coils have low current density and air cooling. Two symmetric coils run around the top and the bottom flux return paths. The turns are made of copper bars (type Cu-HCP UNI 5649-1) 80×15 mm^2; their resistivity is 0.017 $\Omega \times mm^2$. The current density is 1 A/mm^2 for a total current of 1200 A. The total number of turns is 46 (23 per coil). The total length of the conductors is 810 m and their weight 10 ton. The total resistance is 0.011 Ω, the voltage 13.2 V and the power 15.8 kW.

The two flux return paths (top and bottom path) and the multilayer vertical walls are bolted together so they constitute a self supporting structure. The bottom flux return path is bolted to the floor by means of 50 bolts (30 mm in diameter) cemented to the floor concrete. The vertical iron plates are bolted to the bottom return paths. Each multilayer wall consists of plates bolted together. The nuts, screwed on the bolts between the plates, act as spacers for the trackers and tighten the plates together. The bolts and the nuts prevent sliding of the plates making the multilayer wall, together with the return path, a compact structure self supporting and usable, in addition, as a support for the target modules.

A prototype magnet is presently under construction at the Frascati Laboratory. It has full height but a reduced width and wall thickness. It is made of two walls each 8.6 m long and 2.5 m wide, for a total weight of about 70 ton of iron. It will be equipped with RPC inner detectors. Tests will be performed on the mechanical properties, on the installation procedure and on the operation of the RPC's, as well as measurements of the magnetic field.

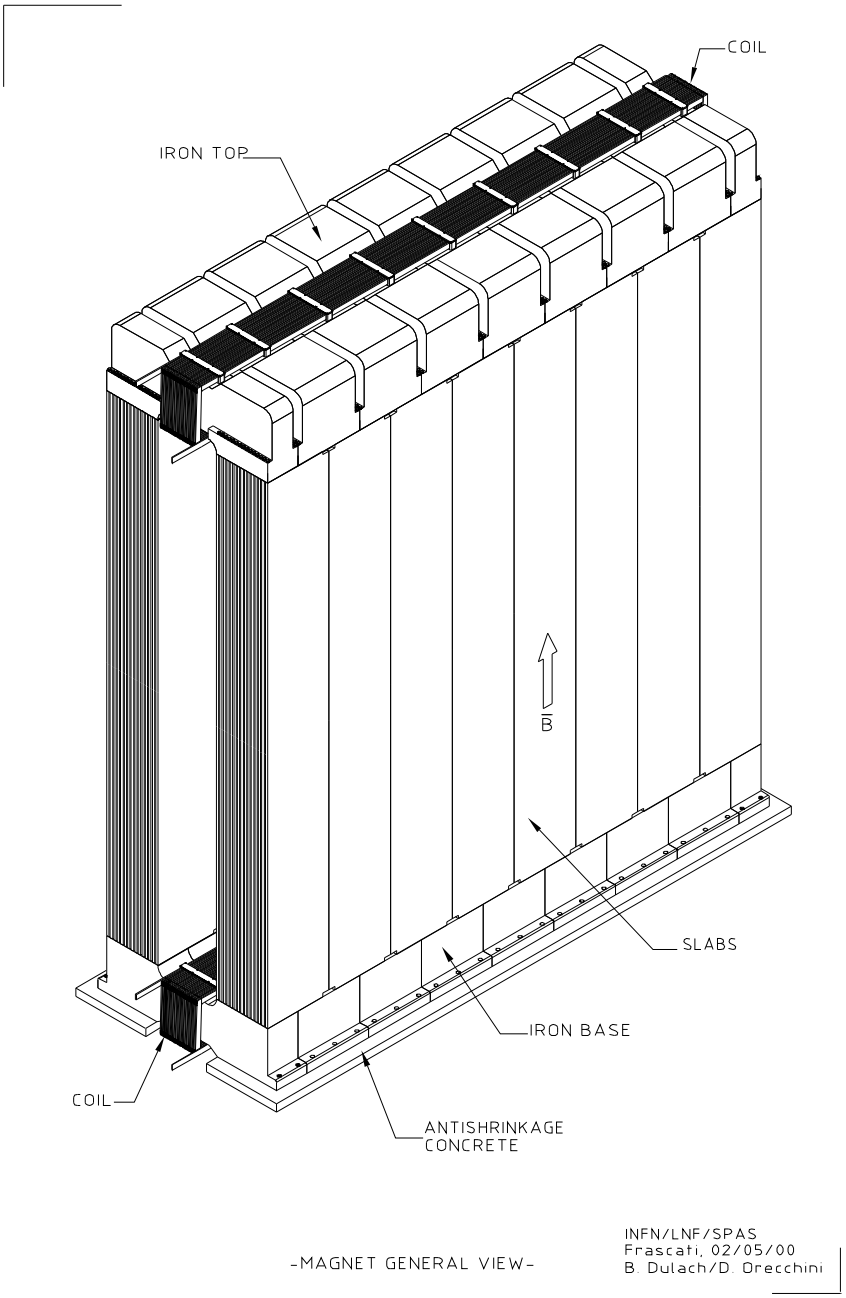

Figure 54: Isometric view of the dipolar magnet.

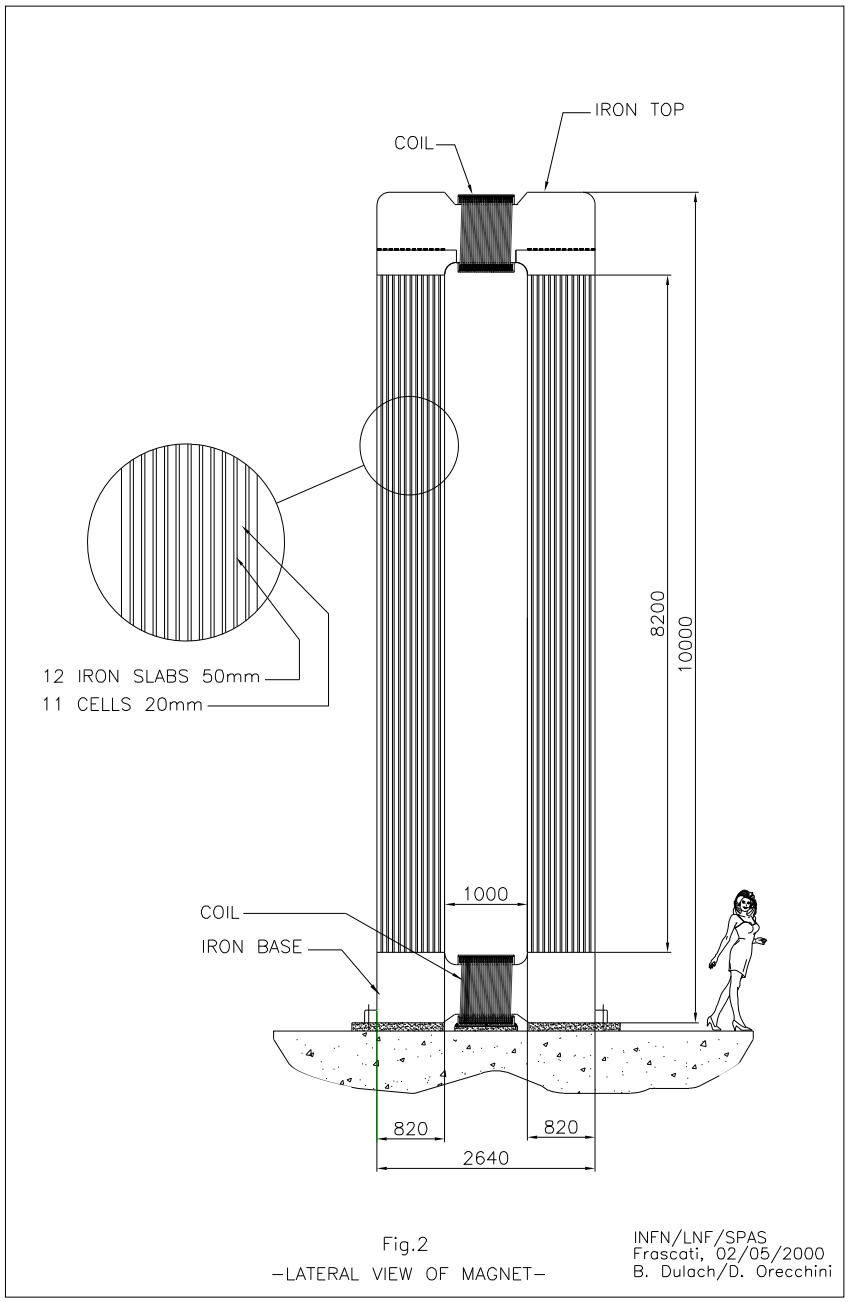

Figure 55: Dipolar magnet (side view).

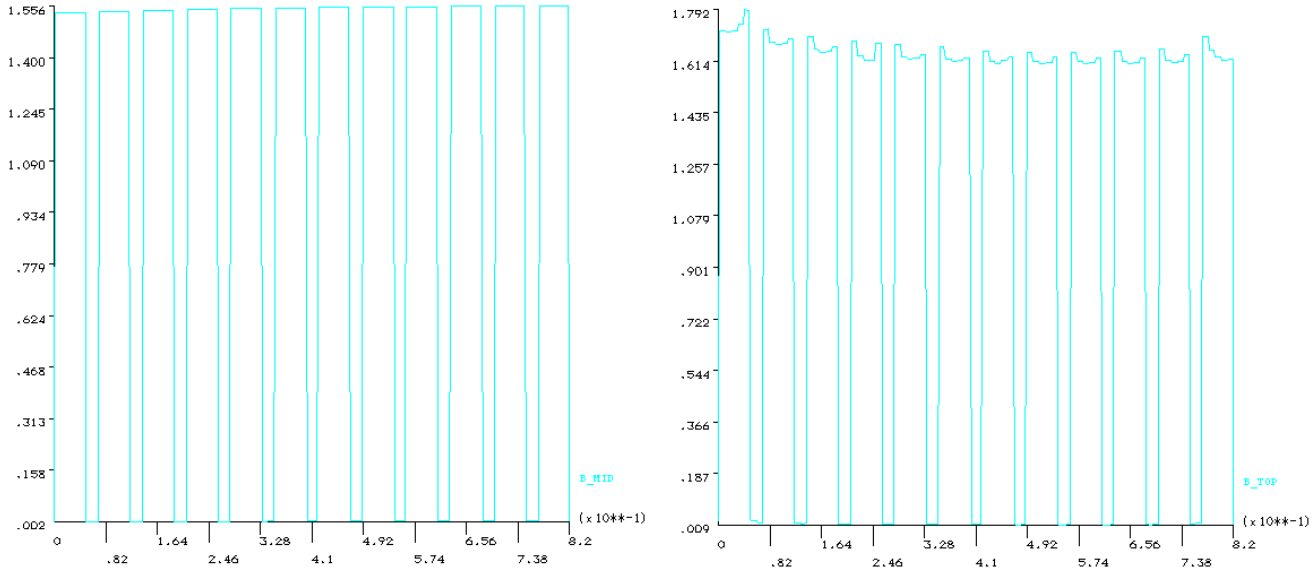

Figure 56: Magnetic field distribution at the centre of the iron plates (left) and at the connection with the top flux return iron (right).

4.5.2 Inner Trackers

RPC's, shown schematically in Fig. 57, are an optimal choice for the instrumentation of the muon spectrometer given their high intrinsic and geometrical efficiency, the low cost, the robustness and the ease of segmentation with the desired shape.

We plan to adopt the technology developed by R. Santonico *et al.* [61, 62], which is used in various accelerator experiments [63], in cosmic rays physics [64] and which is foreseen for the first-level muon trigger systems of the ATLAS and CMS experiments [65]. With a different technology, they are envisaged for the MONOLITH calorimeter [33] and for the ALICE time of flight detector [66]. The knowledge gathered in several years of R&D has already been transferred to industry and the production capabilities are well-matched to the large detector area required by OPERA.

As shown in Fig. 57, the electrode plates are made of 2 mm thick Bakelite (phenolic polymer) with a volume resistivity of $10^{11} - 10^{12}\ \Omega - cm$, painted on the external surfaces with graphite of high surface resistivity (100 $k\Omega$/square) and covered by two 300 μm mylar insulating films. The two graphite layers are connected to high voltage ($\sim 8\ kV$) and ground, respectively. Gap surfaces are treated with linseed oil, which strongly enhances the RPC performance (low noise, high efficiency). Planarity of the two electrodes is assured by Lexan spacers located on a 10 cm-square grid in the sensitive volume. The active area is filled with an argon-based gas mixture at atmospheric pressure.

A charged particle crossing a RPC produces a quenched spark which induces signals on external pickup electrodes. The induced pulses are collected on two pickup planes, with a pitch of 30 mm and 2 mm of separation, made of copper strips glued to plastic foils located on either side of the chamber.

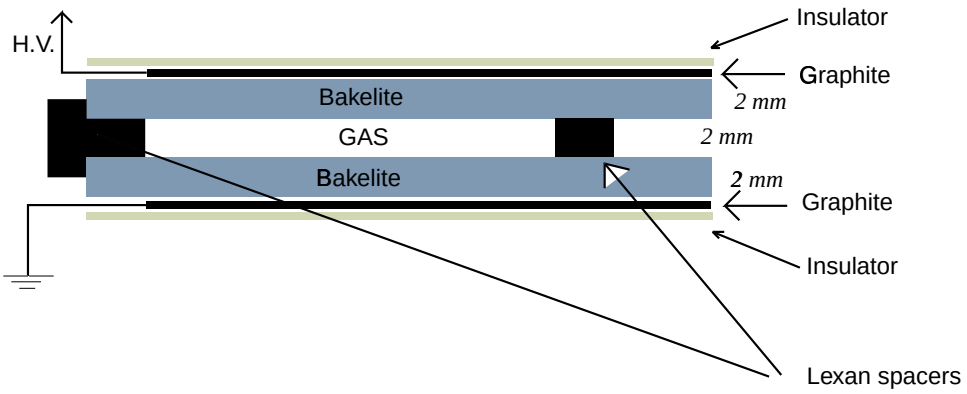

Figure 57: Schematic view of a RPC.

The strips run in two perpendicular directions to provide two-dimensional information. The induced charge is of the order of 100 pC, and the pulse has a rise time of 2 ns and a duration of 10 ns.

The transverse dimensions of the instrumented area of the magnet are 8 m in height and 8.7 m in width. Therefore, the three spectrometers with 22 gaps each, cover a total detector area of $\sim 4600\ m^2$. With 30 mm pickup strips, the total number of readout channels is $\sim$ 37000. The present industrial technology permits the building of RPC's with maximum chamber size of about 1.3 $m \times 3.2\ m$. Within these limits, RPC elements can be built in practically any shape. In order to minimise the number of different element sizes, we have adopted the layout illustrated in Fig. 58. The height is covered by 7 RPC's and the width by 4.

In total we have 28 elements for each gap and only two different elements types (21 have dimensions of 1.14 $m \times 2.50\ m$, 7 have 1.14 $m \times 1.25\ m$ size). The total number of RPC elements for three spectrometers is 1848 (1386 of large dimensions and 462 of small ones). The iron plates constitute also the support onto which RPC's are fixed.

In the L3 experiment [63] where RPC detectors were extensively used, the streamer mode operated with a gas mixture of Argon (58%), Isobutane (39%) and $CBrF_3$ (3%). This mixture is unfortunately highly flammable and contains the freon component $CBrF_3$ which is no longer recommended due to its ozone destroying property. These constraints were considered by the BABAR Collaboration which adopted an ecologically acceptable and inflammable mixture of Argon (48%), Isobutane (4%) and $C_2H_2F_4$ (48%), with rather good performance [67].

The percentage of the quenching components (Isobutane and TetraFluoroEthane) does not seem to play an important role, as reported recently by the Argo Collaboration [68]. They tested, at sea level, mixtures with different percentages (Fig. 59). We intend to pursue an extensive study of the RPC performance as a function of Isobutane percentages, below the flammability limit (6%), as well as of the gas purity.

A simple and reliable system for mixing the different gas components and circulating the mixture serially through the chambers has been designed. To ensure the long term reliability of the RPC per-

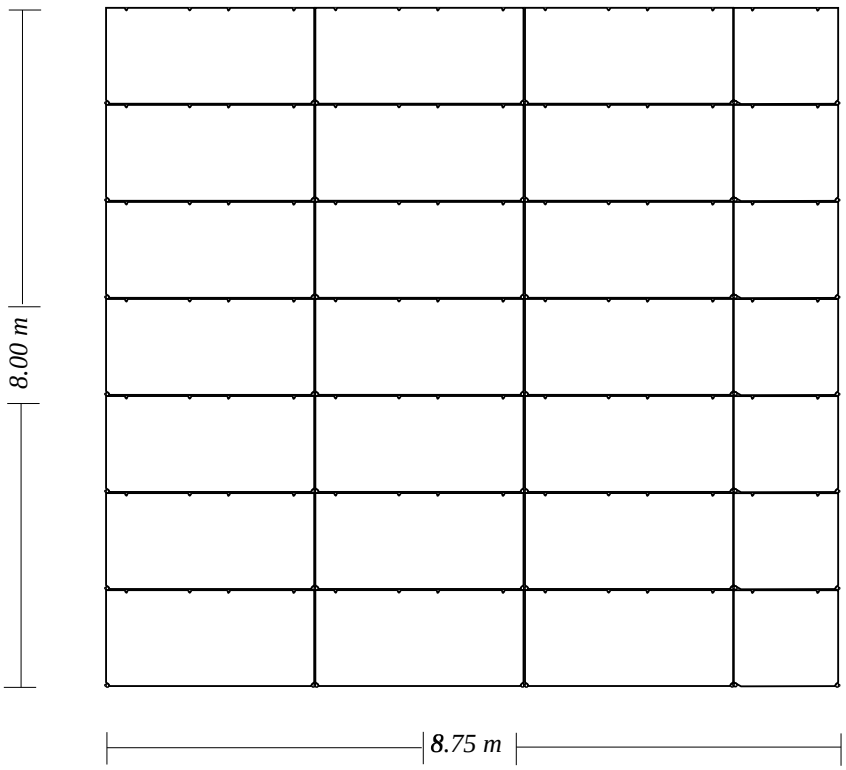

Figure 58: Cross section of an RPC detector plane.

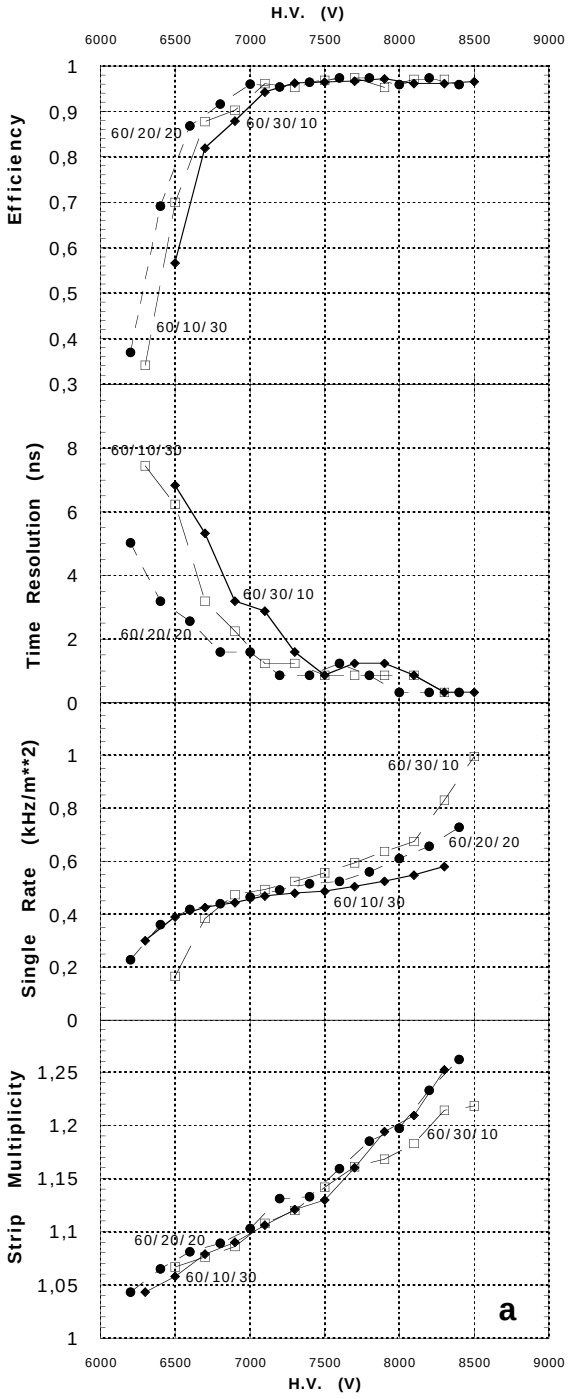

Figure 59: Influence of the gas properties on the RPC performance [68].

formance, it is presently foreseen not to recirculate the gas in close circuit but to recuperate it with a balloon system and send it back to the gas company. Each plane of RPC is serially fed by 7 parallel lines, each line serving the 4 horizontal chambers in order to have a uniform impedance.

With the present choice of the gas mixture the operating voltage of the RPC's is about 8 kV. The current drawn has been measured to be 5 $\mu A/m^2$ and is permanently monitored for each chamber.

The RPC front end electronics is rather simple since the signal pulses are large (100 mV) and no preamplification is needed. Only a digital readout is foreseen. The excellent timing properties of the RPC allow also to form a clock signal for the Precision Trackers. Such an electronic card is already used in the BABAR experiment [63] to readout RPC's (2500 m^2) very similar to those foreseen for OPERA.

A draft overview of the RPC data acquisition system for a plane is shown in Fig. 60. The whole plane is read out with $8 + 9$ 32-channel front end cards linked on an acquisition card in a daisy chain mode. For each trigger (provided by a fast OR of the plane's signals, in coincidence with the adjacent planes) the acquisition card performs a simple formating of the data and adds the time stamp of the event, given by the Global Position System (GPS) through the Pulse Per Second (PPS) clock. The interface of the acquisition card can be either a serial link, a direct Ethernet connection or a VME bus.

Connection of the strips to the boards makes use of twisted and flat cables. The quality of the cables to preserve the timing accuracy of the signal is still to be studied.

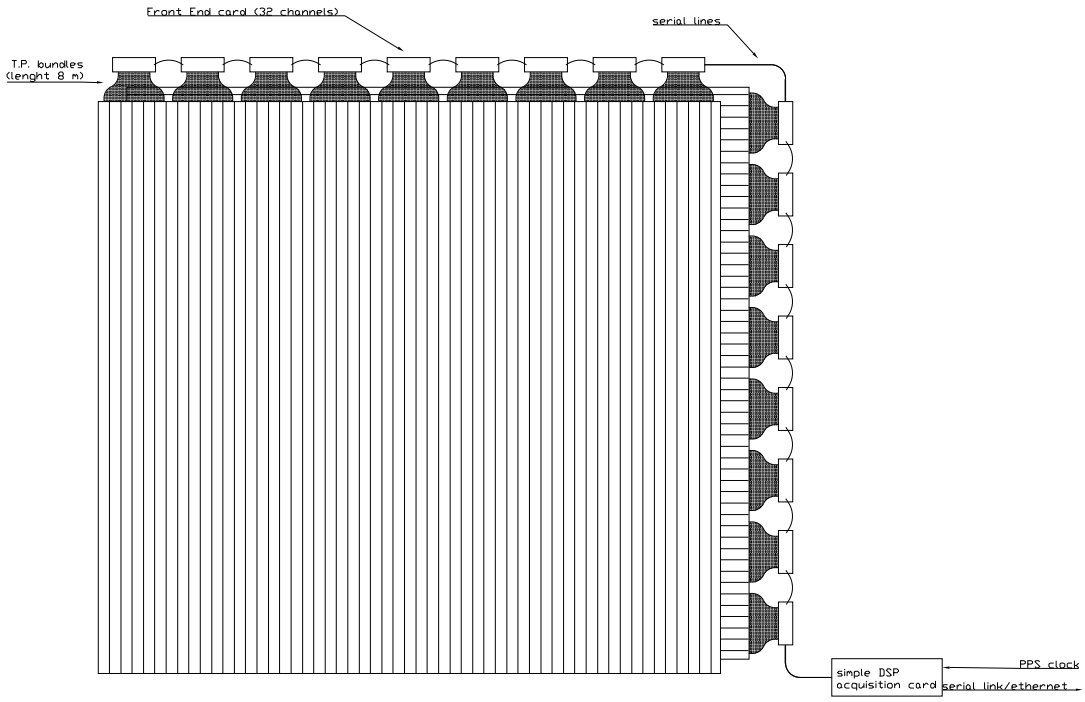

Figure 60: Scheme of the RPC front end electronics and DAQ.

RPC elements are shipped from the industrial producer to the Gran Sasso Laboratory where tests on the gas (tightness and flow), the HV (efficiency curves) and the electronics chain are performed. Only small samples of RPC's are moved to the OPERA laboratories for extensive quality checks.

The construction of the dipole magnets and the installation of the RPC's follow the same path. The installation steps are

- after the installation of the dipole base (the first wall of the dipole) a first complete iron-layer is mounted;
- Y-strips are attached to the surface of the iron-layer. Flat cables soldered to the strips are routed in the dedicated space at the top of the layer;
- RPC's are mounted on their individual supports attached to the iron plate.;
- the gas and HV connections of the RPC planes are implemented;
- tests for gas tightness and flow, as well as on reliability of the HV connections are performed;
- X-strips are fixed to the RPC's;
- finally, the next iron plates, which complete the iron-RPC-iron sandwich, are positioned and fixed by bolts.

During the operation the performance of the RPC's are checked by monitoring high and low voltage, temperature, gas flow meters and gas quality. The efficiency of the RPC planes is monitored by reconstructing muon tracks.

4.5.3 Precision trackers

The Precision Trackers measure the coordinates and the directions of the muon trajectories in front, inside and behind each dipole magnet. The required features are, in addition to the intrinsic spatial resolution, high single track detection efficiency, adequate multi-hit capability to cope with showers developing in the target section and leaking into the magnet and, for safety reasons, absence of toxic materials and flammable gases. Since the track pattern recognition and the muon identification are performed in the target and the Inner Trackers, the granularity of the Precision Trackers should match the spatial resolution of these detectors ($2 - 3\ cm$).

The required precision on a coordinate measurement in the magnetic bending (horizontal) plane may be evaluated as follows. Assuming 6 measuring planes, as shown in Fig. 61, the momentum p of the particle is determined by the measured total bending angle Θ, where $\Theta/2$ is the bending angle in each wall of the dipole magnet. The resulting momentum resolution is given to a good approximation by

$$\frac{\Delta p}{p} \sim \frac{\Delta\Theta}{\Theta} = \sqrt{6(\frac{p\epsilon}{0.3adB})^2 + \frac{1}{d\lambda}(\frac{0.014}{0.3B})^2}$$

where ϵ is the precision of each coordinate measurement; $a = 0.5\ m$ is the lever arm for an angle measurement; $d = 1.2\ m$ is the total thickness of the iron of both magnet sections; $B = 1.55\ T$ is the magnetic field in the iron; λ is the radiation length of iron; p is the muon momentum in GeV and all lengths are expressed in meters.

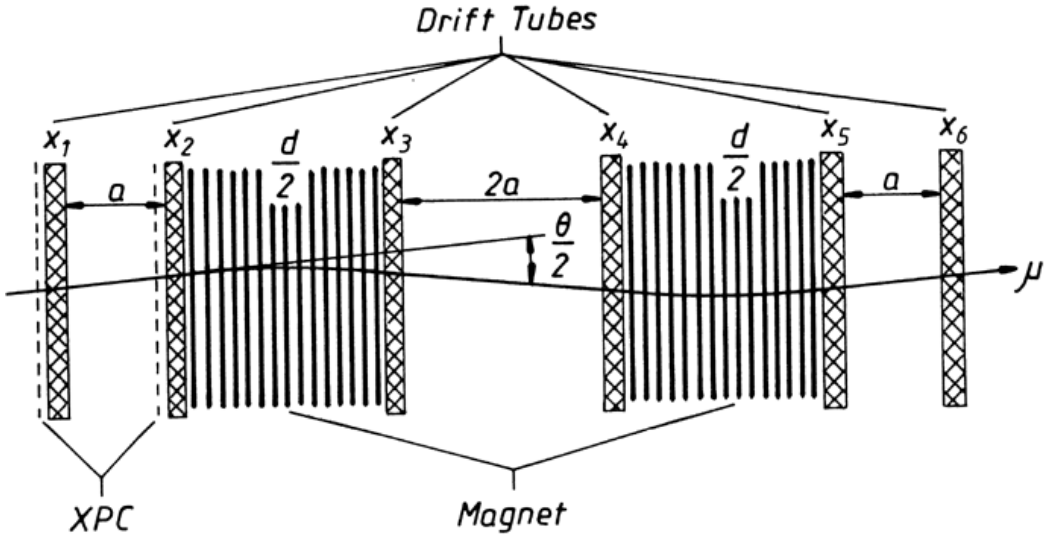

Figure 61: Drift plane arrangement in the muon spectrometer. Also shown are two planes of RPC's with inclined strips (XPC's).

Setting $\epsilon = 0.0005$ in this expression the resulting momentum resolution for small momenta is $\frac{\Delta p}{p} = 0.21$ and for a momentum of 25 GeV/c $\frac{\Delta p}{p} = 0.24$.

Therefore, for the momentum range relevant to muonic τ decay, the sign of the muon charge can be determined to better than four standard deviations if the overall precision of the tracker is better than 0.5 mm over the whole transverse area of the spectrometer. The alignment precision has to be achieved by construction since in the underground hall one cannot rely on an alignment by cosmic rays or beam-related muons. It is thus desirable that the intrinsic precision of the detector elements be about 0.3 mm. Such a precision can be reached with standard drift tubes and standard mechanical alignment techniques.

A drift tube plane covers an area of 8.75×8 m^2. It is made of round metal tubes with an outer diameter of 34 mm. Each layer consists of 256 tubes. To reach full efficiency and sufficient redundancy, staggered layers are added. A complete drift tube plane consists of three staggered single layers (Fig. 62). Since the particles are magnetically deflected in the horizontal plane, vertical tubes are required for the momentum measurement. For each spectrometer, 6 drift tube planes are required, each consisting of three vertical layers. In total there are 4608 tubes.

To resolve ambiguities in the track spatial reconstruction each of the two drift tube planes upstream of the dipole magnet is complemented by a RPC plane (so-called XPC's) similar to the ones used as Inner Trackers. The aluminium strips of the two pickup layers have a pitch of 3 cm with a $+45$ and -45 degrees orientation, respectively (Fig. 63).

The tubes are arranged in units each with a width of 1 m and a length of 8 m. The signal wires

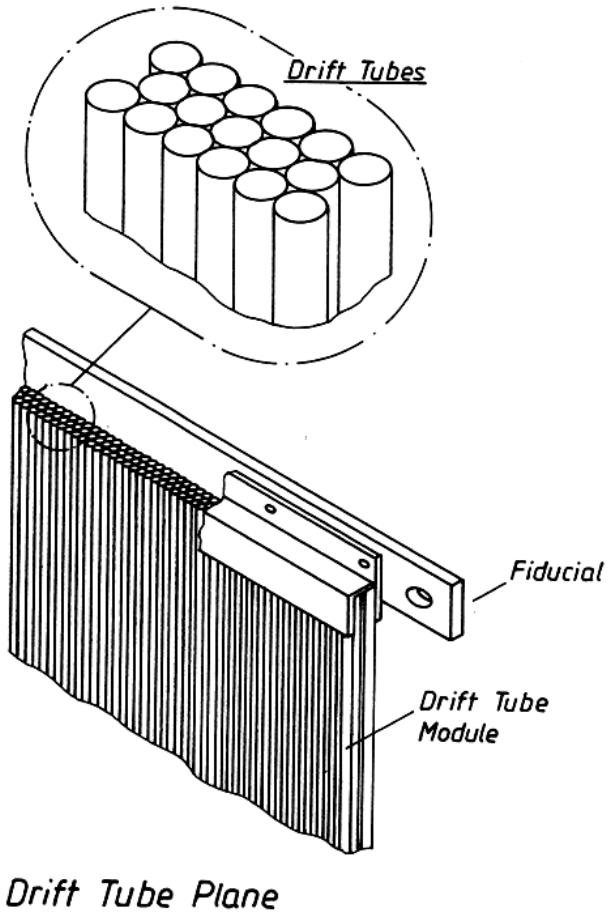

Figure 62: Details of a drift tube plane.

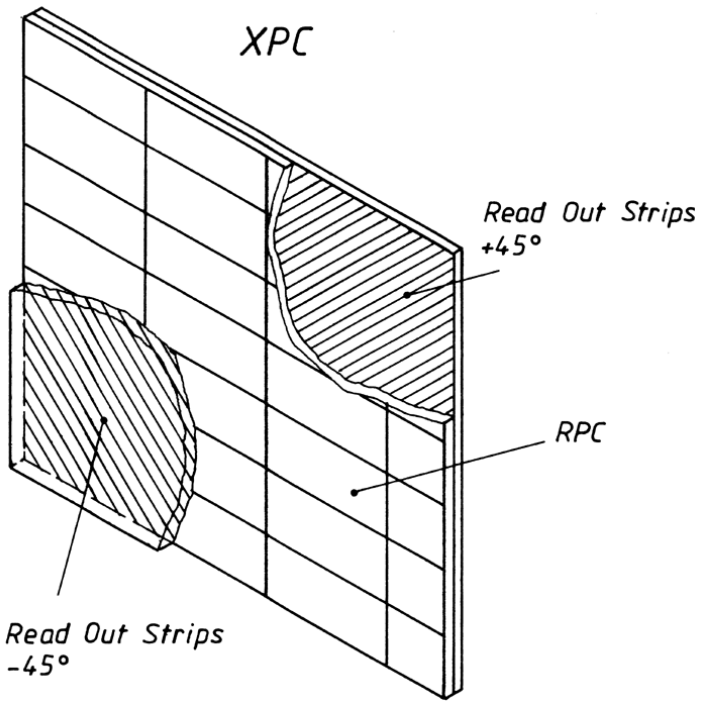

Figure 63: Schematic view of a XPC detector plane.

have a diameter of 50 μm and are stretched over 8 m without any additional support. The tubes are operated with a hydrogen-free gas mixture of Ar, CO2 and CF4.

Much R&D work has already been performed on the front end electronics to be mounted on the drift tubes. Two chips, a front end chip and a TDC chip have been tested with very satisfactory results. Each chip can handle the signals of 8 wires.

The first chip called ASDBLR (Amplifier Shaper Discriminator Base Line Restorer) has been developed for ATLAS by the University of Pennsylvania. It has a low-level discriminator giving a precise time measurement and a high-level discriminator which allows the charge integration and is used to obtain a substantial noise suppression.

The second chip acts as a TDC. It has been developed for HERA-B at DESY and can be adapted to the OPERA requirements. It processes the output of the ASDBLR and provides the drift time measurement with a bin size of 2 ns over a full range of 512 ns. It has sufficient multi-hit capability to resolve up to 8 hits per wire.

4.6 General support structure and alignment

The general mechanical structure of the detector has to hold the target walls while leaving free access on the target sides to the brick manipulator robot. It stands directly on the spectrometer magnets. The structure must also satisfy the stringent anti seismic rules imposed by Italian and LNGS regulations.

As seismic standards are concerned the LNGS region has been classified as second class seismic zone (seismic coefficient S=9). This sets the rules for any civil building or large size mechanical structure to be built in the area.

Because of the peculiar operative conditions of the Gran Sasso Laboratory, its close connection with the highway and the potential risks of large detectors running underground, it has been necessary to settle more stringent safety rules on seismic standards. These rules have been established on the basis of a detailed report commissioned by the LNGS and drawn up by ISMES Italian Institute. In this report two levels of seismic hazard have been defined. The first one, called OBE (Operating Base Earthquake) in accordance with the maximum historical earthquake, has to be used in designing the structures of apparatus with no intrinsic hazards. The acceleration spectrum of OBE calculated in free field conditions is reported in Fig. 64.

The second level called MCE (Maximum Credible Earthquake) related to the maximum virtual earthquake must be used in designing apparatuses with dangerous components. In this case, the spectrum is scaled from the free field conditions to the internal laboratory through appropriate transfer functions. Since OPERA does not contain dangerous components, the OBE seismic level of hazard could be used. In addition the same scale reduction (a factor of two) as obtained in the MCE case passing from the free field (external) conditions to the underground halls could be considered, upon LNGS safety staff agreement.

The detector support structure complies with these rules and consists of longitudinal beams fixed on top of the dipole magnets with some inter-beam diagonal reinforcements. The distance between different dipoles is about 5 m including ~ 1.5 m for assembling and/or installing the walls and the Target Trackers.

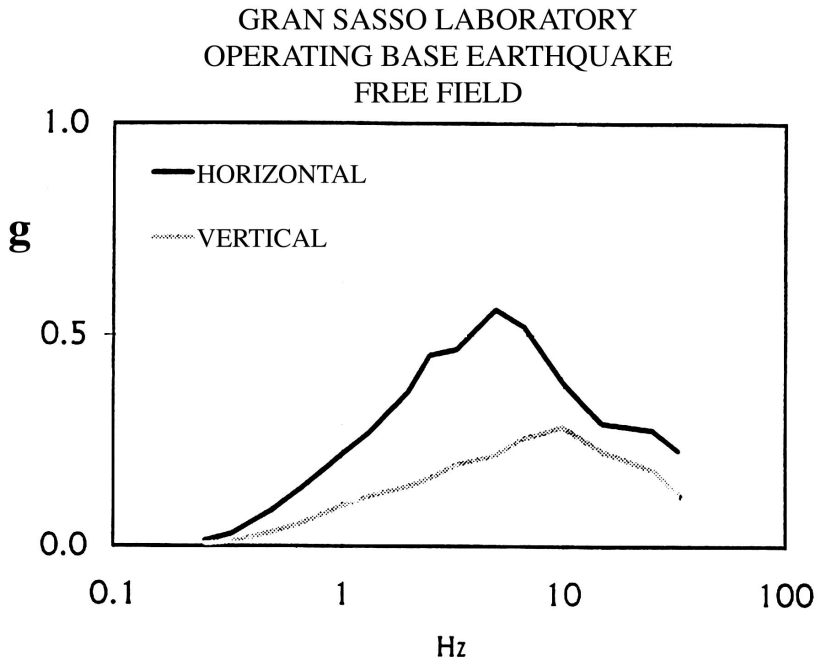

Figure 64: Acceleration spectrum for Operating Base Earthquakes.

For a target weight of about 700 ton per supermodule it has been calculated that 8 longitudinal beams are required, each with 1.2×0.4 m^2 cross section. This is described in Fig. 65.

In order to fulfil the seismic requirements, specially for earthquake waves parallel to the LNGS hall, two designs are under study. The first one foresees longitudinal beams at 45^o inclination fixed on the floor and on the top of the detector at both ends of the general structure. The second envisages longitudinal beams on the floor fixed to the bases of the magnets.

An estimate of the required alignment precision gives 1 mm for the Target Trackers and 0.1 mm for the spectrometer Precision Trackers. An alignment of the spectrometer Inner Trackers within 1 mm is sufficient.

One can use a multi point monitoring system consisting of 4 laser beams positioned at the four corners of rigid frames and pointing to transparent Mylar mirrors, attached to each scintillator or brick wall plane. This method has been proposed for the ALICE experiment; variants of it have been also used in L3 and envisaged for ATLAS. The light reflected at each mirror falls on commercial 2D CMOS sensors, capable of tracing the laser beam movements with a few micron precision. Since the transmittance of the Mylar mirrors is higher than 90% a single laser beam for the 24 stations of the target tracker should be sufficient (one order of magnitude attenuation between the first and last point). If proven insufficient a second laser system starting at the end of the target tracker, could complement the alignment.

The same system is used for the alignment of the spectrometer trackers. The inter-alignment of the two trackers (target and spectrometer) is performed with a similar system connecting the last plane of the Target Trackers to the first plane of the spectrometer trackers.

4.7 Readout, trigger and DAQ

Several detection techniques (scintillators, RPC's, drift tubes) are used in OPERA and thus the DAQ system has to be flexible enough to comply with the different detector requirements. Only the front end electronics, in case a common solution cannot be found, has to be developed separately and adapted to each detector.

4.7.1 DAQ overview

The aim of the DAQ is to create a database of detected events. In OPERA this database is a key element to decide when and which bricks must be extracted and is also used during the final data analysis.

OPERA has no hardware trigger and the DAQ is based on a software selection of events from the noise. Taking advantage of the low rate, data from all the electronic channels are kept until their online analysis is completed. In this way, the trigger algorithm can be adapted to the experiment conditions.

The DAQ architecture is subdivided into three stages (Fig. 66)

- the front end electronics close to the detector;
- the readout interface;
- the processor farm for the real time analysis.

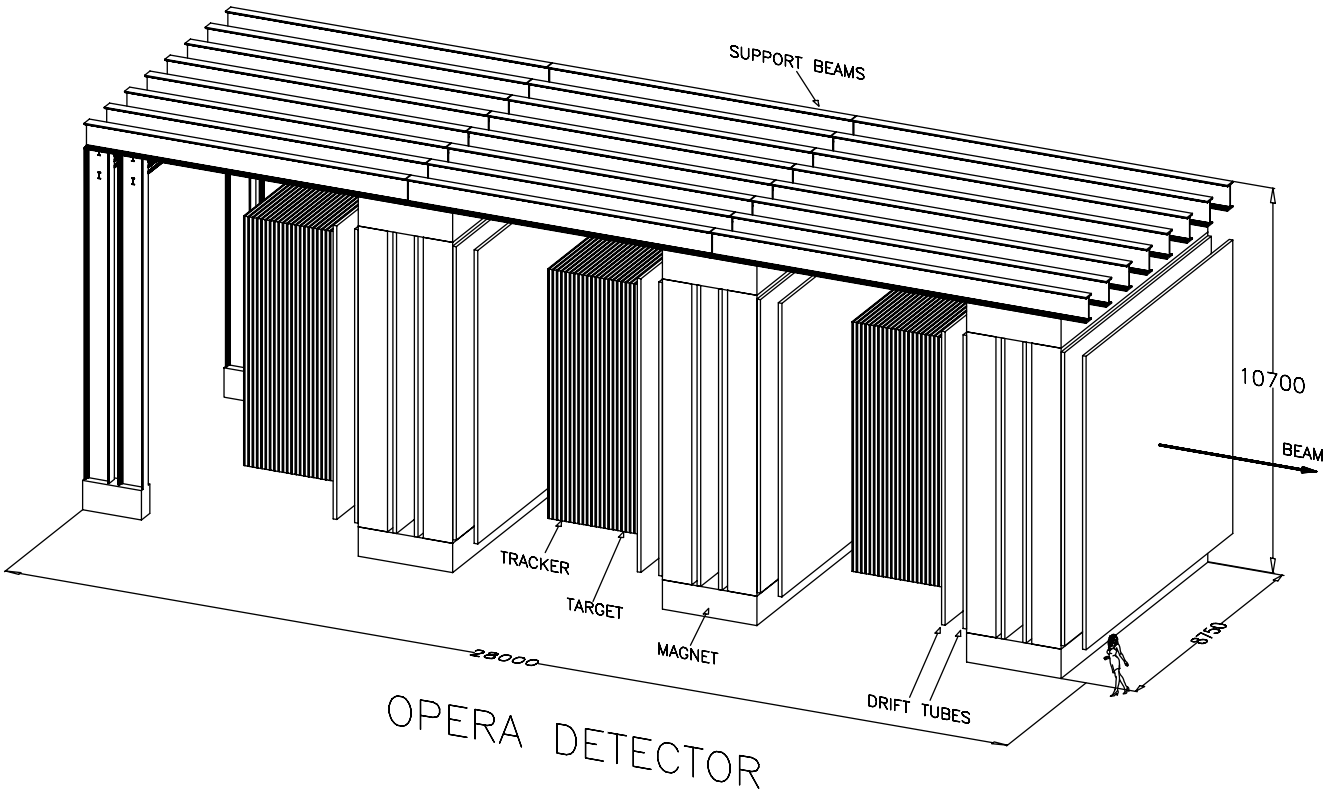

Figure 65: The OPERA detector shown with its support structure.

The whole event reconstruction is based on the channel time correlation. This depends on the accuracy of the electronic channels time-stamps. A time resolution of 5 ns corresponding to the total electronic time jitter has been retained.

A common time reference with respect to the Universe Time Coordinated (UTC) is provided by a Global Positioning System (GPS). The beam bursts are recorded with another GPS at CERN to establish the offline correlation between the recorded events and the beam cycles.

The different detector elements need a slow control system to monitor parameters affecting the detector performance. Some of them are listed below

- scintillator detectors: temperature, high voltages, low voltages and currents of photodetectors;
- RPC's: gas flow and mixture, temperature, atmospheric pressure, high voltages, low voltages and currents;
- drift tubes: gas flow and mixture, temperature, atmospheric pressure, high voltages, low voltages and currents;
- magnet: temperatures, power supplies and cooling, water control of the cooling system, magnetic field, voltages and currents.

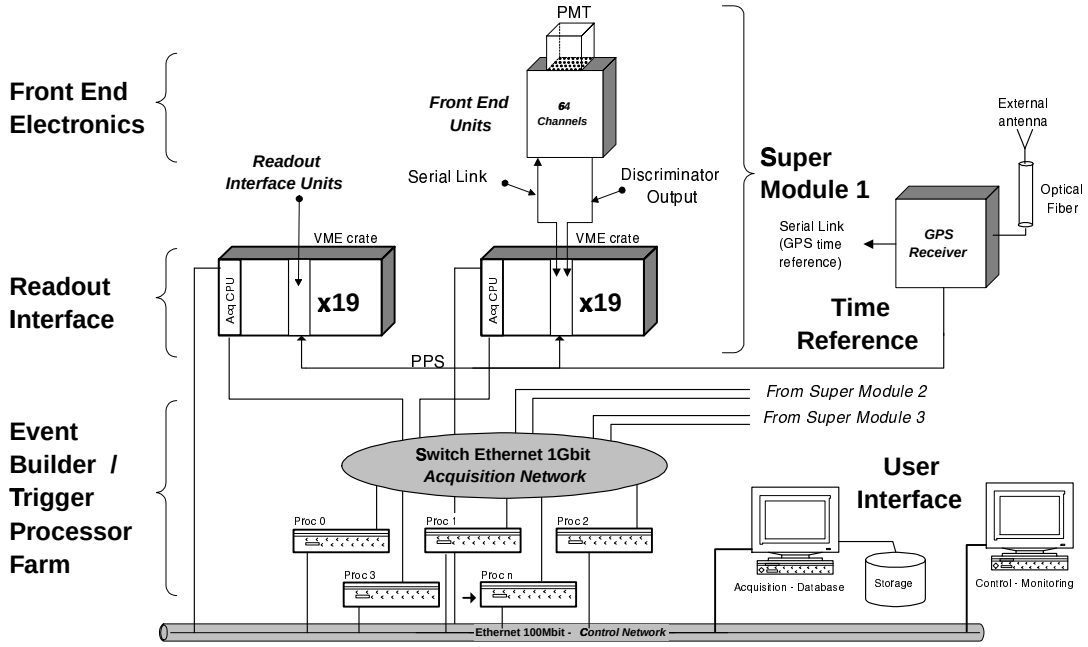

Figure 66: Overview of the data acquisition system.

Table 9: Number of electronic channels in each main detector.

Electronic detector	Nb. of planes	Nb. of channels/plane	Total
Target Trackers	3×48	512	73728
Spectrometer RPC's	3×22	560	36960
Spectrometer drift tubes	3×6	768	13824
Spectrometer XPC's	3×2	790	4740

4.7.2 Data flow

To evaluate the expected data flow from the electronic detectors, we have considered a suitable safety factor, accounting for the largest possible number of electronic channels.

A maximum counting rate induced by natural radioactivity of about 10 Hz per electronic channel is assumed. Detector and electronic noise have to be added. Using the Hamamatsu 64-channel PMT with a threshold corresponding to $1/3$ photoelectron, a noise frequency lower than 5 Hz has been measured, mainly coming from the photocathode thermo emission. The use of HPD's for the scintillator readout could increase the electronic noise by at least one order of magnitude as compared to the PMT for the same threshold.

Taking into account possible noisy elements a mean electronic noise of the order of 50 Hz is considered for the scintillator strips of the target. For RPC's the noise is assumed to be of the same order. The drift tubes of the Precision Trackers require an external time reference. The TDC common STOP could be provided (within a time shorter than 512 ns) by the RPC's associated with the spectrometer. Thus, since the Precision Trackers do not participate in the trigger, the electronic noise of this detector does not significantly disturb the acquisition system. For the data flow evaluation an electronic noise of 50 Hz has also been assumed.

Table 9 gives the number of electronic channels for the three detectors. For each detected hit, at most 12 $byte$ are stored (channel address, signal and time). The total rate amounts to about 90 $Mbyte/s$.

If the final electronic noise rate would be significantly higher, fast time correlations between X and Y channels could be performed before signal digitisation. These correlations could be used as external signal to trigger the front end readout cards and thus, reduce the noise. In any case, the acquisition system must be able to support at least three times the above referred to rate.

4.7.3 Front end electronics

This part of the electronics is the only one which has to be adapted to each specific detector. In this Section, we describe in particular the scintillator readout.

The front end unit includes the following components: the front end chip, the ADC's, the local trigger, the serial link controller and the programmable chip. Its schematic diagram is shown in Fig. 67.

One can make use of boxes close to the photodetector from where the data flow is transmitted by a serial link. The discriminator signal is also sent to the readout interface. Other signals (external trigger,

electronic channel monitoring, etc.) and power supplies are also connected to these boxes. The place allocated to the front end board is limited by the clearance between target walls and by the space required for brick handling.

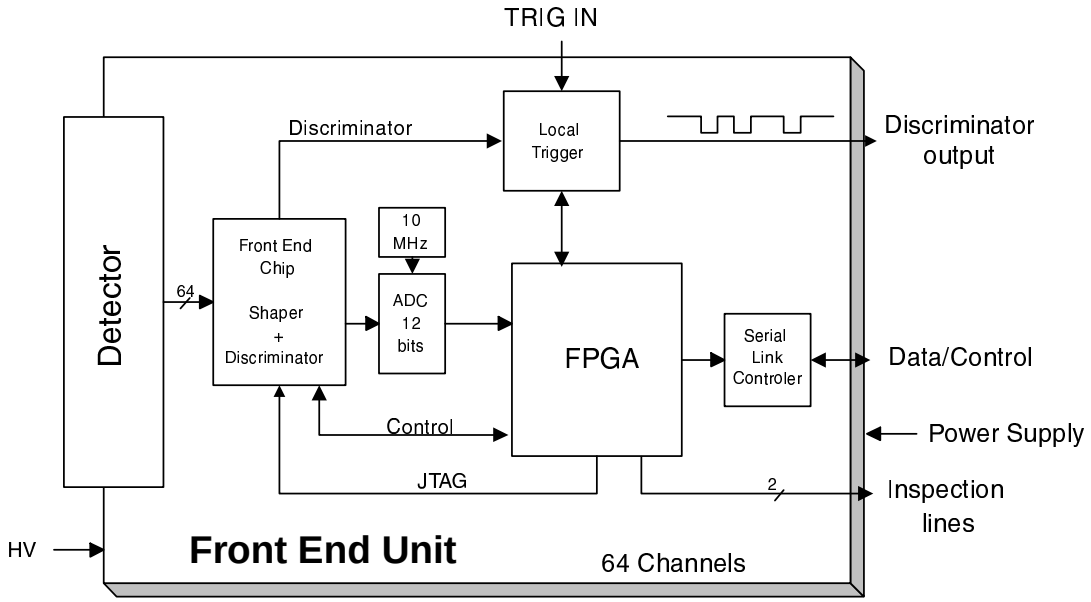

Figure 67: Front end unit diagram.

The front end chip can either be a commercial product or a specially designed chip. In this case, the development of a common chip for PMT's, drift tubes and RPC's could be envisaged (for these three detectors the gain is higher than 10^4).

The front end chip is subdivided into three parts (Fig. 68): the entry amplifier, a slow low-noise shaping amplifier for charge measurement, and a fast amplifier followed by a discriminator for triggering. Due to the different gain of the three detectors and to the dispersion between channels of the same detector (for the PMT a gain dispersion factor of 3 is expected between anodes), a variable gain per channel of the entry amplifier is suitable. This chip includes a logic allowing the readout of the fired channels only. It provides an analog multiplexed signal proportional to the energy level for each channel and a fast discriminator signal for triggering and timing. It has two operation modes

- *autotrigger* mode. In this case the first fired channel of each electronic front end card starts the readout of all channels;
- *calibration* mode. An external trigger gives the start for the readout. This mode could be used by the calibration system of each electronic detector to monitor the time evolution response of each channel. It also allows debugging and monitoring of the acquisition system specially during the installation time.

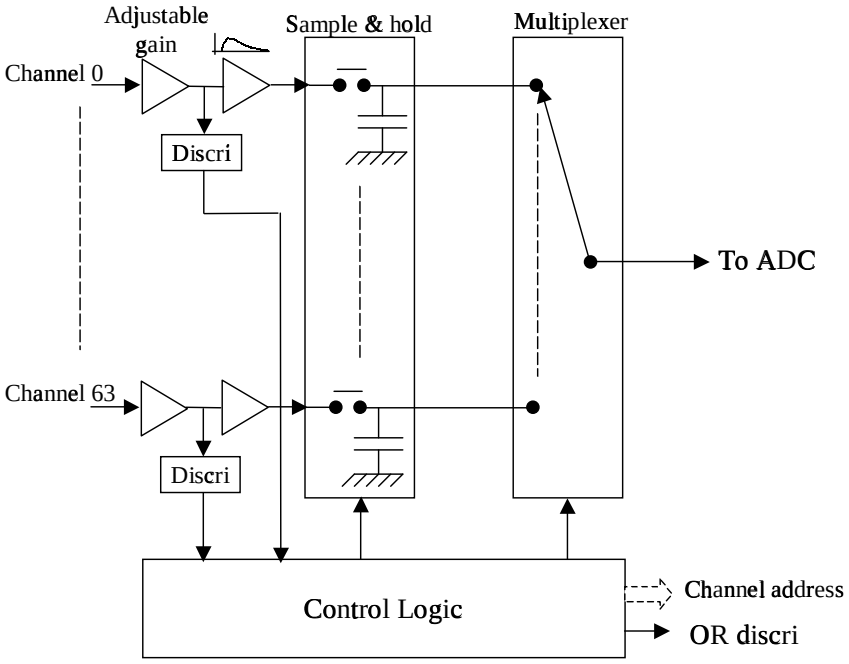

Figure 68: Front end chip diagram.

The number of channels handled by this chip should be adapted to the configuration of each detector. In the following, the assumption of a channel grouping by 64 is made. Its setup can be done by a serial link (JTAG or custom protocol). The peaking time ($< 1\ \mu s$) should be short enough to avoid pileup and random hits.

The ADC's have at least 12 bits to reach the required accuracy and dynamic range and are operated at high frequency ($> 1\ MHz$) to reduce the chip readout time.

The local trigger receives two inputs, the logical discriminator signal from the front end chip and an optional hardware external trigger (see above). It generates a discriminator information to the readout interface.

The serial link controller manages the serial link between the front end units and the readout interface (VME board). The link must be able to accept the maximum estimated rate. In the case of 64 channels, 60 Hz of counting rate and 3 $byte$ per event, the rate is $64 \times 60 \times 3 = 11520$ byte/s.

A daisy chain serial link can be used for some front end units to reduce cabling. If one chains 4 modules together (Fig. 69 for scintillator strips) the above rate is to be multiplied by the same factor in the last link. Keeping a margin factor of 10 leads to 0.5 $Mbyte/s$. The wire length is less than 40 m, which is the maximum distance between a front end unit and the associated readout interface. The RS485 standard could be a good solution (differential link, rate up to 1 $Mbyte/s$ on 50 m). No processors are needed to handle the transmission protocol. Its logic control can be integrated in the Field Programmable Gate Array (FPGA), as shown in Fig. 67.

The dead time is completely defined by the front end chip. The rest of the acquisition can stand the data rate without extra dead time. If only fired channels are read out, present estimates give a dead time of about 0.4%.

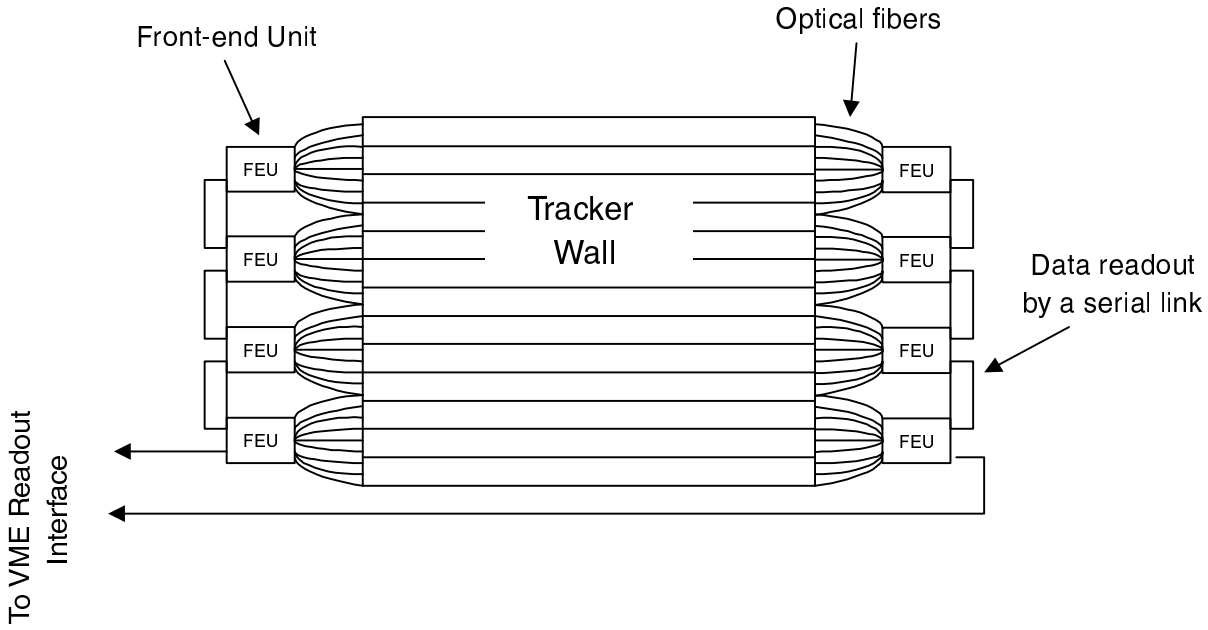

Figure 69: Data readout scheme of the scintillator strips.

4.7.4 Readout interface

The VME board controls two tracker planes (X and Y, 1024 channels). This interface receives the data (serial links) and the discriminator signals from the front end unit (Fig. 70). The first task of the module is to assign a common time stamp to each group of 64 channels.

In order to create the time stamp information from the GPS is needed. One needs a PPS (Pulse Per Second) signal which allows the precise synchronisation of a local counter for all cards and the complete absolute time received by a RS232 serial link. The combination of both information provides an absolute time stamp for each event, as shown in Fig. 71. The time stamp accuracy is defined by the frequency of a local oscillator (200 MHz for 5 ns). The duration of the PPS signal is divided by the period of the local counter oscillator. The counter value gives the precise time between the last PPS edge and the arrival of the discriminator signal.

A local trigger could be implemented on the VME board to handle the external trigger signal (TRIG OUT) for the front end unit. The X and Y correlation or correlations between planes can be performed by this hardware logic, since all the discriminators from the X and Y planes are connected to this module. A TRIG IN signal is also handled to allow a global hardware trigger for the experiment (if necessary).

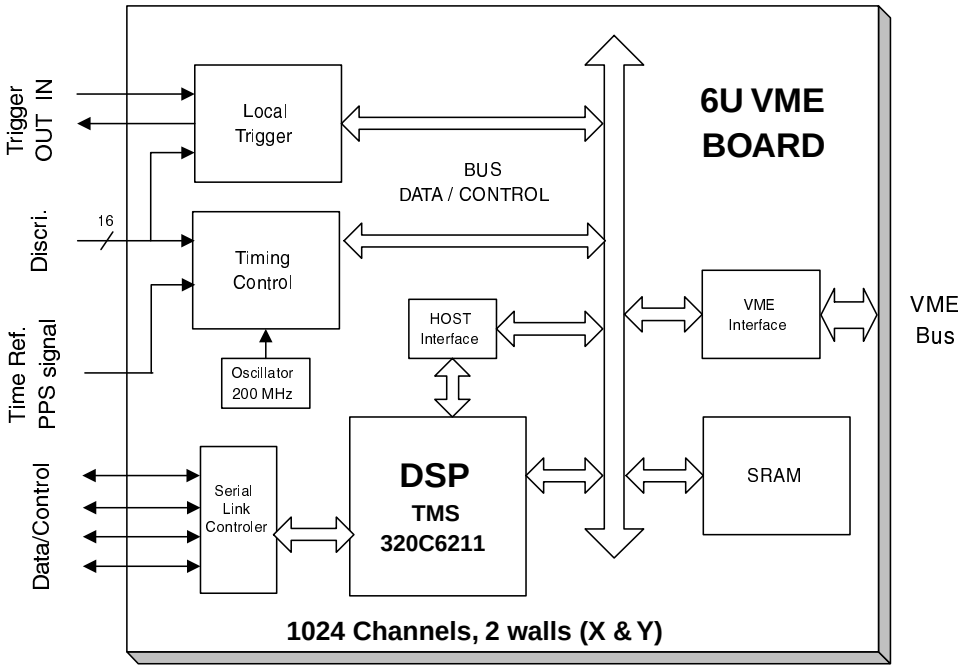

Figure 70: Readout interface unit (VME board).

A Digital Signal Processor (DSP) manages the interface board. This component offers many possibilities for a first step data processing. It also gives the freedom for an autonomous communication with the front end units. This would be useful for an automatic setup. The DSP tasks are the data readout, the data block building and the front end setup (discriminator thresholds, channel masking, variable entry amplifier gain etc.). In addition, it allows histogramming of raw data and handling of test programs.

The VME bus is for the time being the most reliable product on the market with enough bandwidth (up to 160 $Mbyte/s$ in VME64 burst protocol). Cheaper products (*e.g.* Compact PCI) could be used if their features will improve in the future.

4.7.5 Software trigger and real time analysis

The necessary processing power for the event selection is not yet completely estimated. Thus, a scalable configuration for the trigger processor farm is proposed. The number of processors (PCs) can be increased to match the experiment requirements.

The Gbit Ethernet is a good solution for the communication between the readout interface and the processor farm. It only needs one switch for linking all processors. It allows high data flow and is useful for the event dispatching to the different processors, since any processor can communicate with each other. This link will be largely exploited in the next years. Nowadays it is still expensive but its price is expected to rapidly decrease.

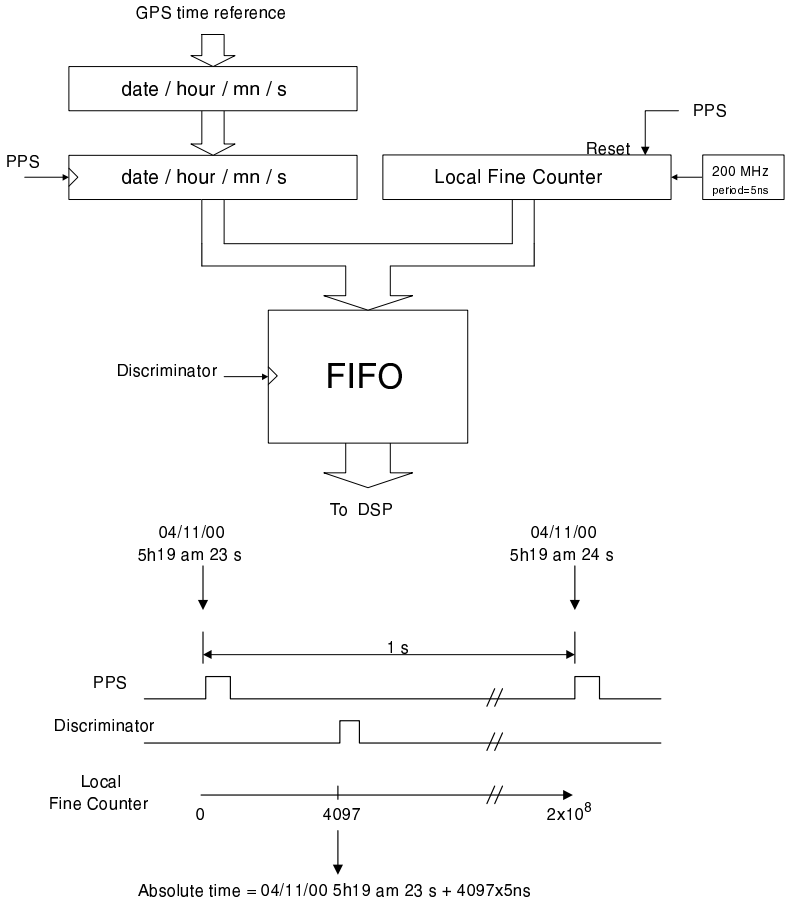

Figure 71: Timing structure of the DAQ.

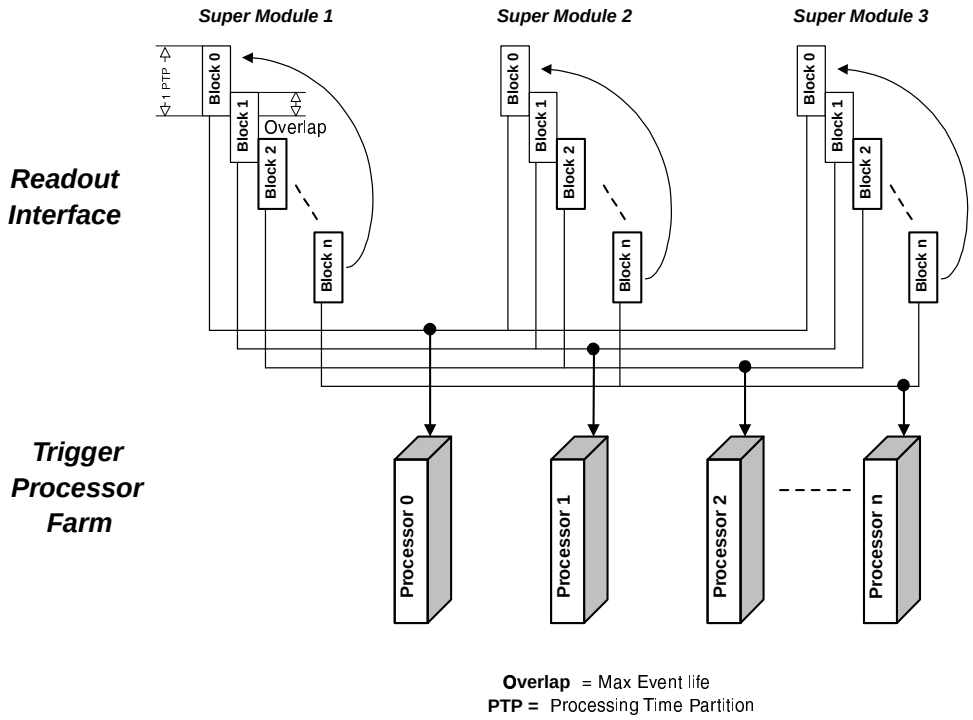

Figure 72: Scheme of the event processing.

Another solution could be the PVIC bus for the communication between the readout interface and the processor. This bus (PCI to PCI) could be useful for our application. It has a large bandwidth (120 $Mbyte/s$) and allows transparent Direct Memory Access (DMA) to a remote memory. Each readout interface processor can write on a processor farm memory without disturbing the chosen processor. All the power is kept and dedicated to the processing and not to data transmission.

The event dispatching to the different processors in the farm uses data blocks defined as a Processing Time Partition (PTP). Each readout interface builds as many blocks as associated processors in the farm and sends them sequentially (Fig. 72). An overlap between blocks avoids the problem of an event to be cut at the end of one block. The overlap should be at least equal to the maximum event duration ($\sim$ 300 ns).

An offline analysis establishes the correlation between the selected events and the accelerator beam cycles. At Gran Sasso and CERN, a GPS provides the absolute time with an accuracy of $\sim$ 20 ns.

The proton beam for the CNGS is extracted from the SPS in a fast mode, with bunch length of 10 μs. With the GPS accuracy it is then possible to reject offline background events occurring between bunches. Commercial products can be used for the GPS receivers. A GPS device and an optical fibre link to an external antenna are already installed in the Gran Sasso hall.

5 Analysis of the electronic detectors data and brick finding

5.1 Event generators and cross sections

Neutrino-nucleon interactions are generated through the JETTA and RESQUE packages [69] developed in the framework of the CHORUS Collaboration. JETTA is based on the LEPTO model for deep-inelastic neutrino interactions. The Fermi motion of the nucleons is treated by using a simple Fermi gas model in which nucleons are considered as free fermions in a finite volume. The reinteractions of hadrons while crossing the nucleus are not taken into account. Hadronic fragmentation at the primary vertex is accomplished according to the LUND string model, with some tuning in order to reproduce experimental neutrino data. For DIS ν_τ interactions the mass of the τ in the final state and its polarisation are taken into account.

The RESQUE package simulates quasi-elastic interactions and resonance production in neutrino scattering. Nuclear effects such as Fermi motion and Pauli suppression are taken into account, but not nuclear reinteractions. The simulation of quasi-elastic events is based on the calculation performed by Llewellyn-Smith [70]. The resonance production cross section is computed by using a simplified version of the Rein and Seghal model [71], which simulates various states up to a W value of 2 GeV without taking into account the interference terms. The effects of the mass of the τ on the kinematic of the final state and its polarisation are also taken into account. A more complete simulation of the resonances based on [71] is being developed also including the effects of the τ mass at the level of dynamics.

5.2 Detector simulation

A GEANT 3.21 simulation has been performed (AIDA) which takes into account the detector geometry and the materials. All the primary tracks from the neutrino interaction in the target are generated according to the event generators and traced through the entire apparatus taking into account all relevant physics processes. Secondaries down to 1 MeV kinetic energy for electrons and γ's, and down to 10 MeV for all other particles are also traced. Information about each particle crossing the active detectors is recorded, to provide data input for the event reconstruction programs. This information, classified as *hits*, includes detector identifier, crossing position, energy deposition, particle kinematics, etc.

Signals produced in the scintillator strips are simulated assuming readout at both ends through 1 m of extra fibre and taking into account the light attenuation along the fibres. In order to validate the simulation of the electronic detectors, AIDA has been used to simulate the setup used in the test beam measurements. In one of these tests, 15 GeV/c pions were sent into a brick wall and the shower centre of gravity was measured by means of scintillator strip planes. The comparison of the differences between the true position of the beam in one transverse coordinate and the reconstructed one is shown in Fig. 73. The agreement gives us confidence in the simulation algorithms.

In addition, a detailed simulation of the bricks has been performed to study the event topology in the vertex region, to estimate the physics background and to study different brick configurations. A standard GEANT 3.21 software requiring high performance in terms of tracking step length, position resolution and machine precision was used for this purpose.

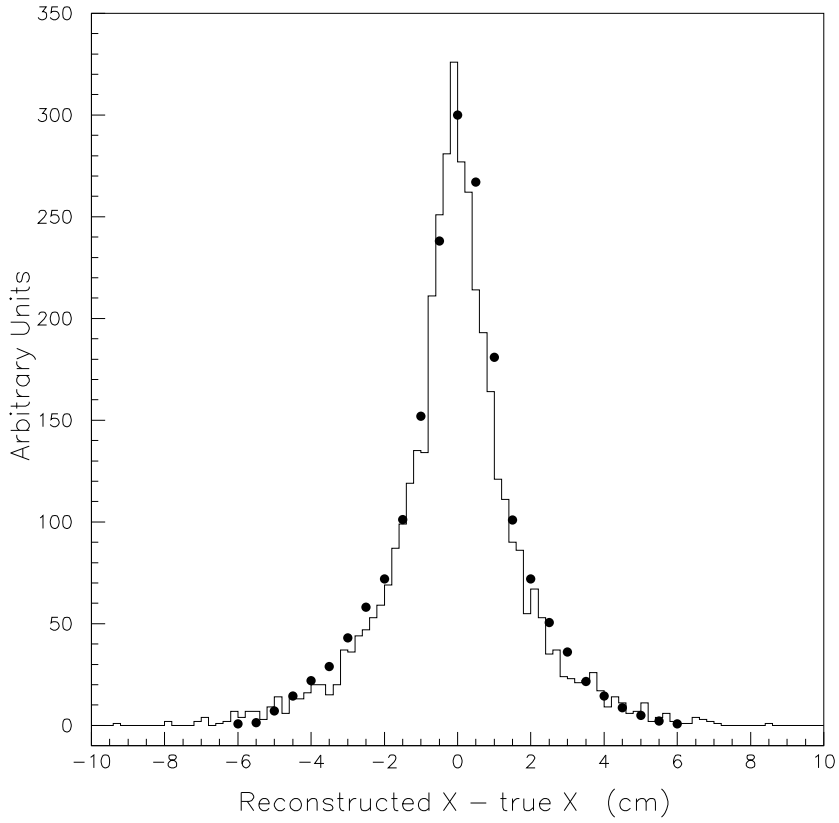

Figure 73: Comparison of the differences between the event vertex X coordinate for 15 GeV/c test beam pions (full circles) and simulated events (solid line).

Track segments on both the emulsion layers of the films are reconstructed from simulated data. The two high resolution space points measured at the plastic base define the high precision (space) segments used for tracking. A position smearing is introduced in order to simulate the measured angular resolution.

5.3 Reconstruction programs

A simple and modular framework for event processing has been developed. It includes specific unpacking routines to handle data input in packed format and provides hooks for reconstruction submodules in the various processing steps (run/event initialisation, data reading, processing, termination). Outside the framework, submodules for reconstruction in the different subsystems (bricks, Target Trackers, spectrometers) are available.

The software has been based so far on Fortran 77, with the support of CERN standard libraries and runs on AIX and Linux platforms. The ZEBRA package is used for memory management and data storage. A long term approach using modern OO-models under development for HEP simulation has been tested to run on different platforms.

OPERA has joined the WIRED project for its event display. WIRED [72] (World Wide Web Interactive Event Display) was created as an event visualisation framework inside a World-Wide Web browser. It is written in Java using the Swing set for its graphical user interface. It is completely portable and runs on any platform that fully supports the JDK (Java Development Kit 1.1 or better). The graphic engine of WIRED handles both 2D and 3D drawings. It supports multiple views and control widgets, which interact with those views. It can access events and detector geometry data by using XML files. A converter from GEANT 3.21 data into WIRED XML data is available.

5.4 Pattern recognition in the target and in the spectrometer

A pattern recognition using target tracker scintillators has been developed following ideas implemented for the NEMO experiment, called the *cellular automaton* technique [73].

In each transverse detector projection one starts by building cells with two scintillator hits in two consecutive planes. Then, one connects cells with a common extremity that do not make a large kink between each other. Once the set of cells and their neighbours are known, one iteratively computes for each cell its index along a possible track. All cells are initialised with an index value of 1. At each iteration, each cell looks for neighbours in the upstream plane and increases its index by one unit if there is a neighbour with the same index. The process stops when there are no more neighbouring cells with the same index value.

The collection of track candidates starts from a cell with the highest index by adding its neighbours with a lower index and so on. The selection of the best candidate is performed with simple criteria such as the lowest mean value of the cosine between two consecutive cells or the lowest dispersion of the hits around the straight line joining the two extremities of the track. When the best candidate is picked up, its hits are removed and a new process of cell collection is performed.

The above algorithm considers the spectrometer as an extension of the target section. For example, a reconstructed charm event is presented in Fig. 74.

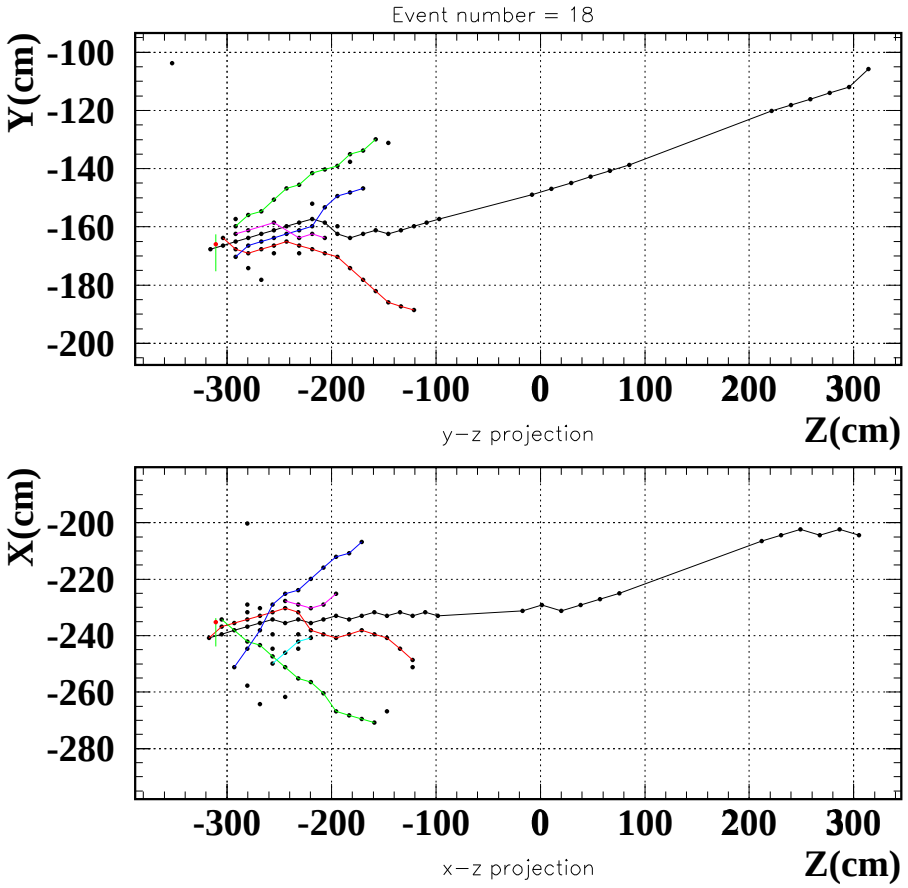

Figure 74: Example of a $\tau \rightarrow \mu$ event. The 24 modules of target trackers have a negative Z coordinate. The broken lines are the results of the pattern recognition method described in the text.

5.5 Brick finding efficiency

The selected brick is determined from the electronic tracker data in two steps. First, one tries to identify the right brick wall and then to find the brick to be removed in that wall. The application of the brick finding algorithm to the location of secondary interactions induced by neutral particles is in progress.

The efficiency of each of the above steps has been evaluated by means of simulations. Test beam measurements have already been performed to validate these simulations (see Section 5.2) and other tests are planned for the future.

5.5.1 Wall finding

An important issue determining the wall finding efficiency is back-scattering. Particles produced by the neutrino interaction may undergo reinteractions on nuclei and produce particles which go backwards with respect to the beam direction. This may lead to a wrong assignment of the wall where the neutrino interaction occurred.

Simulations indicate that the fraction of events which show at least one back-scattered hit is higher for DIS than for QE events. This fraction also increases with the neutrino energy (Fig. 75 and Table 10).

Table 10: Fractions of events with back-scattering and average wall finding efficiencies obtained with a neural network analysis. The statistical uncertainty on the back-scattering fractions is less than 0.5%. The uncertainty on the efficiencies is $0.2 - 0.3\%$.

Event type	mean back-scattering fraction (%)	wall finding eff. (%)	eff. when adding downstream wall (%)
DIS ν_μCC	38.7	90.2	97.3
DIS ν_μNC	40.5	86.6	94.4
DIS $\tau \rightarrow \mu$	40.0	90.7	96.4
DIS $\tau \rightarrow e$	44.8	92.9	97.4
DIS $\tau \rightarrow$ no μ	51.9	90.5	95.9
QE ν_μCC	15.4	89.7	95.4
QE $\tau \rightarrow \mu$	11.7	92.9	96.8
QE $\tau \rightarrow e$	18.1	95.9	98.2
QE $\tau \rightarrow \pi$	28.4	85.5	92.0
QE $\tau \rightarrow \rho$	29.6	93.8	97.2

Several algorithms have been developed to identify the interaction wall on an event-by-event basis: algorithms based on sequential cuts on the number of hit strips per plane; topological methods to locate isolated back-scattered fired strips and neural networks. The neural network analyses give the best wall finding efficiencies, ranging from 85% to 96% according to the Monte Carlo simulations (Fig. 76 and Table 10).

The SNNS [74] package was used to construct a network with eleven input nodes, twenty hidden nodes in one layer and 4 output nodes. We define the first wall of an event as the most upstream in

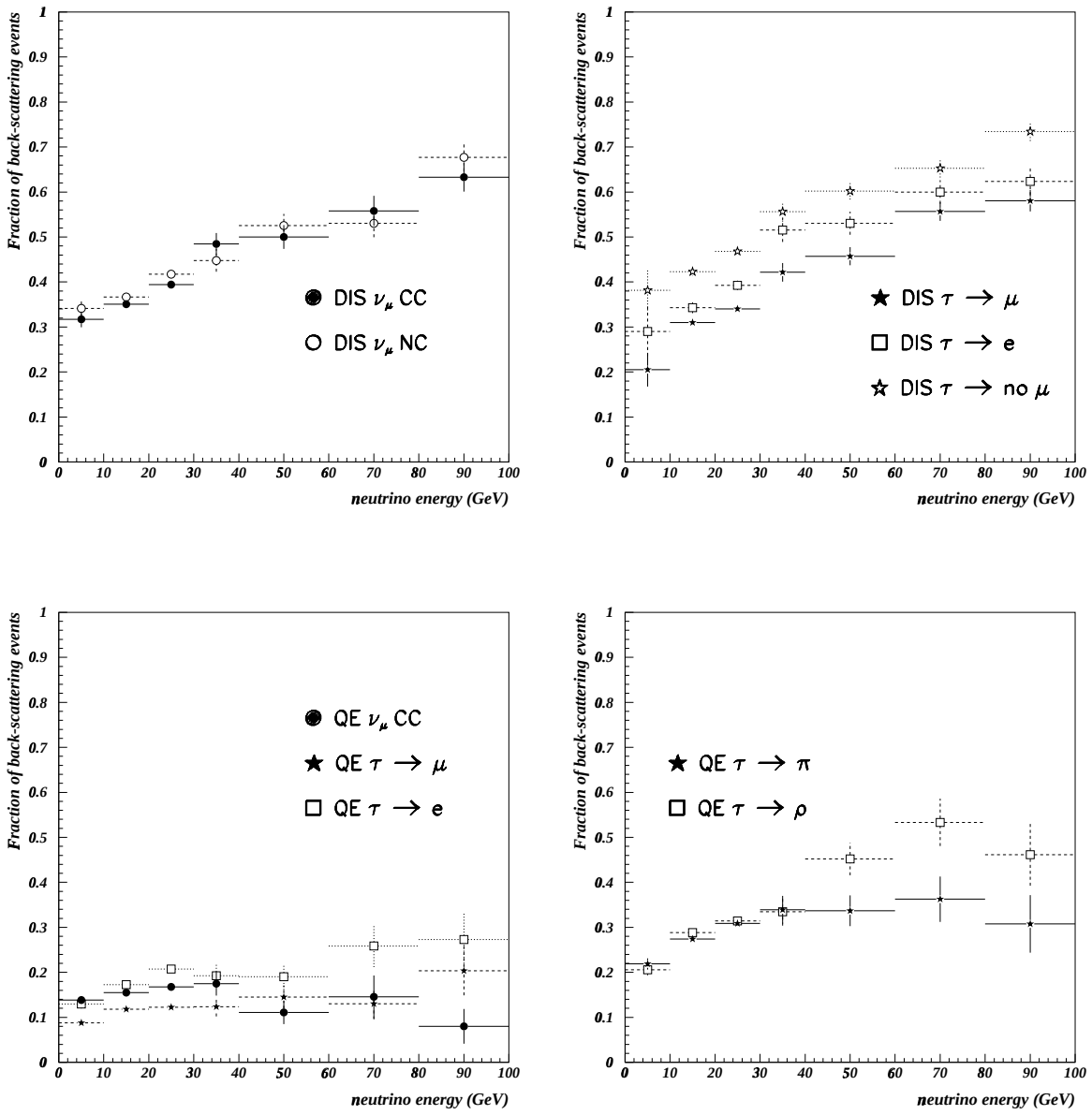

Figure 75: Fraction of back-scattering events as a function of the neutrino energy. Errors are statistical only. Top right plot: the DIS $\tau \rightarrow$ no μ sample includes DIS $\tau \rightarrow e$ and DIS $\tau \rightarrow h$ events.

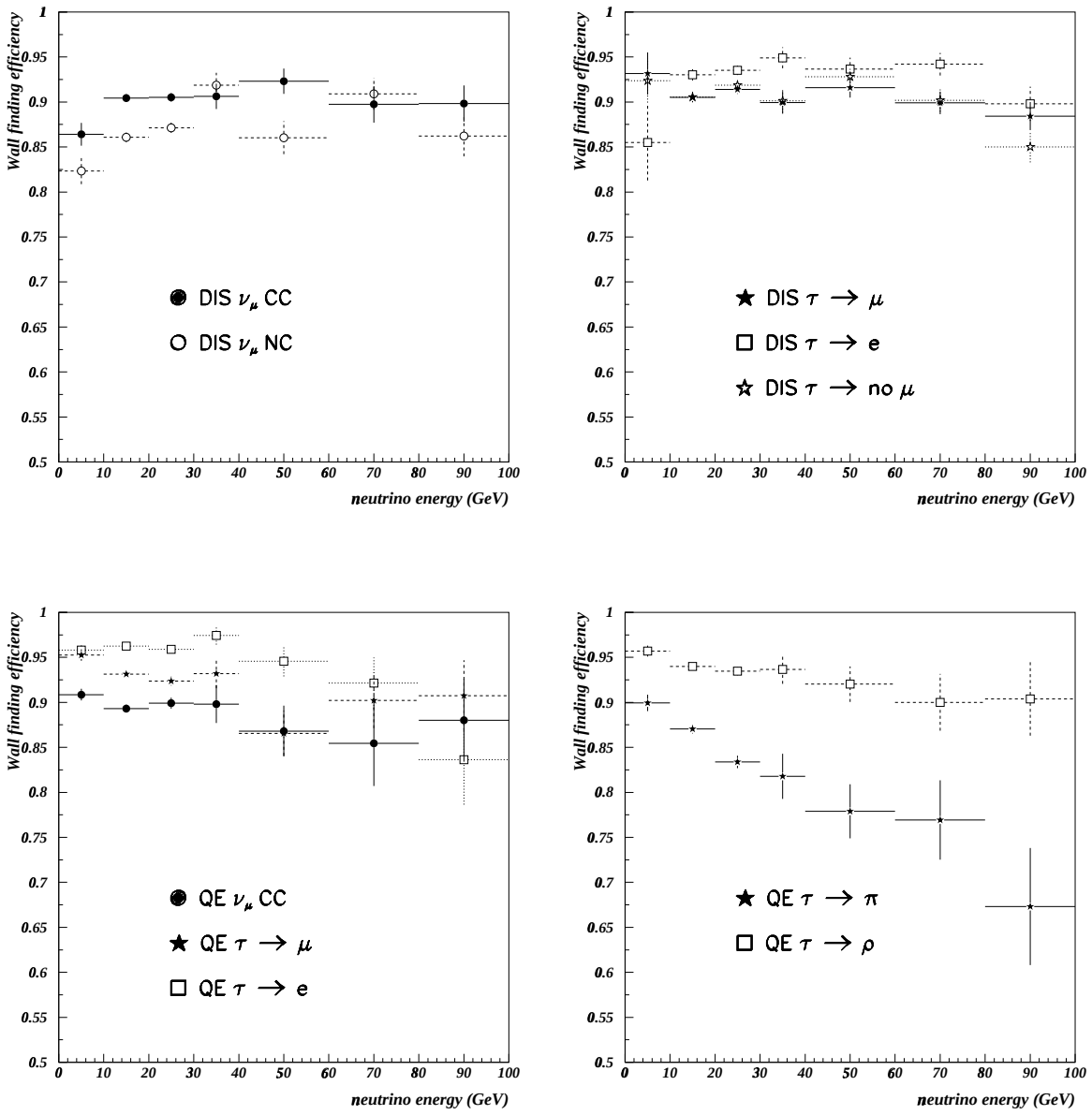

Figure 76: Wall finding efficiency as a function of the neutrino energy. Errors are statistical only. Top right plot: the DIS $\tau \rightarrow$ no μ sample includes $\tau \rightarrow e$ and $\tau \rightarrow h$ events.

the target whose Target Trackers register a signal above the 1 *p.e.* threshold per each projection. The network uses as input

- the distance between the first scintillator plane and the plane with maximum energy deposit;
- the total measured event energy;
- the measured energy, the number of hit strips and the measured shower position in the first three modules of the event.

Fig. 77 illustrates some of the input information used by the neural network.

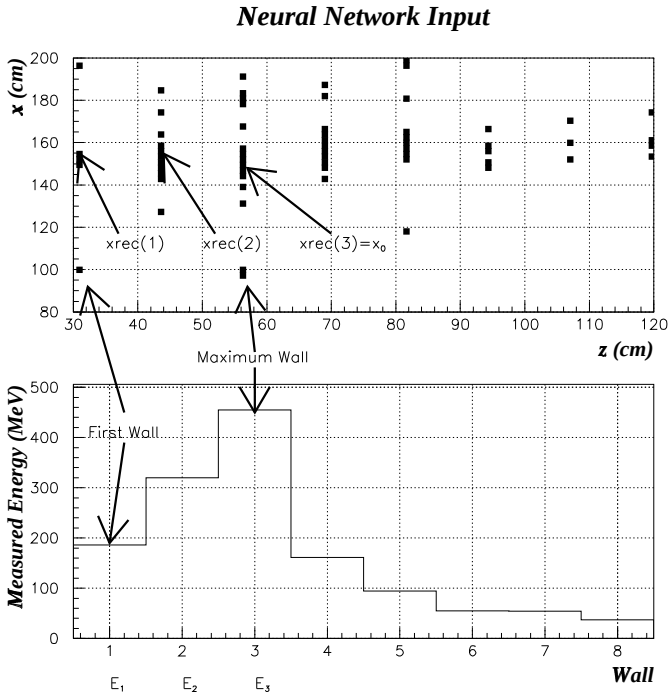

Figure 77: Top: $X - Z$ projection of the hits in a NC event. Bottom: longitudinal energy profile. The plane with maximum measured energy (in this case the third plane) is used as a reference for the shower position and for normalisation of the energy deposits.

For each event the network calculates the probability that the event vertex is located in any of the first four brick walls. Simulations show that these four walls contain more than 97% of the neutrino vertices. The network training was made with a separate set of 5000 simulated ν_μ NC events. The network locates the vertex in the wall characterised by the highest probability. Fig. 78 shows the output of the neural network for events with the vertex in one of the first four walls. The resulting wall finding efficiency is shown for each of the histograms.

The worst case leading to the lowest efficiency corresponds to events where a low energy back-scattering occurs only in the first module upstream the right one (Fig. 78). In fact, in most cases when a wrong wall is chosen, the right one is just the downstream wall. The wall finding efficiency thus goes up to $92 - 98\%$, depending on the decay channel, when the downstream wall is considered (see Table 10). This efficiency is almost independent of the incoming neutrino energy.

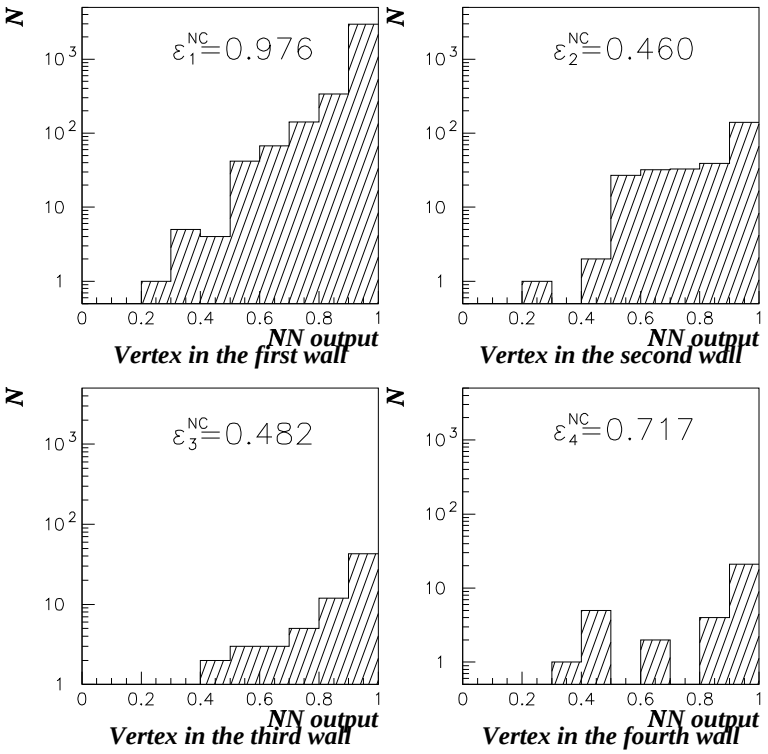

Figure 78: Each plot shows the output of the neural network for events with the vertex in one of the first four walls, respectively. The histograms correspond to events for which the highest neural network probability selects the right wall. The resulting wall finding efficiency ϵ_i^{NC} is given for each histogram.

The highest wall finding efficiencies are obtained for events inducing showers and for low energy interacting neutrinos. The analysis of DIS $\tau \to e$ or QE $\tau \to e$ events is facilitated by the presence of a dense electromagnetic shower with high energy deposit per strip. The wall finding efficiency is slightly lower for NC events and for single track events such as QE ν_μ CC events. In the case of QE $\tau \to \pi$ events, the low efficiency is determined both by a non negligible back-scattering and a by the poor information available in single π showers.

5.5.2 Brick finding

After wall location, the interaction vertex is reconstructed using the scintillator hits in the associated tracker planes. Two algorithms have been developed.

The first method applies to events without a reconstructed muon in the final state. It is based on an iterative computation of the strip position centres of gravity. This procedure leads to a transverse resolution distribution which can be well fitted by two Gaussians: 84% of the event vertices are reconstructed with 1.1 cm resolution, the remaining 16% with a resolution of 3.5 cm.

The second algorithm makes use of the reconstructed muon track to help in the identification of the vertex brick. The transverse resolution distribution is fitted by two Gaussians: 94% of the vertices are reconstructed with a resolution of 0.8 cm, the rest with 2.6 cm. An example is shown in Fig. 79 for ν_μ CC and for NC events, where the benefit of using the muon is clearly seen.

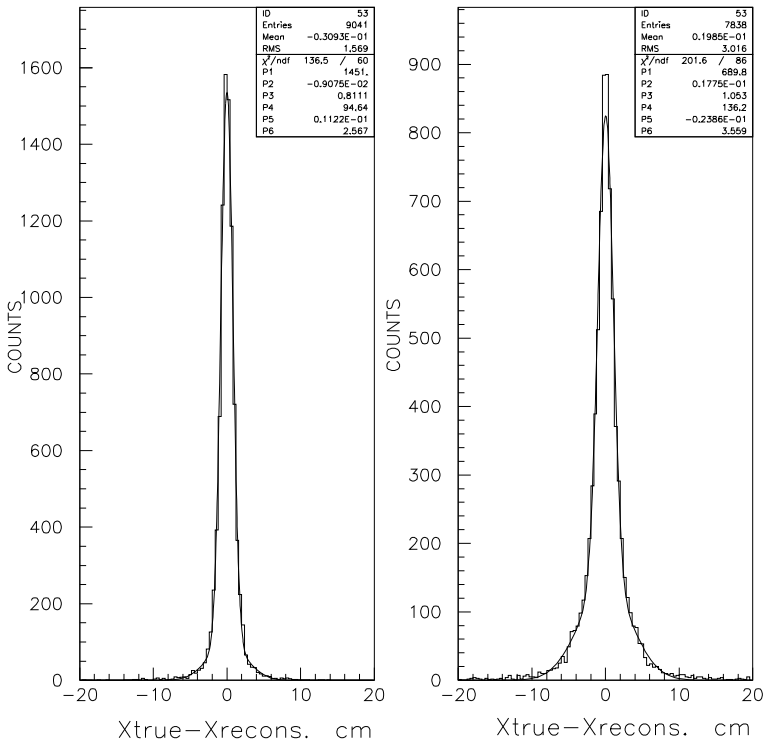

Figure 79: Position resolution in the determination of the neutrino vertex X coordinate in ν_μ CC (left histogram) and NC (right histogram) interactions.

These results are translated into brick finding efficiencies. In the hypothesis of one brick removal per event, according to the simulations the mean brick finding total efficiency is above 80% for the

electromagnetic showering events and around 74% for the other DIS events (DIS ν_μCC events and DIS τ events). The lowest efficiencies (below 70%) are obtained for QE events with a single track (QE ν_μCC and QE $\tau \rightarrow \mu$ events) or QE events without electromagnetic showers such as QE $\tau \rightarrow \pi$ events (Fig. 80 and Table 11). These values include the wall finding efficiency and, for τ events are evaluated for large Δm^2. In Section 7 the Δm^2 dependence of the efficiencies is taken into account.

Table 11: Average brick finding efficiency as a function of the number of bricks removed per event (see the text for details).

Event type	1 brick rem. (%)	2 bricks rem. (%)	3 bricks rem. (%)
DIS ν_μCC	78.3	86.2	92.2
DIS ν_μNC	66.7	77.6	79.6
DIS $\tau \rightarrow \mu$	74.6	84.6	89.2
DIS $\tau \rightarrow e$	81.8	89.4	90.5
DIS $\tau \rightarrow h$	77.3	85.6	86.8
QE ν_μCC	81.7	91.5	95.4
QE $\tau \rightarrow \mu$	75.2	83.5	91.2
QE $\tau \rightarrow e$	83.9	92.6	93.2
QE $\tau \rightarrow \pi$	57.6	71.6	72.9
QE $\tau \rightarrow \rho$	80.0	89.0	89.9

5.5.3 Brick removal strategies

The baseline strategy assumed in this Proposal foresees the removal of one brick per event. The signal detection efficiency and the experiment performance have been evaluated according to this scheme. However, the brick finding efficiency can be improved by allowing the removal of a (fixed) larger number of bricks per event (*static* approach) or by extracting the number of bricks corresponding to a predefined probability of locating the neutrino vertex (*dynamic* approach). In order to reduce the number of removed bricks, the decision to extract a second brick may only be taken if the neutrino vertex is not found in the first brick (*sequencial* approach).

In a static brick removal strategy a predefined and fixed number of bricks to be removed is chosen independently of the event characteristics. We call "2 brick removal strategy" the case in which one removes (in the identified wall) the predicted brick plus the side brick closest to the predicted vertex position. A "3 brick removal strategy" consists of adding to the previous case the removal of the brick which is downstream of the predicted one.

Simulations show that the brick finding efficiency can reach more than 90% for a 2 bricks removal strategy in the case of electromagnetic showering events, and more than 83% for the other DIS showering events. However, at least 3 bricks are needed to go above 80% for (almost) all categories of events.

The "dynamic brick removal strategy" allows to increase the brick finding efficiency without removing too large a number of bricks. It consists of defining the number of bricks which have to be removed on an event-by-event basis.

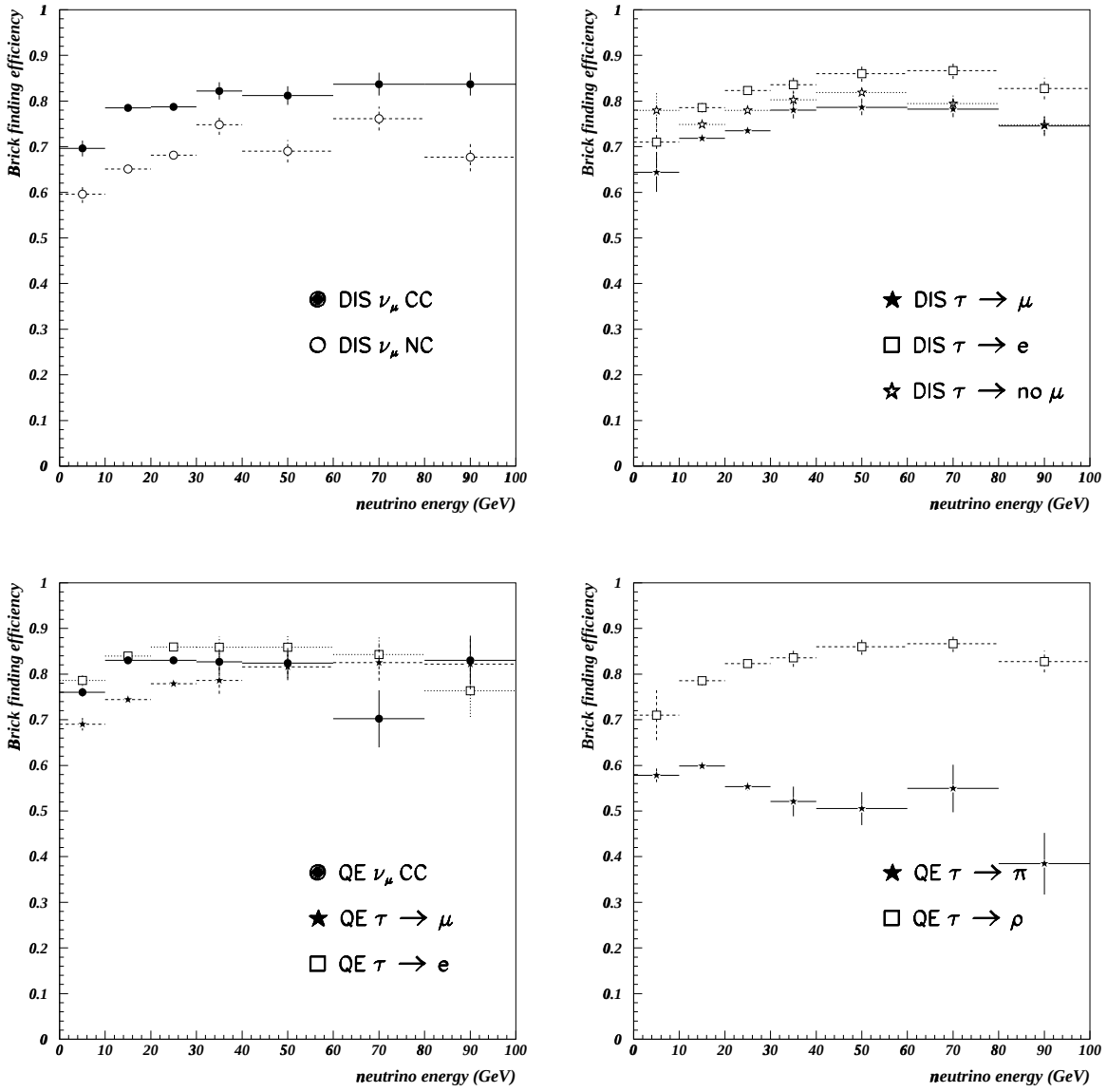

Figure 80: Brick finding efficiency as a function of the neutrino energy in the hypothesis of one brick removal per event. Errors are statistical only. Top right plot: the DIS $\tau \rightarrow$ no μ sample includes $\tau \rightarrow e$ and $\tau \rightarrow h$ events.

Studies on the strategies have started only recently. The underlying idea consists of looking at the sample of bricks which are close to the first predicted brick either in the same wall or in the downstream wall(s). Because of the outputs of the wall finding neural network and to the transverse position of the predicted vertex in the predicted brick, a probability can be associated to each brick of this sample. Bricks are then removed starting from those which have the highest probability until the sum of the probabilities of the removed bricks reaches a predefined threshold.

Fig. 81 shows the brick finding efficiency obtained with dynamic brick removal for DIS ν_μ NC events and DIS $\tau \longrightarrow e$ events, compared to what obtained with the static 2 bricks removal strategy as a function of the average number of bricks removed. In the case of DIS ν_μ NC events the efficiency obtained when 2 bricks are removed for all events (static removal strategy) is 77.6%. In order to reach the same efficiency with a dynamic removal strategy, only 1.5 bricks are needed to be taken out on average.

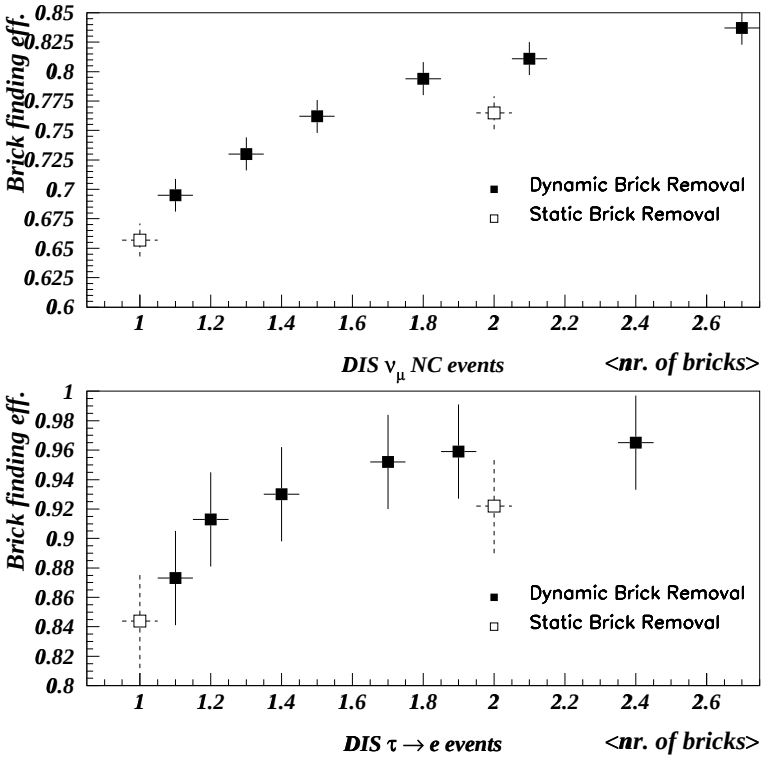

Figure 81: Brick finding efficiency with dynamic and static removal as a function of the average number of removed bricks.

By combining the dynamic with the sequential approaches the number of bricks to be removed per event in order to obtain a given efficiency can be further reduced. Fig. 82 shows that the above 77.6%

brick finding efficiency for ν_μ NC events can be achieved by removing on average 1.3 bricks per event instead of 1.5.

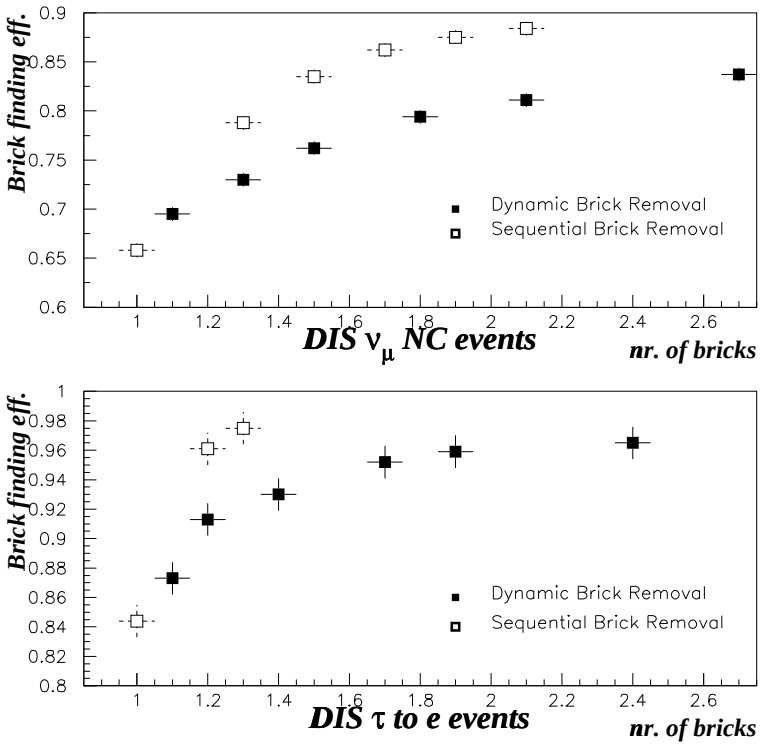

Figure 82: Brick finding efficiency with dynamic and sequential removal as a function of the average number of extracted bricks.

The results of these studies on "brick gambling" look promising. Therefore, these analyses will be further developed and applied to all event categories. More refined algorithms, including for example track reconstruction or the use of spectrometer information for events which start in the last walls of the target volume, may lead to improvements.

5.5.4 Considerations on the vertex-brick finding efficiency

The results presented in the previous Sections have been obtained by means of simulations. Their statistical uncertainty is below 4% and will be reduced in the future to a negligible level.

Test beam measurements have already been performed (see Section 5.2) and others are foreseen in order to validate the simulations. The comparison of real data and Monte Carlo events helps improving the brick finding algorithms and estimating part of the systematic uncertainties. The relevant parameters

which may enter in such a comparison are the fraction of back-scattering tracks, the mean energy per scintillator strip in the target and the event shape (number of hits and energy per plane, number of target/spectrometer planes hit per event, etc.).

Possible sources of systematic error have been considered and some studies have already started

- in the GEANT simulation particles are traced until their energy reaches a predefined threshold. In particular, the results presented above have been obtained by using a threshold of 1 MeV for the tracking of photons and electrons. When this threshold is lowered to 30 keV, the fraction of back-scattering events increases by $\sim 15\%$, which leads to a decrease of 3% of the brick finding efficiency. This result has been obtained using the same neural network for wall finding as the one which has been trained on events with a 1 MeV threshold;
- the effect of misalignment of target scintillator strips has also been studied. Detector strips X and Y positions have been randomly mismatched from generation values up to 6 mm. Fig. 83 shows the effect of alignment errors on the brick finding efficiency for ν_μ CC events. It indicates that mechanical or survey accuracies should be kept below 2 mm for internal tracker geometry. The efficiency is much less sensitive to possible relative brick-tracker misalignments. This leads to looser mechanical tolerances;
- the effect of electronic thresholds on the brick finding efficiency is shown in Fig. 84. For muonic events one observes a reduction of efficiency if the muon track is lost. Neutral current events are rather insensitive to the threshold. The same behaviour is seen for muonic events above 5 $p.e.$ once the muon is no more contributing to vertex finding;
- a study of the effect of mean number of $p.e./mip$ is shown in Fig. 85. Again the muon track degradation is responsible for the reduction in efficiency observed for muonic events. One can deduce that the mean number of $p.e./mip$ should be above 4.

In addition to the above studies the following issues will be addressed

- effect of changes of the fragmentation model parameters: this may affect hit multiplicity, hit energy and event shapes;
- effects coming from the simulation of the support structure of brick walls and scintillator strips;
- uncertainties in the simulation of light production in the strips, and light collection and propagation in the fibres.

More simulations are in progress to clarify those points. Test beam results have already been reported [6] and further beam tests are planned.

5.6 Muon charge and momentum determination

The performance of the spectrometer for the determination of the muon charge and momentum has been studied using Monte Carlo ν_μ CC and $\tau \rightarrow \mu$ interactions randomly distributed in the target volume. An iterative χ^2 minimisation procedure is used to fit the measured muon trajectory, following the method described in [75]. This method is based on the linearisation of the constraint equations as a function of the

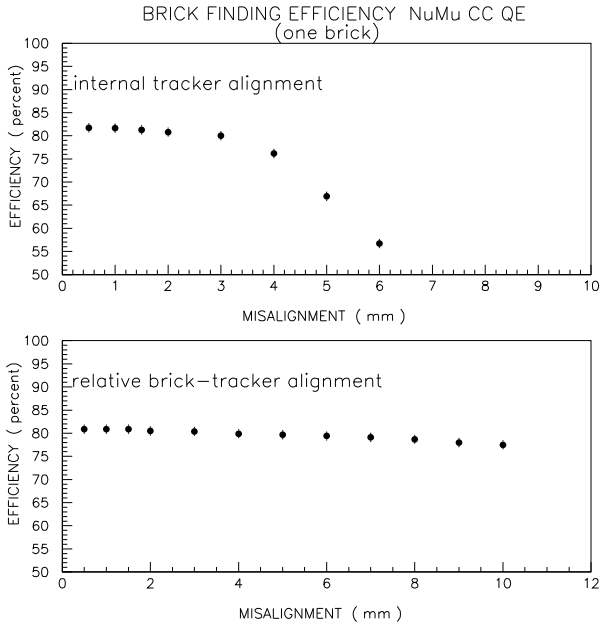

Figure 83: Top: effect of randomly generated strip misalignment on the brick finding efficiency. The abscissa gives the maximum misalignment with a flat generation over a given interval. Bottom: effect of the relative misalignment between bricks and trackers.

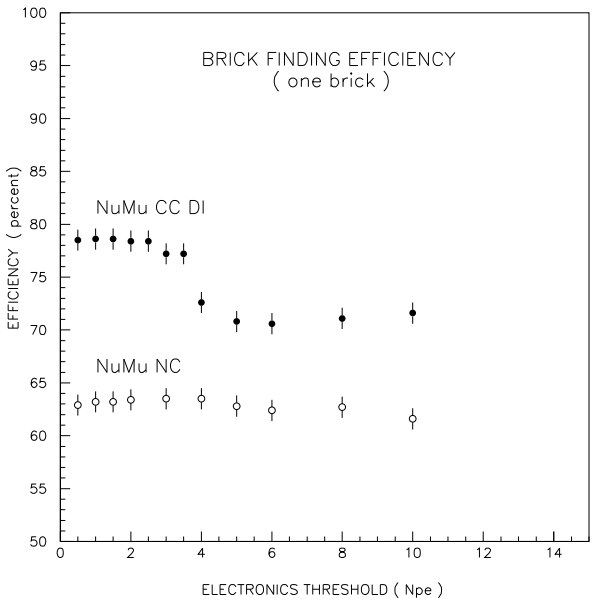

Figure 84: The total brick finding efficiency as a function of the front end electronics thresholds.

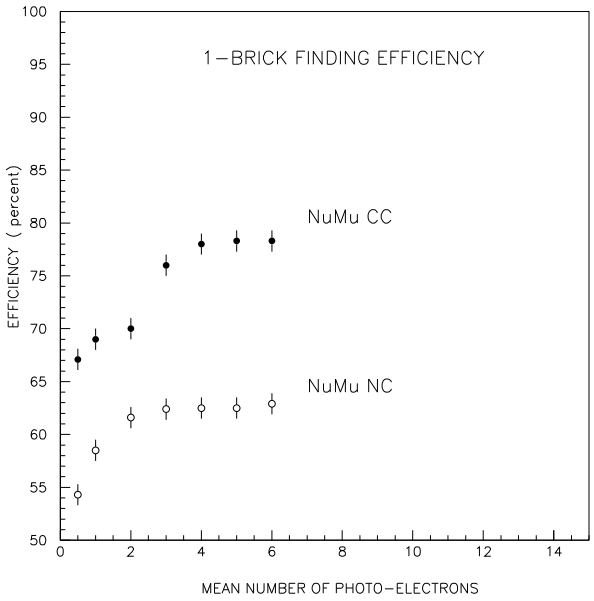

Figure 85: Brick finding efficiency as a function of the mean number of photoelectrons detected for a *mip*.

5 unknown parameters x_0, y_0, $(dx/dz)_0$,$(dy/dz)_0$ and $(1/p)_0$ representing the track coordinates, slopes and inverse momentum at some reference plane $z = z_0$, respectively. For each iteration, the calculation includes the effect of the mean energy loss in the traversed material as well as the correlation terms in the error matrix due to multiple scattering. For muons recognised as stopping in the detector volume, the total visible range is used as an additional constraint on the muon energy.

ν_τ CC interactions with muonic τ decay are generated assuming $\Delta m^2 = 3.5 \times 10^{-3}\ eV^2$. According to the simulation, the muon charge and momentum are measured for 55% of the events. An additional 35% of the muons cannot be analysed in the spectrometers but their total range can be determined. The remaining 10% represent, in about equal proportions, muons outside of the spectrometer acceptance or of too low an energy to allow their reconstruction in the Target Trackers.

It must be noted that in the analysis presented here, no explicit muon identification criteria are required. This issue is discussed later on. Most of the muons without momentum measurement are of low energy and are not tagged as such by the identification algorithms.

We recall that multiple scattering measurement in the ECC bricks gives an additional momentum determination.

The determination of the sign of the muon charge helps reducing the background from muonic charmed particle decay, when the primary muon is not identified. In the $\tau \rightarrow \mu$ sample of events with a reconstructed muon charge, only 0.29% were fitted with the wrong charge assignment. In a ν_μ dimuon sample, the charge of the positive muon from the charmed particle decay can be reconstructed in 37% of the events and, among them, 0.48% are fitted with the wrong charge assignment.

Fig. 86 shows, for the dimuon sample, the acceptance and the fraction of wrong charge assignment as a function of a cut on the number of iron plates crossed by the positive muon. One can see that, if needed, such a cut is a powerful mean for further reducing the fraction of muons with a wrongly reconstructed charge at the expense of a moderate acceptance loss.

For muons from ν_μ CC interactions a fraction of 81.2% can be analysed in momentum by the spectrometers while only the measurement of the total visible range can be used for 12.5% of the events. In 4.2% of the cases, the muon escapes the target outside the spectrometer acceptance and in the remaining 2.1%, no muon track can be reconstructed. The fraction of wrong charge assignment is given in Fig. 87 as a function of the muon momentum. One can see that, up to about 90 GeV/c, the charge recognition inefficiency stays below 1%.

The relative momentum resolution is shown as a function of the true momentum in Fig. 88 and Fig. 89 for stopping muons and for muons traversing at least one spectrometer, respectively.

The curve drawn in Fig. 89 is the result of the analytic expression given in Section 4.5.3 taking into account that muons may cross more than 1 spectrometer. The mean number of traversed spectrometers is shown in Fig. 90 as a function of the muon momentum. Above 20 GeV/c, this number stays constant at ~ 1.95.

A blow up of the momentum resolution distribution is shown in Fig. 91 for momenta below 20 GeV/c, the relevant kinematical range for the τ search. Here again, the drawn curve represents the result expected from the analytic calculation. Since at low momenta the momentum at the vertex is substantially greater

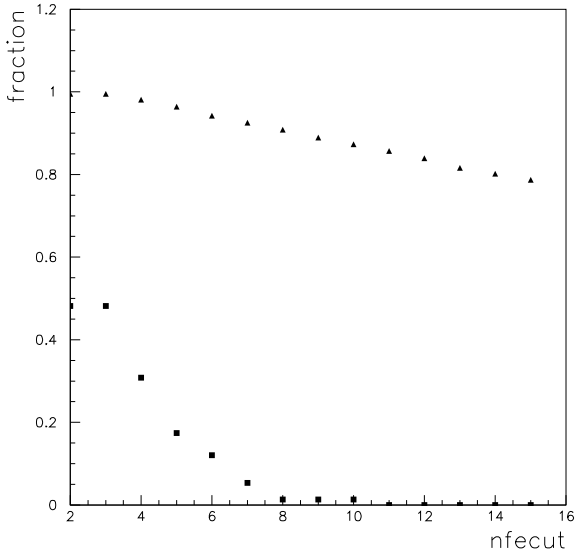

Figure 86: Charge determination of the positive muon in ν_μ CC interactions with a muonic charm decay as a function of a cut on the minimum number of iron plates traversed by the muon. Triangles: acceptance of the cut. Squares: fraction $\times 100$ of wrong charge assignment.

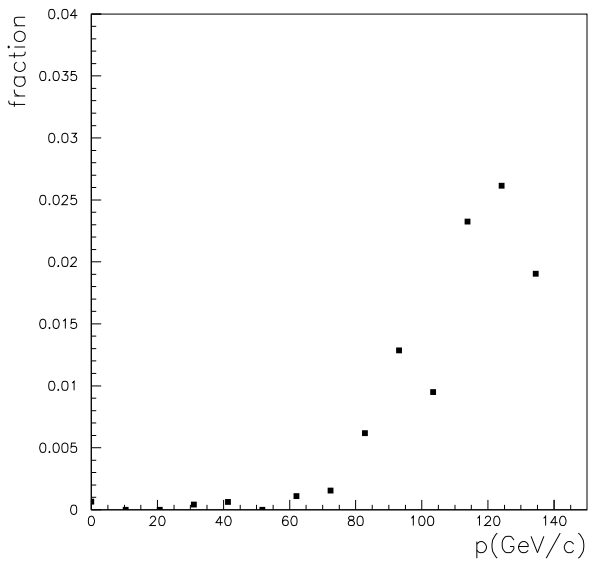

Figure 87: Fraction of wrong muon charge assignment for ν_μ CC interactions as a function of the muon momentum.

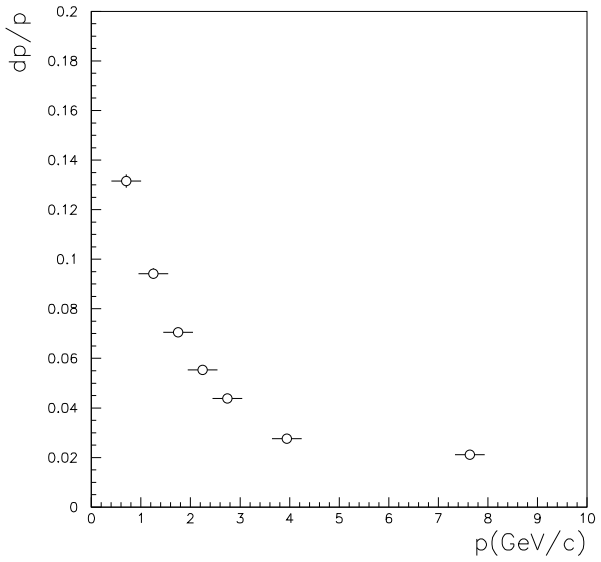

Figure 88: Muon momentum resolution for stopping muons.

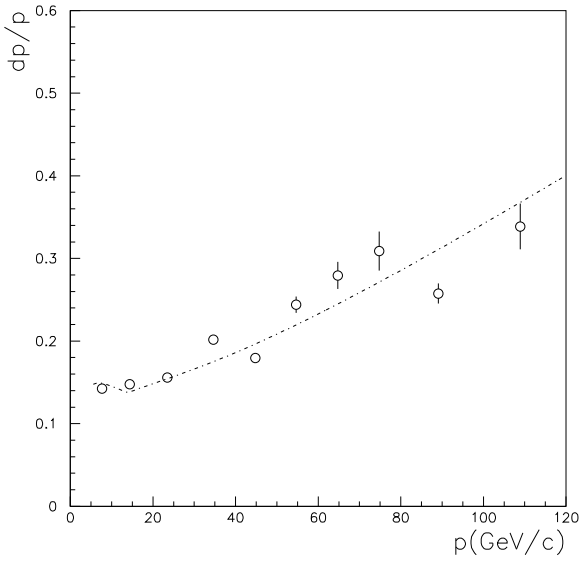

Figure 89: Muon momentum resolution for muons traversing at least one spectrometer. The meaning of the curve is explained in the text.

than in the spectrometers, the analytic expression has been corrected in an approximate way by a global factor $(p(vertex) - 1.6\ GeV/c)/p(vertex)$ where $1.6\ GeV/c$ is the mean momentum loss between the centre of a target supermodule and the centre of the downstream spectrometer. The results of the fitting program are seen to be in qualitative agreement with the expected resolution, considering the above approximations.

For comparison, Fig. 92 illustrates the momentum resolution which can be obtained by the spectrometer inner trackers, without the measurement provided by the high resolution Precision Trackers. The upper curve is for 30 mm strips width, the middle one for 20 mm and the lower one for 10 mm. For 30 mm strips, the momentum resolution varies from 28% at 10 GeV/c to 35% at 20 GeV/c. The fraction of wrong charge assignment as a function of the muon momentum is shown in Fig. 93. For 30 mm wide strips this percentage varies from 5% at 10 GeV/c to 15% at 20 GeV/c.

5.7 Shower energy measurement

The reconstructed hadronic energy E_{rec} can be written as

$$E_{rec} = \gamma(x, y, z)(c_t \sum_{i=1}^{n^t_{strip}} ADC^t_i + c_s \sum_{i=1}^{n^s_{strip}} ADC^s_i + c_0) \quad (1)$$

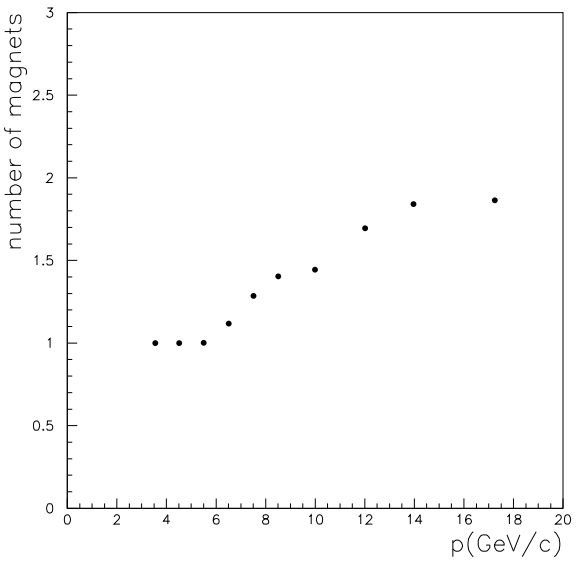

Figure 90: Mean number of traversed spectrometers as a function of the muon momentum (for muons traversing at least one spectrometer).

where $\gamma(x, y, z)$ is a position dependent correction factor; c_t, c_s and c_0 are calibration constants; $ADC_i^{t(s)}$ is the measured energy deposit in target scintillator (spectrometer RPC) strip i. For a digital readout, the values of ADC_i^t and ADC_i^s are simply replaced by 1 for all strips with a signal above threshold.

In order to obtain the constants c_t, c_s and c_0 of equation (1), a calibration of the detector was performed with Monte Carlo single charged-pions. Their vertices were uniformly distributed in the lead target of an OPERA supermodule. Channel-to-channel disuniformities were neglected. The pion energies were selected to match the expected range of hadronic energies from the CNGS beam. The constants c_t, c_s and c_0 have been obtained by minimising the following equation

$$f = (E_\pi - (c_t \sum_{i=1}^{n^t_{strip}} ADC_i^t + c_s \sum_{i=1}^{n^s_{strip}} ADC_i^s + c_0))^2 \qquad (2)$$

The corresponding constants for a digital readout were obtained by using a similar approach.

Fig. 94 shows the reconstructed pion energy as a function of the interaction vertex position. Since no significant effect was observed, the position dependent factor $\gamma(x, y, z)$ in equation (1) was set equal to 1 for all events.

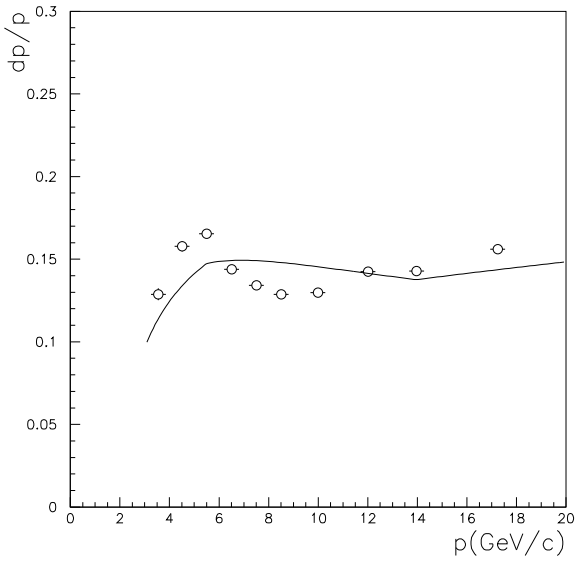

Figure 91: Muon momentum resolution for muons traversing at least one spectrometer. The meaning of the curve is explained in the text.

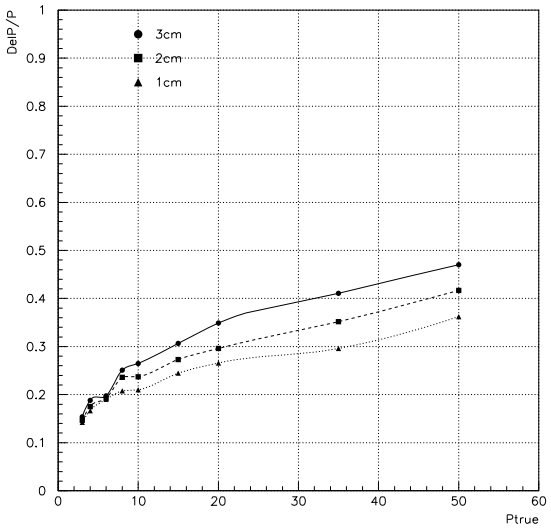

Figure 92: Momentum resolution obtainable with the spectrometer inner trackers as a function of the muon momentum. No use of the Precision Trackers is made for this calculation.

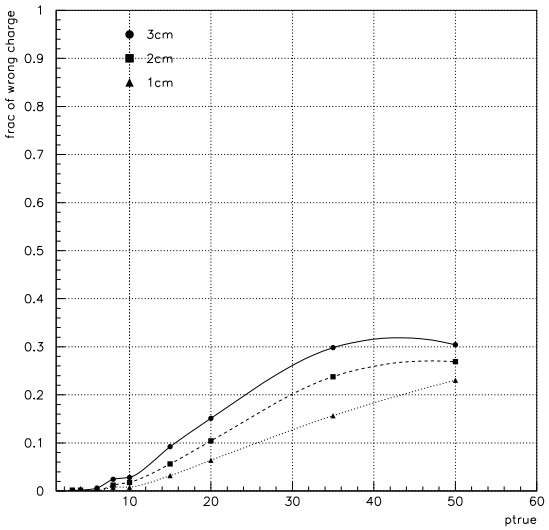

Figure 93: Wrong charge assignment as a function of the muon momentum without using the Precision Trackers.

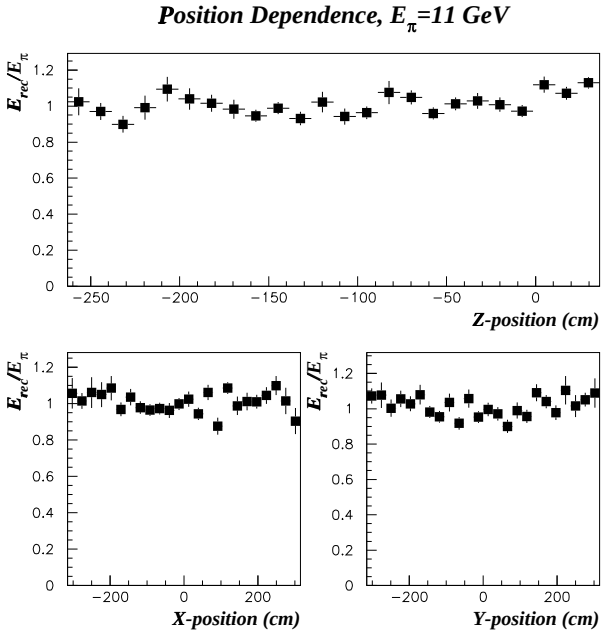

Figure 94: Ratio between the reconstructed and the true hadronic energy for 11 GeV pions as a function of the interaction vertex position.

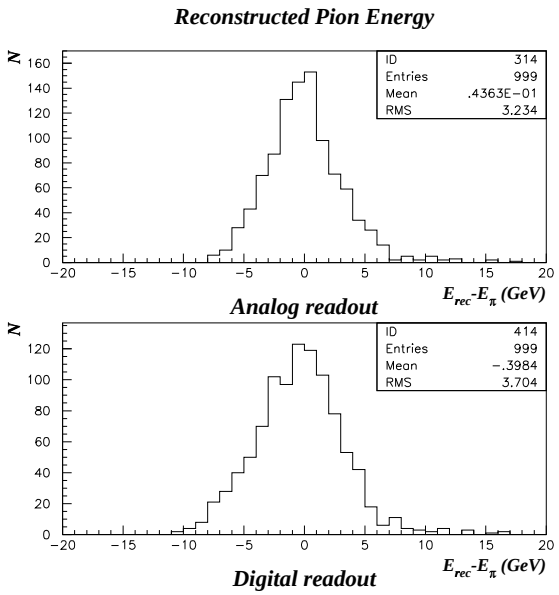

Figure 95: Hadronic energy resolution for 11 GeV pions for analog and digital readout.

Fig. 95 shows the reconstructed energy for 11 GeV pions with 2.5 cm wide scintillator strips. Notice the slightly better performance of the analog readout.

Fig. 96 shows $\Delta E_\pi / E_\pi$ as a function of E_π where $\Delta E_\pi = E_\pi^{rec} - E_\pi$ for 2.5 cm wide scintillator strips. The deviation of the points from zero gives a measurement of the linearity: it is within $\pm 5\%$ for the analog readout and within $\pm 30\%$ for the digital readout. The size of the error bars denotes the width of the $\Delta E/E$ distributions and hence the energy resolution; the difference in size between the analog and digital readout is approximately a factor 1.3. The energy resolution as a function of the pion energy is shown in Fig. 97.

The calibration constants obtained with single pions were used to reconstruct the hadronic shower energy in neutrino interactions. Fig. 98 shows, separately for ν_μ NC and CC events, the difference between the real deposited energy and the energy measured with analog readout. The resolution is about 3.5 GeV, averaged over the CNGS beam energy. In ν_μ CC events, the muon contribution to the energy deposited in the strips was subtracted by approximately considering the muon as a mip.

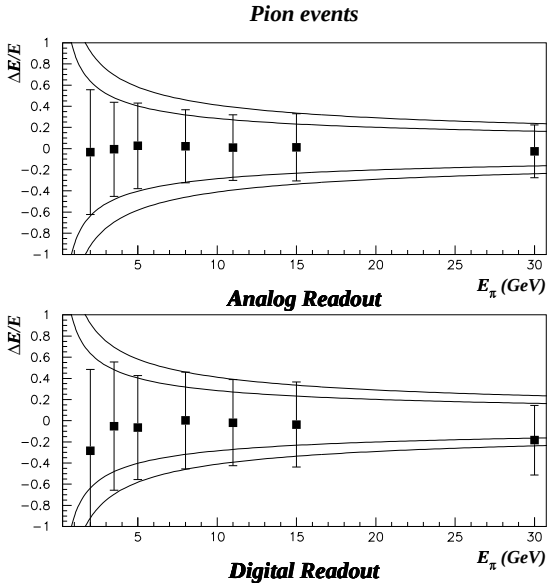

Figure 96: The energy dependence of the reconstructed energy for analog and digital readout with 2.5 *cm* wide scintillators. The error bars show the spread of the $\frac{\Delta E}{E}$ distribution and the superimposed functions show the limits of $\frac{90\%}{\sqrt{E}}$ and $\frac{130\%}{\sqrt{E}}$.

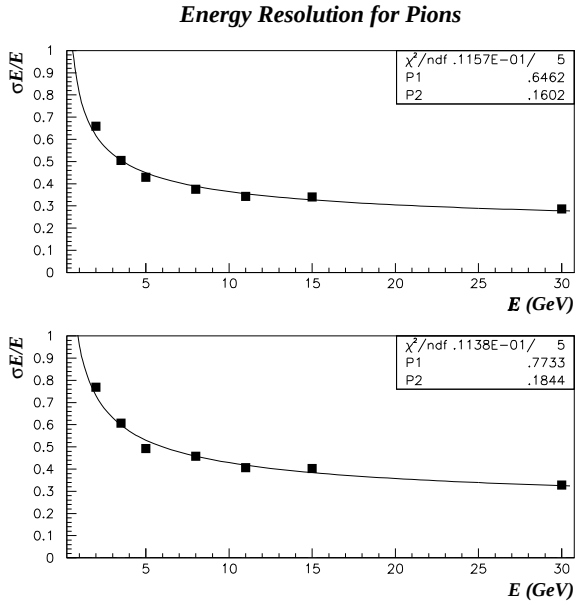

Figure 97: Simulated pion energy resolution as a function of the pion energy for analog (top plot) and digital (bottom plot) readout.

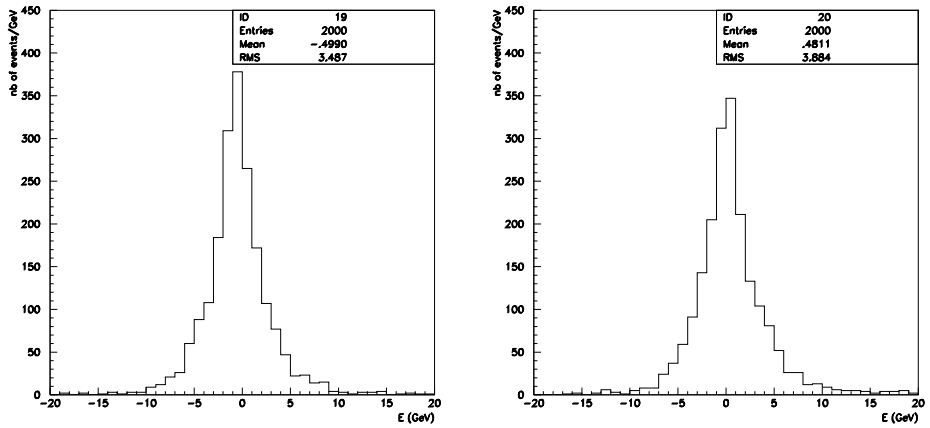

Figure 98: The difference between reconstructed and real hadronic energy for ν_μ NC events (left) and CC events (right).

6 Readout and data analysis of the ECC bricks

6.1 Introduction

As shown schematically in Fig. 99, the selected brick is extracted from the detector and disassembled after exposure to cosmic rays for alignment purposes. The emulsion films are developed and transported to the readout facilities in order to perform the *second level* data taking, namely the extraction of the event information from the emulsion.

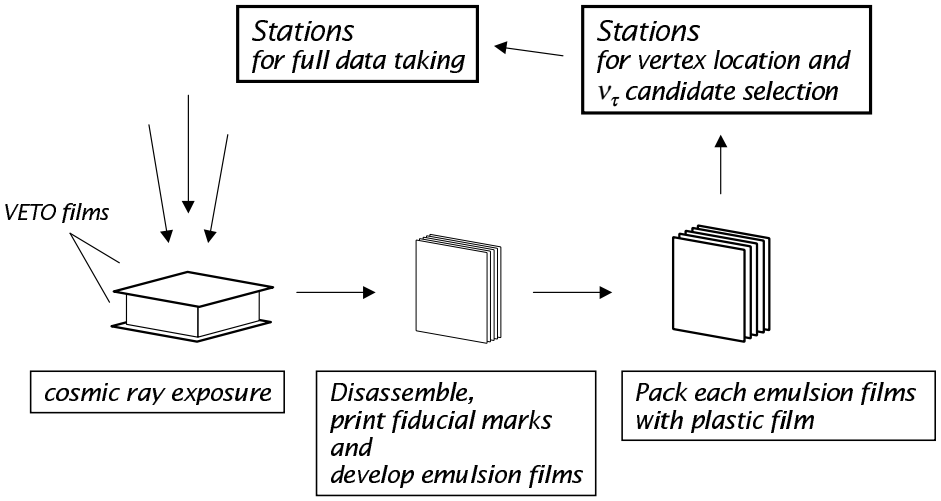

Figure 99: Brick handling procedures.

The Track Selector [9] automates the readout of track information from the emulsion films. Before describing the different steps of the data analysis, we define some terms frequently used in the following.

The track segments recognised by the Track Selector in an emulsion layer of a film are called *micro tracks*. The Track Selector tries to associate the micro tracks found in both layers of a film and, if successful, the two connected micro tracks form a *base track*. Base tracks from different films are aligned and connected by software. A set of connected base tracks defines a *track*.

The Track Selector works in two different modes, the Point Scan and the General Scan mode, defined as follows

Point Scan: searches for a base track with a predicted angle and position. The Track Selector reads out images in an area whose extension is determined by the accuracy of the predicted position, and tries to recognise a micro track in an angular range limited by the prediction angular accuracy and by the possible distortion of the emulsion layers. The existence of a corresponding micro track on the other side of the film is then looked for.

General Scan: reads out all base tracks with any position and angle in a given scanning area of one film. This information is stored on an intermediate disk storage.

By using the above running modes of the Track Selector, two basic scanning procedures are realised

Scan Back: follows a set of base tracks from an emulsion film to the upstream or downstream ones. The existence of the extrapolated base tracks in these films is checked by Point Scan.

Net Scan: performs the General Scan on different emulsion films and align the relative positions of the films by connecting base tracks between them. Computer algorithms then look for and reconstruct topologies such as neutrino interactions, decays or secondary interactions and electron pair creations. Physics quantities such as the momentum of charged particles are also derived from the data obtained by this method.

Although the concept of the Net Scan procedure is rather simple its practical application requires very fast readout devices, only recently made available by the development of the Track Selector system. The Net Scan is presently used by the UTS (the current version of the Track Selector) for the CHORUS Phase 2 and DONUT experiments. A more powerful version, the S-UTS, is planned for OPERA. It is at least 20 times faster than the UTS and able to scan more than 20 cm^2 of film surface per hour.

Since a base track is obtained by connecting two micro tracks on both sides of a film, its position and angle are free from distortions of the emulsion layers. In order to reconstruct event topologies, the films in a brick are aligned by connecting a large number of base tracks. The alignment is better performed on a local basis, by using tracks in a limited surface of the emulsion films. In this way, one eliminates the effect of global deformation of the films.

The first analysis step consists of locating the neutrino interaction vertex in the brick indicated by the electronic trackers. This is done by the Scan Back of tracks expected to come from the neutrino interaction, starting from the most downstream film (referred to as the SS film hereafter), as shown schematically in Fig. 100.

After locating the neutrino interaction vertex the search for a τ decay is performed. The kink topologies corresponding to the decay modes of $\tau \rightarrow \mu$, $\tau \rightarrow e$ and $\tau \rightarrow h$ are reconstructed by the Net Scan analysis. This analysis is nearly the same as that being performed for CHORUS Phase 2 and DONUT. In the case of OPERA, the procedure is expected to be easier since the background track density accumulated in 5 years of CNGS running is 100 times lower than in CHORUS or DONUT.

A full kinematical analysis is performed when a τ candidate event is located. This is done by applying to a relatively large volume a Net Scan in order to measure the momentum of all charged particles and to detect event-related neutral particles such as γ's converting into electron pairs. Downstream ECC bricks can be analysed as well, to provide enough track length for this purpose. An example of this kind of analysis is shown in Fig. 101, as performed in DONUT. The momentum of the τ decay daughter is measured and γ's converted to electron pairs are detected. Fig. 127 shows an example of π^0 event reconstruction, as obtained in a test experiment. This full analysis enables the measurement of the total visible energy of the interaction. Therefore, the energy of the incoming neutrino can be reconstructed for CC interactions.

In order to cope with the expected neutrino interaction rate in OPERA and allow a quasi-online analysis of the events, the analysis tools described here have to be designed and made operational before

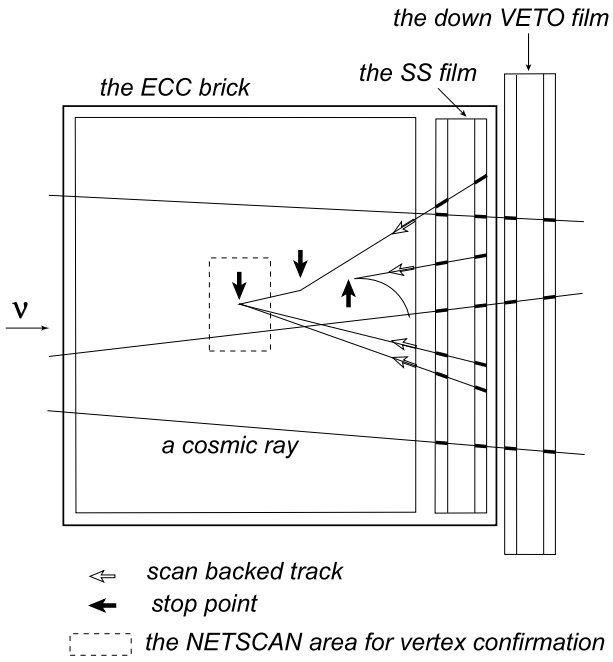

Figure 100: The event location procedure in the ECC brick is shown schematically. See the text for a description.

the CNGS beam starting up. Part of these analysis tools are already being used in CHORUS and DONUT; they will be further improved with the development work planned for OPERA.

6.2 Handling of the ECC bricks

6.2.1 Cosmic ray exposure for film alignment

The cosmic ray and the neutrino fluxes to which the experiment is exposed are very low. The induced track density in the emulsions is, therefore, not high enough for the precise alignment of the films. Nevertheless, this is an essential requirement for the momentum measurement in the ECC brick. One needs, therefore, to expose the selected bricks to high momentum cosmic rays as reference tracks for the precise film alignment.

Before cosmic ray exposure the bricks are sandwiched between two special films (cosmic VETO films) of $14\ cm \times 16\ cm$ dimensions with the purpose of tagging cosmic ray tracks. Then, bricks are moved from the underground laboratory to the cosmic-ray exposure facility. The required track density for alignment is $1 - 2$ per mm^2, for tracks roughly perpendicular to the film surface. This procedure can take a few days for an exposure at a surface laboratory. In that case, suppression of the electromagnetic component of cosmic rays has to be performed by appropriate shielding. Another envisaged solution foresees the exposure to cosmics near the entrance of the Gran Sasso tunnel (see Section 11).

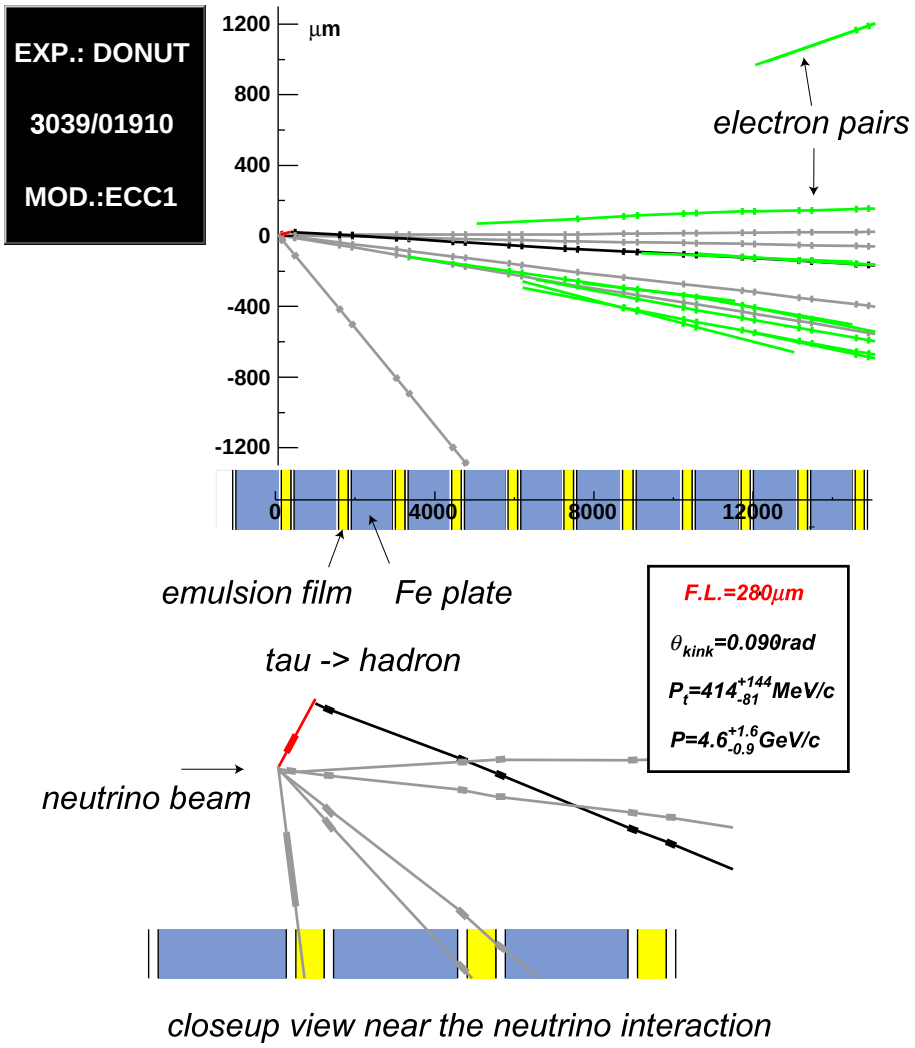

Figure 101: An example of $\tau \rightarrow h$ decay observed in the DONUT experiment. The τ decays after 280 μm with a decay $p_t = 414^{+144}_{-81}$ MeV/c and $\theta_{kink} = 90$ $mrad$. 9 electron pairs are detected.

6.2.2 Brick disassembly and emulsion film development

After the cosmic-ray exposure the ECC bricks are disassembled into films and lead plates. The brick number, the event number, the stacking order of the emulsion films and of the lead plates are recorded. The lead plate thickness is an important parameter to be known when candidate events are to be precisely analysed. Lead plates are stored for measurement on later request.

Prior to the development fiducial marks as well as brick, event and film number are printed on the films by a photographic method. The marks are needed for global correction of the film deformations.

The emulsion films are then developed by semi-automatic machines. These can process ~ 600 films per day, equivalent to 10 bricks. The realisation of such machines is not expected to be critical, because of the experience with similar devices operating daily in modern hospitals for X-ray film development.

The development procedure can be performed at the surface laboratory if the time interval between the brick disassembly and the film development is shorter than about one hour, as expected for the machines we plan to use. This limitation arises to avoid recording of isolated tracks during the disassembly phase. This is crucial for the electron cascade shower analysis in the ECC brick. One needs, in fact, to suppress the density of isolated track down to the level of $\sim 1/mm^2$.

6.2.3 Packing emulsion films for scanning

For efficient track recognition by the Track Selector system, the thickness of each emulsion layer must be large compared to the focal depth of the microscope. For this reason, the emulsion layer is expanded at the development to recover its initial thickness. Materials like Glycerine are infiltrated into the space previously occupied by the AgBr grains.

Each developed film is then packed in a transparent plastic foil as shown schematically in Fig. 102. This foil stabilises the emulsion layer thickness and protects the swelled soft emulsion surface during the scanning operations. All packed emulsion films of a brick are then mounted in a cassette. At the scanning stage, each film is picked up from the cassette automatically and tied onto the microscope stage with vacuum sucking. The plastic foil must have the same refraction index as the emulsion gel in order to preserve the optical visibility.

Packed films are then distributed to the film readout facilities. This transportation can be performed daily and must proceed smoothly, in order to keep the feedback from the readout as prompt as possible. This is required if a decay candidate is identified and the full event analysis by scanning additional bricks has to be performed.

6.3 The analysis stream

The emulsion film analysis stream is subdivided into three phases, as illustrated in Fig. 103. These are the vertex location, the decay candidate selection and the full event analysis. Vertex location and decay candidate selection imply a rather time-intensive work and must be designed and scheduled to be performed quasi-online.

Micro tracks on each side of the emulsion film are read out independently by the Track Selector. By connecting micro tracks on both sides of the plastic base, one obtains an angular resolution of about

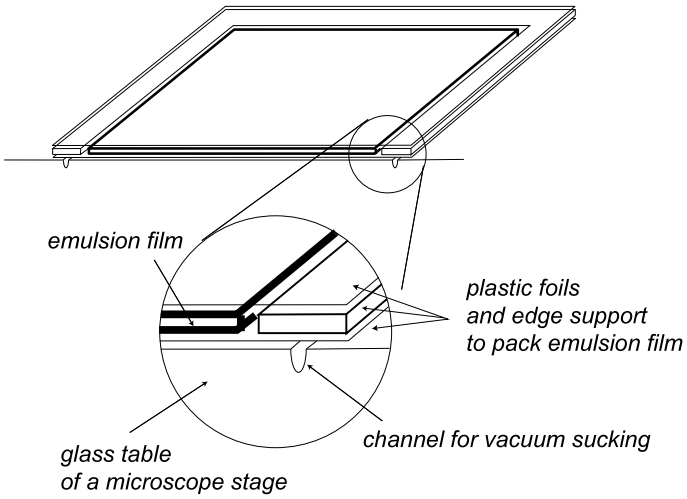

Figure 102: A schematic picture of an emulsion film packed with a plastic foil. All edges of the emulsion film are surrounded by a plastic support used for the vacuum sucking onto the microscope stage.

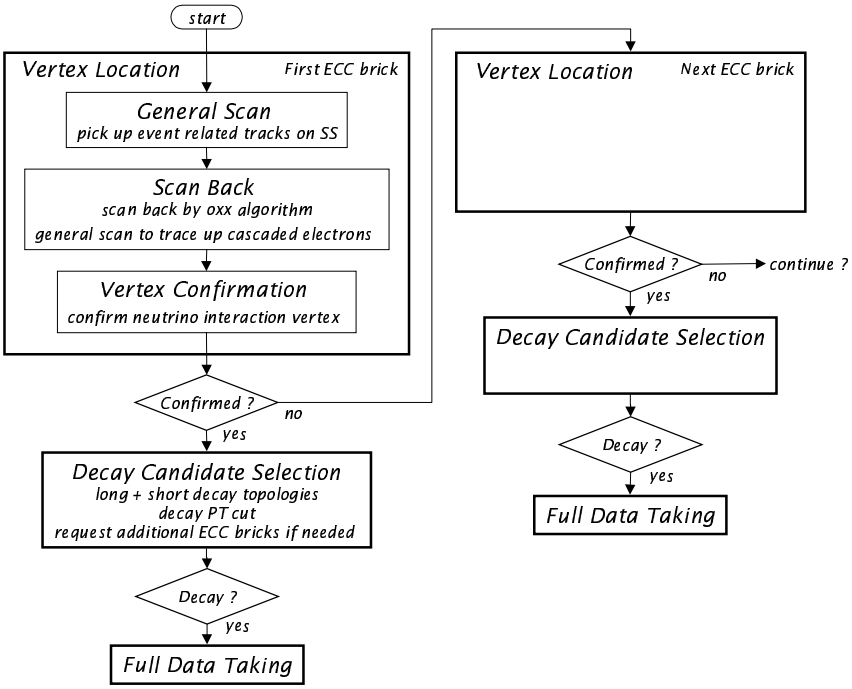

Figure 103: The flow diagram of the ECC brick analysis is schematically illustrated. A detailed description is given in the text.

2.1 $mrad$ as shown in Fig. 104. The corresponding position resolution of a micro track is 0.3 μm. The position of a base track, obtained by taking the mean of two micro tracks, is then defined with a resolution of 0.21 μm.

This, however, is not the ultimate performance. We mentioned that in the films to be used for OPERA, a mip produces about 15 grains/50 μm along its trajectory. The intrinsic resolution limit using these grains is 0.06 μm (see Section 1.3). The large difference with the achieved resolution of 0.21 μm is due to the digitisation accuracy in the CCD camera readout and in the stage coordinate measurement. High accuracy measurements, aiming to achieve the intrinsic resolution of the emulsion film, can be performed for a small sample of τ decay candidates. We point out that the base track angle obtained in such a way is not affected by distortion of the emulsion layer.

The track finding efficiency of the current UTS system is higher than 99%, as shown in Fig. 105. A test to recognise tracks at large angle ($\tan\theta \sim 1$) indicates that high efficiency can be obtained up to $\tan\theta \leq 1$. The overall UTS efficiency obtained in DONUT is presented in Fig. 106. This efficiency is influenced by emulsion defects and damages such as dusts or stains. Moreover, in DONUT, emulsion films are hand-made and some of them are known to have anomalously thin emulsion layers. These bad quality films are responsible for the low efficiency tail.

The S-UTS, now under construction, exploits the same basic algorithms as the UTS. The quality control of the industrial OPERA film production is much more reliable than for previous applications. We can therefore anticipate a similar or better measurement accuracy and efficiency.

6.3.1 Vertex location

The vertex location consists of three steps: "general scan", "scan back" and "vertex confirmation". These steps are shown in Fig. 103 and described in the following.

General scan

All recorded tracks with $tan\theta \leq 0.4$ are picked up in the SS and VETO film by general scanning. Since tracks originating from a neutrino interaction are recorded on the SS and not on the VETO film, they can be selected by subtraction. Cosmic ray events taken in the underground hall and muons associated with the neutrino beam are only recorded on the SS but their density is very small as compared to that of event related tracks.

The relative alignment between SS and VETO films is performed separately by mapping several emulsion areas of about 1×1 cm^2, to select event-related tracks. In this way the alignment is not affected by film distortions. Each area is first roughly aligned using the fiducial marks printed on both the SS and the VETO films and then precisely aligned by matching track patterns.

The SS readout area for a ν_μ CC event is of the order of 5×5 cm^2. A comparable area must be scanned for the downstream VETO film. For a NC event, the scanning area can be nearly the full surface of the film, $i.e.$ about 130 cm^2 due to the lack of well identified muon tracks in the Target Trackers.

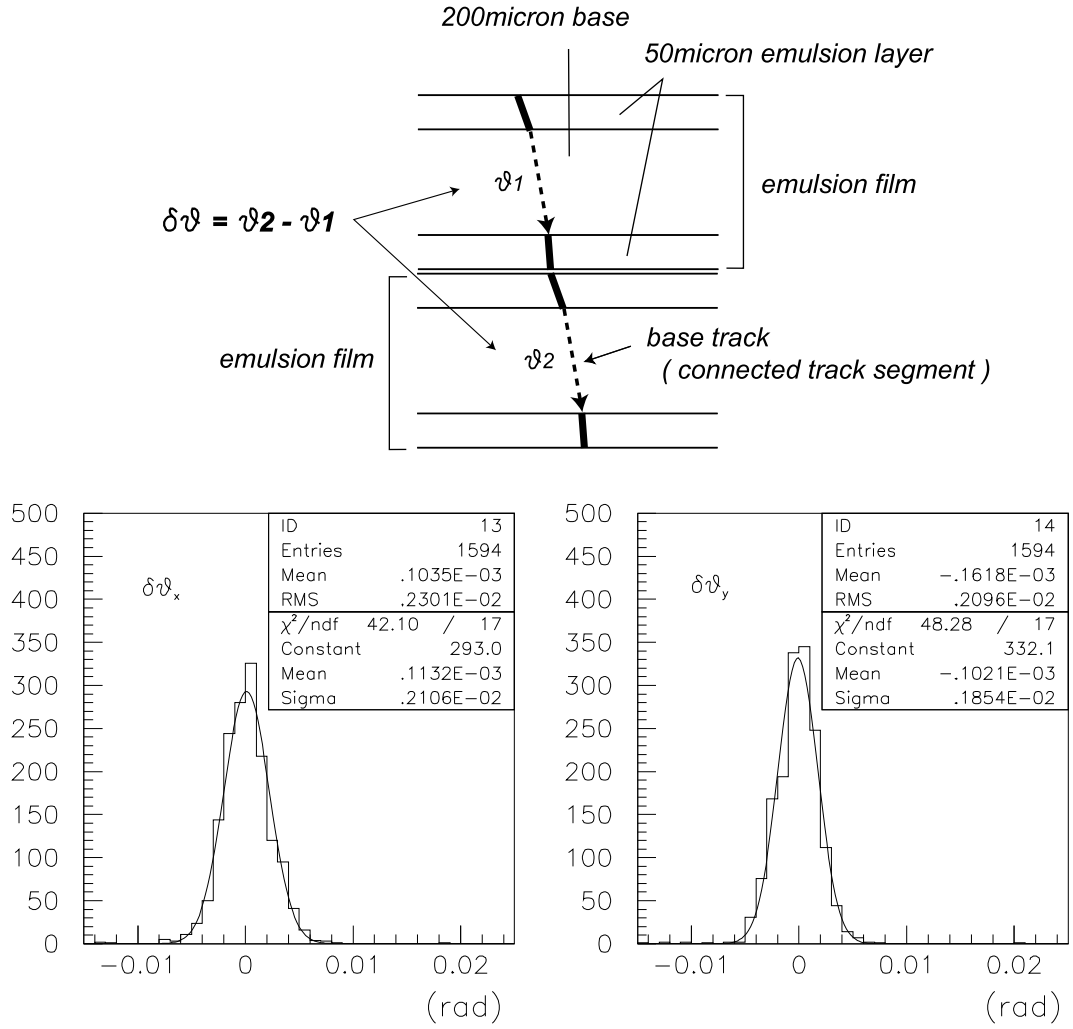

Figure 104: The angular resolution of track segments connected on both sides of the emulsion film. It is evaluated by comparing angles of tracks penetrating 2 films attached to each other. The σ of the Gaussian fit is 2.1 $mrad$ for θ_x and 1.9 $mrad$ for θ_y. Tracks of 15 GeV/c π^- are used for this analysis and their multiple scattering is negligible.

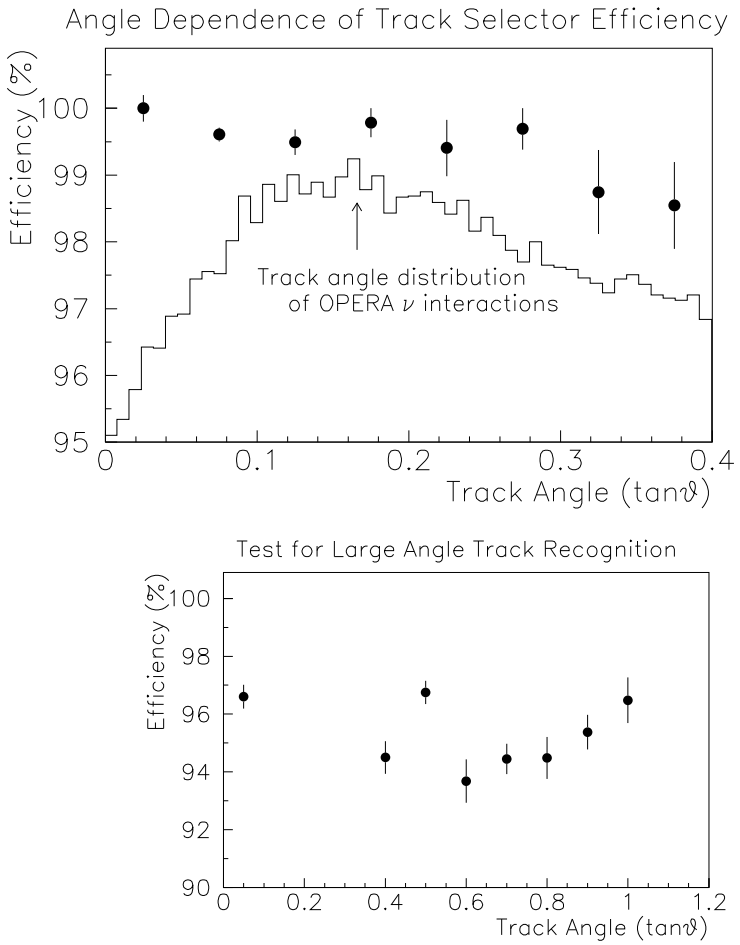

Figure 105: Top: track recognition efficiency of the UTS as a function of the track angle. The track angle distribution expected for ν interactions in OPERA is also shown. Bottom: results of a test on the recognition capability of large angle tracks.

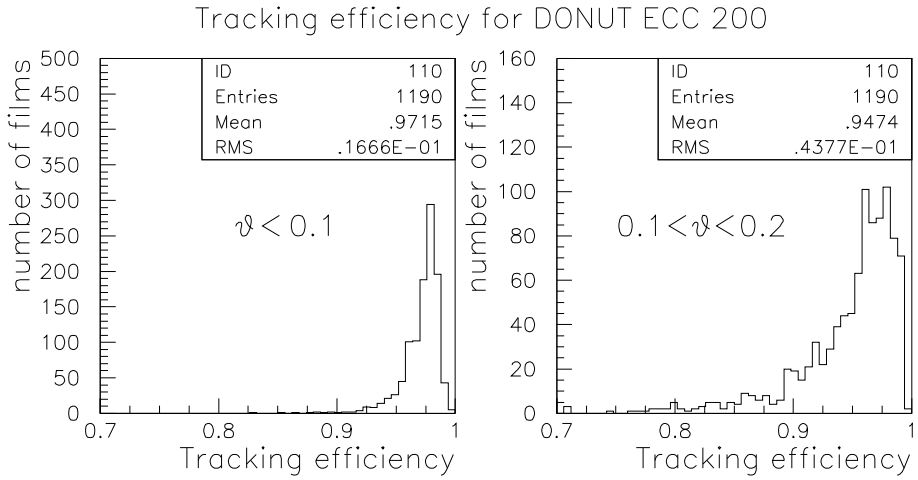

Figure 106: Tracking efficiency of the emulsion films in the DONUT experiment. Left: tracks with $\tan\theta \leq 0.1$; right: tracks with $0.1 \leq \tan\theta \leq 0.2$.

Scan back

The about 10 tracks related to a neutrino event have to be selected among more than 10^4 cosmic rays recorded for alignment. This means that ~ 100 cosmic rays are expected to pass this selection even for a S-UTS efficiency of 99%. This represents the largest fraction of tracks to be followed up. Although it is still an acceptable number, we will attempt to further improve this figure.

Since the alignment parameters are not yet known at the moment of scan back, the first few tracks are searched in a wider area of about $400 \times 400\ \mu m^2$. Approximate alignment is performed with these tracks in order to predict the positions of the other tracks well within a microscope view ($150 \times 120\ \mu m^2$).

Selected tracks are followed upstream until they stop in one of the films. A track is defined as stopping if it is not found in two consecutive films. This algorithm called oxx has been used in the CHORUS Phase 1 analysis and proved to be effective in removing apparent stops due to inefficiencies (dust on the film, bubbles under the objective lens etc.). With this definition, a UTS efficiency of 99% per film leads to ~ 0.5 fake stops when following 100 tracks through the 56 films of a brick.

The wrong connection of base tracks in consecutive films does not represent a problem for CHORUS and DONUT, in which the film track density is at least 100 times higher. It is, henceforth, absolutely negligible in the low track density conditions of OPERA.

Vertex confirmation

A small area Net Scan ($5 \times 5\ mm^2$ and 4 films) is applied around the track stopping point to classify the vertex and to confirm the presence of a neutrino interaction. Reasons for a track to stop are: ν interactions, τ and charged-charm decays, neutral-charm decays, charged secondary-interactions, neutral secondary-interactions, electron-pair creations and low-momentum tracks. Stopping points in the most downstream film are assumed to be due to low momentum tracks and thus are rejected from the vertex

confirmation. Each stopping point is classified as follows by checking the existence of other charged secondary tracks and of a parent track

- Type-1 vertex: a vertex with a charged parent track. This includes charged-charm decays, τ decays and charged secondary-interactions. All parent tracks are followed up again and their stopping points are classified;
- Type-2 vertex: a vertex with no parent and two charged-secondaries with small opening angle. Electron pairs belong to this category;
- Type-3 vertex: a vertex with no parent and not classified as Type-2. ν interactions, neutral charm decays and neutral secondary interactions are included in this category.

For a large part of the events the most upstream stopping point is classified as Type-3 and it needs to be confirmed as a ν interaction. Neutral-charm decays and neutral secondary-interactions misidentified as ν interaction vertices are taken into account in the calculations of the location efficiency (see Section 7.3.3). In the case that all stopping points are confirmed as Type-2, a special scanning is applied as described below, in order to reach the ν interaction point. An example of the vertex confirmation in a brick is shown in Fig. 107 using Net Scan data from DONUT, used to simulate the OPERA experimental conditions.

A fraction of $\tau \rightarrow e$ decays in QE ν_τ interactions are expected to have no hadrons from the primary interaction reaching the SS film, as illustrated in Fig. 108. Only shower electron pairs, initiated by a τ decay daughter, reach the SS in that event. Following up these tracks, one would end up at their conversion point and not at the primary vertex. This is a source of inefficiency in the location of that class of events.

In order to improve the location efficiency for QE $\tau \rightarrow e$ decays a general scan in a $7 \times 7\ mm^2$ area around the stopping points is performed, to pickup parent electrons. These tracks are then followed up to reach the primary vertex. Another way to increase the efficiency is to perform a general scanning in the middle film of the brick, in addition to the above method. Although it requires more scanning time, it could however be applicable for those events for which the primary vertex confirmation failed (see Section 6.3.1).

6.3.2 ν_τ candidate selection

When a vertex is found Net Scan is applied to a larger volume around it in order to detect a possible decay topology. Most of the τ are expected to decay within 1 mm from the primary ν interaction.The analysis is focused on the search of a kink decay topology since the multi prong τ decay modes do not bring a significant improvement of the experiment sensitivity.

The aim of this step is to filter out events with no sign of a possible decay topology and thus to reduce the number of events to be fully analysed. The selection is mainly based on topological information. Momentum roughly measured by multiple scattering in the brick is only used to reject kink like topologies due to low momentum particles. The emulsion area scanned for this purpose is about $5\ mm \times 5\ mm \times 10$ films.

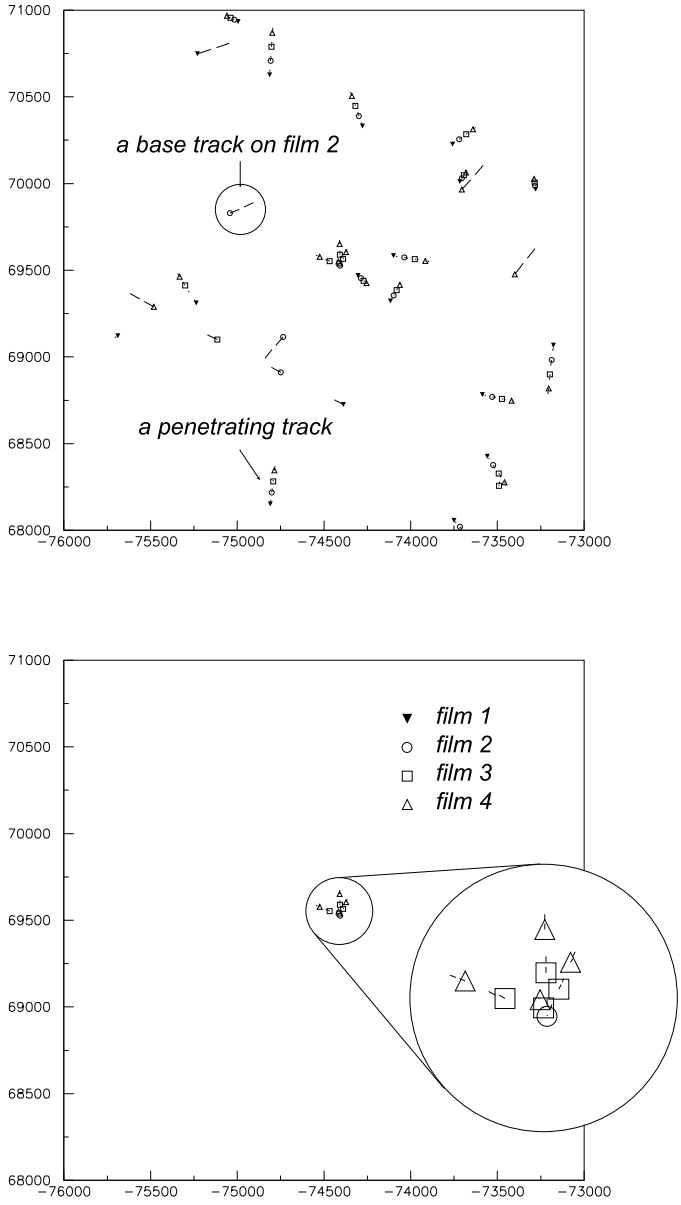

Figure 107: Top: all track segments in a $3 \times 3mm^2$ surface in four emulsion films. These track segments are taken from a Net Scan performed on a DONUT ECC stack. The track density is randomly reduced to about 100 tracks/cm^2 in order to simulate the OPERA conditions. The stack structure is similar to that of the OPERA bricks. Each track segment in a film is represented by a mark with short lines. The upmost film is "film 1" and the downmost one is "film 4". Different marks, as shown in the lower figure, are used to distinguish different films. Bottom: tracks which are not penetrating the 4 measured emulsion films and which connects more than 2 films. These tracks are confirmed to originate from a neutrino interaction vertex by manual scanning.

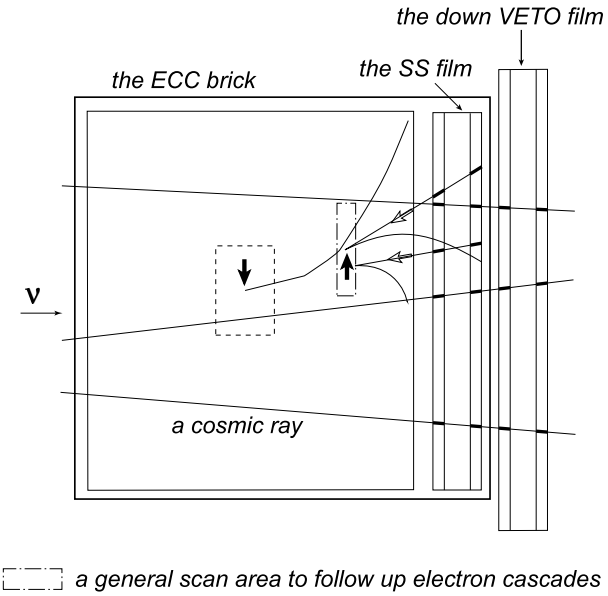

Figure 108: The event location procedure in an ECC brick, schematically shown for the case of $\tau \rightarrow e$ decay. The description is given in the text.

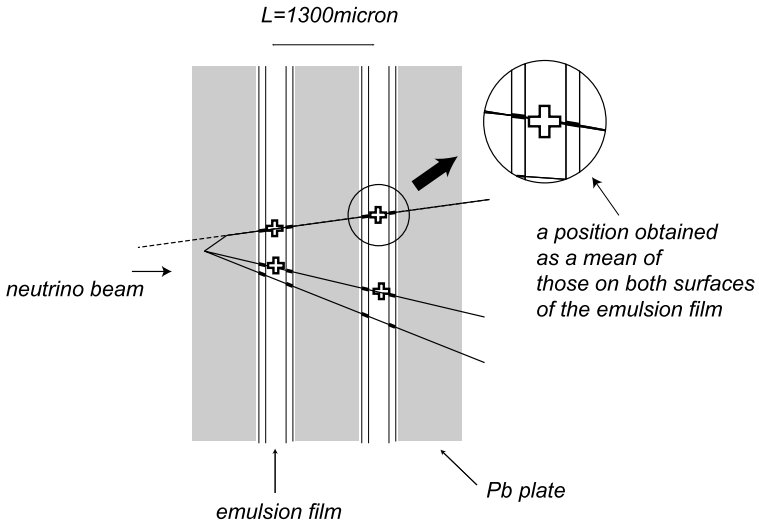

Figure 109: Short decays are selected using impact parameter analysis of any two track combinations. The lines obtained by connecting track positions on both sides of the lead plate are used to evaluate the impact parameter.

Long decays, defined as a decay topology where both parent and daughter tracks are recorded in at least one emulsion film, can be selected by requiring that the parent and daughter tracks converge within the errors and form between them a significant kink angle. The angular resolution of 2.1 $mrad$ in one emulsion film implies a minimum detectable kink angle of 3.0 $mrad$. Events with $\theta_{kink} \geq 3 \times 3.0\ mrad = 9.0\ mrad$ are selected and passed to the full data taking.

Short decays are those where only the daughter track is recorded in the emulsion. The decay occurs in the same lead plate as the primary interaction. They are selected by looking for a combination of two tracks with large impact parameter. The impact parameter threshold is determined as shown in Fig. 109. By connecting two track segments on both sides of the lead plate, the angle resolution $\delta\theta$ is

$$\delta\theta = \frac{\frac{0.3\ \mu m}{\sqrt{2}} \times \sqrt{2}}{1300\ \mu m} = 0.2\ mrad$$

The impact parameter resolution δIP when the vertex is at the upstream surface of the lead plate (the worst case) becomes 0.6 μm. Thus, events with $\delta IP \geq 3 \times 0.6\ \mu m = 1.8\ \mu m$ can be selected and passed to the full data taking.

For both decay topologies trivial backgrounds due to low momentum tracks must be rejected. The momentum resolution of $22 - 32\%$ obtained by measuring multiple scattering in 10 films is adequate for this purpose (see Section 6.6). Surviving events are sent to the full analysis stations for the extensive analysis.

For events occurring in the downstream part or near the side edge of a brick, secondary tracks have to be connected to the downstream or side bricks to provide enough tracking length for the momentum measurement and for the electron identification algorithm. Whether extra bricks have to be extracted for these purposes is decided at this phase of the ν_τ candidate selection procedure.

6.3.3 Full data taking of ν_τ candidate events

The aim of the full analysis is to reject backgrounds for τ decay topologies which are not rejected by the previous quasi-online selection. As a first step, the momentum of the decay daughter is precisely re-measured by tracing it along a full ECC brick ($10X_0$) to tighten the cut on the decay transverse momentum. Other tools for background rejection are then applied.

The two major background components are charm decays with an undetected primary muon (for all τ decay modes) and reinteractions in the lead plate for the $\tau \to h$ decay channel.

Most of the remaining charm background after muon identification by electronic detectors (see Section 7.2) originates from ν_μ CC events for which the primary muon is too soft to be clearly recognised by the electronic detectors. Once the neutrino vertex topology is identified by the emulsion measurements, more stringent identification criteria can be applied to the primary tracks found by the Net Scan procedure.

Those tracks with a momentum higher than $\sim$ 500 MeV/c can be searched for in the Target Trackers and the muon identification algorithm applied (see Section 7.2). Tracks with momentum lower

than 500 MeV/c can be followed downstream to identify the brick where they come to rest. In this brick, pion to muon separation can be achieved by the measurement of the ionisation on the last part (about 10 films) of the track, as described in Section 6.9.

Similarly, the charm background associated to ν_e CC interactions can be suppressed by identifying one of the primary track as an electron, as described in Section 6.7.

The background from hadron reinteraction in the lead plate is mainly relevant for NC events. These events are identified by a large missing p_t at the primary vertex. To measure p_t, all track segments are read out in a cone $tan\theta \leq 1$ for 5 X_0 (3.5 cm or 28 films) length. This corresponds to the scanning of about 1000 cm^2 of emulsion surface, needed to identify all charged tracks associated with the event including γ's converting into electron pairs.

The final selection of τ decays is performed by using dedicated high accuracy microscope stages aiming at the intrinsic resolution limit of the emulsion film. With that, the significance of small angle kinks and small impact parameters can be established well beyond the 3 σ limit used for the initial selection.

6.4 Readout systems

6.4.1 The UTS and the S-UTS

As described above two scanning modes of the Track Selector are used in the OPERA ECC brick analysis, the Point Scan and the General Scan. The first is used in the Scan Back procedure to follow tracks with well known positions and angles. Point Scan proceeds as follows

1. moves the microscope stage to the position where the track is predicted;
2. detects the surface of the upside emulsion layer;
3. reads out 16 tomographic CCD images in this layer;
4. recognises a micro track by using the images;
5. repeats operations 2 to 4 for the downside emulsion layer;
6. checks the existence of a micro track matching the one found in the upside layer;
7. moves the microscope stage to the next track position.

The driving speed of the microscope stage is presently about 2 cm/s. The UTS processes 3 microscope views per second to recognise all micro tracks with $\tan\theta \leq 0.4$ rad present in the view. The scanning time for the Point Scan mode is dominated by the time needed to move the microscope stage. The scanning power achieved by the UTS is adequate for the Scan Back step in the vertex location.

The General Scan mode is used in the Net Scan procedure. In this mode, one reads out all micro tracks in the area with any position and angle with $\tan\theta \leq 0.4$ rad. General Scan is much simpler than the Point Scan but requires a much higher scanning speed.

The S-UTS, the new version of the Track Selector scanning device, is now being developed to fulfil the scanning power required for OPERA. It will be soon operational, well in advance of the experiment starting up. The S-UTS is designed to be at least 20 times faster than the UTS. It has to process

more than 60 views/s recognising all micro tracks with $tan\theta \leq 0.4$ rad. The current view size is 150×120 μm^2 and thus 20 cm^2 film surface or more can be processed in one hour by one system. Since the S-UTS exploits the same basic algorithms of the UTS, it is expected to have similar measurement accuracy and efficiency.

Key features of the S-UTS are the high speed CCD camera with 3 kHz frame rate (120 Hz for the UTS) and a piezo-controlled moving objective-lens, synchronised to the stage motion in order to avoid go-stop of the microscope stage while taking images. A schematic block diagram of the S-UTS is shown in Fig. 110.

Two solutions to avoid go-stop of the stage are being considered, as shown in Fig. 111. Type A implies moving the objective lens along both the horizontal and the vertical axes, to compensate the stage displacement while taking images. Type B consists of moving the objective lens only along the vertical axis and correcting for the horizontal stage displacement on the image data stored in memory. Type A has advantages of requiring less light power and simpler electronics. The disadvantage of Type A is the requirement of a rather accurate control of the objective lens. Type B has opposite features, since it needs more light power and complex electronics but requires a simpler objective lens control.

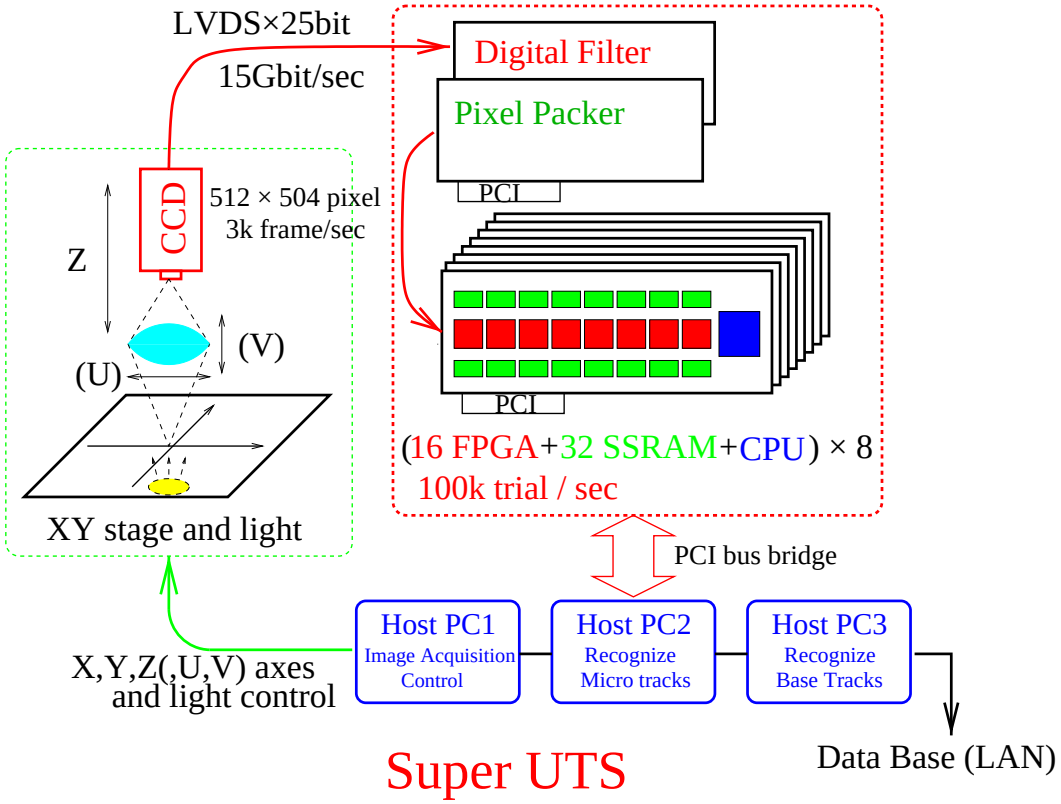

Figure 110: The schematic diagram of the S-UTS being developed.

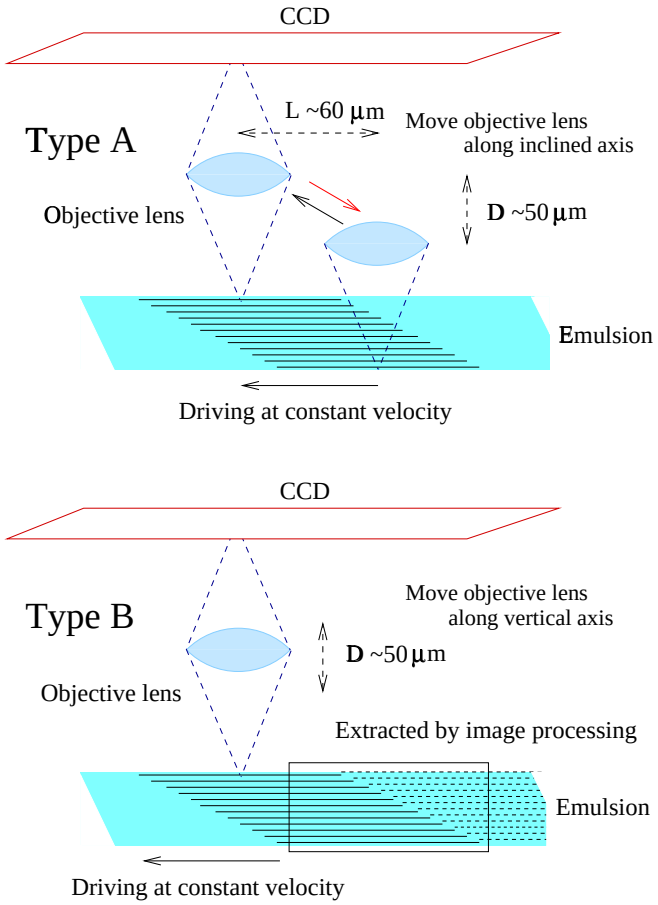

Figure 111: Two methods to avoid go-stop of the microscope stage while taking images are shown.

Table 12: Basic numbers used to design the station for vertex location and decay candidate selection.

Bricks to be processed	> 30 bricks/day
S-UTS speed	20 cm^2/hour
Cosmic rays	$100/cm^2$
Scan area for CC events	5 $cm \times 5$ cm for both VETO and SS
Scan area for NC events	14 $cm \times 16$ cm for VETO and 10 $cm \times 12.5$ cm for SS
NC/CC	1/3
UTS speed	1 cm^2/hour

For each base track the output of the Track Selector consists of the position (X and Y), the angle (θ_x, θ_y), the number of grains per layer (signal pulse height) and the grain dimensions (volume) related to the ionisation loss of the particle.

In normal operation the S-UTS only outputs base tracks. In fact, micro tracks only recognised in one layer (most of them due to β rays from lead radioactivity) are not needed for most of the analyses. However, the decay candidate selection and the full event analysis, can use a S-UTS operation mode which outputs single micro tracks, too.

6.4.2 Stations for emulsion film analysis

A *station* consists of one or several UTS and S-UTS stages controlled by a local area computer network. Two types of stations have to be set up. The first ones have the task of performing the vertex location and the decay candidate selection on $\sim$ 30 neutrino events/day for the whole running period of the experiment.

The stations are fully automated and their design has to be fault tolerant to limit the necessary manpower. They require the major fraction of the S-UTS resources, since their task represents the heaviest scanning load.

The second kind of stations are for the full data taking of the small sample of events selected as possibly containing a decay topology.

The required resources for each step are described below, taking into account the shift schedule of the station. The numbers referred to below are evaluated by using the basic features listed in Table 12.

A schematic diagram of the first type of stations is shown is Fig. 112. Each station has three clusters of S-UTS systems, each corresponding to one or two steps in the analysis flow previously described and illustrated in Fig. 103.

The first cluster is for General Scan. The emulsion surface to be scanned is 150 cm^2 for the VETO and 100 cm^2 for the SS film, evaluated by the weighted mean of CC and NC interactions. Each set of films requires about 8 hours of scanning and thus one S-UTS can process three films in one day. 20 S-UTS are needed to process 30 bricks/day since there is almost no overhead time such as to set films on microscope stage etc.

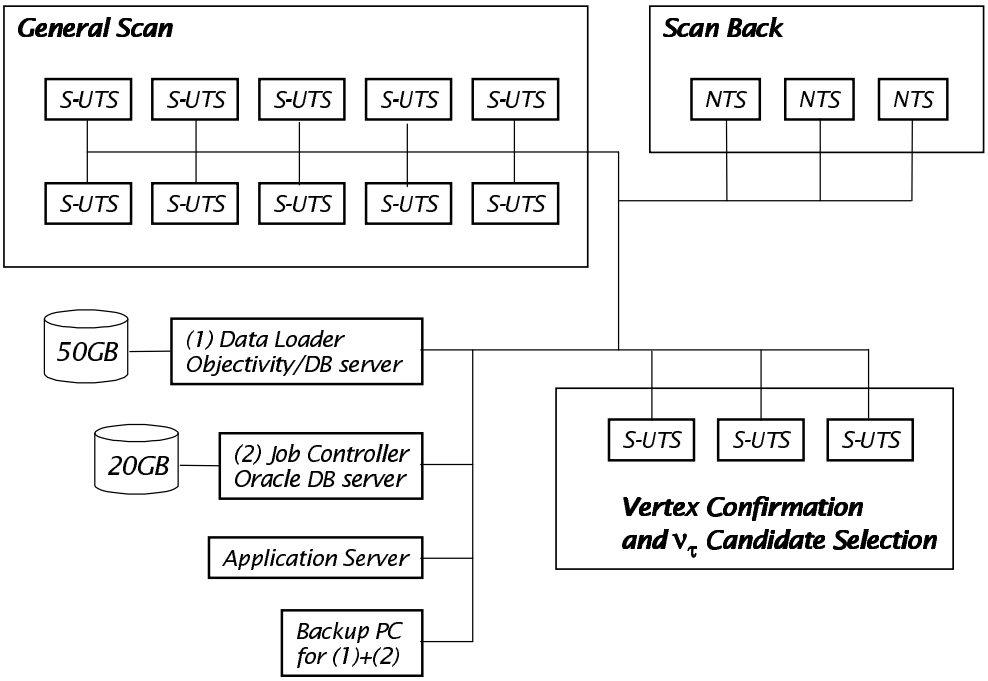

Figure 112: The schematic diagram of a station for vertex location and decay candidate selection is shown. A station for full analysis is set up in a similar way.

The second cluster is for Scan Back. The UTS or the NTS, an older version of the Track Selector, can provide enough scanning speed for this cluster. Most of the time to follow up tracks is spent to move the microscope stage to the predicted positions. This takes about 1 s/track and not more than a few minutes per film ($i.e.$ for 100 tracks). This means that, in order to scan about 50 films/brick (as needed at this analysis phase), the film replacement occurs very frequently (every few minutes).

Robots used to automatically replace films have to be developed and implemented. They are similar to the devices which perform paper-sheet handling in printers or copying machines. The emulsion films of a brick are stored in a cassette. This is brought from its storage room and is manually set on the microscope stage. The robot extracts each film and sticks it onto the microscope stage by vacuum sucking. The external film packing used to control and stabilise the thickness of the emulsion layer also contributes in easing robot operation.

The small area general scan to follow up electron showers takes about 0.5 hours/point. A brick is to be set every 3 hours and this is done manually. 3 UTS or NTS can process 30 bricks/day.

The third cluster is for Vertex Confirmation and for Decay Candidate Selection. An area of 5×5 mm^2 has to be scanned for each film. Scanning only 4 films is adequate for vertex confirmation, while 10 films are needed for decay candidate selection, in order to measure the momentum of secondary tracks. Assuming 3 vertex candidates per brick, about 11 cm^2 have to be scanned. 3 S-UTS can process 30 bricks/day, requiring operator assistance for 12 hours/day (daytime).

Concerning the stations for the full event analysis, about 1000 cm^2 have to be scanned per event,

an area that one S-UTS can process in two days.

Stations for high accuracy measurement are also to be set up. They handle a fraction of the fully analysed events which need to be precisely remeasured for background rejection. This is the case, for example, of τ decay candidates with small kink angle and high momentum decay daughters. Measurements aiming at the ultimate accuracy require specially designed microscope stages and can organised in dedicated stations.

6.5 Emulsion data stream

Unlike in electronic tracking detectors, trajectories of through-going tracks are permanently recorded in the emulsion films. Thus, the emulsions not only work as tracking devices but also as recording media. The basic information stored in an emulsion film is given by the $grains$ due to minimum ionising particles, to Compton electrons etc.

However, reading out these data and keeping them on a disk or on a similar media is not a reasonable choice, given the constraints of the presently available computers and networks. For this reason, a large data reduction from grain information to base tracks is performed by the Track Selector. Its performance is therefore a key issue for OPERA. Although this reduction is adequate for most of the planned analyses, one should keep enough flexibility to allow the access to less reduced (basic) information, as long as required by special analyses for a fraction of the candidate events. Moreover, additional data taking might be requested, specially for the full data taking, when some of the tracks have to be followed further.

In such the above scheme, the software structure is better designed considering the emulsion films as the original data storage and disks as a cache, in order to provide fast access and common interface to the analysis programs. In particular, the analysis has to be able to provide a smooth feedback to the data taking.

The $unit$ data set from an emulsion film is the microscope view which contains base tracks stored in each emulsion layer. A set of views, chosen for specific analysis purposes, are readout by the S-UTS, kept on a disk space and could eventually be discarded after the analysis. Reading out additional set of views might be required to complete the analysis. Objectivity/DB are basic tools to provide this cashing mechanism.

The life time of a cache has to be decided considering the overhead time to re-read from the emulsion film using the S-UTS. All measured tracks on the SS and VETO films must be kept online through the experiment lifetime. Most of these tracks are cosmics and their data size is about 400 $kbyte$ for each film and thus ~ 40 $Gbyte$ in total. The data of all stopped tracks and the vertex information obtained in the decay candidate selection have to be kept online through the experiment lifetime, while those obtained in the vertex confirmation are not. Their data size is marginal and 50 $Gbyte$ disk space is sufficient. Finally, the data size of the full analysis amounts to about 2.5 $Mbyte$ per event (50000 tracks/event). This is about a factor 5 more than for CHORUS Phase 2 but should not cause any particular problem.

In order to automate the analysis all steps have to be controlled, monitored and logged automatically. Oracle (Relational Database) can be used. Software components including this kind of controller jobs are

being developed and tested within the analysis of CHORUS Phase 2, of DONUT and of test experiments for OPERA.

The analysis of emulsion data will be performed in all interested laboratories. To ensure efficient sharing of data among the various scanning stations, common access protocols must be well defined. Since stations are spread over the world and network access is not always fast enough, a tool to browse the online summary of the stations and to create a replicated subset of the data in each laboratory will be required.

6.6 Momentum measurement by multiple scattering in the ECC bricks

The momentum of a charged particle can be measured from its multiple scattering in the ECC bricks. The basic unit for this measurement (cell) is one lead plate 1 mm thick sandwiched by two emulsion films, as shown in Fig. 113. One brick has 56 cells and thus about 100 independent measurements of the track angle in two projections can be obtained for each passing track.

When a particle of momentum p and velocity βc traverses a material of thickness X measured in units of radiation length (for a 1 mm lead plate $X = 1/5.6$) the distribution of the scattering angle in a plane is approximately Gaussian with a RMS given by

$$\theta_0 = \frac{13.6\ MeV/c}{p\beta}\sqrt{X}$$

6.6.1 Angular method

One can measure θ_0 by simply taking the difference of angles in two consecutive emulsion films, as shown in Fig. 113. One uses the angle obtained by connecting two track segments on both surfaces of a film. The typical resolution is $\delta\theta = 2.1\ mrad$ as previously described. Under the assumption that $\theta_0 \geq 2\delta\theta$, the maximum detectable momentum is 1.4 GeV/c.

The RMS of the measured scattering angles, θ_M, is the quadratic sum of the scattering *signal* θ_S and of the measurement error $\delta\theta$

$$\theta_M^2 = \theta_S^2 + \delta\theta^2$$

With this method θ_S is equal to θ_0.

The error on θ_S, due to both the statistical error on θ_M and to the measurement errors when N independent measurements are performed, is

$$\frac{\delta\theta_S}{\theta_S} = \frac{1}{1-(\delta\theta/\theta_M)^2}\frac{1}{\sqrt{N}}$$

Using N_{film} emulsion films, this method provides $N = (N_{film} - 1) \times 2$ since each of the two projections of a set of films gives independent measurements. Therefore, one can obtain $\delta p/p \sim 10\%$ with about 50 films.

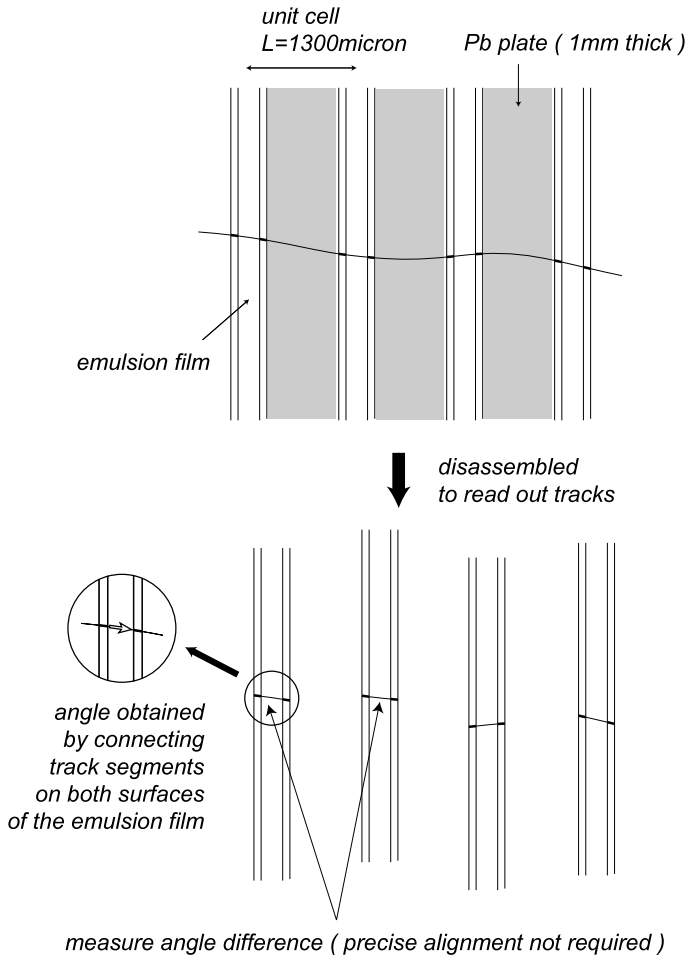

Figure 113: The angular method used to measure the multiple scattering is shown schematically. The scattering angle is obtained directly by measuring the difference of angles on each film. This method does not require precise alignment of the emulsion films.

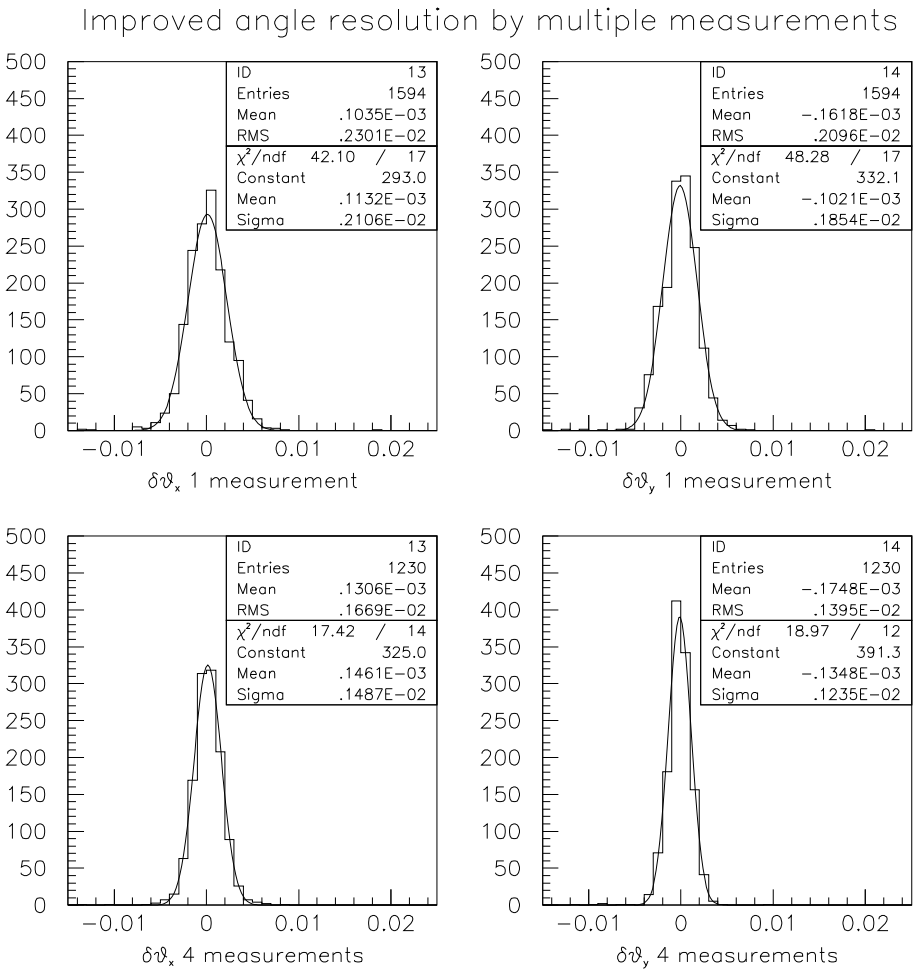

Figure 114: Top: angular resolutions for the X and Y projections as obtained by a single measurement. Bottom: improvement in the resolution obtained by computing the mean angle from 4 measurements for each emulsion film.

We recall that the intrinsic position resolution of the emulsions is 0.06 μm, which gives $\delta\theta = 0.4\ mrad$ and, hence, a maximum detectable momentum of 7.1 GeV/c. Since $\delta\theta$ originates from the position measurement error on the films, one can perform precise measurements by means of specially designed microscope stages and/or by multiple position measurements, in order to improve the accuracy. An example illustrating the improvement obtainable by multiple measurements is given in Fig. 114. By averaging over four measurements, the error on the angle is reduced by a factor of about 0.7 to $\delta\theta = 1.5\ mrad$, a bit worse than the expected $1/\sqrt{2}$. This corresponds to a maximum detectable momentum of about 2 GeV/c.

The above method will be extensively studied in the next future, since it has the advantage that the error only depends on the measurement accuracy (*i.e.* it does not depend on the alignment precision among the emulsion films). However, the film and the plates are required to have a surface parallelism better than 1 $mrad$. This is needed in order to measure the angle difference without relying on the relative angle with respect to reference tracks. This requirement is expected to be fulfilled, as described in Section 4.2.

6.6.2 Coordinate method

The coordinate method is more sensitive to high momenta and consists of measuring the position displacement as shown in Fig. 115. The effective measured scattering angle θ_M in one plate is obtained by measuring the displacement Δx over a cell length L (Fig. 115)

$$\theta_M = \frac{\Delta x}{L}$$

In this method, θ_M is expressed as for the angular method by $\theta_M^2 = \theta_S^2 + \delta\theta^2$. The relation between θ_S and θ_0 takes a slightly different form

$$\theta_S = \sqrt{\frac{2}{3}}\theta_0$$

This method is more sensitive to higher momenta since it measures angles by using a longer lever arm than in the angular method. In order to measure Δx, only 3 emulsion films have to be precisely aligned. The cosmic ray exposure of the brick is designed to provide enough reference tracks for this alignment.

One can evaluate the maximum detectable momentum and the momentum resolution achievable by this method from the position resolution obtained in DONUT. As shown in Fig. 116, the position accuracy for micro tracks is about 0.3 μm in a $3 \times 3\ mm^2$ emulsion area for tracks with $\theta \leq 100\ mrad$. Emulsion films were aligned by using tracks over a surface of about $3 \times 3\ mm^2$. By averaging micro track positions in both sides of the base one can obtain $1/\sqrt{2}$ better position resolution (*i.e.* 0.21 μm) on the base track position. The variation among different films obtained in DONUT is also shown in Fig. 116.

The measurement error $\delta\theta$ can be expressed as

$$\delta\theta^2 = 6(\frac{\delta x}{L})^2 + (\theta_M \frac{\delta L}{L})^2$$

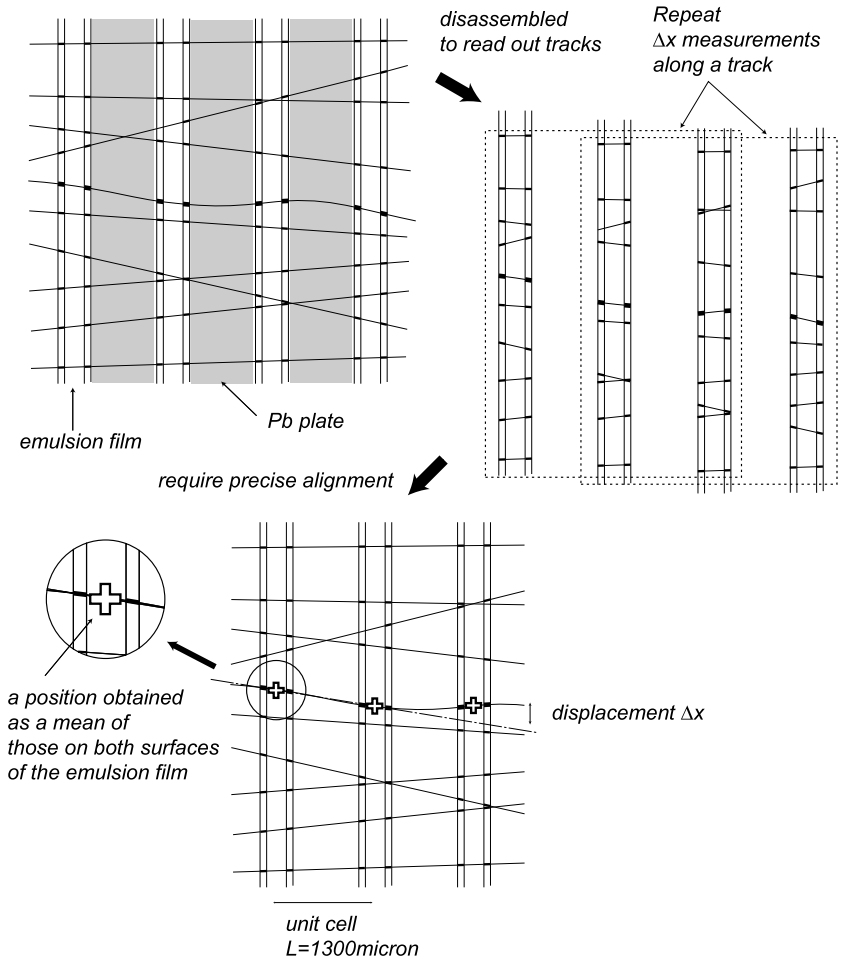

Figure 115: The coordinate method to measure multiple scattering is schematically shown. For this purpose, 3 films have be precisely aligned over a small film surface.

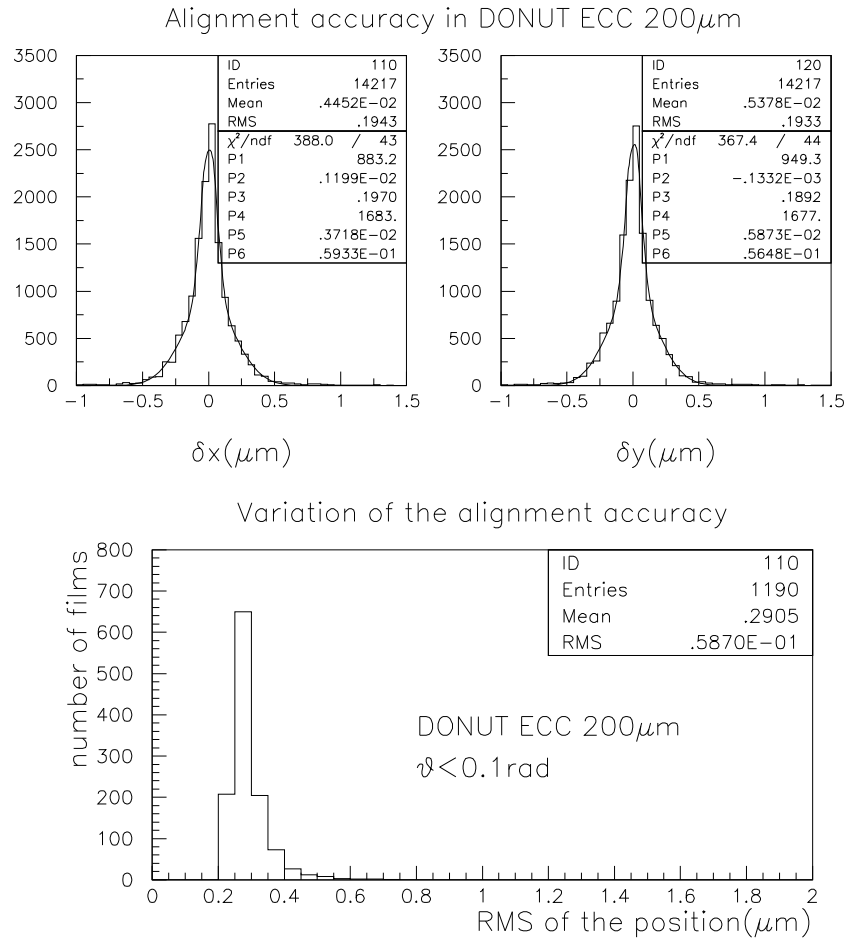

Figure 116: The top histograms show the position resolution of the UTS as obtained in DONUT. It is evaluated as residuals from a straight line fitted to penetrating tracks. These tracks pass through 9 Fe plates (1 mm thick) and 9 emulsion films. Since most of the tracks are due to beam muons with a wide momentum spread, multiple scattering effects affect the distributions. A two-Gaussian fit shows the presence of a narrow component with a resolution of 0.06 μm. The bottom histogram shows the variation of these RMS among the different emulsion films.

From the expected lead plate uniformity, δL is about 10 μm and the second term becomes negligible for momenta above 500 MeV/c. Using $\delta x = 0.21$ μm one obtains from the first term $\delta\theta = 0.4$ $mrad$. The condition $\theta_S \geq 2\delta\theta$ is then equivalent to

$$p_{max} = \sqrt{\frac{2}{3}}\,\frac{5.75\ MeV/c}{2\delta\theta} = 5.9\ GeV/c$$

As described above, $\delta\theta$ is dominated by δx. To obtain a better momentum resolution or a higher $p\beta_{max}$, either a longer cell length has to be used or δx has to be reduced. Indeed, $\delta x = 0.21$ μm is not an intrinsic limit, but is just the limit of the digitisation errors of the Track Selector. Therefore, there is room for reducing δx for small samples such as τ decay candidates. We also note that δx is composed of both measurement and alignment errors unlike the angular method. δx worsens as the track slope increases. Since particles emitted at large angles tend to have a lower momentum, this effect is somehow compensated.

In Fig. 117 the momentum distribution of τ decay daughters is shown as a function of their emission angle. 73.9% of the daughters fall in a region with $\theta_S \geq 2\delta\theta$ and 96.9% have $\theta_S \geq \delta\theta$; using twice the cell length, 99.4% have $\theta_S \geq 2\delta\theta$.

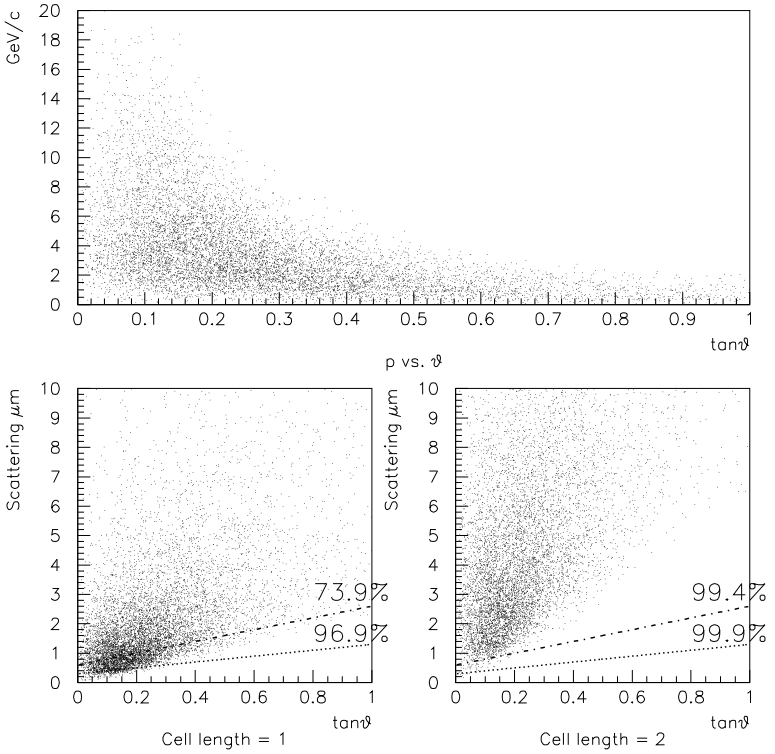

Figure 117: Top plot: momentum distribution of τ decay daughters as a function of the emission angle. Bottom plots: Δx distributions as a function of the emission angle using one cell length (left) or twice the cell length (right).

The error on θ_S due to both the statistical error on θ_M and the measurement error $\delta\theta$ when N independent measurement are performed is expressed in the same form as for the angular method. Using N_{film} emulsion films, the coordinate method provides $N \sim (N_{film}/2) \times 2$, about half than for the angular method. This is because it requires a set of 3 films for each 2 independent measurements. Therefore, one can obtain $\delta p/p = 14\%$ (slightly worse than for the angular method) by following a track for one entire brick.

A test of the above method has been performed by using an ECC brick exposed to a 4 GeV/c pion beam at KEK. This brick is made of 23 lead plates of 1 mm thickness interspaced with the emulsion films. It has a radiation length of 4 X_0. An area of 11×9 mm^2 was scanned and 396 penetrating tracks were obtained; 301 of them with an angle within ± 20 $mrad$ around the beam direction were used for the analysis. Fig. 118 shows the measured momentum distributions for data and for Monte Carlo simulated 4 GeV/c pions.

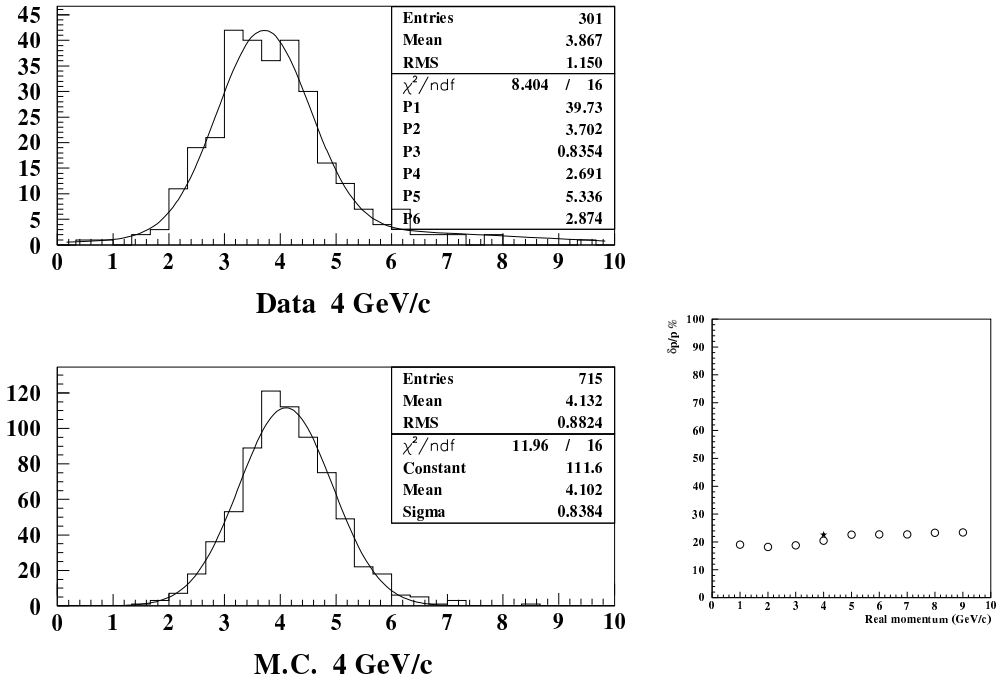

Figure 118: Results of a test experiment on the coordinate method. An ECC brick with $4X_0$ thickness was exposed to a 4 GeV/c pion beam at KEK. The bottom-right plot gives the momentum resolution.

The error $\delta p/p$ is determined by a two-Gaussian fit to the data and by a single Gaussian for Monte Carlo simulated tracks. The obtained momentum resolution shown in Fig. 118 well agrees with the expectations. Δx is measured using twice the unit cell length and $11 \times 2 = 22$ independent measurements are performed for each track. The expected statistical error is $1/\sqrt{22} = 0.21$, consistent with the

experimental result.

The momentum resolution for the angular and the coordinate methods is summarised in Fig. 119 for tracks followed over an entire brick. Three ECC bricks have been exposed at the CERN PS to pions of 2, 4 and 8 GeV/c, to confirm the angular and the coordinate methods for different track angles and different momenta. They have also been exposed to cosmic rays to confirm the design alignment accuracy and to evaluate the minimum cosmic ray density suitable for the procedure. The analysis of these data is in progress.

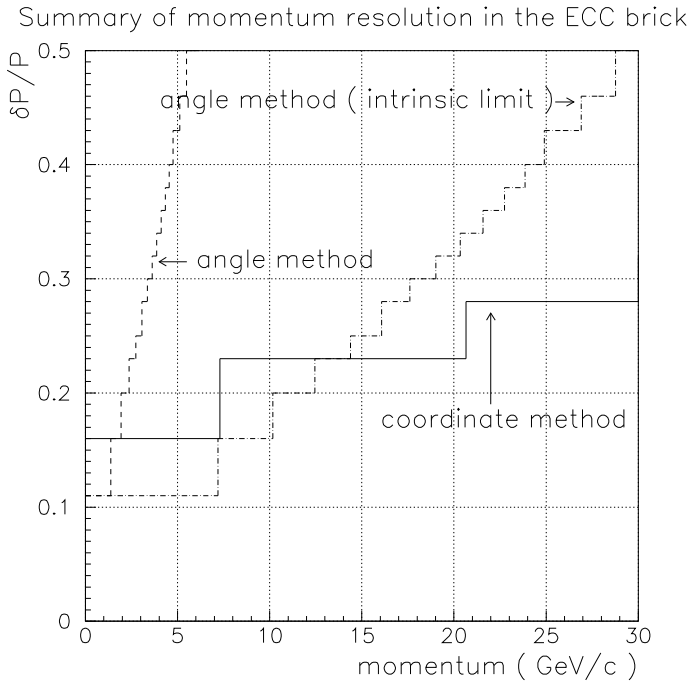

Figure 119: Momentum resolution for both angular and coordinate methods. It refers to tracks followed for one brick (56 emulsion films). Each step in the resolution corresponds to a change in the cell length L, in order to satisfy the condition $\theta_S \geq 2\delta\theta$.

6.6.3 Effect of hadronic interactions

Unlike muons, hadrons interact in the brick and it becomes impossible to follow their trajectory to obtain more measurements. Pions have a collision mean free path of 116.2 g/cm^2 or 10.2 cm in lead. Fig. 120 shows the results of a simple calculation of the fraction of pions for which a given number of cells is available for the momentum measurement (or, equivalently, the statistical error on θ_M). The full kinematical reconstruction of secondary interactions of hadrons from $\tau \longrightarrow h$ decay daughters which interact before traversing a sufficient number of cells must be performed to estimate the decay hadron energy.

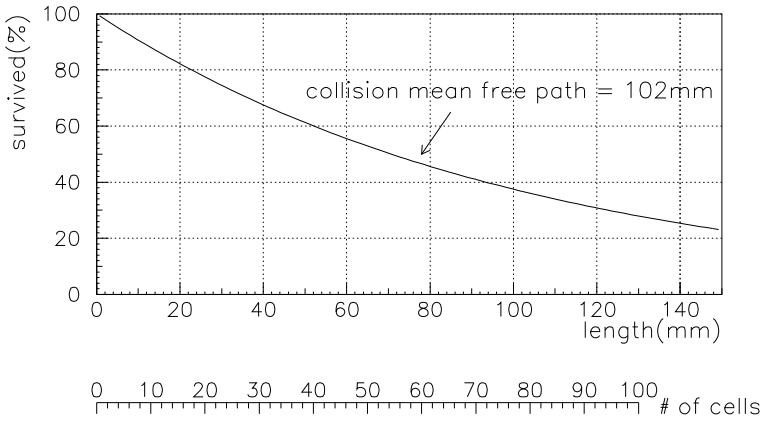

Figure 120: Fraction of pions which have a given number of brick cells available for momentum measurement.

6.7 Electron identification and γ detection

Typical examples of electrons observed in a test experiment with an ECC brick are shown in Fig. 121.

Both the multiple scattering before the shower starts and the number of electrons when the shower develops are used for the identification and the energy measurement of electrons.

In order to reconstruct the energy of a primary electron starting an electromagnetic shower, one can measure by multiple scattering the energy of those (few) electrons produced in the early development of the shower. This method has been exploited by many past experiments, but it becomes today very powerful when applied to OPERA. One can, in fact, exploit the capability of the Net Scan analysis over larger scanning volumes.

6.7.1 Multiple scattering analysis

Energy or momentum measurement by multiple scattering has been discussed in Section 6.6. However, the energy loss features are different for electrons and hadrons. The energy loss of electrons proceeds through bremsstrahlung, with an exponential dependence as a function of the material crossed in units of X_0

$$E_e(x) = E_0 \, e^{(-\frac{x}{X_0})}$$

Hadrons, instead, mainly undergo ionisation losses

$$E_h(x) = E_0(1 - \frac{dE}{dx}x)$$

This difference is used to distinguish electrons from hadrons. The χ^2 values corresponding to the above expressions is used as an electron/hadron separator, allowing E_0 to vary in the physical range. The particle type assignment (electron or pion) which gives the smaller χ^2 is taken and the corresponding E_0 assumed as the particle energy. The χ^2 is defined as

$$\chi^2 = \sum_{i=1}^{N-1} \frac{[(\Delta\theta_i - \theta_{i,i+1}^{MCS})/\theta_{i,i+1}^{MCS}]^2}{N(N-1)}$$

where N is the number of measured segments, $\Delta\theta_i$ is the spatial angular difference between two segments and $\theta_{i,i+1}^{MCS}$ is the angular variation due to multiple scattering after 1 mm lead for the energy E_i (see Fig. 122).

6.7.2 Shower analysis

Counting track segments associated to the shower is also a way of identifying electrons. This analysis has to be confined in a relatively small emulsion region, in order to suppress background track segments which are not related to the shower. Examples of shower induced by 2 and 8 GeV electrons detected in a test experiment are shown in Fig. 121. The lateral spread of the shower is of the order of 1 mm. The brick thickness is 10 X_0 and thus a shower is well confined within a single brick. The S-UTS is able to readout most of the electrons related to the shower and the Net Scan analysis to reconstruct the shower structure.

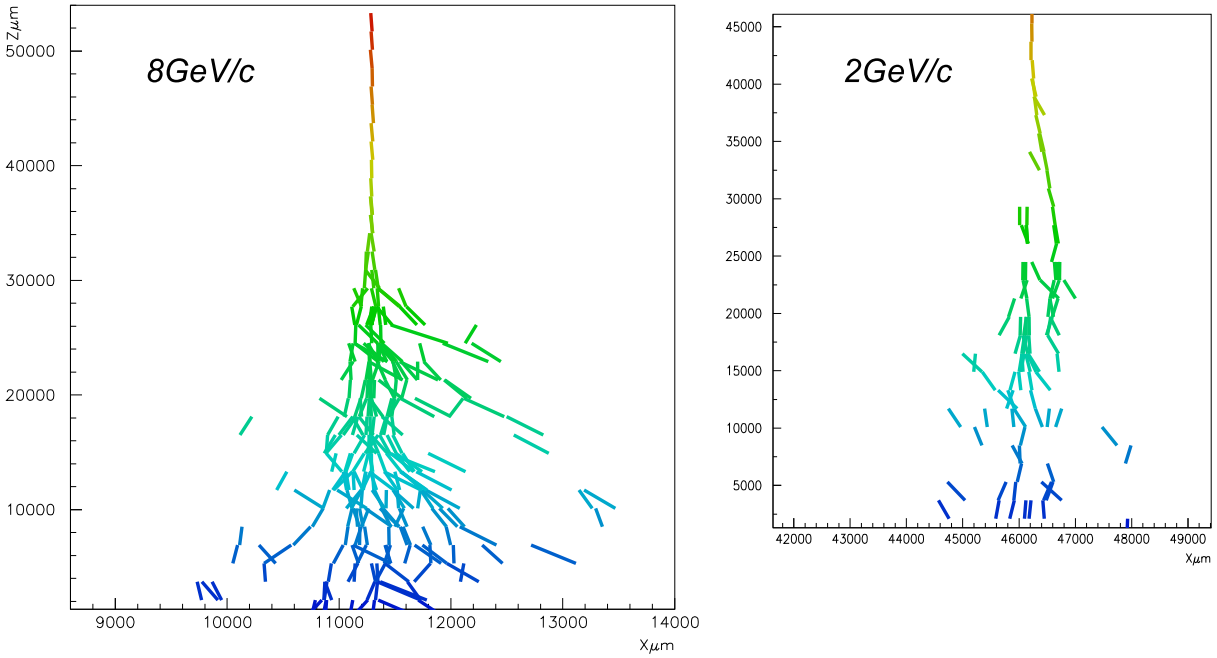

Figure 121: Electromagnetic showers observed in a brick exposed to an electron beam.

Particle tracks recorded while the emulsion films are not assembled in the ECC brick, *i.e.* before packing and after disassembling, become track segments not related to the electromagnetic shower. Cosmic rays and muons in the ν beam do not constitute backgrounds, since they can be distinguished as penetrating tracks. In order to limit the density of these background track segments below $1/mm^2$, controlled fading of the emulsion films is applied prior to the brick installation. In addition, the time between brick unpacking and film development is kept short, as described in Section 6.2.2.

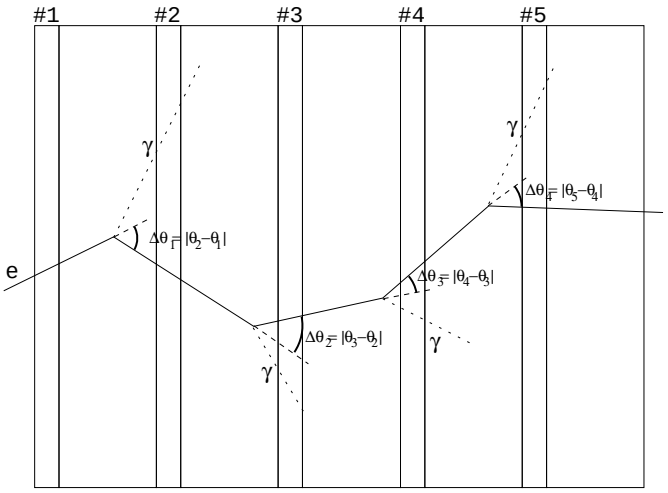

Figure 122: Schematic view of an electron propagating through a brick and variables entering into the χ^2 definition.

Since electrons in a shower are mostly produced around the critical energy of the medium (10 MeV for lead), it is important to be sensitive to electrons with such an energy. However, electron tracks have to be connected on both sides of the emulsion film to reject β's from a neighbouring lead plate. This condition imposes a minimum detectable energy for the electrons.

The connection efficiency as a function of the electron energy is shown in Fig. 123 by using the connection condition of $\delta\theta \leq 50\ mrad$ and $\delta r \leq 6\ \mu m$ at the centre of the film. The efficiency degradation for lower electron energy is due to multiple scattering in the emulsion films. The figure shows that the minimum detectable energy for electrons is close to the critical energy of lead. The number of β's accidentally connected on both sides of the film is expected to be $1/mm^2$ for a β density of $10^5/cm^2$. This value is still acceptable, but further study must be done to optimise the connection efficiency.

The electron energy can be simply inferred by counting the number of track segments in a cone along the track. The cone dimensions have to be optimised to include the largest number of cascade electron pairs without integrating a too large number of background tracks. A cone of $\pm 50\ mrad$ and a relative angle $\delta\theta \leq 200\ mrad$ to the primary track is used in the Monte Carlo study described in Section 7.1. One obtains a resolution $\Delta E/E$ of about 20%, as shown in Fig. 124.

The space and angular region to be used for the electron identification and shower energy measurement are not yet optimised. A test experiment and extensive Monte Carlo studies have to be performed for this purpose.

An algorithm for electron/hadron separation can be realised, which makes use of a χ^2 fit which combines the energy loss features and the counting of track segments in the cone around the track. The performance of this algorithm applied to simulated tracks is described in Section 7.1.

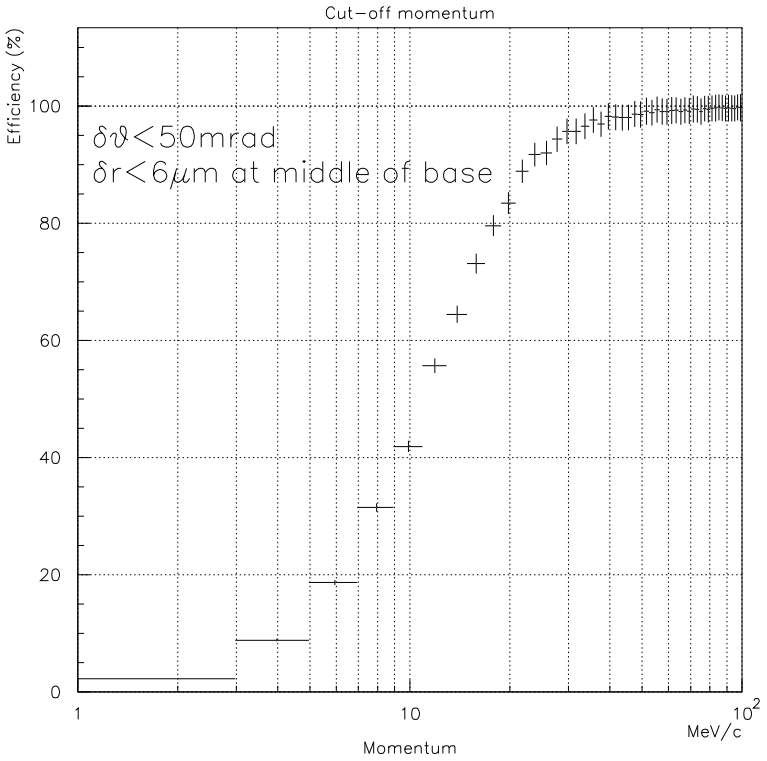

Figure 123: Electron *connection* efficiency as a function of the energy.

6.8 γ detection

The OPERA ECC bricks have a conversion length of about 7.2 mm. This means that most γ's produced at the interaction vertex convert into electron pairs in the brick and can then be detected. This is relevant for two aspects, both related to the $\tau \rightarrow h$ decay mode. The first is the measurement of the total missing p_t of the event, a tool to reduce the background from hadron reinteractions in the lead plate. The second is the detection of $\tau \rightarrow \rho\nu$ by reconstructing $\rho \rightarrow \pi\gamma\gamma$.

Reinteractions of hadrons produced in NC interactions can fake a $\tau \rightarrow h$ decay topology. However, in these events the mean missing transverse momentum is higher than in ν_τ CC interactions and its determination can be used to discriminate the two reactions.

The momentum of all charged particles emitted at the primary neutrino vertex is measured as previously described. The converted γ's from π^0 decays can be detected as shown in the example of Fig. 127. Most of the electrons from γ conversion have an energy below 500 MeV (Fig. 125). The measurement of the multiple scattering of low energy electrons in only 5 films leads to a $\delta p/p \sim 0.3$. A similar resolution is obtained by the base track counting method described in Section 6.7. The optimal way to combine the two methods will be studied in order to improve the energy resolution.

The $\tau \rightarrow \rho\nu$ channel has a 27% decay branching ratio. The ρ is identified by detecting the two γ's and reconstructing the ρ mass from the measured momenta of π and γ's. One has to distinguish whether the observed γ's are produced at the neutrino interaction vertex or at the τ decay vertex. A Monte Carlo

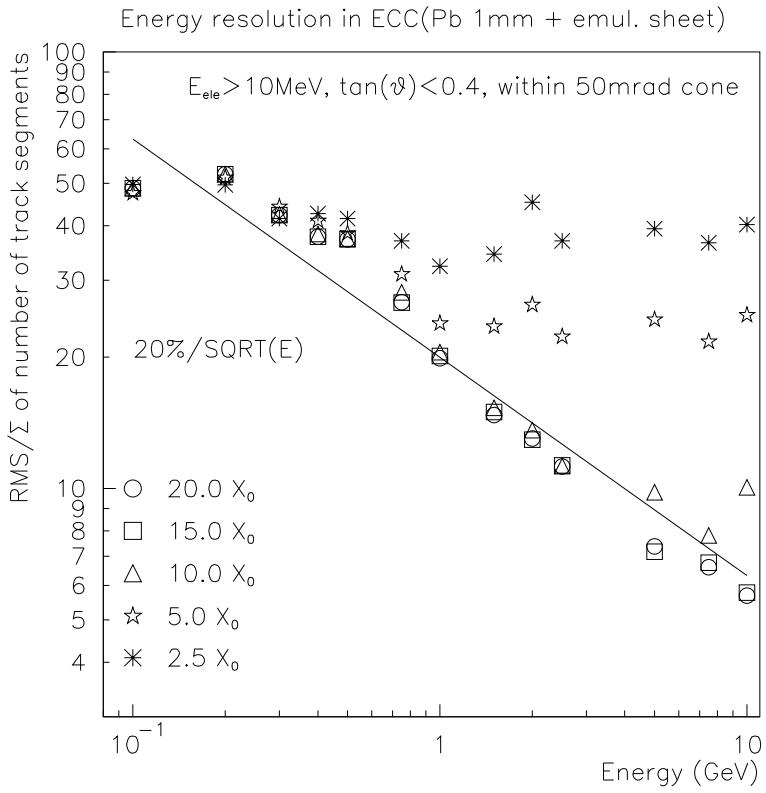

Figure 124: Energy resolution for electrons as obtained by Monte Carlo. The energy is measured by simply counting the number of track segments produced in the electromagnetic shower induced by the electron.

study shows that about 40% of the γ's from ρ can be unambiguously distinguished from those produced at the primary interaction (see Fig. 126).

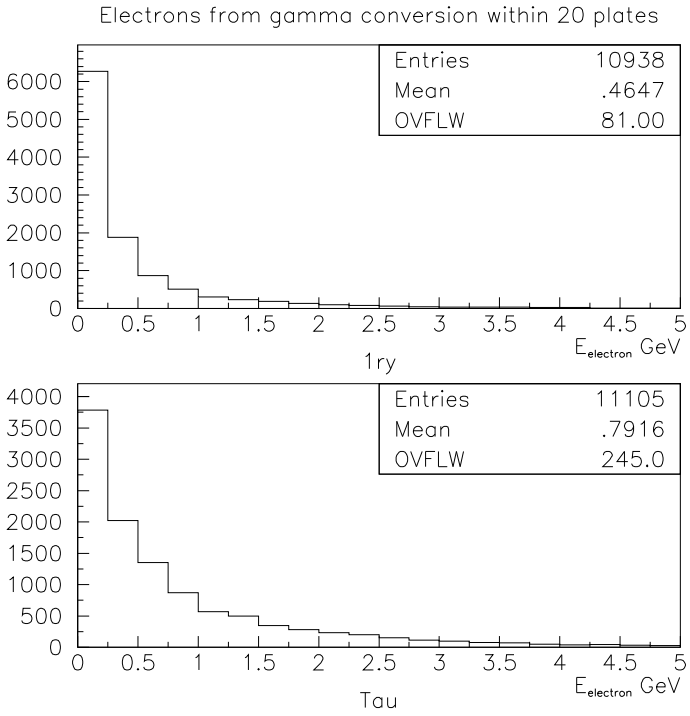

Figure 125: Energy distribution of electrons created by γ conversion.

6.9 Low momentum muon identification

The method of identifying particles by observing their energy loss in the non-relativistic regime when they are about to stop is well established [76]. In this regime, the energy loss rate is given by $I = dE/dx = k/\beta^2$. Using $E = M\beta^2/2$, one can derive $M = (4/k)I^2x$. Therefore, the particle mass can be inferred by measuring I at a distance x from the stopping position. The error on the mass δM is then $(\delta M/M)^2 = (2\delta I/I)^2 + (\delta x/x)^2$.

When a particle stops in a brick, $\delta I/I$ is the dominant component of the error on its mass. The number of grains in the emulsions per unit length (grain density) is related to I. Fluctuation of the grain density amounts to about $(30 \pm \sqrt{30})/100\ \mu m$. One can then obtain $\delta I/I \sim 0.18$ by only measuring one emulsion film of the brick.

Muons and pions are expected to travel through about 10 films after entering in their non relativistic regime. With 10 independent measurements of I, a $\delta M/M = 0.12$ is achievable, corresponding to $\delta M = 16\ MeV$ for a pion. The value of δM can be used to separate muons from pions, with $M_\pi - M_\mu = 34\ MeV/c^2$. A test experiment is planned to confirm the feasibility of this method in the case of OPERA.

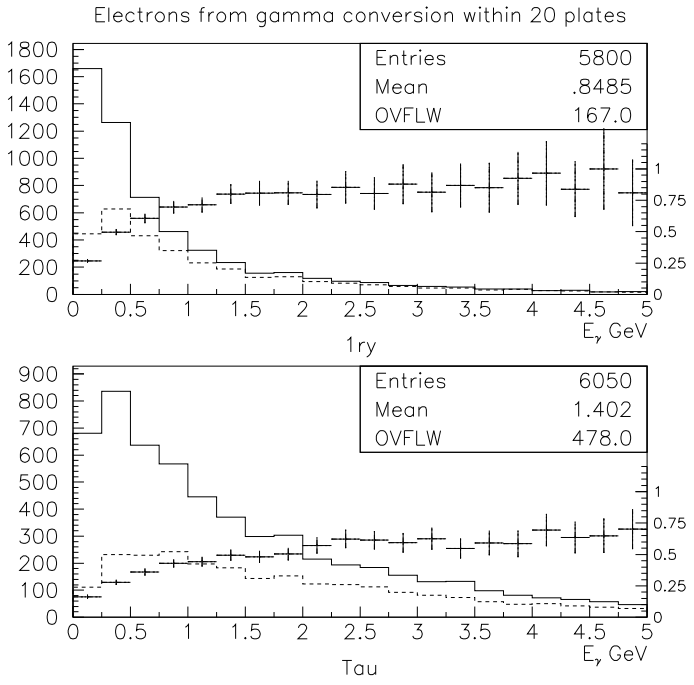

Figure 126: Efficiency for γ's to convert into electron pairs correctly attached to their origin. Top: γ's from the primary vertex; Bottom: γ's from $\tau \to \rho\nu$ *long* decay vertex. The solid lines show the γ energy distribution. The dashed lines show the energy distribution of γ's unambiguously attached to their origin.

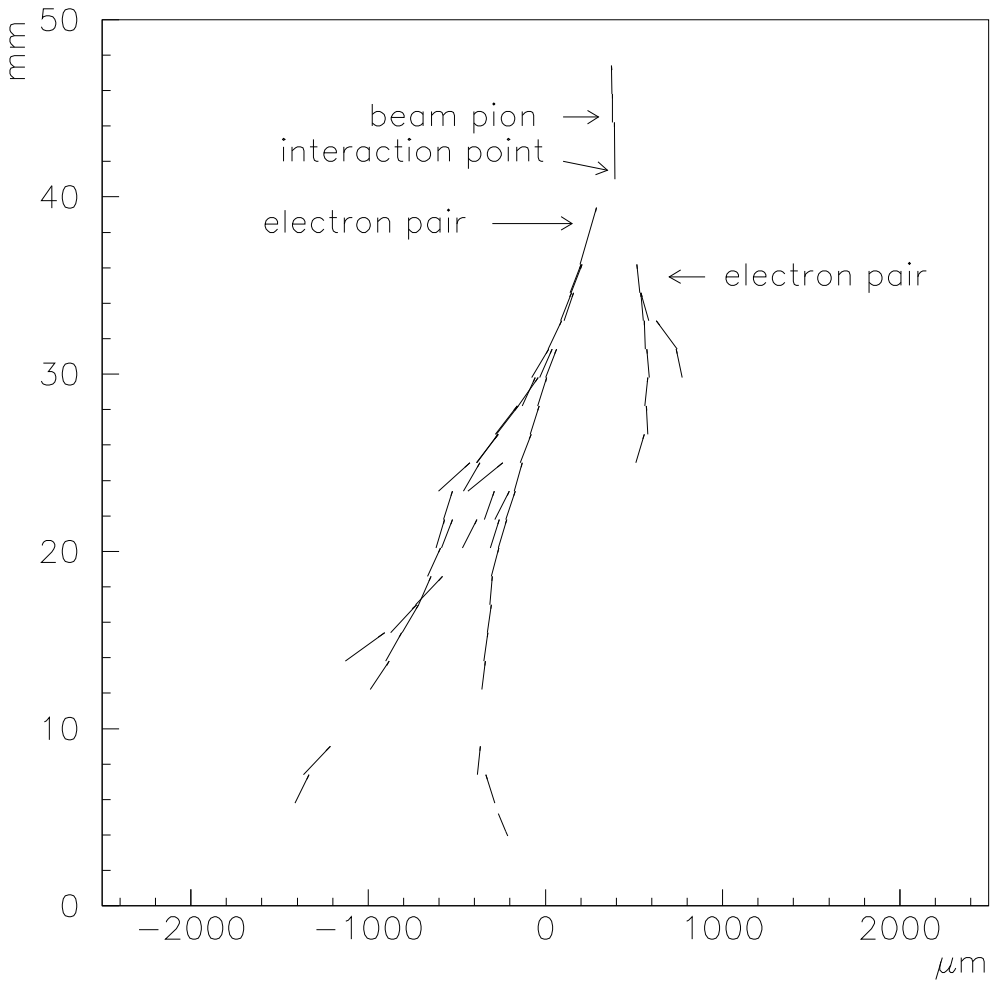

Figure 127: A $\pi^0 \to 2\gamma$ decay observed in a test experiment using a 8 GeV/c pion beam. The track of an interacting π disappears after traversing three emulsion films. Two electromagnetic showers are initiated 2 and 3 films downstream of the π interaction point, respectively. The measured invariant mass of the two γ's is (157 ± 24) MeV/c^2.

7 Physics performance

7.1 Electron identification efficiency

A method for electron identification has been presented in Section 6.7. The performance of the algorithm was studied by simulated electrons and pions with energy in the range from 1 GeV to 11 GeV with a distribution of the longitudinal vertex position in the brick according to the material distribution. The vertex position in the transverse plane is at the centre of the brick. Edge effects in the transverse plane have been studied separately.

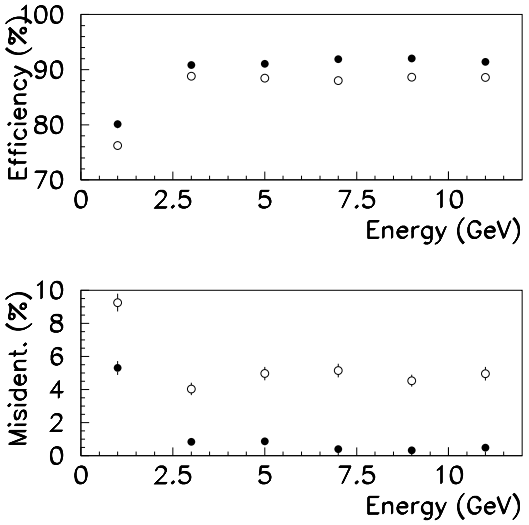

Figure 128: Efficiency and misidentification probability averaged over the longitudinal brick thickness for pions (full circles) and electrons (open circles) as a function of the energy.

Fig. 128 shows the efficiency for correct identification of electrons and pions as well as the misidentification probability, averaged over the longitudinal brick thickness. In Fig. 129 these quantities are given for 1 GeV and 11 GeV electrons as a function of the longitudinal position of the vertex in the brick. A few X_0 are adequate for electron identification.

The total length of the tracks in an electromagnetic shower is proportional to the energy of the parent particle. Therefore, by counting the number of segments inside the cone defined in Section 6.7.2 it is possible to measure the energy of the electron. Monte Carlo simulations show that for electrons with energy below 1 GeV the energy resolution is $\Delta E/E = 30\%$, while for higher energies one obtains $\Delta E/E = 20\%$.

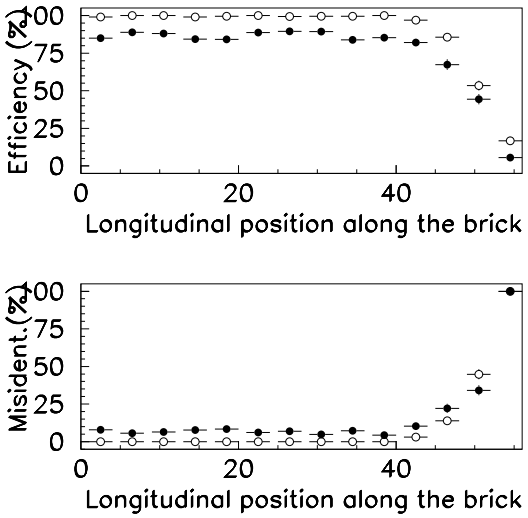

Figure 129: Efficiency and misidentification probability for 1 GeV (full circles) and 11 GeV (open circles) electrons as a function of the longitudinal position of the vertex in the brick. The abscissa gives the number of lead plates which are traversed. Each bin is the average over four adjacent lead plates. The first bin corresponds to the average of the most upstream four plates of the brick.

7.2 Muon identification efficiency

Adequate muon identification efficiency is needed for the selection of $\tau \rightarrow \mu$ decays. As already discussed in Section 4, the muon identification is also an important issue for background reduction since single charm production only occurs in CC neutrino interactions. If the primary muon is identified charm decay does not constitute a background to τ decays.

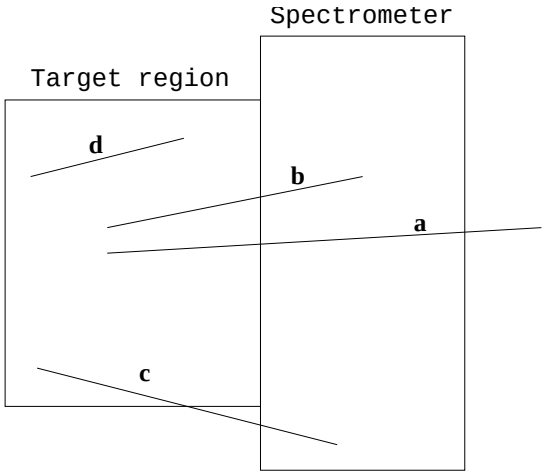

Figure 130: Different muon topologies.

Muon identification is performed by the target trackers, the muon spectrometers and the emulsions themselves.

Possible muon topologies are shown schematically in Fig. 130. Averaging over the full supermodule 82.4% of the primary muons from charm events cross the spectrometer (a) and 11.3% stop inside it (b). Among the muons stopping in the spectrometer, 10.3% leave the target from its last wall and 1% leave the target from the sides (c) but are in the acceptance of the spectrometer. The other muons (6.3%) stop in the target before reaching the spectrometer (d) or, in a small fraction, exit from the sides of the target without reaching the spectrometer. Muons which traverse completely the spectrometer (a) have an identification efficiency of nearly 100%.

The muon identification algorithms combine the 3D track information from the emulsion films with the signals from the downstream electronic trackers in the target and in the spectrometer. The pattern recognition algorithm (described in Section 5.4) is applied to the hits in the target and in the spectrometer to reconstruct tracks independently in the two projections. The muon identification algorithm is based on the track range and on the event topology

1. the longest track is selected as a muon candidate;
2. if this track exits from the back of the spectrometer it is identified as a muon;
3. if this track stops before the end of the spectrometer, it is identified as a muon if it traverses at least 10 target walls or spectrometer iron plates and if it satisfies isolation cuts defined in the following.

The isolation cuts makes use of the fact that hadron tracks are usually embedded in a hadronic shower, while the muon track tends to be more isolated. For each plane one computes the distance between the hit belonging to the candidate muon track and the position of the centroid of all the other hits. Excluding the first 3 planes after the vertex, the average of this distance is taken as the first discriminating variable between muons and hadrons.

The second variable is the number of planes containing no other hits than the one belonging to the track. Tracks for which the average distance from the plane centroid is larger than 20 cm or the number of planes on which they are isolated is higher than 6 are identified as muons (Fig. 131).

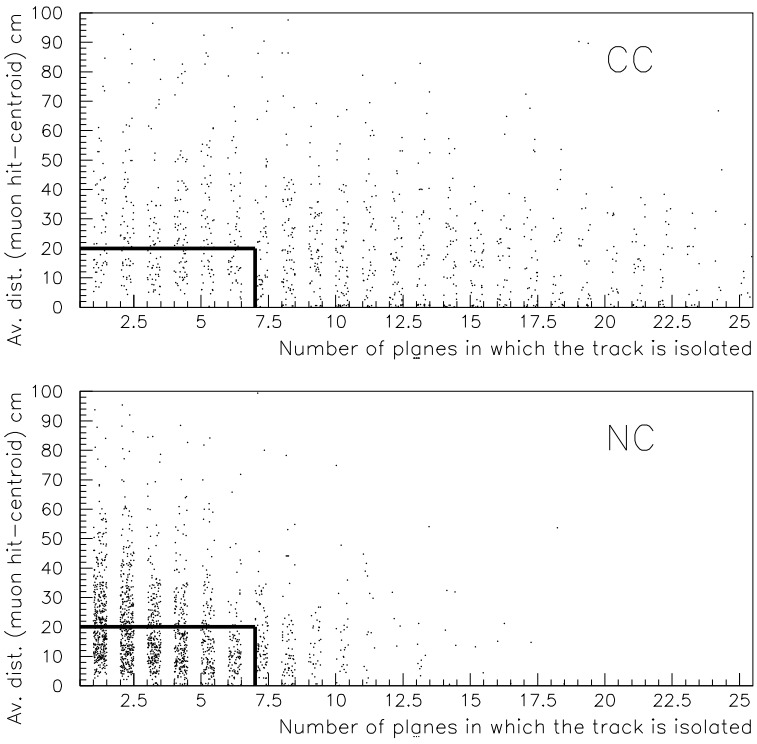

Figure 131: Effect of the topological cut on events with the longest track longer than 10 hits but not reaching the end of the spectrometer for ν_μ CC and NC events. The events falling in the box are classified as NC.

The combination of range and topology cuts on the longest track in the event results in the efficiencies shown in Table 13. These efficiencies are calculated on unbiased samples of events before the application of any other analysis cut. In the complete analysis, the muon identification efficiencies are generally higher, because low energy events are rejected by other cuts.

In order to increase the identification efficiency for low momentum muons one can also use a method

Table 13: Muon identification efficiencies for various event samples.

Sample	Muon id. efficiency (%)
Charm (excluding muonic decays)	94.8
Charm (muonic decays)	96.4
ν_μ CC	94.7
ν_μ QE	98.2
$\tau \to \mu$ DIS	85.4
$\tau \to \mu$ QE	88.2

based on momentum-range consistency. The momentum of the muon candidate determined by measuring the multiple scattering in the brick cells is compared with the one estimated by range. This method is currently under study.

Muons are then matched to the tracks measured in the emulsion films, either at the primary vertex or at the decay vertex. Events containing a track identified as a muon but not matching any emulsion track are also rejected from the ν_τ candidate sample.

7.3 τ detection efficiency

The τ detection efficiency has been estimated by simulations which take into account the experience gathered with CHORUS and DONUT as well as with test measurements. In the kinematical range of interest for the experiment the efficiency mildly depends on the event kinematics and therefore on the oscillation parameters. The following estimates are calculated for $\Delta m^2 = 10^{-3}\ eV^2$ and for full mixing.

A flow diagram of the analysis chain to search for ν_τ events is shown in Fig. 132. The first two steps fully rely on the electronic detectors in order to select neutrino interactions and to locate the brick where the interaction took place (see Sections 7.3.1).

The next step consists of finding the neutrino interaction vertex by scanning the emulsion films (see Sections 7.3.2 and 7.3.3). After vertex finding, all tracks attached to the primary vertex are reconstructed. Particle identification as well as momentum measurement are performed according to the methods described in Sections 6.6 and 6.7.

A minimum amount of traversed X_0 (see Sections 6.6 and 6.7) is needed in order to have adequate momentum (energy) resolution and identification efficiency. Tracks which leave the brick from the side or downstream having traversed an insufficient amount of material have to be followed in the adjacent and/or downstream bricks. In Section 7.3.4 we describe how the brick-to-brick connection is performed and we give the connection efficiency as a function of the particle type and momentum.

If a track attached to the primary vertex is identified as an electron or a muon, the event is classified as a CC event with charm production and rejected, even if a kink is detected.

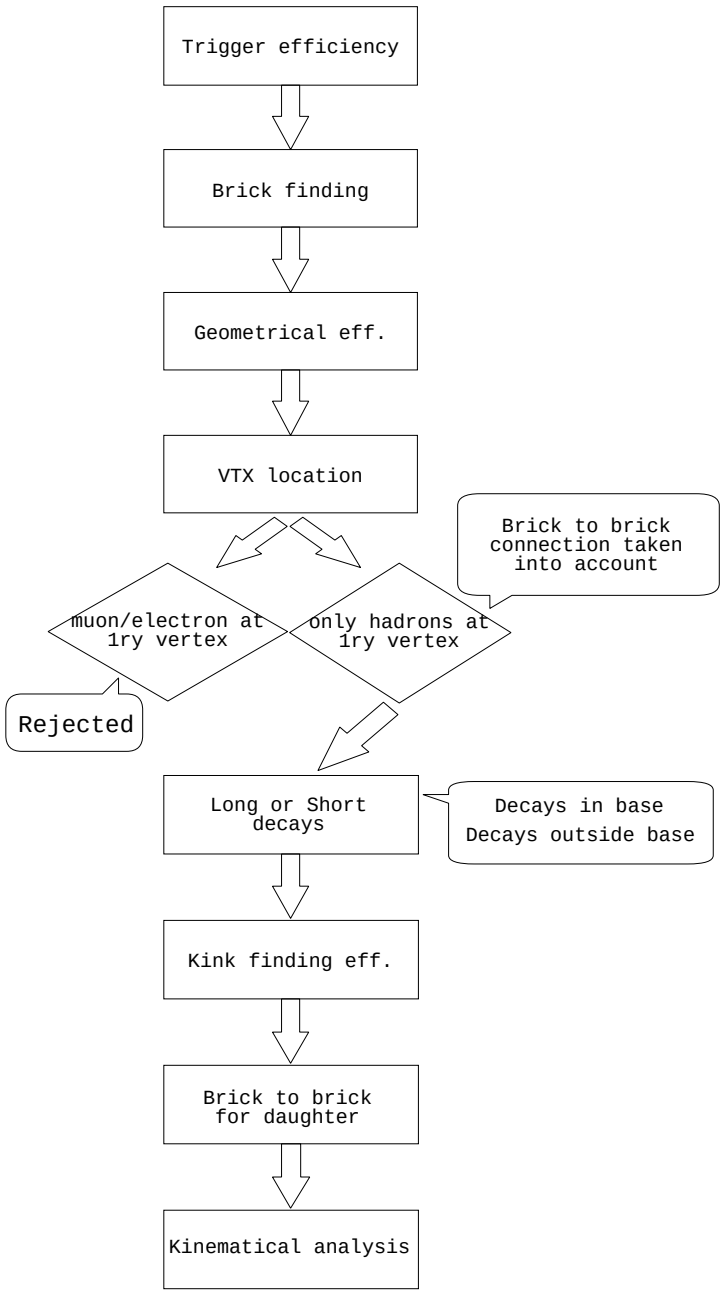

Figure 132: Flow diagram of the analysis chain to search for ν_τ induced events.

Table 14: Brick finding efficiency for the different decay channels.

Int.	$\tau \rightarrow e$ (%)	$\tau \rightarrow \mu$ (%)	$\tau \rightarrow h$ (%)
DIS	79.4	73.5	76.0
QE	81.4	72.1	74.0

For events surviving the above cuts a decay search inside the *decay volume* is applied and tracks at the primary vertex are carefully measured for kinematical analyses (see Sections 7.3.6 7.3.8, 7.3.9 and 7.3.10).

7.3.1 Trigger and brick finding efficiency

The neutrino interaction trigger and the brick location are based on the information from the target electronic trackers.

The trigger logic requires a minimum number of hit modules with a minimum deposited energy. At least two modules with both $X-Z$ and $Y-Z$ hit strips with one or more *p.e.* per projection are required. When this condition is not fulfilled, at least one module with at least five photoelectrons per view is required. This last condition allows to trigger on QE ν_τ events with an electron decay for which the electromagnetic shower is contained within the wall downstream of the vertex module. Simulations show that the trigger efficiency ($\varepsilon_{trigger}$) is above 99% for all event categories.

An experimental cross-check of the trigger efficiency for QE $\tau \rightarrow e$ events was performed by using test measurement data (Section 8.2.2). Given the 4.7 GeV average energy of the daughter electrons from QE $\tau \rightarrow e$ events, Fig. 158(c) indicates that the Monte Carlo result ($\varepsilon_{trigger} = 99\%$) is consistent with data ($\varepsilon_{trigger} > 98\%$).

Brick finding algorithms and efficiencies have been described in details in Section 5.5. Awaiting further studies and an optimisation of the brick removal strategy, here we consider the simplest case in which only one brick is removed per event. The corresponding brick finding efficiencies (including wall finding efficiencies) for τ events are reported in Table 14.

7.3.2 Geometrical efficiency

The geometrical efficiency (ε_{geom}) includes all losses due to edge effects in the bricks. Test measurements show that emulsion films can be scanned up to 200 μm from the edges (see Section 4.2.2). In the following, it is assumed that tracks can be reconstructed up to 1 mm from the emulsion edge. Edge effects are independent of the specific decay channel and cause a fiducial volume inefficiency of about 3.5%. Losses due to τ decays outside the brick are negligible (less than 1%), because of the special most downstream cell in the bricks, which consists of two emulsion films separated by a plastic spacer.

Events occurring in the last wall of a supermodule or at its outer boundaries have a lower efficiency for particle identification and momentum measurement. This leads to an additional volume loss of about 2.5%.

Table 15: Vertex finding efficiencies for different channels as obtained by Monte Carlo simulations. The overall efficiencies are averaged over the longitudinal vertex position. The numbers within brackets refer to results obtainable with the special procedure reported in Section 6.7.

Int.	$\tau \to e$ (%)	$\tau \to \mu$ (%)	$\tau \to h$ (%)	ν_μ CC (%)	ν_μ NC (%)
DIS	77.8 (86.6)	95.8	94.7	98.6	85.9
QE	34.7 (60.0)	87.0	82.6	99.1	-

The overall geometrical efficiency due to emulsion edges and overall fiducial volume effects amounts to 94% and it is common to all τ channels.

Other sources of geometrical inefficiency depend on the particular τ decay mode and are related to the kinematical analysis. They originate from losses in connecting two bricks to perform the momentum measurement by multiple scattering, electron identification, etc. This contribution is evaluated separately for each decay channel and discussed later.

7.3.3 Vertex finding efficiency

Once the brick where the neutrino interacted has been identified, the scanning proceeds according to the methods discussed in Section 6. We have estimated the vertex finding efficiency (ε_{vert}) by Monte Carlo simulations driven by real data and by directly using CHORUS and DONUT data.

The experimentally measured quantities related to the scanning (S-UTS track finding efficiency and angular acceptance, plate to plate connection) are taken into account in the Monte Carlo, whereas the presence of possible background tracks is not. Due to hadronic reinteractions and to electron energy losses, ε_{vert} is a function of the longitudinal position of the vertex in the brick as shown in Fig. 133. The results averaged over the brick thickness are summarised in Table 15.

The vertex finding efficiency for the electron channel is lower than for other decay modes due to the higher probability for an electron to induce an electromagnetic shower in the 10 X_0 thick brick. By using the procedure described in Section 6.3 one can substantially increase ε_{vert} for the $\tau \to e$ channel for both DIS and QE events. The results obtained with this method are also reported in Table 15.

Two analyses employing real neutrino data have been performed to check the above results and to give an experimental estimate of ϵ_{vert}.

The first analysis makes use of the CHORUS data. Given the detector target mass and the total number of neutrino interactions, ~ 3.6 neutrino events are expected per cubic centimetre of CHORUS emulsions. About 24 cm^3 of these emulsions were fully scanned (*minimum bias* volume scanning) with an UTS scanning system. One would then expect 85 neutrino interaction vertices to be located in the scanned volume, to be compared with 91 identified primary vertices. This result can be translated into a lower limit for the vertex finding efficiency ($\epsilon_{vert} > 90\%$ at the 90% CL), which is consistent with the Monte Carlo simulations.

The second result is obtained from the DONUT ECC data [42]. The DONUT vertex finding efficiency is about 58%, indicating an efficiency substantially lower than in the estimates and CHORUS results given above. However, one should note that the limited scanning area ($5 \times 5\ mm^2$) analysed with the current scanning power is not sufficient to obtain 100% coverage of the volume where the vertex could be situated. Furthermore, DONUT has a more than two orders of magnitude higher track density than expected in the OPERA emulsion films.

In conclusion, the vertex location efficiencies given in Table 15 and their dependence on the neutrino energy as given in Fig. 133 are assumed for the different τ decay channels.

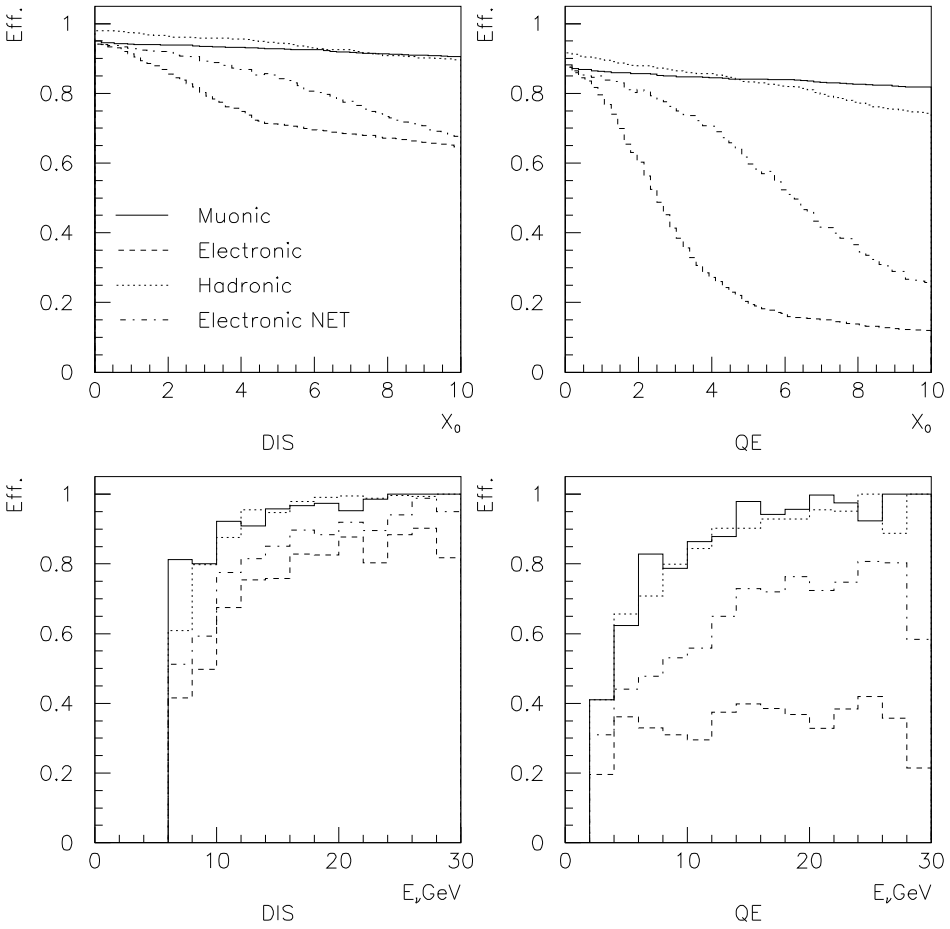

Figure 133: Vertex finding efficiency as a function of the vertex position inside the brick and of the neutrino energy, as estimated by Monte Carlo simulations.

7.3.4 Brick-to-brick connection

The brick-to-brick connection is needed to fully exploit the possibility of a kinematical event analysis. About 5 X_0 are needed in order to have sufficient resolution for the measurement of the momentum by multiple scattering and efficiency for electron identification. Therefore, one sometimes needs to search for a track in the brick downstream or adjacent to the vertex one. The connection is not really crucial for the electron energy measurement. In fact, the counting of all segments inside the cone described in Sections 6.7 and 7.1 is sufficient to measure the energy of an electromagnetic shower.

The brick-to-brick connection efficiency has been studied by means of a full Monte Carlo simulation which takes into account the material between bricks both in the longitudinal and in the transverse directions. We have assumed that emulsion films can be efficiently scanned up to 1 mm from the edge. This value is critical for connection to side bricks.

All track segments in two different bricks which are within 5 mm from the extrapolated position and which differ from the original direction by less than 100 $mrad$ in space are considered as *connected* into a single track. The brick connection procedure is similar to the one adopted in CHORUS to search in the Special Sheet (SS) for tracks previously found in the Changeable Sheets (CS) which are situated downstream of the SS [7]. In CHORUS the motivation for the SS-CS gap was to have sufficient opening between the tracks to be reconstructed by the electronic trackers, which are close to the CS. The distance SS-CS is 51.8 mm, while in OPERA the brick-to-brick distance is ~ 44 mm.

In order to find in the emulsions a given track reconstructed by the electronic detectors a low background track density is needed. This requirement was fulfilled in CHORUS by replacing the CS every 3 weeks, contrarily to the SS and to the *bulk* emulsion which were always in place during the run. In this respect, OPERA is an ideal detector, the expected background track density being very low.

The brick-to-brick connection efficiency (ε_{b2b}) is parametrised as a function of the momentum at the exit of the brick and by considering two types of tracks (leaving the brick from downstream and from the side) and three types of particles (electron, muon and hadron). Fig. 134 shows the brick connection efficiency as a function of the momentum at the exit point from the brick.

7.3.5 Detection of a fake lepton at the primary vertex

After determination of the vertex position the presence of a lepton (either an electron or a muon) is searched for. An efficient identification of the primary lepton is crucial in order to reduce the background from charm production. In the following we denote as $\varepsilon_{fake-e(\mu)}$ the probability for a hadron at the primary vertex to be identified as an electron (muon).

The electron identification algorithm described in Sections 6.7 and 7.1 is applied to each track attached to the primary vertex. Because of the low efficiency of the algorithm for soft particles, one only considers tracks with measured momentum above 2 GeV/c. Studies performed with simulated events show that, due to hadron tracks misidentified as electrons, about 3% of the τ produced in DIS interactions are classified as background and rejected. For QE interactions no signal events are rejected.

Taking into account the bias due to the brick finding efficiency and to the vertex location, the muon identification algorithm described in Section 7.2 gives a probability of about 10% to detect a fake μ in

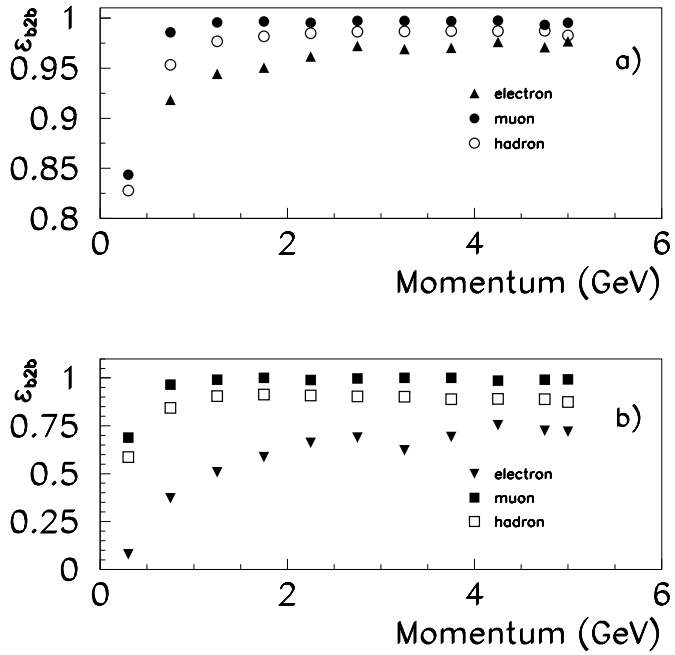

Figure 134: Brick-to-brick connection efficiency for particles leaving the brick downstream a) and leaving the brick from the side b), according to Monte Carlo simulation.

ν_μ NC, in DIS $\tau \to e$ and in $\tau \to h$ and of 4% in DIS $\tau \to \mu$ events. Studies are in progress in order to improve the purity of the muon identification algorithm.

7.3.6 Short and long kink events

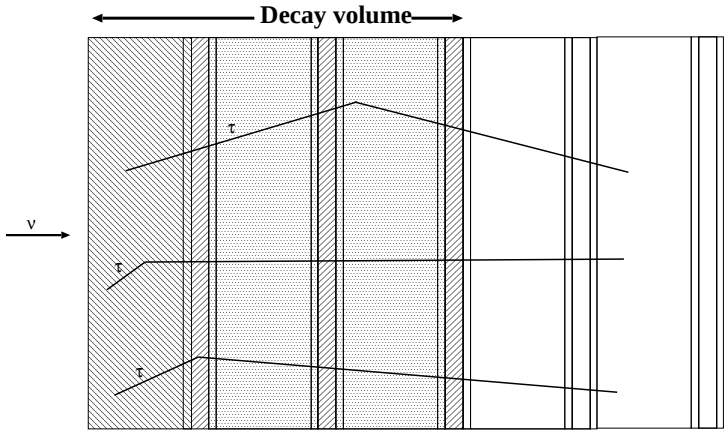

Figure 135: Different decay topologies: *short decays* (left-hatched region); *long decays in base* (right-hatched region); *long decays outside the base* (shaded region); *very long decays* (white region), not shown.

The decays inside an ECC brick can be classified into four categories as shown in Fig. 135

- *short decays*. These are decays occurring inside the lead plate in which the interaction occurred;
- *long decays in the base*. These decays occur in the base of the emulsion film;
- *long decays outside the base*;
- *very long decays*. These decays occur outside the decay volume and are not shown in Fig. 135.

The fractions of τ decays occurring in the various elements of the cells downstream of the vertex plate are given in Fig. 136. The total fraction of long (in the base or outside the base) and short decays are $\varepsilon_{long} \simeq 39\%$ and $\varepsilon_{short} \simeq 60\%$, respectively. If one considered a third lead plate in the long kink sample, the signal would increase by only $\sim 1\%$, whereas the background would increase by about 50%. Unless otherwise specified in the text, the decay is meant to be long.

The criterion used to select a kink candidate is independent of the τ decay channel, but it depends on where the decay occurs. For long decays, τ candidates are searched for by measuring the kink angle in space and taking into account the worse angular resolution for decays in the base. For short decays an impact parameter method is applied. About 60% of the τ decays are short. However, the kink detection efficiency is rather small due to the strong cuts applied for background rejection (Sections 7.3.8, 7.3.9 and 7.3.10).

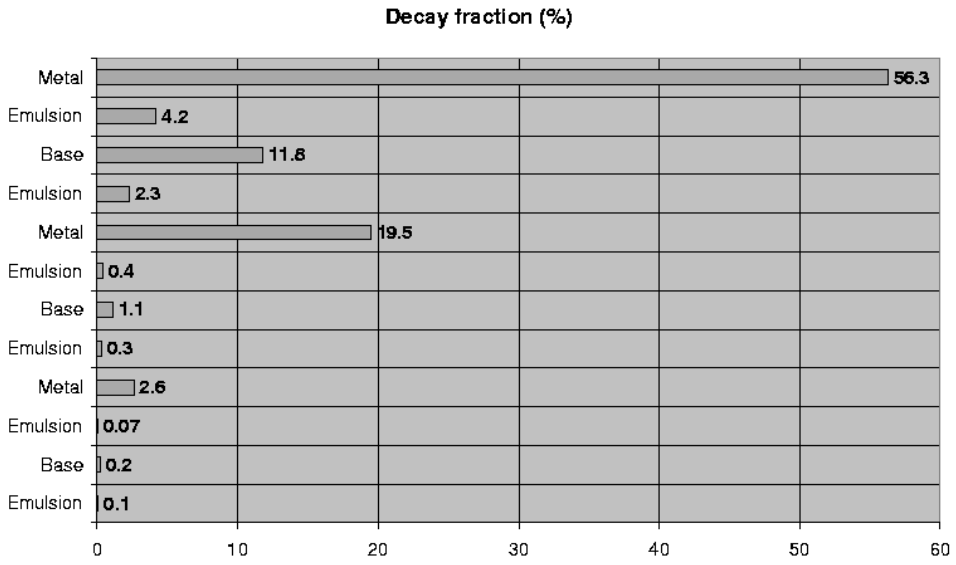

Figure 136: Distribution of τ decay in the vertex lead plate (short decays) and in the various elements of the cells downstream of the lead plate in which the ν_τ interaction occurred.

Table 16: ε_{kink} for the different τ decay channels.

Event	$\tau \to e$ (%)	$\tau \to h$ (%)	$\tau \to \mu$ (%)
DIS	88.2	90.2	89.8
QE	90.5	89.6	91.7

7.3.7 Kink detection efficiency for long decays

The inefficiency in the kink detection results from the need of rejecting small-angle and very large-angle kinks. The upper cut ($> 500\ mrad$) is motivated by considerations related to the scanning efficiency of the automatic microscopes, as shown in Fig. 105 for CHORUS data. The lower cut (20 $mrad$ in space) has been assigned taking into account that the OPERA background is presently estimated by using data down to such an angle. The excellent intrinsic angular resolution of the emulsion films used in OPERA (see Section 6) would allow a substantially looser cut. Nevertheless, awaiting background measurements extended to lower angles, we maintain the conservative 20 $mrad$ cut.

The kink finding efficiency (ε_{kink}) for the different τ decay channels is given in Table 16.

7.3.8 Detection efficiency for the e channel

If an event has been located and a decay topology has been detected, a *high resolution* scanning is applied on the daughter track in order to determine its identity and energy. These are essential ingredients to

efficiently discriminate between signal and background by means of kinematical criteria. Due to brick-to-brick connection inefficiency, $\sim 96\%$ of the electrons produced in τ decays can be fully measured.

In order to reduce the background from low energy electrons ($\gamma \rightarrow e^+e^-$) the τ daughter is required to have an energy higher than 1 GeV. This cut also allows to have a better electron identification (see Section 7.1). In addition, an upper cut (15 GeV) on the electron energy reduces the background from prompt electrons produced in ν_e CC interactions. The distribution of the τ daughter energy is shown in Fig. 137. The overall efficiency of the above energy cuts is $\varepsilon_E \sim 90\%$ for both DIS and QE events.

The distribution of the transverse momentum at the decay vertex (p_t) is shown in Fig. 137. A lower cut on p_t (ε_{p_t}) is applied in order to reduce the background from ν_e CC interactions (see Section 7.4.3). By requiring a p_t larger than 100 MeV/c, more than 99% of the $\tau \rightarrow e$ decays are kept while all candidates from ν_e CC events are rejected.

Finally, we determine the probability for an electron produced in a τ decay to be identified as such ($\varepsilon_{e \rightarrow e}$). Results for both DIS and QE events show that $\sim 97\%$ of the daughter electrons are identified as such, 1% as hadrons and 2% cannot be classified.

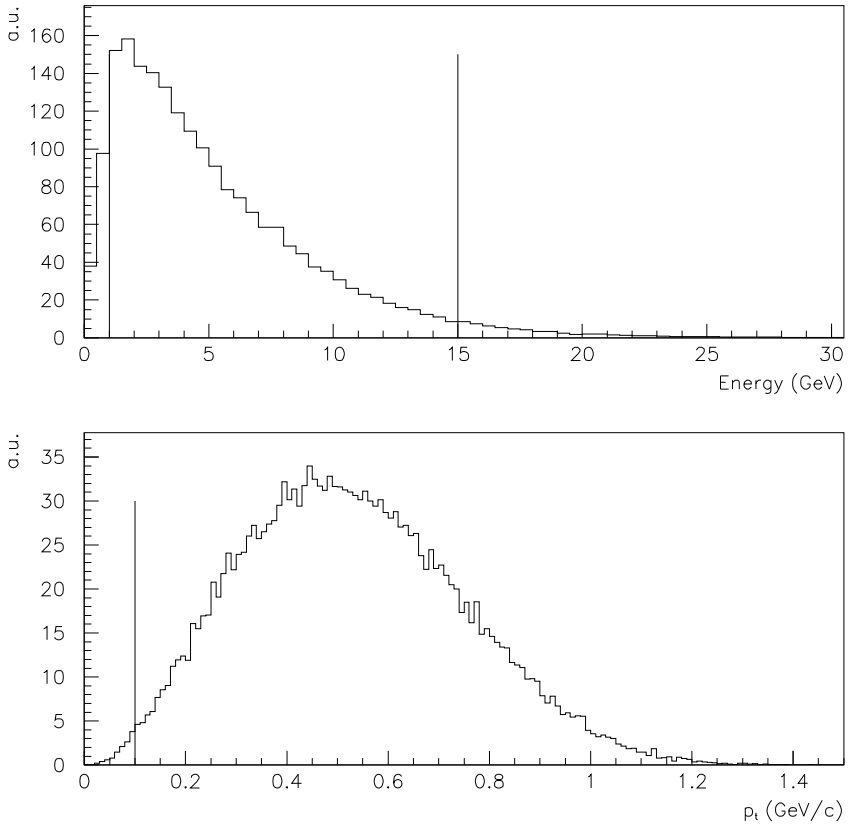

Figure 137: Distribution of the reconstructed τ daughter energy (top) and of the reconstructed transverse momentum at the decay vertex (bottom) for DIS $\tau \rightarrow e$ decays. Vertical lines show the applied cuts.

For long decays the overall efficiency of the kinematical analysis ($\varepsilon^L_{kin} = \varepsilon_{b2b} \times \varepsilon_E \times \varepsilon_{p_t} \times \varepsilon_{e\to e}$) is $\varepsilon^L_{kin} \simeq 83\%$ and $\varepsilon^L_{kin} \simeq 84\%$ for the DIS and QE samples, respectively.

In the case of short decays the τ cannot be detected by searching for a kink angle in space. Therefore, a method which relies on the detection of a large impact parameter of the τ daughter with respect to the primary vertex is used. To apply this method at least one track, besides the daughter one, has to be reconstructed. For this reason only DIS events are considered. We will study the possibility to recover some of the QE events.

Although short decays have essentially no charm background (see Section 7.4.2), some cuts must be applied in order to reduce the background from low energy tracks. Indeed, their scattering inside the lead could result in a large IP. Therefore, the particles giving rise to tracks used to compute the IP are required to have momentum larger than 1 GeV/c. The overall efficiency of this cut is $\varepsilon_{1ry} \simeq 66\%$.

An event is selected as a τ candidate if the electron track impact parameter is larger than a given value which depends on the vertex position inside the lead (ranging from 5 μm to 20 μm for the vertices in the most downstream or upstream part of the lead plate, respectively). The efficiency of this cut is $\varepsilon_{IP} \simeq 45\%$. An upper cut on the electron energy is applied as in the case of long decays with an efficiency $\varepsilon_E \simeq 79\%$.

A cut on the minimum transverse momentum at the decay vertex (p_t^{min}, see Fig. 138 for its definition) rejects background from ν_e CC interactions. By requiring $p_t^{min} > 50\ MeV/c$, $\sim 97\%$ of the decays are kept.

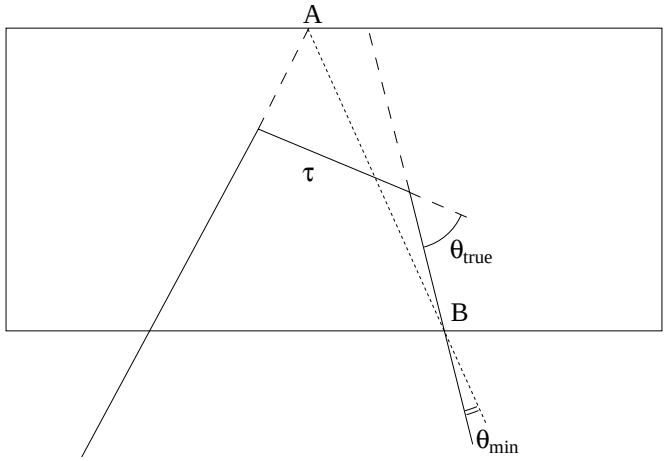

Figure 138: The p_t^{min} for short decays is defined as $p \times \theta_{min}$. θ_{min} is the minimum decay angle compatible with the observation of an IP. It coincides with θ_{true} if the interaction occurs in A and the decay in B.

The overall kinematical efficiency for DIS short decays is $\varepsilon^S_{kin} = \varepsilon_{1ry} \times \varepsilon_{IP} \times \varepsilon_E \times \varepsilon_{p_t^{min}} \times \varepsilon_{e\to e} \simeq 22\%$.

7.3.9 Detection efficiency for the μ channel

The detection strategy for $\tau \rightarrow \mu$ decays is similar to that of the electron channel.

In addition to the loss due to the muon identification, which amounts to $\sim 5\%$, one requires that the energy of the muon lies in the range $1 - 15\ GeV$. The lower cut allows to reject events for which the μ identification is poor and to reject possible background from low energy hadrons. The upper cut reduces ν_μ CC events by about 30% with a small loss of the signal. This selection reduces the background from scattering of a prompt muon in the lead (see Section 7.4.4). The total efficiency of the energy cut is $\varepsilon_E \sim 90\%$.

A cut on the p_t at the decay vertex is also applied. By requiring $p_t > 0.25\ GeV/c$ an efficiency for the signal $\varepsilon_{p_t} \sim 90\%$ is obtained.

We take into account the probability that the daughter muon identified in the electronic detector is not matched to the correct emulsion track. This results in an additional loss of about 10% ($\varepsilon_{\mu-match}$). The brick to brick connection does not play a crucial role in the $\tau \rightarrow \mu$ channel ($\varepsilon_{b2b} > 99.5\%$).

The efficiency of the kinematical analysis ($\varepsilon^L_{kin} = \varepsilon_{b2b} \times \varepsilon_E \times \varepsilon_{p_t} \times \varepsilon_{\mu\rightarrow\mu} \times \varepsilon_{\mu-match}$) for long decays is $\varepsilon^L_{kin} \sim 70\%$ for both DIS and QE events.

Presently, muonic short decays are not considered because of charm background. However, we are investigating the possibility of its rejection by kinematical criteria.

7.3.10 Detection efficiency for the h channel

The hadronic single-prong decays of the τ are selected among the events with no detected muon or electron daughter.

In order to keep the background for this channel as low as possible severe kinematical cuts are applied both at the decay and at the primary vertex.

The kinematical analysis at the decay vertex is qualitatively similar to that of the electronic and muonic channels. However, the cut applied on p_t is harder ($p_t > 600\ MeV/c$) and the daughter particle is required to have a momentum larger than $2\ GeV/c$. The p_t cut is justified by the relatively small $< p_t > (\lesssim 100\ MeV/c)$ in elastic or inelastic pion interactions, while the maximum p_t in hadronic τ decays is $\sim 900\ MeV/c$. The cut on the daughter momentum eliminates low energy hadrons which are copiously produced in ν_μ CC interactions.

The kinematical analysis at the primary vertex uses the variables p_t^{miss}, defined as the missing transverse momentum at the primary vertex, and ϕ, which is the angle in the transverse plane between the parent track and the shower direction. The p_t^{miss} and ϕ distributions both for the signal and the background are shown in Fig. 139.

Due to the unobserved outgoing neutrino, p_t^{miss} is expected to be large in NC interactions. Conversely, it is expected to be small in CC interactions. For τ candidates the measured p_t^{miss} is required to be lower than $1\ GeV/c$.

The ϕ angle is expected to peak at π, because the τ and the hadronic shower are back-to-back in the transverse plane. Conversely, in NC interactions the hadron faking a $\tau \rightarrow h$ decay is produced inside the hadronic shower. Therefore, ϕ peaks near 0. For τ candidates the ϕ angle is required to be larger than $\pi/2$.

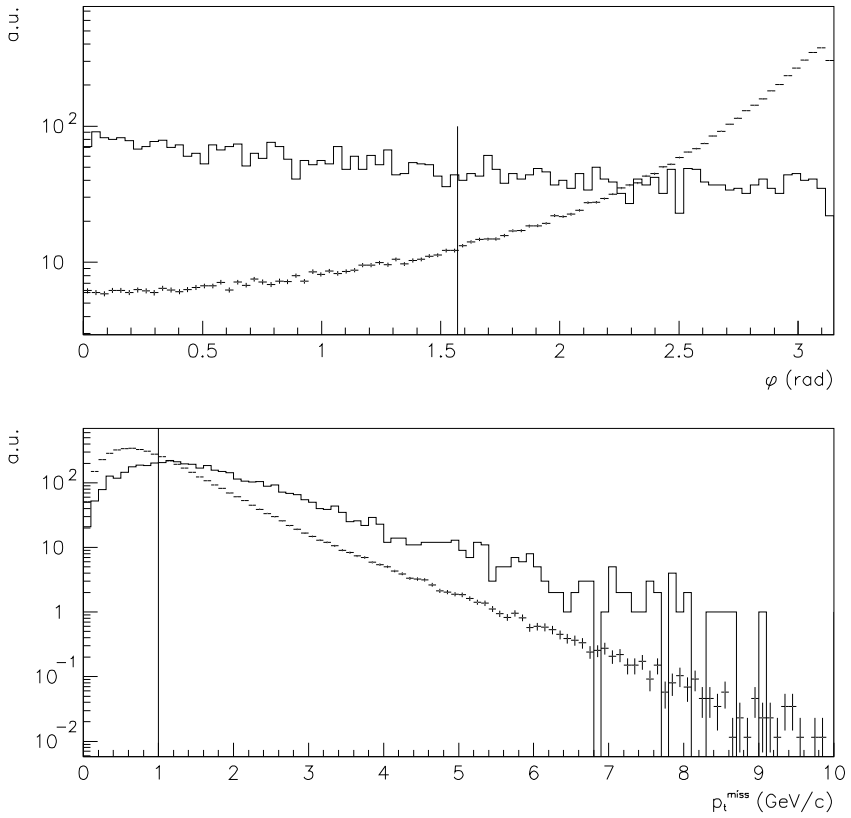

Figure 139: Distribution of the reconstructed ϕ angle (top) and of the reconstructed missing transverse momentum at the primary vertex (bottom) for DIS $\tau \rightarrow h$ decays (crosses) and ν_μ NC events (continuous histograms). The cuts applied are indicated as vertical lines.

The cuts on p_t^{miss} and ϕ can only be used if there is at least one fully measured track besides the candidate τ parent at the primary vertex. For this reason we split the $\tau \rightarrow h$ sample in two sub-samples

- *low multiplicity (LM)* events, in which only the parent track is measured. QE and low multiplicity DIS events belong to this sub-sample;
- *high multiplicity (HM)* events, in which at least another track besides the parent is fully measured.

For LM events the kinematical analysis at the primary vertex cannot be applied. Table 17 shows the relative fractions of LM (f_{LM}) and HM (f_{HM}) events for both DIS and QE events.

Table 17: Low and high multiplicity fractions for both DIS and QE events.

Event	f_{LM} (%)	f_{HM} (%)
DIS	7.9	92.1
QE	38.8	61.2

Table 18: Summary of all the efficiencies which contribute to ε_{kin}^{L} for both DIS and QE events.

Event	ε_{b2b} (%)	ε_{p} (%)	ε_{p_t} (%)	$\varepsilon_{p_t^{miss}+\phi}$ (%)	$\varepsilon_{h\rightarrow h}$ (%)
DIS (HM)	98.7	71.2	44.4	64.9	97.7
DIS (LM)	98.7	71.2	44.4	-	98.2
QE (HM)	98.8	73.3	47.5	73.0	97.6
QE (LM)	98.8	73.3	47.5	-	97.9

The overall efficiency of the kinematical analysis for long decays can be written as $\varepsilon_{kin}^{L} = \varepsilon_{b2b} \times \varepsilon_{E} \times \varepsilon_{p_t} \times (f_{LM} \times \varepsilon_{h\rightarrow h} + f_{HM} \times \varepsilon_{p_t^{miss}+\phi} \times \varepsilon_{h\rightarrow h})$ and it amounts to about 20% and 28% for DIS and QE events, respectively. All the terms which contribute to ε_{kin}^{L} are given in Table 18.

The hadronic single-prong decays of the τ can be split into two sub-samples: $\tau \rightarrow \pi\nu_{\tau}$ and $\tau \rightarrow \rho\nu_{\tau}$. The first one is a pure two body decay, while the second one appears in the final state as a three body decay (the ρ immediately decays into $\pi\pi^0$). If only charged particles are used to compute the p_t the efficiency for the $\tau \rightarrow \rho$ channel is much lower than for the pure two body decay. In these calculations we assume that the π^0 from ρ decay is not measured at all. Studies are in progress in order to include the π^0 in the kinematical analysis of the $\tau \rightarrow \rho$ channel (Section 6.8).

Due to the less favourable signal to noise ratio, we do not include short decays for the evaluation of the sensitivity of the experiment. However, we evaluate efficiency and background since these events can be used for special studies. As in the case of the electron channel, only DIS events are considered to search for short τ decays. We will study the possibility to recover some of the QE events.

For short decays the hadronic reinteraction background is by a factor of 4 smaller than for long decays, due to shorter path length in lead (on average, 0.5 mm for short decays, 2 mm for long decays). Nevertheless, with the impact parameter method, severe cuts must be applied in order to keep the reinteraction background as low as possible.

The daughter track and at least two primary tracks with momentum greater than 1 GeV/c are required. Furthermore, the space angle between the two primary tracks must be larger than 50 $mrad$ and at least one track slope should be smaller than 200 $mrad$. This allows to determine the neutrino interaction vertex position in the lead plate with good accuracy (~ 1 μm).

A τ candidate is selected if the impact parameter of the daughter track with respect to the measured primary vertex is larger than a given value which depends on the vertex position inside the lead (from 10 μm to 30 μm if the vertex is in the most downstream or upstream part of the lead, respectively).

Table 19: Summary of the kinematical efficiencies for different τ decay modes, topologies (long and short) and type of events (DIS and QE). The value given in brackets does not contribute to the sensitivity evaluation.

Decay mode	$\varepsilon^L_{kin}(DIS)(\%)$	$\varepsilon^L_{kin}(QE)(\%)$	$\varepsilon^S_{kin}(DIS)(\%)$
$\tau \to e^-$	83	84	22
$\tau \to \mu^-$	78	76	-
$\tau \to h^-$	20	28	(2.9)

Once a τ candidate is selected a kinematical analysis is performed in order to further reduce the background. The background from hadron reinteractions is efficiently reduced by applying a cut on p_t^{min}, which is required to be larger than 300 MeV/c.

The overall kinematical efficiency for $\tau \to h$ short decays is $\varepsilon^S_{kin} = \varepsilon_{1ry} \times \varepsilon_\theta \times \varepsilon_{IP} \times \varepsilon_{p_t^{min}} \simeq 2.9\%$.

7.3.11 Overall detection efficiency

One can now evaluate the overall signal detection efficiency for long and short decays for all the channels and for both DIS and QE events. The kinematical efficiencies for all the channels are summarised in Table 19.

For a given channel the overall τ detection efficiency for long and short decays can be written as

$$\varepsilon^L_{TOT} = \varepsilon_{trigger} \times \varepsilon_{brick} \times \varepsilon_{geom} \times \varepsilon_{vert} \times (1 - \varepsilon_{fake-e(\mu)}) \times \varepsilon_{long} \times \varepsilon_{kink} \times \varepsilon^L_{kin} \times BR$$

$$\varepsilon^S_{TOT} = \varepsilon_{trigger} \times \varepsilon_{brick} \times \varepsilon_{geom} \times \varepsilon_{vert} \times (1 - \varepsilon_{fake-e(\mu)}) \times \varepsilon_{short} \times \varepsilon^S_{kin} \times BR$$

By multiplying all factors and accounting for DIS and QE interactions, one obtains the efficiencies given in Table 20. A 15% uncertainty is assumed for the evaluation of the sensitivity to oscillations. The main contribution is due to the τ production cross section.

In [6] only long decays into leptons were considered for compact bricks, for a total efficiency of 5.6%. These efficiencies are confirmed by the present calculations. Short $\tau \to e$ decays and long hadronic decays are now included and a 8.7% total detection efficiency is reached.

7.4 Background

The background evaluation has been performed by means of a full simulation which includes the beam properties, the physics processes and the detector structure. Background sources are

- prompt ν_τ production in the primary proton target and in the beam dump;
- one-prong decay of charmed particles;

Table 20: Summary of the τ detection efficiency ($\times$ BR) for different τ decay modes, topologies (long and short) and type of events (DIS and QE). Hadronic short decay efficiencies (in bracket) are not accounted for.

Decay mode	DIS long (%)	QE long (%)	DIS short (%)	Total (%)
$\tau \to e^-$	3.0	2.6	1.3	3.7
$\tau \to \mu^-$	2.7	2.8	-	2.7
$\tau \to h^-$	2.2	2.8	(0.5)	2.3
Total	8.0	8.3	1.3	8.7

- background from π^0 and prompt electrons;
- large angle muon scattering;
- hadronic reinteractions.

The contribution of the above sources to the total background depends on the actual decay channel.

7.4.1 ν_τ prompt background

Prompt ν_τ originate from the decay of τ's produced in the CNGS target by the decay of D_s mesons. The rate of ν_τ production from the interaction of 450 GeV/c protons in a Be target and in the downstream beam dump has been evaluated in [77,78] for the CERN Wide Band Beam. These results must be scaled taking into account the features of the CNGS beam and the distance of the experiment from the source. Following the method of [77], we expect $\mathcal{O}(10^{-6}) \times N_{CC}$ ν_τ interactions, where N_{CC} is the total number of ν_μ CC events collected. If one also takes into account the detection efficiency, the contribution to the background is completely negligible.

7.4.2 Charm production and decay

Charmed particles are produced in CC and NC neutrino interactions through the reactions

$$a)\ \nu_\mu N \to c\,\mu X, \qquad b)\ \nu_\mu N \to c\bar{c}\,\mu X, \qquad c)\ \nu_\mu N \to c\bar{c}\,\nu_\mu X$$

Charmed mesons have masses and lifetimes similar to those of the τ. The above processes may thus constitute a background to the oscillation signal, if one fails to detect the primary muon (reaction a), the charm partner (reaction c) or both (reaction b).

The most relevant source is given by single charm production, *i.e.* reaction a. The corresponding background is evaluated here below.

In order to evaluate the expected charm background we must take into account the theoretical uncertainties on the charm production cross section in DIS neutrino interactions ([79] and references therein). In fact, the fraction of ν_μ CC interactions with a charmed hadron in the final state strongly depends on the value assumed for the charm quark mass. It also depends on the parton distributions, which in turn are functions of the QCD scale (μ), whose dependence on Q^2 and x-Bjorken is not well

known. Because of these uncertainties, we adopt an empirical parametrisation as a function of the neutrino energy (Fig. 140) which reproduces the E531 data [80]. By convoluting this parametrisation with the CNGS neutrino spectrum [58] one obtains

$$\frac{\sigma(\nu_\mu N \to \mu^- cX)}{\sigma(\nu_\mu N \to \mu^- X)} \equiv \frac{\sigma_c}{\sigma_{CC}} = (3.3 \pm 0.5)\% \tag{3}$$

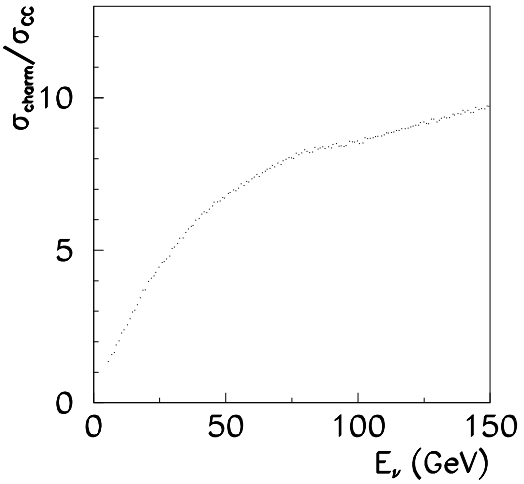

Figure 140: Parametrisation of the relative charmed-particle production rate in ν_μ CC interactions, as a function of the neutrino energy reproducing the E531 data. The vertical scale is in %.

We then assume the factorisation theorem to obtain the charmed hadron (C) cross section, which can be related to the charm quark (c) cross section through fragmentation functions

$$\frac{d^5\sigma(\nu_\mu N \to \mu^- CX)}{dxdydzdp_t^2} = \frac{d^2\sigma(\nu_\mu N \to \mu^- cX)}{dxdy} \times \sum_h f_h \times D_c^h(z, p_t^2) \tag{4}$$

where $D_c^h(z, p_t^2)$ is the probability distribution for the charm quark fragmenting into a hadron h carrying a fraction z of the longitudinal momentum of the quark and transverse momentum p_t with respect to the quark direction.

The quantity f_h is the fraction of σ_c in which a charmed hadron h is produced. We assume $\sum_h f_h = 1$ with the sum extended to the hadrons considered below. From equation (4) it follows that f_h depends on the chosen hadronisation scheme *i.e.* on the functions $D_c^h(z, p_t^2)$. Several sets of these functions exist [79].

We have used functions determined from fits to neutrino charm production data [80, 81]. The charmed hadron fractions f_{D^0}, f_{D^+}, $f_{D_s^+}$ and $f_{\Lambda_c^+}$ are given in [81] as a function of the neutrino energy. Since the charmed hadrons have different $c\tau$ the expected background depends on the values of f_h which in turn are function of the neutrino energy. In the case of the CNGS beam one obtains

$$f_{D^0} = 0.45 \pm 0.14, \quad f_{D^+} = 0.10 \pm 0.03, \quad f_{D_s^+} = 0.18 \pm 0.05 \text{ and } \quad f_{\Lambda_c^+} = 0.26 \pm 0.08$$

The branching ratios of the charged charmed hadrons have been taken from the PDG [82].

For the special case of quasi-elastic charm production, one has

$$\frac{\sigma(\nu_\mu n \to \mu^- \Lambda_c^+)}{\sigma(\nu_\mu N \to \mu^- X)} = 0.6\%$$

The background from this process is negligible.

To evaluate the background from single charm production we must treat separately muonic and non muonic decay channels.

For the electronic and the hadronic charm decay channels the expected background can be written as follow

$$\begin{aligned} N_{bg} &= \frac{\sigma_c}{\sigma_{CC}} \times f_{C^+} \times \varepsilon_{trigger} \times \varepsilon_{brick} \times \varepsilon_{geom} \times \varepsilon_{vert} \times \varepsilon_{long} \\ &\quad \times \varepsilon_{kink} \times (1 - \varepsilon_\mu^{charm}) \times \varepsilon_{kin}^{L(S)} \times BR \times N_{DIS} \end{aligned}$$

where ε_μ^{charm} is the efficiency in detecting the primary muon in events with a charmed hadron in the final state and N_{DIS} is the total number of DIS events. The contribution from QE neutrino interactions is negligible.

For the muonic channel we must account for the fact that the present μ identification algorithm (see Section 7.2) reconstructs only one muon per event. Therefore, we have three categories of events

- events with the primary muon identified (77.1%);
- events with neither primary nor daughter muon identified (3.6%);
- events with the daughter muon identified (19.3%).

The first category of events does not contribute to the background. The second one contributes to the background of the hadronic channel. Nevertheless, given the kinematical analysis efficiency and the small $C^+ \to \mu^+$ branching ratio, it is completely negligible. The third category of events contributes to the background only if the charge of the positive muon is either wrongly measured or not measured at all. Monte Carlo simulations show that only $\sim 6\%$ of the events with the daughter muon reconstructed have the charge either not measured or wrongly measured.

Table 21: Expected charm background for the different channels and for the different charmed hadrons. The values are normalised to 10^6 DIS events.

	$\tau \to e$	$\tau \to \mu$	$\tau \to h$	Total
Long D^+	4.3	0.7	2.7	7.7
Long D_s^+	2.6	0.4	4.1	7.1
Long Λ_c^+	0.1	0.3	0.2	0.6
Long (total)	7.0	1.4	7.0	15.4
Short D^+	0.4	-	(0.3)	0.4
Short D_s^+	0.5	-	(0.8)	0.5
Short Λ_c^+	0.2	-	(0.2)	0.2
Short (total)	1.1	-	(1.3)	1.1
Total	8.1	1.4	7.0	16.5

The expected background from charm decays for the different channels is given in Table 21. The contribution from $\overline{\nu}_\mu$, ν_e and $\overline{\nu}_e$ to the charm background is in any case negligible, as they constitute only a small contamination of the ν_μ beam.

The other potential source of charm background is given by the associated charm production, in which two charmed hadrons are produced and one of the two escapes detection. This process has been only observed by E531 [80] with only one event compatible with the NC production of a pair of charmed particles ($D^0 - \bar{D}^0$). From this event the rate of a neutral current $c\bar{c}$ production can be estimated to be

$$\frac{\sigma(\nu_\mu N \to c\bar{c}\nu_\mu X)}{\sigma(\nu_\mu N \to \nu_\mu X)} \equiv \frac{N_{c\bar{c}}}{N_{NC}} = 0.13^{+0.31}_{-0.11}\%$$

If instead one makes the assumption that in the observed event the muon from the primary vertex was not identified, the following upper limit on $c\bar{c}$ production in CC interactions is obtained

$$\frac{\sigma(\nu_\mu N \to c\bar{c}\mu X)}{\sigma(\nu_\mu N \to \mu X)} < 0.12\%$$

In the following we assume that $c\bar{c}$ production is the same both for NC and CC neutrino interactions. In order to extrapolate the above results to OPERA one needs to know how the produced charm quark is dressed, *i.e.* the charmed fractions f_h and $\bar{f}_h$. There are no experimental measurements of these quantities. Therefore, we have to use the z and p_t^2 distributions valid for single charm production. The results are shown in Table 22.

The associated charm production cross section is one order of magnitude smaller than that for single charm production. Furthermore, the associate charm production constitutes a background if at least one of the two charmed hadron is not detected. Therefore, we can safely assume that the expected background from this process is one order of magnitude smaller than the one expected from the single charm production process.

Table 22: Probability to have a given pair of charmed particles in the final state ($f_{CC'}$), shown as a matrix. The value in bracket corresponds to a final state which does not contribute to the background.

	D^0	D^+	D_s^+	Λ_c^+
$\bar{D}^0$	(0.203)	0.045	0.081	0.117
D^-	0.045	0.010	0.018	0.026
D_s^-	0.081	0.018	0.032	0.047
Λ_c^-	0.117	0.026	0.047	0.068

Table 23: Fraction of events surviving the various kinematical cuts, as a function of the electron energy. The cuts are applied one after each other (multiplicative efficiencies). No event survived the p_t cut.

Energy (GeV)	ε_{kink} (%)	ε_E (%)	ε_{p_t} (%)
1	12.6	4.9	0
3	3.5	14.2	0
5	2.5	11.1	0
10	1.30	9.9	0
20	0.66	8.3	0

We assign to the present estimates of the total number of events from charm a $\sim 15\%$ systematic error, mainly due to the uncertainty on the charm production cross section. The precision on the background evaluation will benefit from the charm studies foreseen for the CHORUS phase 2 analysis.

7.4.3 Background from π^0 and prompt electrons

In addition to charm production (see Section 7.4.2), two other sources must be considered as possible background for $\tau \rightarrow e$ long decays: kink-like events from scattering of primary electrons produced in ν_e CC interactions and pion charge exchange process ($\pi^- p \rightarrow \pi^0 n$) in ν_μ NC interactions.

The background from prompt electrons has been studied by means of a full Monte Carlo simulation. A total of 50000 events have been simulated but no event survived the cuts described in Section 7.3.8. The fraction of events surviving the kinematical analysis as a function of the electron energy is shown in Table 23. From these values and taking into account that the ν_e and $\bar{\nu}_e$ contamination of the beam is less that 1%, we can conclude that the background from prompt electron is smaller than $1 \times 10^{-6} \times N_{CC}$.

If in a ν_μ NC interaction a π^- undergoes a pion charge exchange process, the electrons produced in

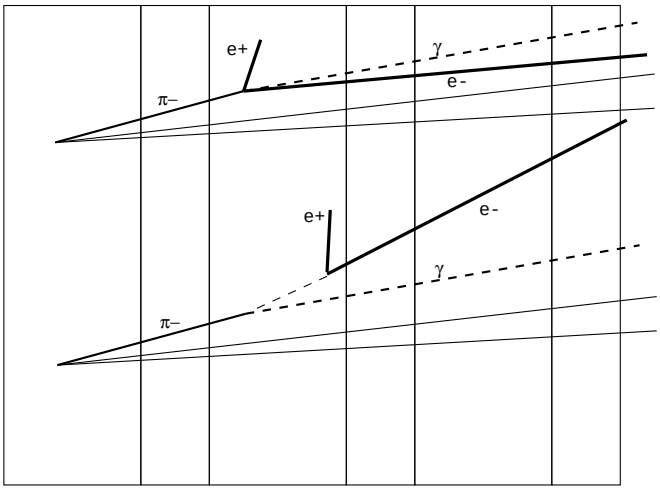

Figure 141: Background to the electron channel from pion charge exchange processes, occurring when the electron or the positron track is absorbed in the lead.

the π^0 conversion could mimic a τ to electron decay, as shown schematically in Fig. 141. Simulations indicate that the expected background from this process amounts to $0.2 \times 10^{-6} \times N_{CC}$ events.

Possible sources of background for short decays are prompt electrons and electrons produced in the conversion of a γ inside the vertex plate. By applying the kinematical cuts described in Section 7.3.8, the expected background is $\sim 0.1 \times 10^{-6} \times N_{CC}$.

7.4.4 Background from muon scattering

Muons produced in ν_μ CC events and undergoing a scattering in the lead plate following the vertex plate could mimic a muonic τ decay.

A first estimate of this background was made in [6] with a GEANT 3.21 simulation. About 70000 ν_μ CC events in the compact bricks were simulated according to the CNGS beam spectrum. In 0.5% of the events, the prompt muon had an *apparent* kink angle larger than 25 $mrad$ in the lead plate downstream of the vertex plate. For these events (see Fig. 2.25 of [6]) the muon transverse momentum was shown as a function of the momentum. In the same plot the τ candidates were also shown. The correlation between the two quantities was used to apply a combined cut, as shown in the same figure. Two events survived the cut, both with quite a large angle, greater than 80 $mrad$.

Taking into account the other factors contributing to the detection efficiency (ε_{geom}, ε_{brick} and ε_{vert}), the two survivors correspond to a normalised background of $1.3 \times 10^{-5} \times N_{CC}$ events for a 1 mm lead plate. Since decays are searched for in two consecutive lead plates behind the vertex one, the total background becomes $2.6 \times 10^{-5} \times N_{CC}$.

More recently it became clear that GEANT overestimates large angle muon scatters background. This was clearly observed in the NOMAD experiment by comparing the muon reconstruction efficiencies

between data and the Monte Carlo, also based on GEANT 3.21.

GEANT simulates Coulomb multiple scattering accordingly to the Moliere theory [83]. This theory is valid provided that the angular deflections are small and that many scatterings contribute to the total deflection of the particle. The tails at large angles are instead simulated in the so-called plural scattering regime by generating single scatters with a cross section given by the classical Rutherford formula

$$\frac{d\sigma}{\theta d\theta} = 2\pi(\frac{2Ze^2}{pv})^2\frac{1}{(\theta^2+{\chi_\alpha}^2)^2}$$

where the factor χ_α takes into account the screening of the nucleus by the electrons at large impact parameter and avoids that the cross section diverges at small angles. This formula describes the scattering of a spin-less muon by a point-like nucleus of charge Z, providing very large deflections for small impact parameters (large Q^2).

The muon reconstruction in NOMAD was performed by matching track segments reconstructed in drift chambers behind a filter (equivalent to about 135 cm of iron) with those reconstructed in the spectrometer. A class of events in which the muons underwent large angle scatters in the filter (more than 140 $mrad$) was clearly present in the Monte Carlo simulation but not in the data. These events contributed to the muon identification inefficiency. High statistics (of the order of a few millions of events) samples of through-going muons from the data were compared to the Monte Carlo simulation, showing that the Monte Carlo overestimates large angle scatters (> 140 $mrad$) by about a factor 30 [84].

A modified version of the cross section for single Coulomb scattering corrected for a nuclear form factor directly measured on lead [85] and also taking into account the inelastic contribution [86] has been developed. When convoluted with the muon spectrum of ν_μ CC in OPERA, it predicts a background of $0.2 \times 10^{-5} \times N_\mu$ for scattering angles greater than 20 $mrad$ and $p_t > 250$ MeV/c.

The direct measurements of muon scattering off thin layers of material ($\mathcal{O}(0.1\ X_0)$) are rather scarce.

In a measurement of muon scattering on a 1 X_0 copper target at 7.3 GeV [87], three events without visible recoil and with angles larger than 20 $mrad$ per projection were observed, out of ~ 31000 incoming muons. This rate, $(1 \pm 0.3) \times 10^{-4} \times N_\mu$, rescaled to 2 mm lead target and 10 GeV/c momentum translates to $\sim 2.3 \times 10^{-5} \times N_\mu$, with a large error. The scaling from copper to lead has been done under the assumption of a $Z^2\rho/Ap^2$ dependence of the effect.

Notice that, given the angular cut and the muon momentum, only scatterings with $p_t > 200$ MeV/c are considered. Furthermore, the beam used for this measurement had a not negligible contamination (2%) of pions which may undergo large angle scattering. Therefore, the above number can only give an upper limit on the expected background in OPERA ($p_t > 250$ MeV/c).

In the CHORUS experiment a sample of 130000 ν_μ CC was analysed searching for $\tau \to \mu$ decays in emulsions. This sample corresponds to the scanning of a total muon track length of 1.5×10^6 mm. No muons were found with a kink angle in space larger than 25 $mrad$ and $p_t > 250$ MeV/c. This search translates into an upper limit of $2.3/1.5 \times 10^6 = 1.5 \times 10^{-6}$ mm^{-1} at the 90% CL. Taking into account 2 mm of lead and the different momentum spectrum, this yields $< 4.1 \times 10^{-5} \times N_\mu$ for the OPERA conditions.

Table 24: Estimates of the rate of muon scattering off 2 mm lead as obtained from Monte Carlo simulations and from experimental data with different materials.

	Rate on 2 mm lead
Monte Carlo on lead	$0.2 \times 10^{-5} \times N_\mu$
Scattering on copper	$< 2.3 \times 10^{-5} \times N_\mu$
Scattering on emulsion	$< 4.1 \times 10^{-5} \times N_\mu$
Scattering on lead	Evaluation in progress

We recently undertook a dedicated measurement of large-angle muon scattering from thin lead plates in the momentum range of $6-10$ GeV/c using emulsions as well as electronic trackers. The data analysis of this experiment, described in Section 8.3, is still in progress. Preliminary results for an average muon momentum of 9 GeV/c and 2 mm lead target indicate a rate consistent with the previous upper limits.

In conclusion, as rate for scattering from $(1+1)$ mm lead with $p_t > 250$ MeV/c we take $1 \times 10^{-5} \times N_\mu$.

By taking into account all the efficiencies, the expected background can be written as

$$N_{\mu scatt} = \varepsilon_{brick} \times \varepsilon_{geom} \times \varepsilon_{vert} \times \varepsilon_{\mu ID} \times \varepsilon_{p_\mu} \times 1 \times 10^{-5} \times N_{CC}$$

where $\varepsilon_{\mu ID} \simeq 95\%$ is the muon identification efficiency, $\varepsilon_{p_\mu} \simeq 68\%$ gives the fraction of muons with momentum in the range $1 - 15$ GeV/c and $N_{CC} = N_{DIS} + N_{QE}$.

This yields an expected background $N_{\mu scatt} \simeq 5 \times 10^{-6} \times N_{CC}$. Given the lack of experimental data and the uncertainty on the Monte Carlo simulations, we assume for this background a 50% uncertainty.

7.4.5 Hadron reinteractions

An important source of background to the hadronic decay channel is due to reinteractions in the lead of hadrons produced in ν_μ NC and in ν_μ CC interactions in which the primary muon is not identified. Although the muon identification efficiency is high (see Section 7.2), the latter class of events gives a background which is comparable with that from ν_μ NC events. The reasons are the following

- the cross section ratio favours CC events ($\sigma_{NC}/\sigma_{CC} \simeq 1/3$);
- even if the primary muon is not identified, the kinematics at the primary vertex is that of CC events. Therefore, the kinematical analysis described in Section 7.3.10 is not effective for these events (*i.e.* for genuine ν_μ NC events $\varepsilon_{p_t^{miss}+\phi} \simeq 20\%$, while for ν_μ CC with the μ not identified $\varepsilon_{p_t^{miss}+\phi} \simeq 60\%$).

Table 25: Expected background from hadron reinteractions. The contribution as a function of the track multiplicity at the primary vertex is also given. The numbers are normalised to 10^6 DIS events.

Events	HM	LM	Short	Total
ν_μ NC	2.1	0.6	4.1	6.8
ν_μ CC	2.3	$\ll 0.1$	2.0	4.3
Total	4.4	0.6	6.1	11.1

Table 26: Expected background for the different channels. The numbers are normalised to 10^6 DIS events.

	$\tau \to e$	$\tau \to \mu$	$\tau \to h$	Total	Error
Long: charm	7.0	1.4	7.0	15.4	$\pm 15\%$
Long: ν_eCC and π^0	0.2	-	-	0.2	$\pm 10\%$
Long: μ scatt.	-	5.0	-	5.0	$\pm 50\%$
Long: had. reint.	-	-	5.0	5.0	$\pm 50\%$
Long total	7.2	6.4	12.0	25.6	-
Short: charm	1.1	-	(1.3)	1.1	$\pm 15\%$
Short: ν_eCC and π^0	0.1	-	-	0.1	$\pm 10\%$
Short: had. reint.	-	-	(6.1)	(6.1)	
Short Total	1.2	-	-	1.2	
Total	8.4	6.4	12.0	26.8	

This background has been evaluated by simulating 1×10^7 NC and CC events with GEANT 3.21. The results are shown in Table 25.

Hadron reinteractions can also contribute to the $\tau \to \mu$ channel when a hadron, produced either in ν_μ NC or ν_μ CC interactions with the muon not identified, is misidentified as a muon (see Section 7.3.5). The evaluation of this background is in progress.

Data on hadronic reinteractions are being analysed [88, 89]. An experimental evaluation of the reinteraction background is expected soon. In the present situation of the analysis and given the large Monte Carlo uncertainties, we presently assume a 50% error on this background.

7.5 Sensitivity to $\nu_\mu \leftrightarrow \nu_\tau$ oscillations

For the evaluation of the sensitivity of the experiment we assumed the τ detection efficiencies given in Section 7.3.11 and the backgrounds in Table 26, with the referred to uncertainties.

Since we do not plan to replace with new bricks those which are removed for the event analysis, but rather with peripheral bricks, the mass of the detector decreases as a function of the exposure time. In

Table 27: Expected numbers of τ and background events collected by OPERA in five years of data taking ($2.25 \times 10^{20} pot$). Signal events are given for full mixing and for three values of Δm^2: the most recent best fit by Super-Kamiokande [30] and the two 90% CL limits. 22 events would be observed for the previous best fit value ($\Delta m^2 = 3.5 \times 10^{-3}\ eV^2$ [28]).

τ decay mode	Signal $(1.5 \times 10^{-3} eV^2)$	Signal $(3.2 \times 10^{-3} eV^2)$	Signal $(5.0 \times 10^{-3} eV^2)$	BG
e^- Long	1.3	5.9	14.2	0.16
μ^- Long	1.3	5.7	13.8	0.13
h^- Long	1.1	4.9	11.8	0.25
e^- Short	0.4	1.8	4.3	0.03
Total	4.1	18.3	44.1	0.57

the following we assume the removal of a single brick per event and the removal of about 10% more bricks for further analyses. By averaging over 5 years of data taking with the CNGS expected flux, the corresponding average mass of a supermodule is 600 ton (640 ton the first year, 560 ton the fifth year).

In order to evaluate the sensitivity to $\nu_\mu \leftrightarrow \nu_\tau$ oscillations, the energy dependence of the neutrino spectra and of the detection efficiencies is taken into account. The conventional two-flavour approximation is assumed.

The expected τ and background events for the individual decay channels are given in Table 27. The total number of events expected at $\Delta m^2 = 3.2\ \times 10^{-3}\ eV^2$, the Super-Kamiokande best fit for full mixing [30], is about 18 with an expected background of about 0.6 events. For the previous Super-Kamiokande preferred solution, $\Delta m^2 = 3.5\ \times 10^{-3}\ eV^2$ [28], ~ 22 events are expected.

Fig. 142 gives, as function of Δm^2, the number of events (which grows quadratically with Δm^2) expected in 5 years at full mixing as well as the expected background.

The number of observed events allowing for a claim of $\nu_\mu \leftrightarrow \nu_\tau$ oscillation discovery at the 4σ level is defined by the $1.0 - (6.3 \times 10^{-5})$ CL upper limit of the Poisson distribution with a mean value corresponding to the expected number of background events. For a 4σ discovery claim, about 5 events are required. More generally, Fig. 143 gives the statistical significance (expressed in terms of equivalent σ for a Gaussian distribution) as a function of the number of events observed.

The sensitivity calculation is carried out within the unified statistical framework proposed by Feldman and Cousins (F&C) and described in [90]. The computation has also been performed with the statistical method proposed by Junk [91], which was used in [6].

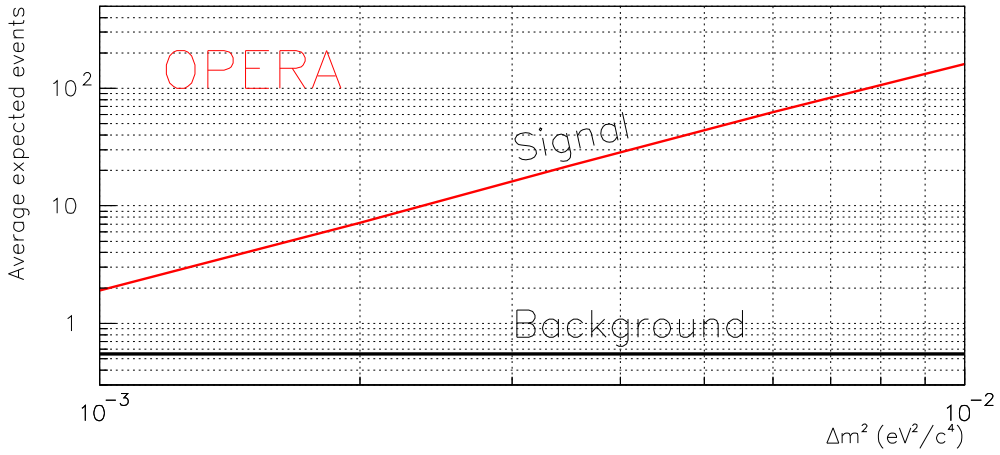

Figure 142: Shown are the average number of expected events as a function of Δm^2 and the expected background level.

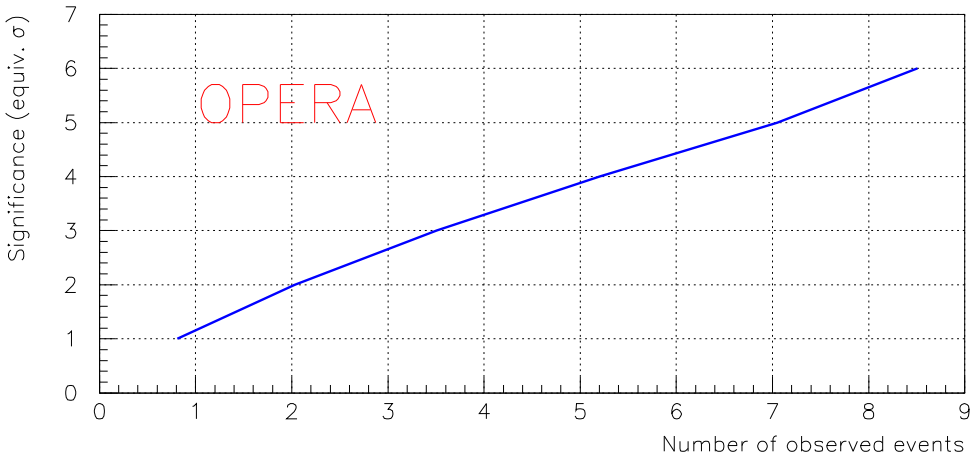

Figure 143: Statistical significance of the OPERA $\nu_\mu \leftrightarrow \nu_\tau$ oscillation discovery claim as as function of the number of events observed in a five years run.

Table 28: Sensitivity at the 90% CL on $\sin^2 2\theta_{\mu\tau}$ (at large Δm^2) and on Δm^2 (for full mixing) as a function of exposure time calculated following the F&C approach [90]. The results obtained with the T.J. approach described in [91] for 5 years data taking are also shown.

	T.J. 5 years	F&C 5 years	F&C 4 years	F&C 3 years	F&C 2 years
$\sin^2(2\theta)$ at large Δm^2	6.3×10^{-3}	6.0×10^{-3}	7.0×10^{-3}	1.0×10^{-2}	1.4×10^{-2}
Δm^2 at $\sin^2(2\theta) = 1$	$1.3 \times 10^{-3} eV^2$	$1.2 \times 10^{-3} eV^2$	$1.3 \times 10^{-3} eV^2$	$1.5 \times 10^{-3} eV^2$	$1.9 \times 10^{-3} eV^2$

Each τ decay channel is characterised by a specific background and signal rate. An additional constraint on the detected signal can be obtained from the internal consistency among various channels, which are therefore combined together as independent measurements. An overall uncertainty of 15% is assumed on the number of expected signal events. The corresponding background uncertainty is taken to be 15% for charm and 50% for hadronic interactions and muon scattering. Calculations and test beam measurements are under way or planned in order to reduce this uncertainty in the future.

The sensitivity is computed as the average upper limit which would be obtained, in the absence of a true signal, by an ensemble of identical experiments. A large number of experiments has been simulated in order to take into account background fluctuations. The average upper limit at the 90% CL which would be obtained on the oscillation parameters from a negative search is shown in Fig. 144 for 2 and 5 years exposure.

Fig. 144 also shows the most recent result of a global fit to the Super-Kamiokande data from atmospheric neutrinos [30]. At the 90% CL the allowed region covers the Δm^2 range of $1.5 - 5 \times 10^{-3}\ eV^2$, instead of $2 - 6 \times 10^{-3}\ eV^2$ as in the previous fit [28]. The best fit value $3.2 \times 10^{-3}\ eV^2$ has to be compared with the previous value of $3.5 \times 10^{-3}\ eV^2$.

Already after two years of exposure, the sensitivity covers most of the region presently allowed by Super-Kamiokande, as shown in Fig. 144. Due to the low intrinsic background of the experiment the statistical significance of the observed signal improves linearly with the exposure time.

As shown in Table 28 both statistical approaches [90] and [91] give similar results. Using the unified approach, the sensitivity at the 90% CL on $\sin^2 2\theta_{\mu\tau}$ (at large Δm^2) and on Δm^2 (full mixing) are shown in Table 28 as a function of the number of years of data taking.

The sensitivity of the experiment to $\nu_\mu \leftrightarrow \nu_\tau$ oscillations is such that even a negative search would be relevant for the understanding of the experimental scenario.

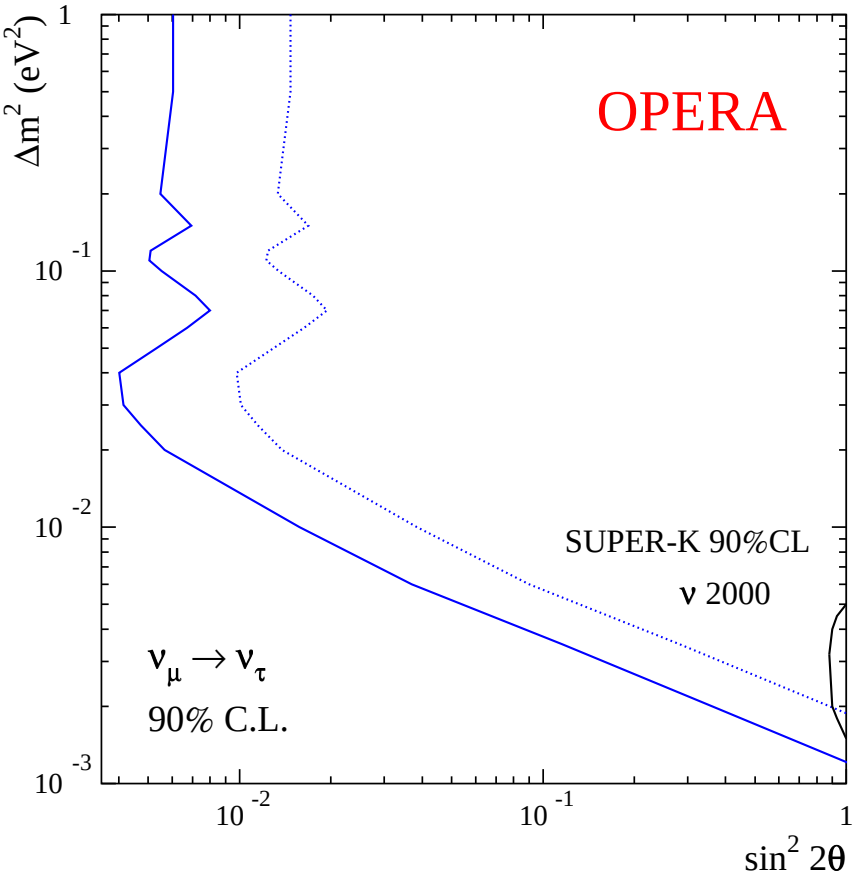

Figure 144: Sensitivity of the OPERA experiment to $\nu_\mu \leftrightarrow \nu_\tau$ oscillations at the 90% CL for 2 (dotted line) and 5 (continuous line) years exposure. The region allowed by the Super-Kamiokande analysis is also shown.

7.6 Determination of the oscillation parameters

A measurement of the oscillation parameters can be obtained from the number of detected τ events. An automatic transition from upper limits to central confidence intervals is guaranteed with the unified approach of [90].

We consider the observation of a number of τ events which corresponds to the best fit and to the 90% CL limit recently given by Super-Kamiokande (Table 27). The resulting 90% CL regions for the Δm^2 measurement are given in Table 29. In the case of the best fit of Super-Kamiokande, Fig. 145 shows how the number of observed events can constrain the allowed region for the oscillation parameters and improve the Δm^2 measurement.

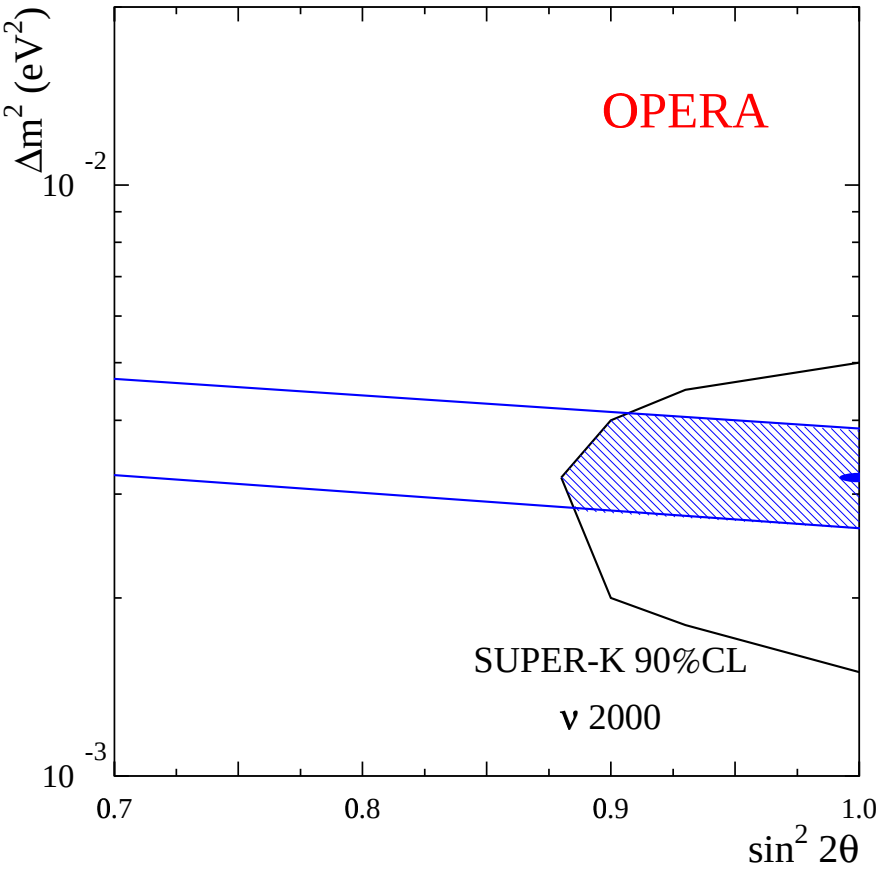

Figure 145: The band gives the 90% CL allowed region of the oscillation parameters as determined by OPERA observing a number of events corresponding to what is expected for full mixing and $\Delta m^2 = 3.2 \times 10^{-3}\ eV^2$.

The above determination is based on the sample of events with very low background, retained for the

Table 29: 90% CL limits on Δm^2 defining the OPERA allowed region for full mixing. In the three columns we assume to observe a number of events corresponding to the best fit and to the 90% CL limits given by Super-Kamiokande.

True value	$1.5 \times 10^{-3} eV^2$	$3.2 \times 10^{-3} eV^2$	$5.0 \times 10^{-3} eV^2$
Upper limit	$2.1 \times 10^{-3} eV^2$	$3.8 \times 10^{-3} eV^2$	$5.6 \times 10^{-3} eV^2$
Lower limit	$0.8 \times 10^{-3} eV^2$	$2.6 \times 10^{-3} eV^2$	$4.3 \times 10^{-3} eV^2$
(Upper-Lower)/2 × True	41%	19%	12%

detection of ν_τ appearance. However, we point out that additional constraints can be extracted from the reconstruction of the event topology and that, therefore, additional decay channels may be included in the analysis, such as muonic and hadronic τ decays in the lead (short kinks) or a specific ρ search in the hadronic channel. The determination of the oscillation parameters may therefore be improved.

7.7 Additional physics subjects

7.7.1 Search for $\nu_\mu \leftrightarrow \nu_e$ oscillations

Because of the very good electron identification, OPERA is also sensitive to $\nu_\mu \leftrightarrow \nu_e$ oscillations. Together with the $\nu_\mu \leftrightarrow \nu_\tau$ appearance search this measurement allows to perform an analysis of neutrino oscillation with three-flavour mixing.

A background source for the $\nu_\mu \leftrightarrow \nu_e$ search is the $\sim 1\%$ ν_e ($\bar{\nu}_e$) contamination of the ν_μ beam. Another one is given by electrons from the Dalitz decay of neutral pions produced in ν_μ NC interactions ($\pi^0 \rightarrow e^+e^-\gamma$) and photon to electron conversions in the lead plates ($\pi^0 \rightarrow 2\gamma$ followed by $\gamma N \rightarrow e^+e^-N$). The latter contribution is reduced by selecting neutrino interactions with one identified electron (positron) of measured energy greater than a given threshold. The contamination from pions misidentified as electrons has to be included as well.

The statistical error on the background estimate determines the sensitivity of the measurement of the oscillation parameters together with systematic errors due to the uncertainty on the ν_e content of the beam and on the number of pseudo-prompt electrons produced by π^0's.

The calculation of the detection efficiency, of the background and of the sensitivity is in progress. An estimate of the sensitivity has been given in [6], showing the capability of detecting $\nu_\mu \leftrightarrow \nu_e$ oscillations.

7.7.2 Oscillation search through NC/CC ratio measurement

The expected performance of the detector target as a calorimeter for shower energy measurement and the presence of spectrometers for the identification and the momentum determination of muons allow a

measurement of the ratio between ν_μ NC and ν_μ CC events (NC/CC). The NC/CC ratio is related to the oscillation probability. For more details of oscillation searches through the study of the NC/CC ratio we refer to [17].

The separation between NC and CC events is based on the detection of a muon track in the detector. Unless this muon is very soft, it can travel along the detector and traverse the spectrometer (Fig. 146). The energy release of a CC event in the target scintillators exceeds that of a NC interaction. This is due to the additional contribution from the muon. The same argument applies to the number of hit scintillator strips. These features have been exploited to train a neural network [74] on a sample of four kinds of events classified into in two categories

- CC-like: ν_μ CC events and ν_τ CC with a τ decaying into a muon;
- NC-like: ν_μ NC events and ν_τ CC with a τ decaying into anything but a muon.

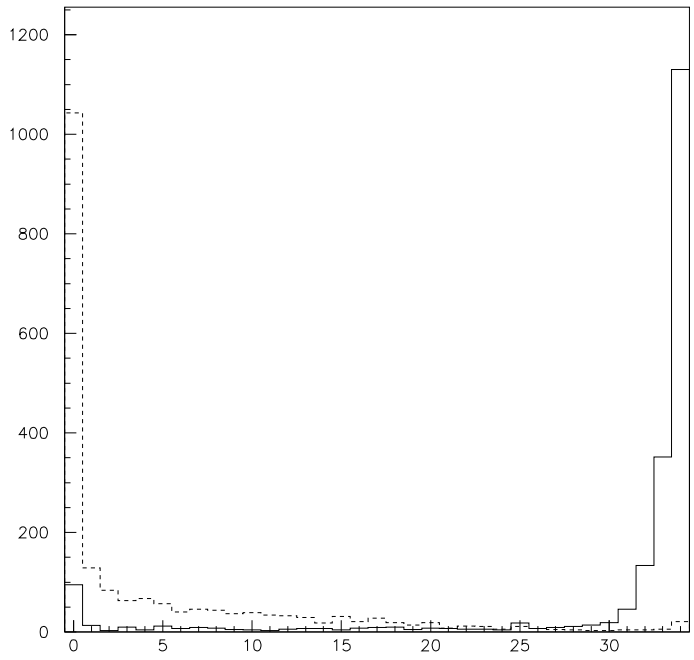

Figure 146: Number of hit planes in the spectrometer Inner Trackers for NC (dashed line) and CC events (continuous line).

Independent samples were then used to study the event selection efficiency by using the trained neural network. The results are presented in Fig. 147 for the two classes of events discussed above. As an indication of the efficiency of this separation, Table 30 shows the selection efficiency when the output

variable is taken to be larger than 0.4. An energy dependent efficiency can be deduced for each sample and then used for each set of oscillation parameters $(\sin^2(2\theta), \Delta m^2)$ in order to extract the NC/CC ratio.

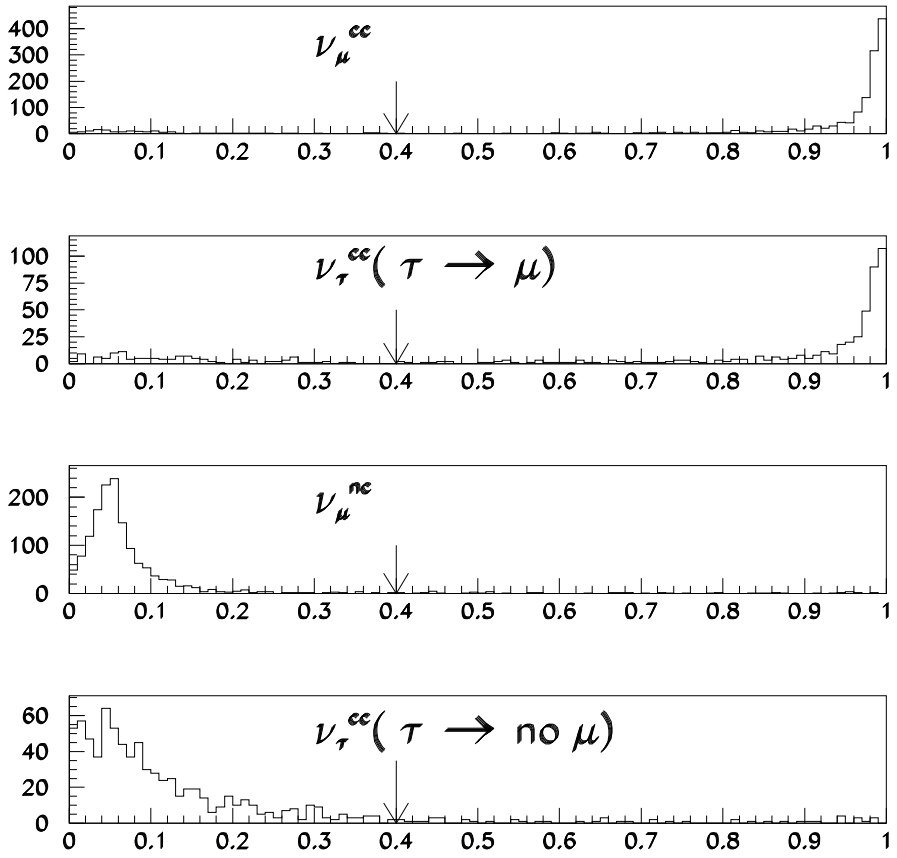

Figure 147: Neural network output variable for different event samples.

We denote with R and R_0 the ratio NC/CC in the presence and in the absence of neutrino oscillations, respectively. In addition to the statistical uncertainty on the NC/CC ratio measurement and on the event selection efficiency mentioned above, some additional systematic uncertainties are present. The main contributions are given by the neutrino energy measurement, by the uncertainty related to the input value of R_0 and by the uncertainty on the neutrino cross sections.

The oscillation probability can be measured through the determination of R. The deviation with respect to R_0 is then translated in the number of standard deviations of the NC/CC ratio uncertainty

Table 30: Neural network recognition efficiency for the output variable larger than 0.4. By definition the CC-like output is expected to be 1, and the NC-like to be 0.

Event sample	efficiency (%)
ν_μ CC	88
$\tau \rightarrow \mu$	78
ν_μ NC	4
$\tau \rightarrow no\ \mu$	6

(σ_R). An oscillation signal can be then obtained at the 90% CL when the deviation $(R - R_0)/R$ is larger than 1.25 σ_R.

Further studies are required to estimate the uncertainty which can be achieved. With 10% systematic error on the neutrino beam and 5% systematic uncertainty on R_0, the sensitivity of the NC/CC ratio measurement would reach for full mixing $\Delta m^2 = 4.5 \times 10^{-3} eV^2$. Although OPERA is not designed for this purpose a NC/CC measurement could be included in a study of the oscillation parameters in a general three-flavour scheme.

8 Test measurements and results

8.1 Measurements on ECC brick components

8.1.1 Emulsion films

In additions to the extensive studies of emulsion films from Fuji presented in Section 4.2.2, we also performed test measurements with industrial emulsion films produced by the Fomos company.[17] Bricks made with these films were exposed to muons at the CERN SPS.

The films are made up of two 55 μm emulsion layers coated on both sides of a 180 μm plastic base. The emulsion gel has a dilution factor of three. The measured sensitivity is of 25 grains/100 μm for a minimum ionising particle. The fog density varies from 4 to 8 grains per 1000 μm^3, depending on the development conditions. These features are compatible with the OPERA requirements.

The beam test data allowed us to study, in particular, edge effects. The results are shown in Fig. 148 and indicate that the track finding efficiency stays rather constant near the film edge. A drop in the efficiency is measured for distances lower than ~ 300 μm from the edge.

We also determined the angular resolution of the emulsion films, by measuring the angles of penetrating muons in two emulsion films separated by 1 mm of lead. This is shown in Fig. 149.

8.1.2 Lead radioactivity measurements

With the aim of identifying suitable materials for the brick lead plates, we performed extensive measurements of the radioactivity of commercial lead samples supplied by companies in Japan, USA and Europe.

The α and β rays emissions were measured at the Nagoya University by using emulsion films and a gas proportional counter with 2π geometrical acceptance and surrounded by cosmic ray veto counters.

A measurement of the γ radioactivity was performed by high purity germanium detectors (HPGe) placed in the Modane Underground Laboratory (Fréjus tunnel).[18] A detailed GEANT 3.21 simulation of all the decay products of the ^{210}Pb radioactivity, namely the $Pb \rightarrow Bi \rightarrow Po$ chain, was also performed. These tools had been successfully tested in the ultra-low radioactivity domain of the double beta decay NEMO experiment.

Recognition of α particles in emulsion films is rather straightforward, since α's leave short black-trajectories in the emulsion layers. By counting these tracks one can estimate the emission level. Conversely, the estimate of the β radioactivity level is not trivial, due to Compton electrons produced from the natural γ ray background. Therefore, the reported emulsion measurements only refer to the α emission. In the case of gas proportional counter, instead, α and β can be separately measured by signal pulse height discrimination.

The results of the measurements are summarised in Table 31. The α level as measured by a proportional counter well agrees with the measurement done with emulsion films. As the source of the emission

[17] Fomos, 7 Leningradsky prospect, 125167, Moscow, Russia.

[18] We thank F. Hubert and P. Hubert from the CENBG laboratory, France, and H. Ohsumi from the SAGA University for the lead radioactivity measurements.

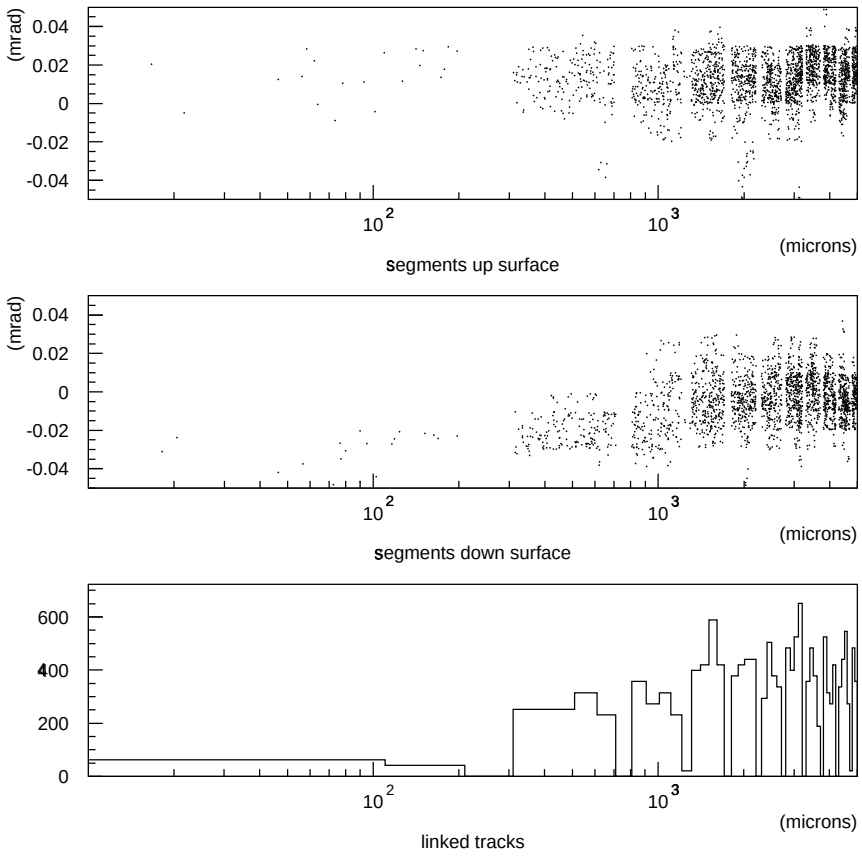

Figure 148: Study of edge effect in the reconstruction of tracks with Fomos emulsion films. The top plots show the distortion of reconstructed segments in each of the two emulsion layers as a function of the distance from the edge. The bottom plot gives the number of reconstructed tracks (associated segments).

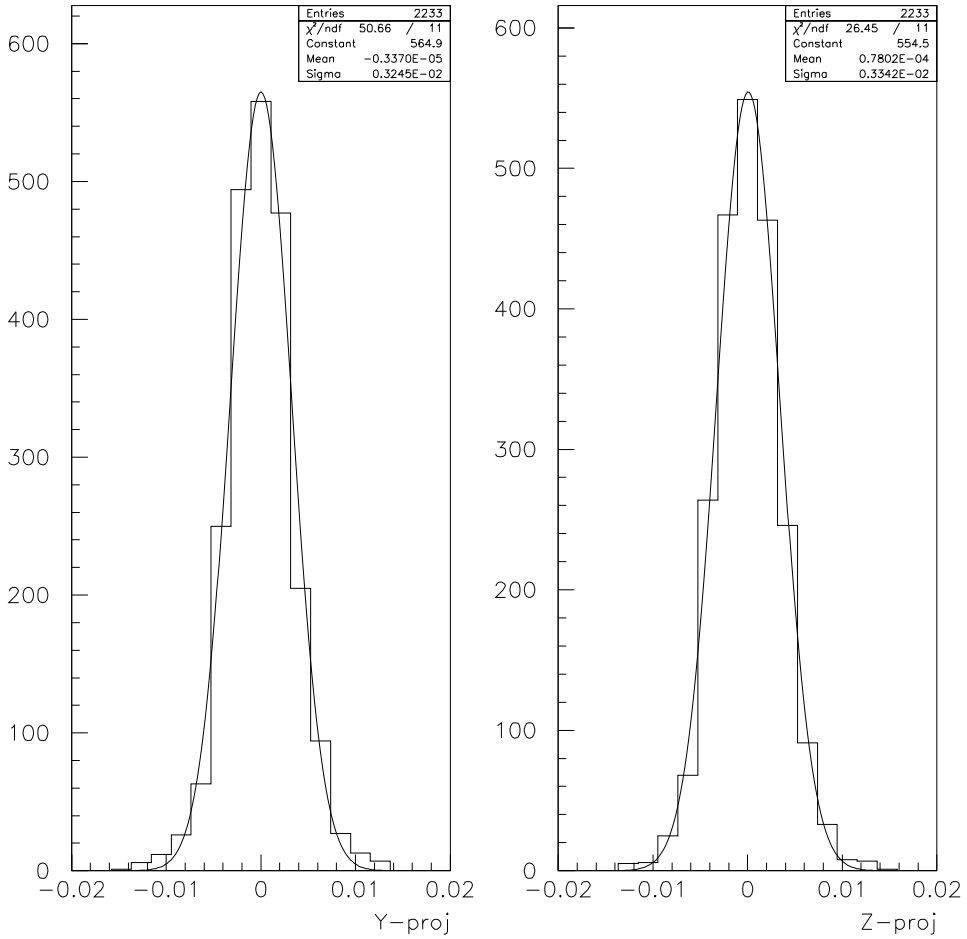

Figure 149: Angular resolution obtained with a brick made with Fomos emulsion films exposed to a muon beam.

Table 31: Radioactivity measurements of lead samples by gas proportional counter and emulsion films. T is the thickness of the material. Measured α emission levels by emulsion films are shown in bracket in the fourth column. G01, G02 and G03 have a surface coating which prevents the α measurement.

Sample	Origin	T [mm]	α [$/cm^2/day$]	β [$/cm^2/day$]
TH 00	Japan	1	64 (78)	480
TH 01	"	1	32 (28)	510
TH 02	"	0.5	27 (23)	500
TH 03	"	1.5	76 (86)	540
MT 01	"	1.5	29	5770
MT 02	"	1	12	490
MB SP	"	5	0	0
MB 01	"	1	6	910
MB 02	"	2	8	1270
NL	"	0.1	71	470
KS	"	1	53	3990
FERMI 01	USA	2	8	42
FERMI 02	"	1	10	38
G 01	EC	1	-	310
G 02	"	1	-	230
G 03	"	1	-	610

is ^{210}Pb, the difference of the α to β ratio mainly comes from the difference in the time passed after the lead purification (smelting).

We identified two low radioactivity lead samples. One is the MB SP supplied by Mitsubishi Material[19] and the other is the FERMI sample, produced by the Doe Run company[20] for Fermilab. The former is a special low radioactivity lead used for soldering components in LSI applications. A quantity of the order of ≤ 1 $kton$ of such a lead could be supplied by the company. The Doe Run is a large lead smelting company. Although the radiation level is not controlled in their production, the total production capability is large (~ 220 $kton$/year) and they could supply ≥ 1 $kton$ lead with low radiation level.

Concerning the γ ray measurement four kinds of different samples have been measured so far. Fig. 150 shows an example of the raw data spectrum and the results are given in Table 32. The errors on the measurements are of the order of 10%, mainly due to the not perfect knowledge of the setup geometry. One can see that the lead radioactivity level is spread over two order of magnitudes.

From the simulation side the equivalent of 1 Bq/g ^{210}Pb activity has been uniformly distributed among the 56 lead plates of a brick. The number of electrons, γ's and α particles entering an emulsion film are reported on Table 33.

Low energy electrons are mainly originating from the surface of the two lead plates directly attached to the emulsion film and from Compton interactions of γ's coming from all the other lead plates in the

[19] Mitsubishi Corporation, 6-3, Marunouchi 2-chome, Chiyoda-ku, Tokyo 100-8086, Japan.
[20] Doe Run Company, 1801 Park 270 Drive, Suite 270, St. Louis, MO 63146.

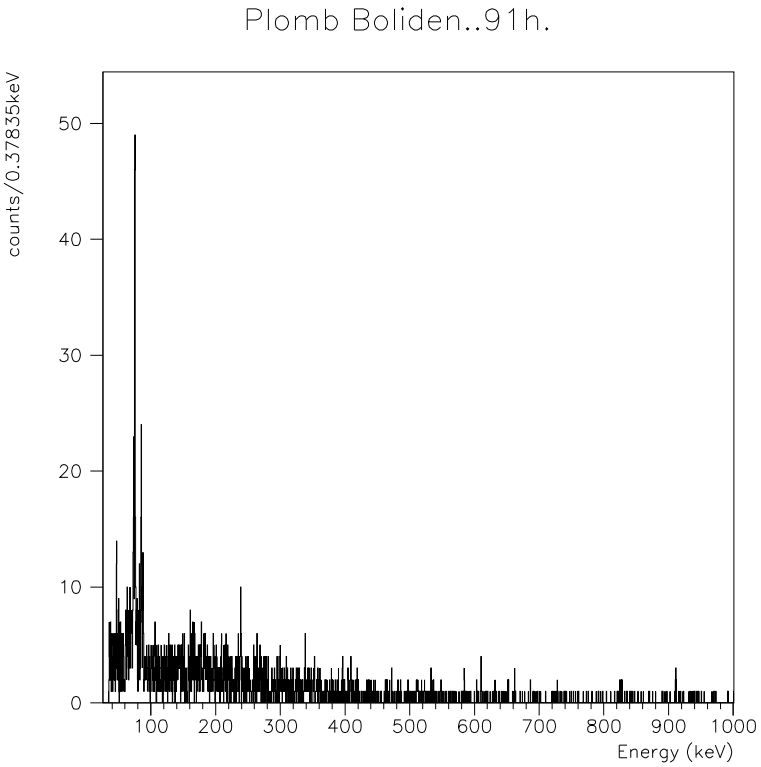

Figure 150: Radioactivity spectrum for one lead sample. One can see the X-rays structure on top of the continuous bremsstrahlung spectrum.

Table 32: Activity measurements by the HPGe technique at the LSM Laboratory (Fréjus) expressed in Bq/g for different lead samples. The last column is the result on beta counting using a gas counter performed at the Nagoya University. t is the material thickness. The three samples from Boliden mine were randomly extracted from a 25 ton batch.

Ref.	Geometry (mm)	Weight (g)	Activity (Bq/g) ^{210}Pb	β $(/cm^2/day)$
Atlas	70×60, t=1.5	72.1	0.23	
FERMI 02	$\emptyset = 70$, t =1	43.7	0.017	38
TH 00	$\emptyset = 70$, t =1	43.0	0.29	480
KS	$\emptyset = 70$, t =0.5	27.4	3.29	3990
Boliden 1	$\emptyset = 50$, t =4.0	89	0.017	
Boliden 2	$\emptyset = 50$, t =4.0	89	0.018	
Boliden 3	$\emptyset = 50$, t =4.0	89	0.018	

brick. There is approximately a factor three enhancement of the γ and electron fluxes compared to a single lead plate simulation.

Table 33: Results of a full GEANT simulation of a brick and the ^{210}Pb decay chain products.

Particle type	Energy cut (keV)	flux ($/cm^2/day$)
e^-	10	7.0 10^3
γ	10	4.2 10^3
α	500	3.7 10^2

To be safe one could select lead originating from low activity mines such as the one used for the Fermi sample from the Doe Run mine. However, for reasons of cost of transportation to Gran Sasso, it would be better to find a suitable lead in Europe. In particular, we are evaluating the possibility of using lead from the Boliden mine in Sweden. The measurements of different samples show an acceptable level of radioactivity ($< 0.02\ Bq/g$) and a good uniformity among a 25 ton sample (see Tab. 32). This uniformity is important for the survey strategy of the lead plate production.

In conclusion, we assume that with suitable selection of commercial lead the radioactivity background can be kept at a tolerable level over the lifetime of the experiment.

8.2 Tests on electronic detectors

8.2.1 Prototype scintillator strip modules

We have built four small scintillator detector prototypes in order to evaluate their performance and gain experience for the construction of large planes. Each unit is made of 32 scintillator strips arranged in an array of 16 rows of two strips each. The strips were produced by injection moulding technique. They have a cross section of $20 \times 9\ mm^2$ and a groove of $1.3 \times 1.3\ mm^2$ centred on one face. The strip length ($30\ cm$) is limited by the existing mould. Each strip is coated (except for the groove) by using the method developed by Uniplast.[21] Double clad 1.2 mm diameter Bicron BCF 91A WLS fibres are glued into the grooves with a transparent silicon couplant. On one side of the module the fibres are routed to a 4×4 multi anode Hamamatsu M16 PMT through a cookie. On the other side of the module the fibres are gathered in a bundle and routed to a block of Plexiglas with a built-in LED pulser. A photograph of the prototype is given in Fig. 151.

The PMT signals are transmitted via a screened twisted pair ribbon cable (55 m long) amplified with a $\times 9$ gain amplifier and digitised with the LeCroy 4300 11-bit ADC.

A mixed beam of negative pions and muons with momenta up to 15 GeV/c was used in the measurements at the CERN PS T9 test beam. The following issues were addressed in these tests

- performance of individual modules (the average response to minimum ionising particles, the efficiency and uniformity across the strip planes);

[21] Uniplast Vladimir, Russia.

Figure 151: Prototype scintillator strip modules at the assembly site.

- location accuracy with a prototype scintillator strip tracker and a dummy brick target.

The modules were stacked, with their planes perpendicular to the beam, on a remotely controlled platform which could be moved vertically (along the Y axis) and horizontally (along the X axis) across the beam. This allowed to scan the sensitive area of the modules and measure their response at different positions across and along the strips.

The beam spot had a full width of about 3×5 cm^2. The trigger telescope includes scintillator counters and four multi-wire beam profile chambers (BPC's). Only non-interacting beam particles with less than 2 mip deposit in each trigger counter are selected for the analysis. Additional cuts are imposed on the beam incidence angle and impact position, as measured by the BPC's.

The module PMT's are calibrated with the LED pulser tuned so as to measure the response of each pixel to a single photoelectron. Single photoelectron signals are clearly separated from the pedestals (Fig. 152). This allows us to express raw strip signal pulse-heights (PH) in photoelectrons, defined for each strip as the PH at the maximum of its single photoelectron peak. The effect of pixel-to-pixel gain variations is eliminated.

Due to pixel-to-pixel crosstalk in a PMT, small signals (≤ 1 $p.e.$) appear in pixels adjacent to the one coupled to the hit strip. Therefore, we associate a hit in a mip event with the strip producing the largest pulse-height ($\mathrm{PH_{max}}$). Fig. 153 (left) shows the average $\mathrm{PH_{max}}$ as a function of the corresponding strip number in one module. The strip response fluctuates by 6% due to variations in scintillator strip and WLS fibre light yield, light attenuation in fibres, strip-fibre and fibre-PMT coupling, light trapping efficiency, etc., and also due to the photocathode disuniformity. Fig. 153 (right) shows the overall $\mathrm{PH_{max}}$ distribution measured at the far end of one module (at 84 cm from the PMT). The mean value of this distribution is 7.7 $p.e.$ for events with $\mathrm{PH_{max}} > 1$ $p.e.$ A single $p.e.$ signal is still recognisable in the $\mathrm{PH_{max}}$ distribution.

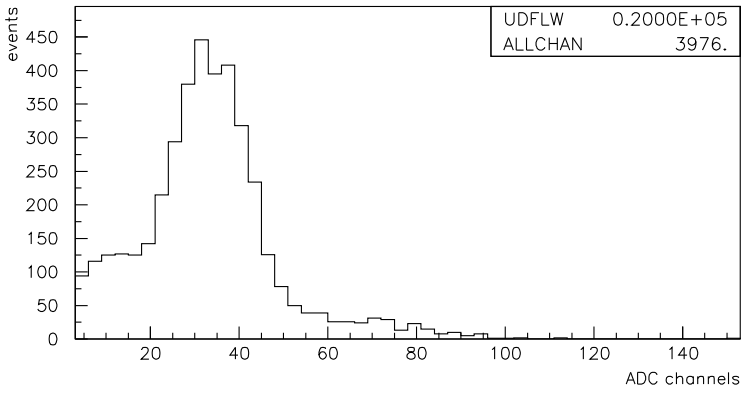

Figure 152: A typical PMT response to a LED pulse in the single photoelectron region. Pedestals are subtracted.

The inefficiency peak at zero PH is mainly due to a dead space between strips. This is illustrated by Fig. 154 showing a detailed $\langle \mathrm{PH_{max}} \rangle$ distribution around one of the strips. The peak contains about 1.5% of all *mip* events and quantifies the module hermeticity. A cut of $\mathrm{PH_{max}} < 1$ *p.e.* eliminating the cross talk signals introduces an additional inefficiency of 0.2%.

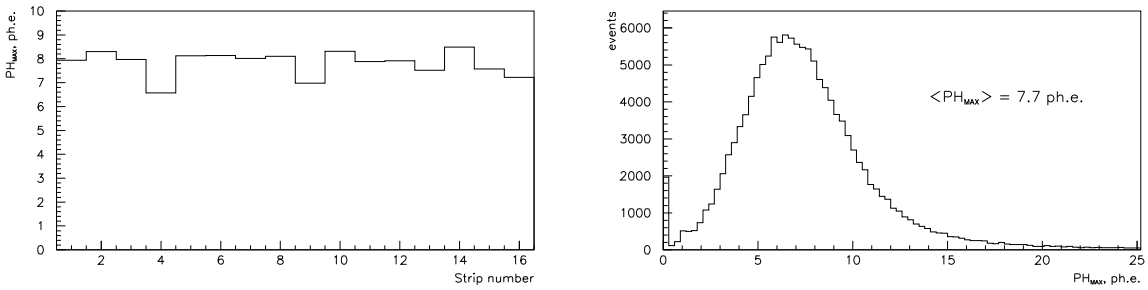

Figure 153: Scintillator strip response to a *mip* at 84 *cm* from the PMT. Left: average $\mathrm{PH_{max}}$ across one module, with each entry corresponding to a single strip. Right: the $\mathrm{PH_{max}}$ distribution in one module.

8.2.2 Tests on brick finding with scintillator strip detectors

The experimental setup simulating two OPERA target modules is shown in Fig. 155. It consists of two mini-walls of four dummy bricks, each followed by a pair of prototype scintillator strip planes oriented horizontally and vertically. The two pairs of strip planes are staggered transversally by 1 *cm* with respect to each other. Two types of dummy bricks were tested: one simulating OPERA bricks with spacers and containing 30 cells, and the other simulating compact bricks with 56 cells. In both, 1 *mm*

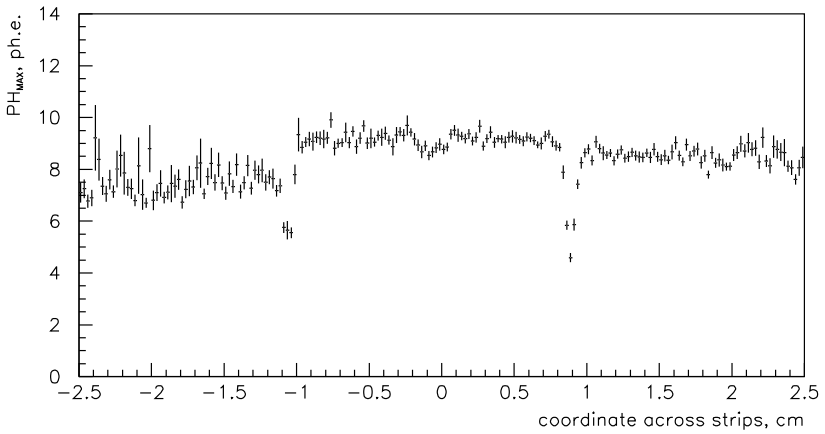

Figure 154: Average PH_{max} around one strip.

thick lead absorbers are used. The beam telescope includes the BPC's and scintillator counters C1-C3. An additional larger counter C_μ, installed downstream behind a wall of 1.6 m iron and 2 m concrete, was used to tag beam muons. The setup was exposed to 15 GeV/c mixed beam of negative pions and muons, shifted diagonally by 2.5 cm away from the brick wall centre and defocussed to illuminate the area of $\sim 5 \times 5$ cm^2 (defined by the trigger counter C1).

We analysed two types of events: muon events, simulating CC neutrino interactions with a single leading track emerging from the brick (*e.g.* quasi-elastic events), and pion interaction events simulating deep-inelastic muon-less neutrino events. Muons are selected by requiring a hit in the C_μ counter and less than 6.5 mip for the total PH in the first three strip planes. Events with no hit in C_μ and more than 6.5 mip in the first three planes are identified as pions, mostly interacting in the first brick wall.

In each scintillator strip plane, the centres of gravity of the pulse-heights are calculated. Only strips with signals above 1 *p.e.* are retained. The pulse-heights are expressed in mip units to equalise all strips. The vertex position in one projection is determined as the mean value of the centres in two planes with the same orientation. The actual beam impact point in each event is accurately measured by the BPC's. The difference Δ (vertex) between the true and the reconstructed vertex positions is plotted in Fig. 73.

For muon events with predominantly one strip hit per plane the RMS vertex resolution is 0.62 cm. The Δ (vertex) distribution for muons can be approximated by two Gaussians with σ of 0.46 cm and 1.8 cm, the broader one containing less than 1% of events.

For pion interactions the hit multiplicity is much higher (up to all 16 strips per plane) and the RMS spread in Δ (vertex) increases to 1.8 cm. The pion Δ (vertex) distribution, when approximated by two Gaussians, shows a narrow peak containing about two thirds of the events and having a σ of about 0.8 cm and a broad one with a σ of 2.2 cm.

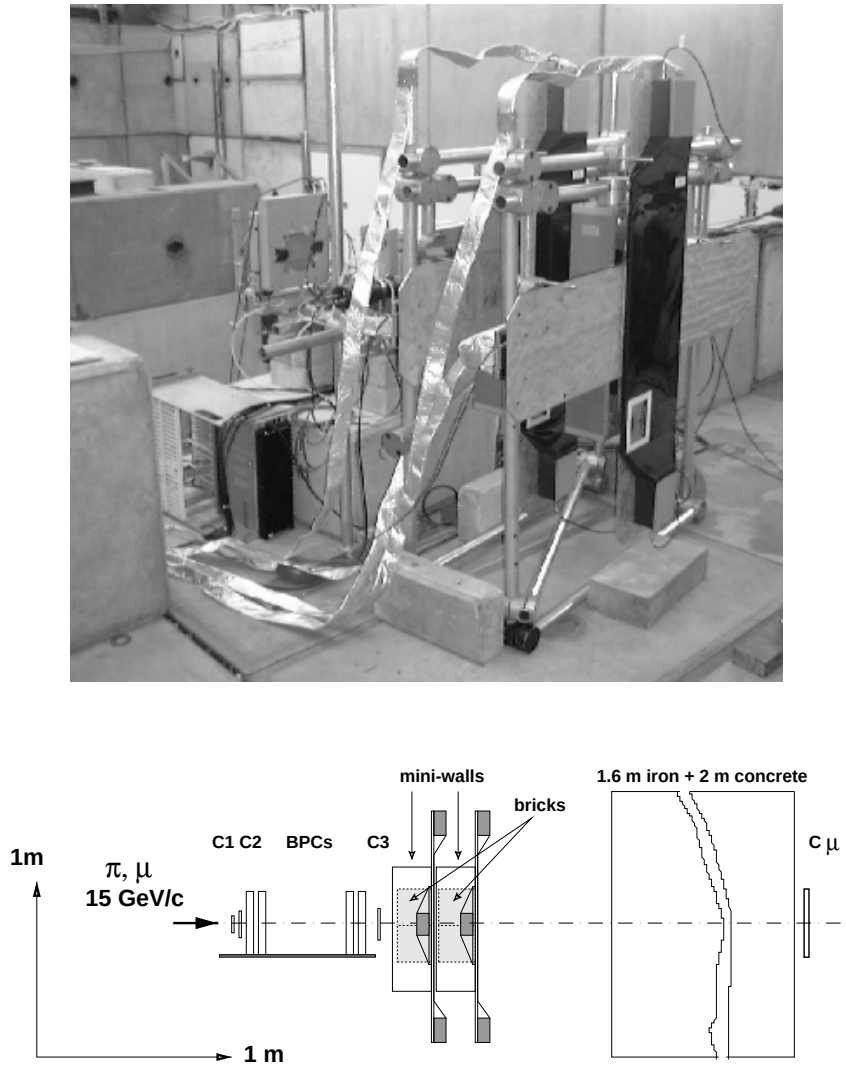

Figure 155: The experimental setup with prototype OPERA tracker mini-modules at the CERN PS T9 zone. Top: a general view. Bottom: a schematic layout of the setup.

Similar results are obtained for compact bricks. In another measurement the entire setup was turned by 100 $mrad$ with respect to the beam, to simulate an average hadronic shower angle in neutrino events. Practically no change was found for both types of bricks.

We also performed a dedicated exposure with PS T9 electrons of 1 to 6 GeV/c, tagged with two CO_2-filled Čerenkov counters.

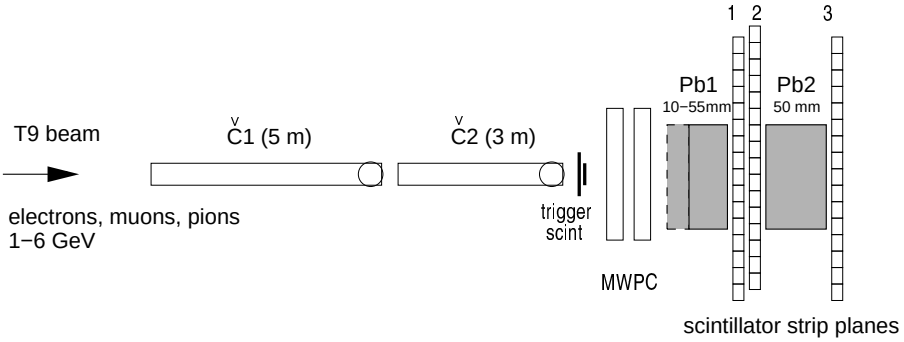

Figure 156: A schematic drawing of the experimental setup at the PS T9 test beam to study the vertex resolution and the trigger efficiency with electrons.

The setup (Fig. 156) consisted of three prototype scintillator strip planes placed horizontally behind bulk lead blocks simulating the OPERA brick walls. The thickness of the upstream block $Pb1$ could be varied from 10 to 55 mm to study the response to electrons produced at different depths in the lead target, while the thickness of the downstream block was fixed at 50 mm. The online trigger required a coincidence of Č1 and the scintillator counters in front of the setup. The impact $X - Y$ position of the beam particle was determined with an accuracy of 1 mm by means of two double-gap wire chambers.

One purpose of this test was to measure the vertex resolution for for single-electron events, the signature for the QE τ production with a subsequent $\tau \rightarrow e\nu\bar{\nu}$ decay. The vertex position was reconstructed by calculating the centre of gravity in scintillator plane 1. Fig. 157(a) shows the Δ(vertex) distribution obtained for 1 GeV/c electrons and 20 mm thick target. Fig. 157(b) shows the RMS spread of Δ(vertex) as function of target depth and electron momentum. At the target depth of $25 - 30$ mm, it is typically 5 to 7 mm. Only hits with ≥ 3 $p.e.$ were taken for the vertex reconstruction.

The second important objective of the test was to study the detection efficiency for electrons. For comparison with Monte Carlo simulations, several different trigger conditions have been used in the offline analysis. The results are displayed in Fig. 158.

Fig. 158(a) shows the detection probability for a minimum bias trigger defined as a presence of at least one hit with PH ≥ 3 $p.e.$ in either of the two consecutive tracker planes after the vertex, separated by a brick wall (planes 1 and 3 in our case). The efficiency for this trigger is $\geq 98\%$ at momenta starting from 2 GeV/c.

Fig. 158(b) corresponds to a stricter minimum bias trigger requiring a hit with PH ≥ 3 $p.e.$ in the plane immediately following the vertex brick (plane 1). Some loss in the trigger efficiency is observed in

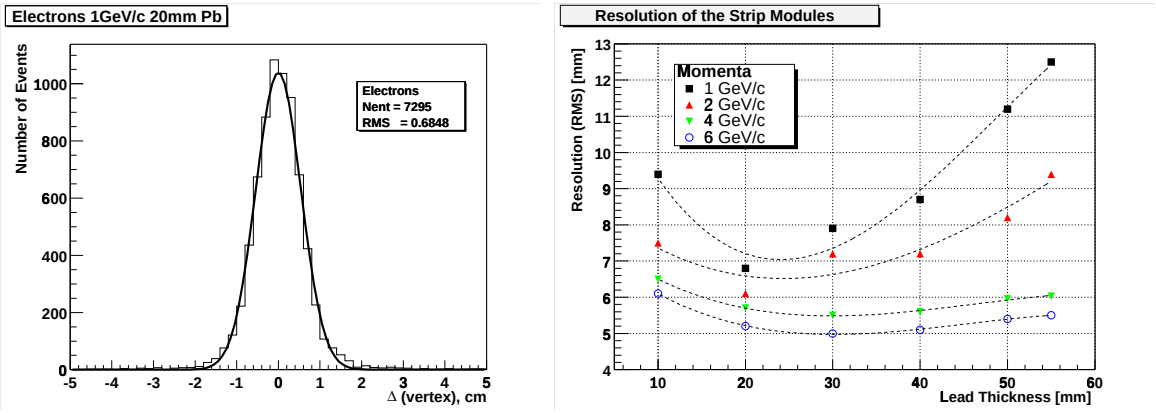

(a) (b)

Figure 157: (a): Δ(vertex) distribution obtained for 1 GeV/c electrons and 20 mm thick target. (b): Δ(vertex) RMS spread for different target depths and electron momenta.

this case only at 1 and 2 GeV/c, particularly at 10 mm. This can be explained by the fact than at these momenta the probability for an electron to traverse $1 - 2\ X_0$ without initiating a cascade is still relatively high. The detection efficiency is almost the same as for mip events and defined by the plane hermeticity (Section 8.2.1) and the cut on the strip PH.

Finally, Fig. 158(c) and (d) correspond to the OPERA electron trigger requiring at least 5 $p.e.$ signal in each of the tracker planes following the vertex brick (planes 1 and 2). For this purpose, we lowered the strip hit threshold down to 1 $p.e.$, the bare minimum required to cut off the PMT cross talk. In (c), the ≥ 5 $p.e.$ condition is applied to the sum of all hits in a plane, while in (d) a presence of at least one single hit with PH≥ 5 $p.e.$ is required in each of the planes 1 and 2.

In summary, the detection efficiency for electrons of ≥ 4 GeV/c is found to be greater than 98%. At lower momenta a significant dependence of the detection efficiency on the vertex position in the target brick is observed. For vertices located in the upstream part of the brick, the efficiency of the trigger requiring ≥ 5 $p.e.$ for total pulse-heights in two adjacent tracker planes after the vertex drops down to less than 97% at 2 GeV/c, and less than 80% at 1 GeV/c.

8.2.3 Measurements with photodetectors

A detector made of 54 scintillator strips made by different methods with three different types of WLS fibres has been tested with 15 GeV/c pions, by using an EBCCD for the readout.[22]

A MegaPixel EBCCD tube with 40 mm photocathode and demagnification of 1.61 was used. The EBCCD chip has 1024×1024 pixels with active area of 13.4×13.4 mm^2. The useful area on the photocathode is 21.4×21.4 mm^2. A total of 525 fibres with 1 mm diameter can be read out by such a

[22]The work presented here has been carried out in collaboration with S. Golovkine, I. Kreslo and A. Medvedkov (IHEP, Protvino) and with the group of G. Martellotti (INFN Rome).

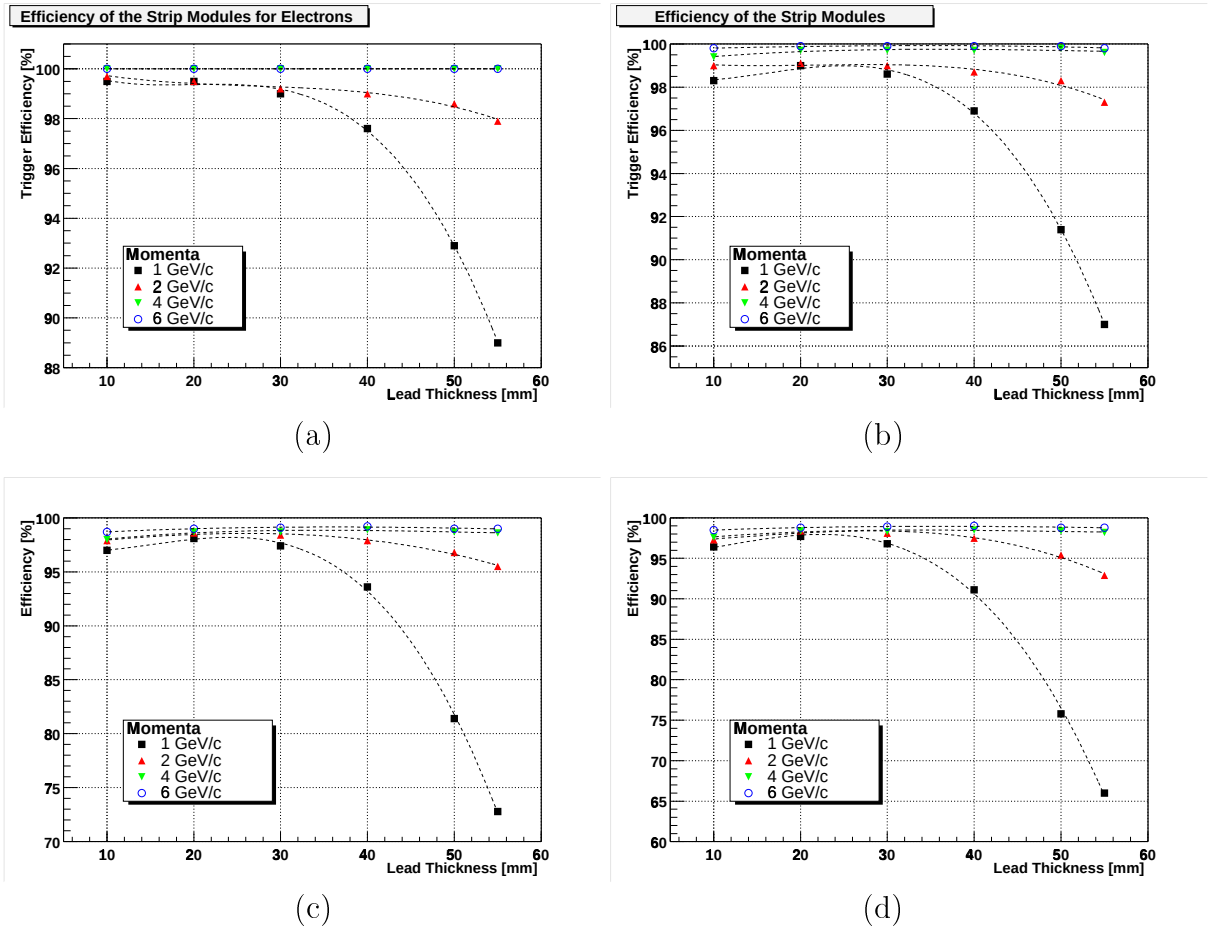

Figure 158: Trigger efficiency for single electrons at different beam momenta and target depths, for different trigger conditions: (a) – for events with at least one hit with PH $\geq$ 3 *p.e.* in either of planes 1 or 3; (b) – same, for plane 1 alone; (c) – for events with total pulse-heights of $\geq$ 5 *p.e.* in each of the planes 1 and 2 (requiring PH $\geq$ 1 *p.e.* for individual hits); (d) – for events with at least one hit with PH $\geq$ 5 *p.e.* in each of the planes 1 and 2.

tube. An Image Intensifier (II) by Geosphaera with high quantum efficiency and optimised for green light (20% at 520 nm) was coupled to the EBCCD tube in order to increase the quantum efficiency by up to a factor two. A 10 bit ADC and a frame grabber connected to a PC was used to digitise the EBCCD signals.

We tested various scintillator strips with different cross sections, produced either by extrusion or by injection moulding. The length of the strips is in the range of $30 - 75$ cm. Polystyrene scintillator was used with three combinations of dyes: 1.5% PTP + 0.01% POPOP, 1% PTP + 0.01% POPOP and 1% PPO + 0.01% POPOP. Strips are coated by different materials: Teflon, tyvec, tetratec, aluminised mylar. Three different types of double cladding WLS fibres with 1 mm diameter were used: Pol-Hi-Tech S248, Kuraray Y11, and Bicron BCF91A. The far ends of the fibres had no mirrors.

Figure 159: Typical image from the EBCCD, showing the single photoelectron signal from six WLS fibres for through-going mip.

Fig. 159 shows images of single photoelectrons from 1 mm WLS fibres 2.7 m long for a typical event, obtained from mip crossing 6 strips with cross section of 18×25 mm^2.

The test beam data are being analysed. Preliminary results are reported here. The best results were obtained with 18×25 mm^2 cross section made by extrusion, coated by tyvec with Y11 fibres. The fibres were glued at the centre of each strip. A mip produced 22.6 $p.e.$ at 1.25 m, 21 at 2.7 m and 13.4 at 5.7 m. This corresponds to a light attenuation length of 7.7 ± 1 m. For a similar strip 8.5 mm thick with the fibre glued in a groove on its surface 13.3 $p.e.$ were obtained at the distance of 2.7 m.

The same strips with 9×20 mm^2 cross section and 30 cm length made by Uniplast, previously tested with PMT readout, were also measured with EBCCD readout. A BCF91A fibre 1.2 mm in diameter and 2 m long was used. A light yield of 9 $p.e.$ at the distance of 1.85 m from the beam was measured. A light output of 7.7 $p.e.$ was obtained by PMT readout at a distance of 0.84 m. Extrapolated to the distance of 1.85 m according to the fibre attenuation curve, it corresponds to about 4.5 $p.e.$. This agrees well with the EBCCD measurement when taking into account the lower quantum efficiency of the PMT of about 10%.

We also tested three cells made of extruded white polycarbonate profiles with inner cross section of 10.4×9 mm^2 with 0.9 m length. The cells were filled with liquid scintillator EJ-399-01 (Eljen Technology, USA) and read out by Kuraray WLS fibres with 1.2 mm diameter. The result is 5.6 $p.e.$, measured at a distance of 2.5 m from the beam, 4.5 $p.e.$ at 5 m and 3.7 $p.e.$ at 6.5 m. This corresponds to an attenuation length of 9.2 ± 1 m.

A new Megapixel EBCCD chain coupled with full length (about 6 m) scintillator detector prototype has been studied in a test beam in May 2000 with a 70 GeV/c muon beam. The EBCCD has improved electronics with 12 bit ADC on the board. A compact high voltage source and gate are placed inside the housing to avoid any high voltage cables and connectors. Three different scintillator detectors, coupled simultaneously to the EBCCD chain with input useful area of 31×31 mm^2 were tested. Fibres from each detector were assembled in separate bundles, glued, cut together and coupled directly to the EBCCD chain.

The first detector was made of two 9×25 mm^2 cross section, 6 m long polystyrene scintillator strips (1.5% PTP + 0.01% POPOP) made by extrusion, coated by Tyvec with 1.2 mm Y11 fibres. We used these plastic strips as a reference. The second one was made of three cells of polycarbonate profiles with inner cross section of 9×10.4 mm^2, 6 m length filled with liquid scintillator and read out by 1.2 mm Y11 fibres. The third detector was a large polycarbonate panel with 1 m width, 6.3 m length. The panel is filled with liquid scintillator by pumping at one end. All fibres of the three detectors had mirrors on the far ends.

Fig. 160 shows the number of photoelectrons versus the distance from the photocathode for the plastic strips. 20.2 $p.e.$ were obtained at a distance of 2.5 m and 14.4 $p.e.$ at 6.5 m. An attenuation length of 11.8 m was derived. For the three cell liquid scintillator detector 9 $p.e.$ and 6.9 $p.e.$ were measured at a distance of 2.5 m and 6.5 m, respectively. This corresponds to an attenuation length of 14.3 m for 1.2 mm fibres with mirrors, to be compared with 9.2 m obtained in previous test with the same fibres but without mirrors.

Preliminary tests have been performed with HPD photodetectors readout by VA-TA front end electronics and the so-called VA-DAQ acquisition system. Details of these systems are given in Section 8.2.5. The HPD is plugged on a front end board through a 80-pin support, close to the front end chips. Fig. 161 shows a DEP 61-pixel HPD mounted on the front end board hosting the two 32-channel VA-TA chips.

The features of the HPD are summarised in Table 8.2.3.

Table 34: HPD characteristics.

photocathode	S20 bialkali
quantum efficiency (at 480 nm)	16.7 %
active area	18 mm
input window	fibre optics
number of pixels	61
operating voltage	-12 kV
diode active area par pixel	3.5 mm^2
gap between pixels	50 μm
depletion depth	300 μm
depletion voltage	60 V
capacitance	4 pF

The noise and gain variation when the detector is connected have been measured both for the slow

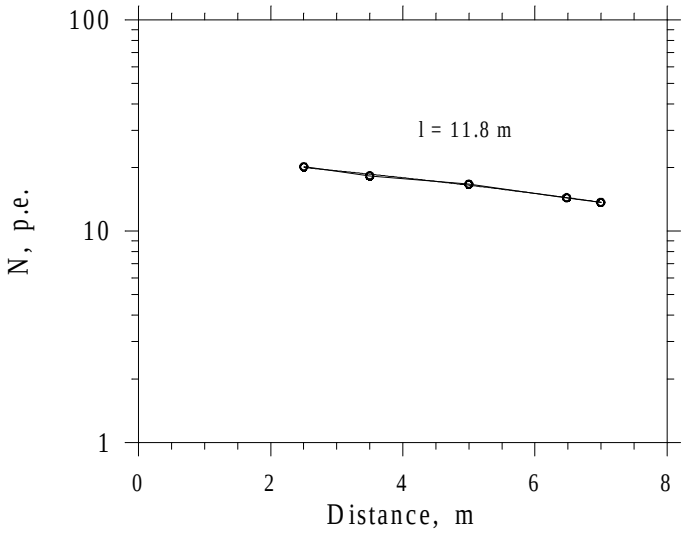

Figure 160: Photoelectron yield of minimum ionising particles obtained with scintillator strips equipped with Y11 1.2 *mm* fibres and read out by an EBCCD, plotted as a function of the distance from the photocathode.

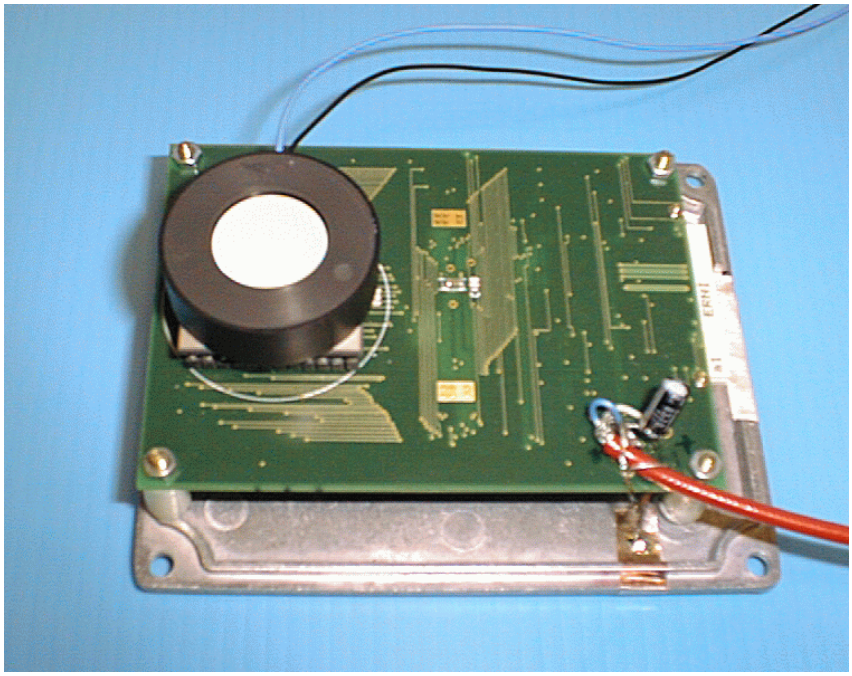

Figure 161: Photograph of the HPD-VA-TA system.

and the fast shaper. Preliminary results led to an observed increase of the noise from 450 e^- to 650 e^- for the VA and from 750 e^- to 1000 e^- for the TA. This increase is mainly due to the capacitance added at the entrance by the HPD. The spread of the TA threshold voltage is of the order of 1 $p.e.$ This implies that with the present chip it is not possible to set a threshold of the order of one photoelectron or less.

This problem can be overcome with an upgraded front end board (including shorter connections from the HPD to the chips) and a channel-to-channel adjustable threshold. For the present tests we have simply flashed one pixel with a pulsed light source (trigger pixel) and look at the neighbouring pixels. Pulses are typically 40 ns wide (longer than the LED rise time) and have 5 V amplitude. The average number of $p.e.$ on the trigger pixel is around 15 under these operating conditions.

The characteristics of the LED are given in Table 8.2.3. The repetition rate is around 500 Hz, namely the maximum readout speed of the acquisition.

Table 35: LED characteristics.

Intensity (mcd)	I (mA)	V (V)	λ (nm)
40	10	4.8	470

The light is distributed to the HPD through 70 cm long clear fibres (1 mm diameter). The fibres are collected in a cookie. The hexagonal pattern of the fibres in the cookie matches the pattern of the 61-

HPD's pixels (Fig. 162). The cookie is fixed on a box housing the HPD and the VA-TA. One can adjust the alignment of the fibres with the pixels and the distance between the end of the fibre and the edge of the photocathode. On the other side, fibres are gathered in a larger cookie with a light distributing box.

One can attenuate the light with calibrated optical filters. The system can house two HPD's with their electronics. The acquisition is outside of the box. The high voltage supply must have low ripple. We adopt the Matsusada[23] HV-15N-HP with 3 mV ripple for 15 kV. The bias voltage is provided by a floating battery box. This ensures the low noise level required by the direct connection of this bias voltage on the front end board.

Figure 162: Test setup for a HPD-VA-TA system.

Fig. 163 shows the spectrum obtained after an acquisition of 100 s, corresponding to 20000 triggers.

The following measurements are presently being performed: HPD uniformity, cross-talk and linearity. Preliminary results are encouraging. A prototype hodoscope using scintillating fibres has also been designed and tests using radioactive sources and cosmics are foreseen with the HPD-VA-TA system.

[23] Matsusada Precision Inc., 745 Aoji-cho Kusatsu Shiga 525-0041, Japan.

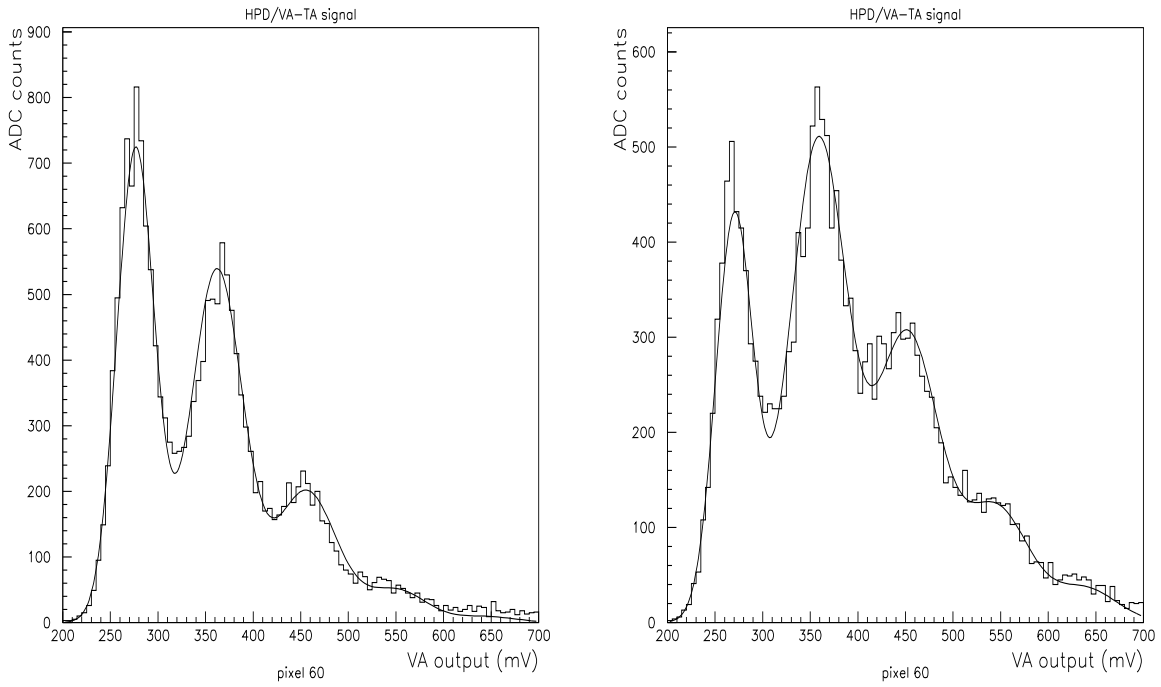

Figure 163: Spectrum of one channel near the trigger pixel for two different light yields. The photoelectrons peaks are clearly visible. A global fit has been applied to the data. The peaks are fitted with a Gaussian and the photoelectron peaks are fitted with a Poisson distribution. The mean number of photoelectrons is around 0.9 in the left plot and 1.3 in the right one.

A complete system has been designed to test the M64 PMT's (its schematic is given in Section 4.4.3). The front end electronics of this system is a two stage circuit (Fig. 164). The first one uses the differential amplifier AD8138 which provides a fixed gain of 4, while the second stage has an adjustable gain of up to 5 and a buffer (BUF601) which transmits the signal to the ADC. Between the two stages, a splitting system can also provide an output for an electronic discriminator.

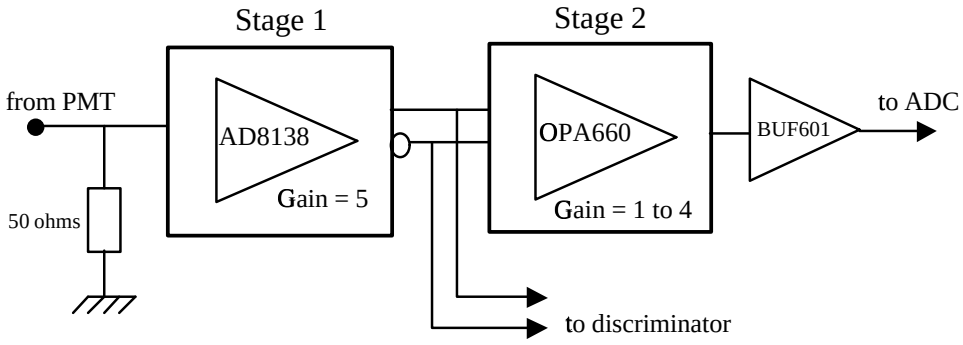

Figure 164: Schematic view of the front end electronics used for the PMT tests.

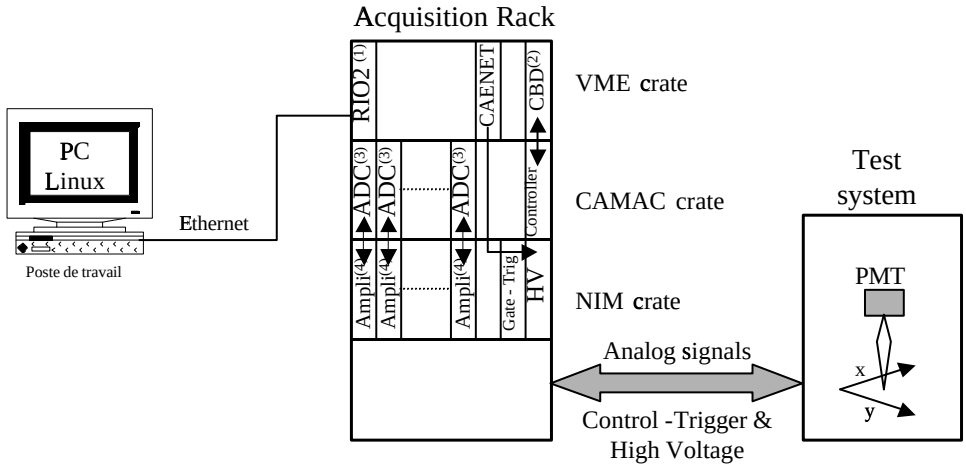

(1) : CES VME processor card (RIO2 8062) based on PowerPC 604e
(2) : CBD (CAMAC Branch Driver)
(3) : ADC Lecroy 2249 W
(4) : Amplifier card developed at IReS

Figure 165: Schematic view of the acquisition system used for the PMT tests.

The charge measurement is done by a Lecroy CAMAC ADC 2249W. The data readout and the setup of the acquisition is controlled by a VME processor and a VME CBD (Fig. 165). The data flow, data recording and run control are managed by the CASCADE software [92]. The processor controls the

$X - Y$ table motion and position with steps of 12.5 μm.

8.2.4 Tests of RPC detectors

Preliminary tests have been performed with RPC detectors both at Gran Sasso and LNF laboratories. The experimental setup consists of two-sided RPC chambers (70 $cm \times 60$ cm) produced by industry, [24] following the scheme shown in Fig. 57.

Bakelite with smooth surface and frames made of Lexan have been used. In fact, for the BABAR chambers the main source of dark current is the ohmic conductivity of the vetronite frames.

The chamber active area was filled with an inflammable mixture of Argon (48%), Isobutane (4%), and C2H2F4 (48%) at atmospheric pressure. Chambers were operated at different high voltage in order to determine the working point of the plateau. The current drawn at voltages higher than the plateau values is of the order of few tens of nA, confirming the improved performance of the new design.

Each chamber is equipped with one plane of copper pickup strips, with a pitch of 30 mm and 2 mm separation. Induced signals were discriminated and simply counted. Preliminary results at Gran Sasso indicate a single counting rate in the plateau region of the order of 100 Hz/m^2 and a $0.6 - 0.8$ Hz/m^2 rate for the coincidence of two closely adjacent chambers.

Studies of RPC performance will be pursued with different gas mixture, below the flammable limit and different strip pitch widths. The detection efficiency and the spatial resolution will be measured and front end electronics will be tested.

8.2.5 Tests of electronics

Various tests have been performed on the front end electronics and the data acquisition system.

In particular the VA-TA front end chips have been studied for the readout of HPD's (see Section 4.4.4). Two shaper amplifiers share the same preamplifier outputs. One has a peaking time of 75 ns (the TA chip) and is used to trigger the other one (the VA chip) which has a peaking time of the order of 2 μs.

In the VA the outputs of the preamplifier enter a multiplexer. Its switches are controlled by a bit-register running in parallel. The output of the multiplexer goes to the output of the chip via a buffer. Only one of the channels is seen on the output at a readout step. The speed of readout is then limited by the multiplexer clock which makes the bit in the register ripple from one channel to the next. The clock frequency is 10 MHz. This chain is triggered by an event and the sampling is performed after a hold delay which matches the value of the peaking time. The chip can be operated in test mode via another multiplexer/bit-register on the input running in parallel with the output multiplexer.

Each channel in the trigger chip is followed by a level-sensitive discriminator, with adjustable threshold, a serial shift-register to select the channels allowed to trigger and a monostable. The outputs are ORed together to give a single trigger for the whole chip.

[24] General Tecnica S.r.l., Frosinone, Italy.

The acquisition system (VA-DAQ) used for the tests was designed by IDE AS. The VA-DAQ is fully controlled through the parallel port of the PC by LabVIEW executables. This software permits the measurements of the performance of the chips and also the data acquisition from a detector. Relevant parameters are the bias settings, the pedestal and noise measurements, the gain measurement, the control of the peaking time, the signal profile as a function of the input charge.

The biases are adjustable via the software applications and they affect the VA signal waveform. Once the performance of the chip have been scanned one can set the optimal biases for the application. Our choices were guided by the requirement of the lowest level of noise. This is critical for HPD's. With a typical noise of 700 e^- ENC, the signal/noise ratio amounts to about 6.

The common mode noise (of the order of 4 mV for one chip) can be subtracted. The gain is measured in a calibration mode in which a charge is injected into the chip via an external 1.8 pF capacitor. Symmetric measurements are performed for the fast trigger chip (TA). The scan over a threshold voltage range gives, for a particular calibration charge, the threshold for which each channel starts triggering. The threshold is set at 50% trigger efficiency. This procedure also defines the noise of the channel which is scanned. The standard deviation of the threshold is around 4 mV. The results for two 32 channel VA-TA chips are summarised in Table 36.

Table 36: VA32c and TA32c performance. The numbers in parenthesis refers to the results obtained with a HPD plugged onto the front end board with a 60 V bias and operated at 10 kV. TA-thresholds are evaluated for a 4 fC injected charge.

VA32c		
	average gain (mV/fC)	150 (130)
	noise (e^- ENC)	450 (700)
	pedestals (mV)	230 (300)
TA32c		
	average gain (mV/fC)	15 (12)
	noise (e^- ENC)	750 (1000)

The linearity of the front end electronics over the full required dynamic range ($1 - 200$ $p.e.$ corresponding to $0.6 - 120$ fC) can be checked in the calibration mode. The VA is linear in the range ± 11.5 fC. The ability of the fast shaper to set a low threshold is a crucial issue. In a calibration mode the lower limit corresponds to an injected charge of 1.5 fC.

The VA-DAQ system performs the data acquisition through a 14-bit ADC (AD7871 from Analog Devices). The readout of a single channel is done at a rate of 10 $k\,events/s$. The readout rate of the 64 channels drops to 500 $events/s$ for a standard PC running Windows-95. The acquisition software divides the collection of data in cycles of adjustable duration. Results obtained with that acquisition system are shown in Section 8.2.3.

8.3 Measurement of the muon scattering background

A test experiment to measure large-angle muon scattering in lead plates of the OPERA target bricks had been performed at the CERN PS in May 2000. The setup (Fig. 166) consisting of a 2 m iron dump, a dipolar muon spectrometer, the target and MWPC trackers was exposed to the 13 GeV/c mixed T9 test beam.

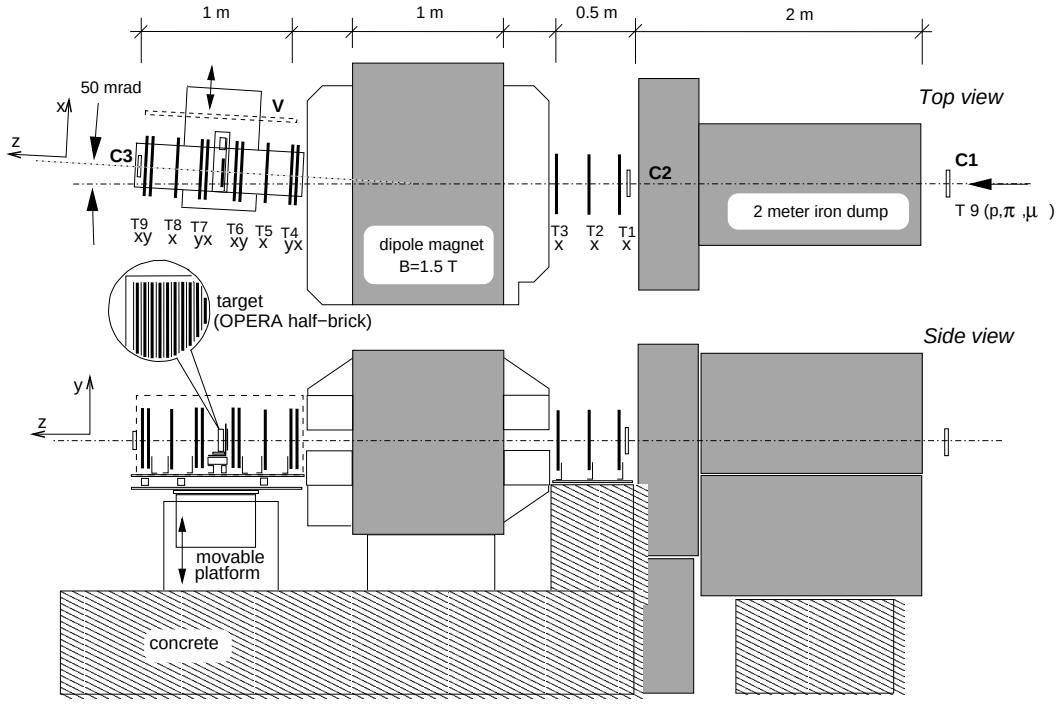

Figure 166: The experimental setup to study muon scattering in the PS T9 beam.

The iron dump (and, partially, the magnet yoke) served to absorb hadrons of the beam and obtain a muon beam with a mean momentum of 9.1 GeV/c and hadronic contamination of less than 0.1% above 8 GeV/c. Muons were selected by a coincidence of scintillator counters $C1$, $C2$ and $C3$ defining the incoming and outgoing particle areas of $6 \times 6\ cm^2$ ($C2$) and $10 \times 10\ cm^2$ ($C3$), respectively. Background side muons were tagged by the veto counter V. The downstream arm of the setup was rotated by 53 $mrad$ in the bending plane to match the most probable muon momentum of about 10 GeV/c. The maximum raw muon rate on $C2$ was ~ 900 particles per 350 ms spill.

Muon tracks were measured with three trackers, each consisting of three wire chambers separated by 20 cm gaps. The chambers, equipped with delay-line readouts and bipolar signal shapers, had an accuracy of $300 - 350\ \mu m$ within the useful area of $8 \times 8\ cm^2$. Four chambers ($T4$, $T6$, $T7$ and $T9$) [93], were capable of measuring two projections (X and Y), while the other five [25] only the X projection.

[25] These chambers, constructed at ITEP (Moscow) had a larger sensitive area and a different mechanical design.

The upstream tracker $T1$-3 between the dump and the dipole magnet measured the incoming track in the bending plane (X-projection). The middle tracker $T4$-6 between the magnet and the target served for two purposes: to measure the beam particle's deflection in the magnet and to determine its position and the angle at the target.

The downstream tracker $T7$-9 measured the parameters of the track emerging from the target. Using X-Y chambers, the events with scattering in the target could be reconstructed in space. The middle chamber in each tracker provided a redundant measurement in X-projection, required to eliminate occasional background events with overlay tracks and δ-rays.[26]

The muon momentum was determined by a deflection in the 17 cm wide air gap of the 1.5 T dipole magnet with the effective field length of 118 cm. The resolution $\Delta p/p \approx 0.006 \times p(GeV/c)$ corresponds to the 3 $mrad$ measurement error of the deflection angle. The redundant momentum measurement by the positional displacement of the track at $T6$ with respect to the extrapolation from $T1$-3 was found to be very effective for rejection of overlaying incoming tracks and muons scattered off the magnet yoke. Fig. 167 shows the measured spectrum of muons satisfying the trigger and incoming track quality conditions.

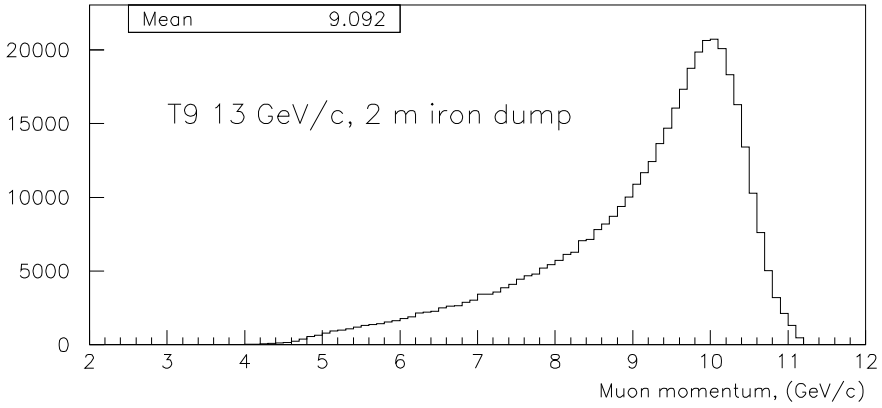

Figure 167: The measured momentum distribution of the muon beam after the 2 m iron dump. The primary T9 momentum is 13 GeV/c.

As the main target in this experiment we used a half of an OPERA brick, composed of 28 1 mm thick lead plates interleaved with emulsion films. During the exposure, the electronic trackers recorded all muons satisfying the trigger and crossing the target. The kink candidates were tagged by a large angular difference between track segments before and after the target. For these events, the predictions for the incoming track position and angle at the target were obtained from the tracker data, for subsequent

[26] MWPC with a delay-line readout are unable to reliably identify events with two charged particles crossing the chamber next to each other. However, hit positions in such events are distorted and the resulting track appears as a broken, rather than a straight, line.

search for the scattering vertices inside the brick and checking whether or not they represent genuine kinks.

In order to explore rates of large angle scattering down to $\leq 10^{-5} N_\mu$ for a 2 mm lead scatterer, the equivalent number of muons on the 28 mm stack has to be of the order of 10^5 or more. However, for a a reliable track prediction with our trackers, the track density should not exceed 10 cm^{-2} or, taking into account the beam profile, ~ 500 tracks over the useful area of 8×8 cm^2. To overcome this limitation, we have used the technique of a movable emulsion sheet, in which a separate sheet of emulsion pressed against the upstream surface of the target was periodically shifted during the exposure by 100 μm across the beam, by means of a PC-controlled stepper mechanism. This technique permitted to identify the incoming tracks stored in the upstream emulsion film at every movable sheet position. With this method, the total exposure was limited only by the number of the shifter steps (200 in our case), and the required level of 10^5 muons could be reached.

To further increase the statistics the same brick target was exposed three times, at three different angles (-6°, 0°, and $+6^\circ$) to the beam axis. The trigger rate during these exposures was about 50 events per spill and the movable sheet was shifted every 10 spills. The dead time due to data acquisition was 2%.

Besides this measurements with the lead/emulsion brick target, we took data with passive 2 mm and 7 mm thick lead targets, as well as without target (empty target), to estimate the large-angle muon scattering rate from electronic measurements alone. The empty-target rate was subtracted from the rates with real targets, to remove effects of the tracker resolution, δ-rays and scattering outside the target. For alignment and calibration purposes, empty-target data were also taken at different beam momenta, with and without dump.

Fig. 168 shows the angular and positional resolutions at the target, for tracks measured in empty-target runs. The scattering angle is measured with the average accuracy of better than 1.6 $mrad$, while the impact parameter with the accuracy of about 0.5 mm. The measurements with passive targets were done at a highest possible recording rate (210 events per spill, on average).

The event statistics accumulated in this test experiment is summarised in Table 37. Fiducial area and incoming track quality cuts retain about 72% of the raw data.

Table 37: Event statistics of the muon scattering measurement.

Target, thickness	Recorded events (/1000)	after cuts (/1000)
Lead-emulsion, 28 mm	307	221
Empty, 0 mm	2453	1828
Lead, 2 mm	4058	2948
Lead, 7 mm	502	366

Fig. 169 shows an example of a kink candidate event with a measured p_t of 267 MeV/c. The raw rate of such events observed in electronic trackers is consistent with the limit of 4.1×10^{-5} N_μ derived

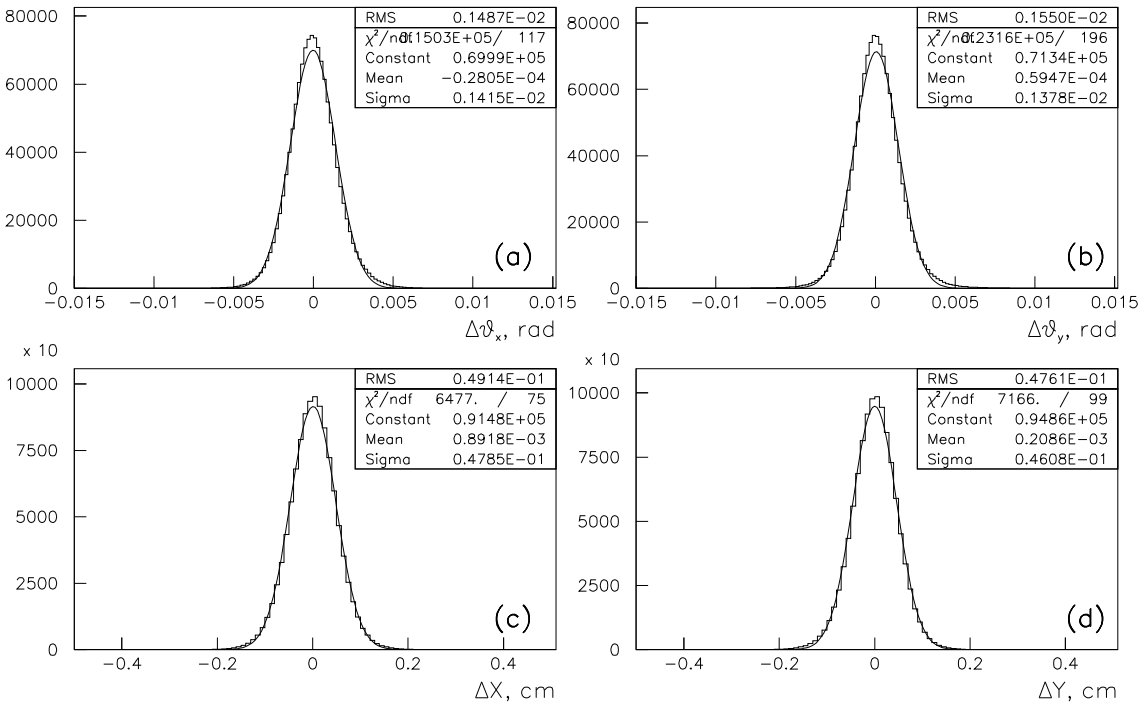

Figure 168: Distributions of the apparent scattering angle (a,b) and the impact parameter (c,d) in X and Y projections, for tracks measured without scattering target. The Gaussian fits are only to quantify the distribution widths.

from the CHORUS measurements (Section 7.4.4), but it is premature to quote any firm result yet. The data analysis of both emulsion and passive target exposures is continuing.

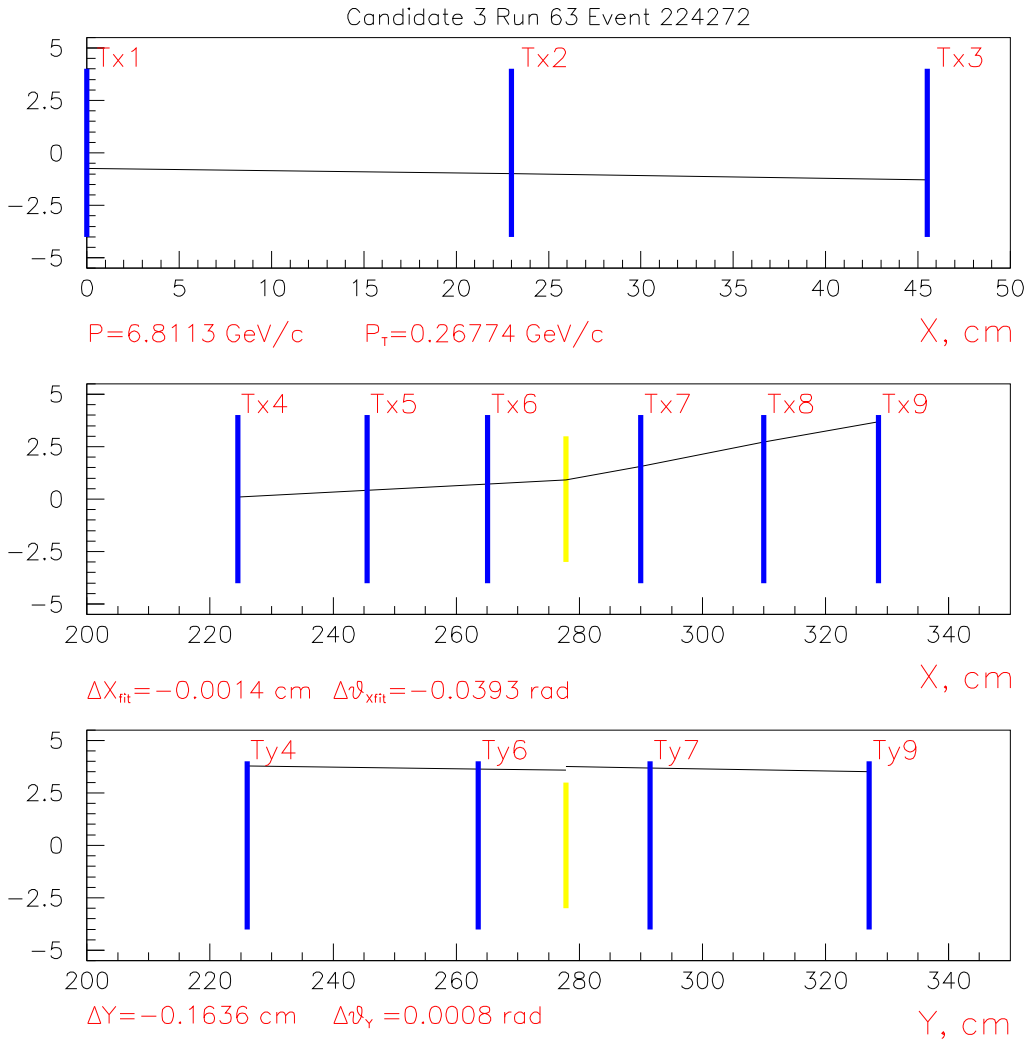

Figure 169: Example of a large-angle scattering event observed with the 2 mm passive target. Top box: chambers $T1-T3$ (X-projection), middle box: chambers $T4-T9$ (X-projection), bottom box: chambers $T4-T9$ (Y-projection). In this event, scattering angles $\Delta\theta_x = 39.3\ mrad$, $\Delta\theta_y = 0.8\ mrad$ and impact parameters $\Delta X \approx 0\ mm$, $\Delta Y = 1.6\ mm$ are observed for a 6.8 GeV/c muon.

9 Detector options, developments and R&D

In this Section we report on studies on additional detector and technological solutions. In some cases we deal with alternative detector options which have not been retained in the baseline experiment design outlined in this Proposal. Some of the issues, instead, concern further developments with the aim of improving the potential of the experiment.

9.1 Other detector options

9.1.1 Bricks

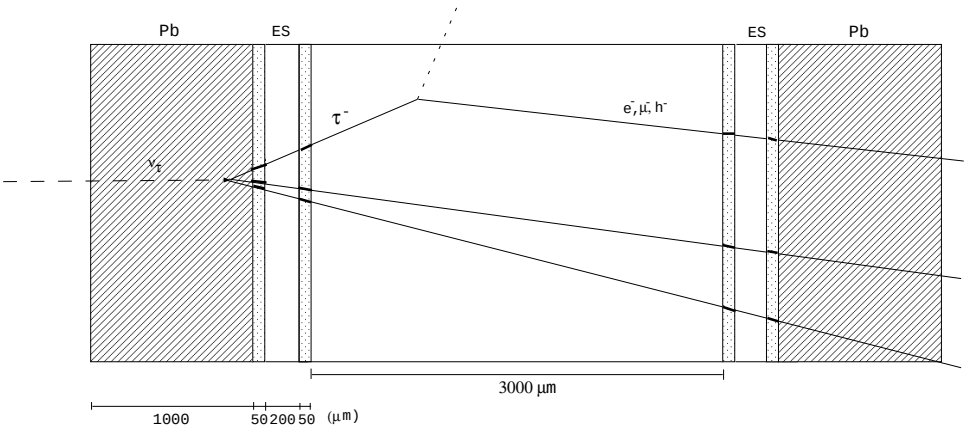

Figure 170: Schematic structure of a spacer cell.

A possible ECC cell structure (called *spacer cell*) foresees the insertion of a low density spacer between consecutive emulsion films [3–6] (Fig. 170). The gap between the emulsion films allows direct detection of the τ decay kink, as with the compact cell of Fig. 3. In this case, however, the low density of the spacer makes the hadron reinteraction probability negligible. This results in a substantial background reduction for the τ hadronic decay channels, which have the largest branching ratio. A possible design foresees a cell composed of a 1 mm thick lead plate followed by a film, a spacer of 3 mm and another film, as shown in Fig. 170. A brick can be built by stacking 30 cells with 14 cm thickness (5 X_0).

The main requirements for the spacer material are a low density, adequate mechanical properties and a low radioactivity. Several possibilities have been envisaged: Rohacell, PVC, polystyrene foam, paper honeycomb. For all these materials, the density is lower than 35 kg/m^3, *i.e.* within the experiment requirements. We have performed test measurements on prototypes. Satisfactory results have been obtained with Rohacell and polystyrene foam, the latter being about five times cheaper. Rohacell density is 31 kg/m^3. With polystyrene one could reach 25 kg/m^3. Since density uniformity is also an issue, honeycomb structures does not seem to be an appropriate choice.

In [6] we have evaluated the performance of supermodules built with spacer bricks. Further studies will be needed to study the capability of electron identification and of momentum measurement by

multiple scattering, given the smaller thickness of a spacer brick in terms of radiation lengths (5 X_0), as compared to compact bricks.

9.1.2 Brick packing

An alternative brick packing method based on the use of plastic boxes is being studied. The idea is to employ a box without cover into which lead and emulsion films are stacked. A plastic cover is then welded onto the top of the box by an ultrasonic technique.

Acrylonitrile Butadiene Styrene (ABS) boxes turn out to be dull to light and well sealed with the closing lid (ultrasonic welding). The plastic container eases the brick manipulation and allows a precise positioning of the brick (and consequently of the emulsion films) on the wall mechanical support. On the box it is possible to place appropriate grips and templates to facilitate gripping and centring during the manipulation. The box thickness does not exceed 2 mm.

Early prototypes of plastic boxes have been produced by gluing together the box walls and by welding the base and the cover by ultrasonic technique. These prototypes were not vacuum proof due to gluing instead of welding and of defects in the corners of the glued parts. We plan to build prototypes of moulded boxes without cover and to test the vacuum tightness after welding the cover. The plastic box option, if successful, could be a possible alternative to the origami packing, giving an improved precision of the brick dimensions and a smoother movement inside the wall structure during brick installation and removal.

We have started in collaboration with industry [27] the development of a BAM for packing bricks closed in plastic boxes. A design of such a machine is shown in Fig. 171. A pallet line conveyor feeds the boxes. The latter are transferred on a rotating table that handles them and stops precisely in correspondence of the stations loading the lead plates and the emulsion films (number of complete turns on the rotating table equal to the number of layers required).

The loading of the lead plates and of the emulsion films relies on two automatic stations, which take the components from rotating tables used for storage. The sampling and loading of the lead plates is made by a pneumatic manipulator. The emulsion films are taken with the help singularised with the help of a man-like robot. Intermediate stops are done to check the thickness of the plates and to avoid the accidental loading of more than one plate (or film).

After filling the box is transferred again on the pallet line conveyor for closing. The lid is sampled from a rotating table warehouse and loaded by a pneumatic manipulator. The box then proceeds under the ultrasonic welding machine that seals the lid. Before unloading, a bar code is applied on the box to file production data such as date, hour and any features of the content. To comply with production schedule two twin machines have to operate under servo-control by a central pallet line. The entire production line is held in a dark and air conditioned room.

On the pallet line, in correspondence of the ultrasonic welding machine, it is possible to insert a bell with the internal welding sonotrode to produce the vacuum inside the boxes before sealing.

[27] Primon F.lli S.r.l., Crusinallo di Omegna (VB), Italy.

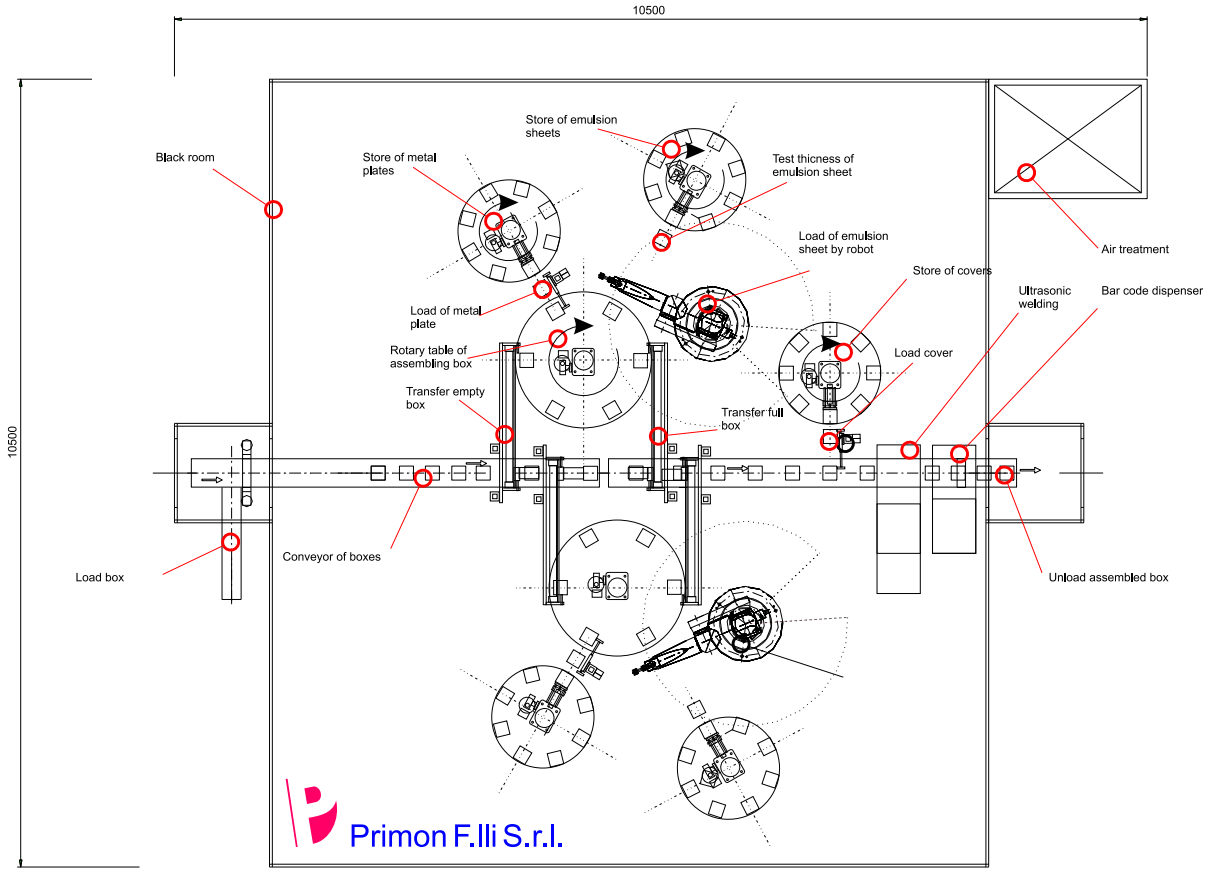

Figure 171: Brick assembly machine for bricks with plastic box.

9.1.3 Wall support structures

An alternative approach for brick support, installation and removal foresees a vertical movement of ladders where bricks are allocated. In this case, the ladder strings shown in Fig. 172 are used both as weight support and as brick carriers for installation and replacement.

As a possible merit of this structure with respect to the baseline option, three detector sides (up, left and right) are fully available to install and access the tracker readout electronics. A disadvantage is given by the interference of the ladder pulling system with the hall cranes. The design of a structure with reduced height is under investigation. The brick handling can be automated.

One ladder string consists of thin shelves supported by eight carbon-fibre strips with a width of 10 mm and a thickness of 0.2 mm. The total length is 6.7 m, corresponding to a 64 brick load. The tolerable weight of the structure is calculated to be ~ 4 ton, which is about eight times the mass of one ladder (~ 530 kg). The extra detector mass given by the support structure is only 0.3% of the target mass.

The string is hung by a wire to the top support made by an I-beam matrix supporting the ladder strings. The wires have a latching mechanism at the top, which allows to release the ladder from the support when brick replacement is required.

Two prototype ladders have been constructed. Their lengths are 1 m and ~ 3 m. Using these prototypes, preliminary tests on the load tolerance, on the procedure for ladder construction and on the required mechanical tolerance for inserting and extracting bricks have been performed.

Brick can be replaced as follows. Firstly the string which contains the selected brick is hung from the top crane. The latching mechanics is at the top part of the ladder. After releasing the latch, the ladder starts to go down. When the position of the lowest brick comes to the right place for extraction, the automatic machine situated at the bottom fixes the shelf and extracts the brick to the stack position on the roller conveyor. By the same procedure, all the bricks placed below the selected brick are extracted and stored in the stacking position by the roller conveyer. When the brick is extracted, a new brick can be inserted into the ladder. The re-insertion of the extracted bricks is repeated by lifting up the ladder. After completion, the top crane sets the ladder on the support.

The average time needed for the replacement of one brick is estimated to be about one hour. Since about 10 bricks are replaced per day per supermodule, the procedure can be accomplished within one shift per day.

9.1.4 Electronic trackers

Alternative designs have been proposed and studied for the electronic trackers in the target and in the spectrometer. These solutions are the complementary of the baseline options: scintillator strip in the spectrometers and RPC's in the target. The motivations for the baseline options have already been stressed in Sections 4.4 and 4.5. For the Target Trackers the analog readout of the scintillator system gives a larger brick finding efficiency than the digital RPC system. The performance is similar for the energy measurement and the muon tracking. The lower cost and the simplest insertion of the RPC planes in the spectrometers justify the choice of this technique as baseline for the Inner Trackers.

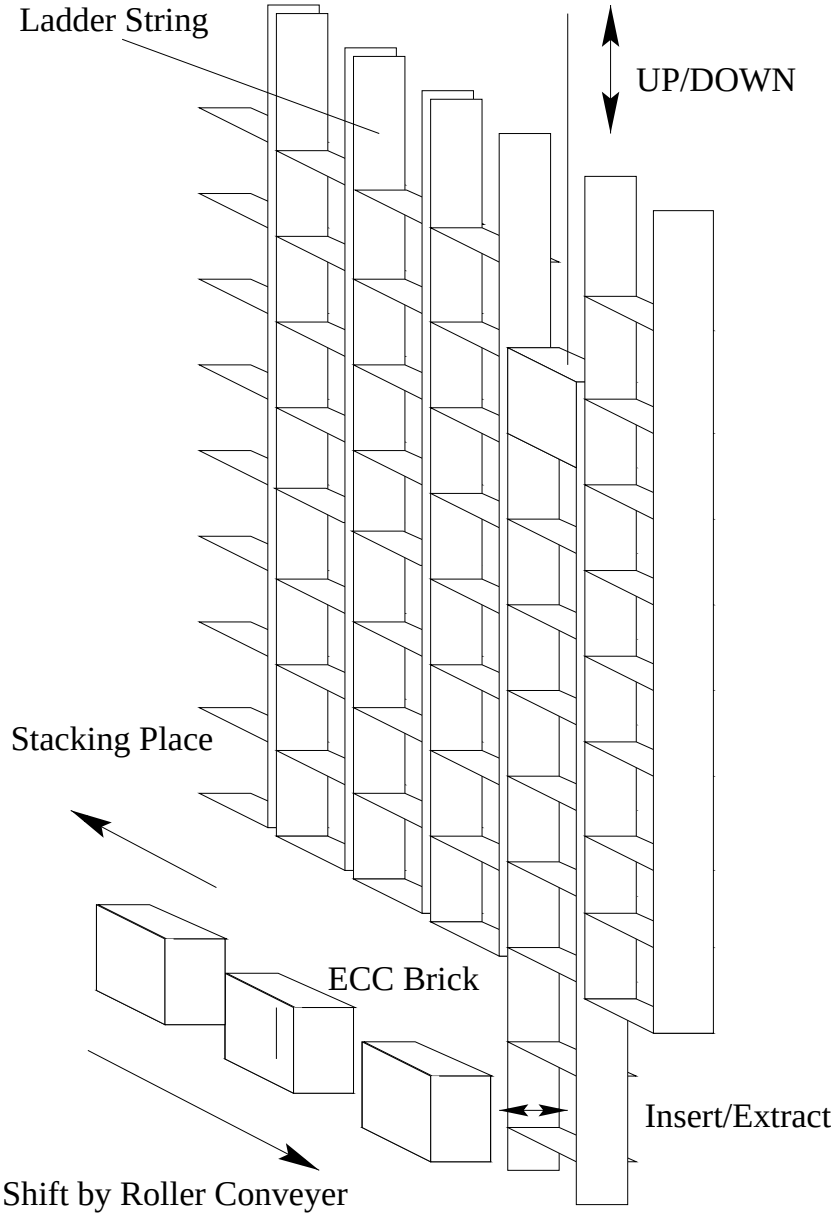

Figure 172: Ladder string wall (schematic view).

Nevertheless, the possibility to use scintillators in the spectrometer can be considered, in order to have a slightly better measurement of the energy (relevant for the NC/CC study, for example). Furthermore, the scintillator system can be calibrated with roughly the same procedure than the one which has been defined for the Target Trackers. The scintillator technique has already proven to be suitable for a spectrometer [38].

The scintillator strips are equipped with WLS fibres, as in the target region. Scintillator planes are made of 4 cm wide and 1 cm thick strips, very similar to those used by MINOS [38]. The strips in two consecutive gaps are alternatively arranged horizontally and vertically. The WLS fibres, 1 mm diameter, are read out by multi-pixel analog photodetectors as for the Target Trackers. The photodetectors must not be affected by the presence of the magnetic field. This is the case for the proximity focused HPD's which are almost insensitive. For the multi anode PMT's one has to be careful, although the MINOS measurements indicate that the perturbations are less than 10 % for up to 10 Gauss magnetic fields.

A possible scheme for the insertion of the scintillator modules in the 2 cm gap between the iron plates is shown in Fig. 173. For horizontal strips, each plane is split along the vertical axis in two halves, each half containing 200 strips of 4.4 m length. The WLS fibres are read out from each of the magnet sides. A mirror is sputtered on the other end of the fibre. Assuming the light yield shown in Fig. 44 for a 1 mm diameter fibre and a mirror reflectivity of 80%, the efficiency for the detection of a mip exceeds 97% even at the strip end far from the photodetector. A typical mirror reflectivity of 80% with smaller diameter fibres (0.5 mm) has been achieved by CHORUS. Similarly, each plane made of vertical strips is split along a horizontal axis. Each half contains 220 strips of 4 m length. The light is read out in correspondence of the middle plane of the magnet, while the other end of the fibre is equipped with a mirror. The light is transferred to clear fibres to reach the photodetectors located on both sides of the magnet, so that the length of the longest clear fibres is only slightly over 4 m.

The total length of the fibres does not exceed 10 m, which corresponds to the longest fibre used and tested in MINOS with a full length prototype. The two half walls are 1 cm thick and are longitudinally displaced from each other along the beam axis to allow fanning out of the clear fibres. The largest inefficiency along the strip reaches 6% for a mip at the far end from the photodetector. This follows from the same assumptions as above, a 10 m attenuation length for clear fibres and a loss of 10% at the fibres connection.

This geometry avoids dead space at the top and bottom of the magnet. The strips which run along the bolts and screws used for the iron plates assembly can be made wider to allow a circular cut without intercepting the fibre.

The strips are assembled, prior to installation, in light-tight sleeves with 1 mm walls. The size of the modules has to match the space between the bolts of the iron plates of the magnet. The magnet is assembled by installing the sleeves after the corresponding iron layers.

9.1.5 Magnet design

An alternative option for the spectrometer magnets is based on the use of iron toroids [6]. Each magnet is subdivided into 17 sandwiches, each made of a 3 cm thick steel plate and of an inner tracker plane. 1 cm thick planes of plastic scintillator strips are possible replacements for the RPC's as Inner Trackers.

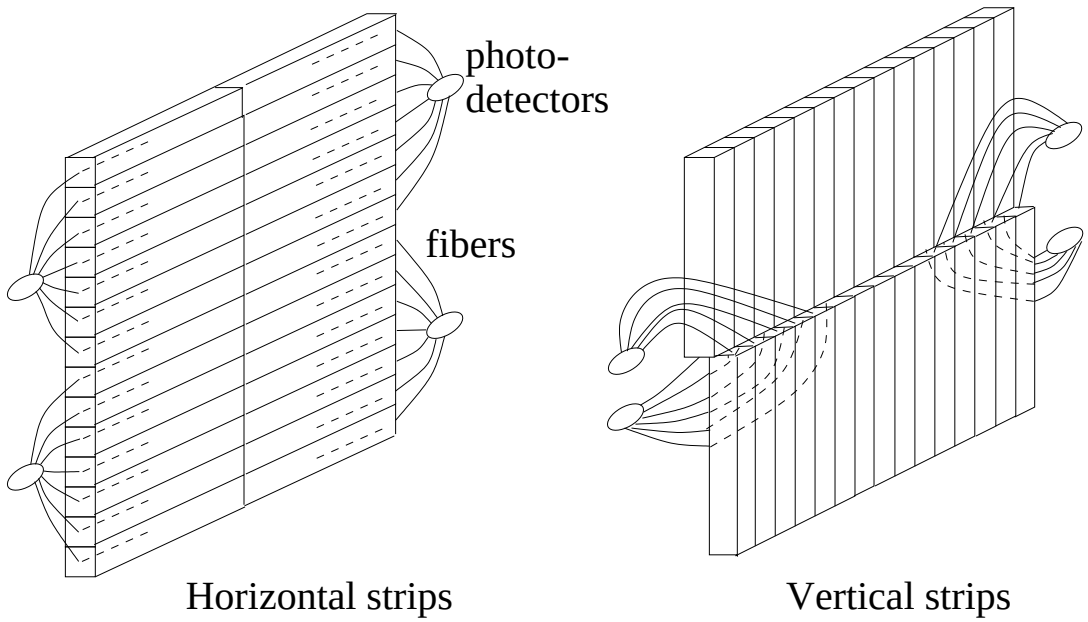

Figure 173: Schematics of the scintillator strips readout in the spectrometer.

They can be mounted inside a 3 cm gap leaving space for the fixation system. The overall length of one magnet is 102 cm. The spectrometer consists of two magnets. Its overall volume is $7.5 \times 7.5 \times 3.1$ m^3 and its weight 400 ton (Fig. 174).

The steel plates are similar in size and magnetic requirements to those foreseen for MINOS, except for their circular shape. Extensive use has been made of the information available from the MINOS Technical Design [38] and the published NuMi notes. A carbon content in the steel plates in the range $0.04 - 0.06\%$ has been found adequate for the BABAR return yoke [94] and for the MINOS magnets [38].

Plates of up to 3.75 m wide and 3 cm thick with no practical limitation in length can be produced by industry. Therefore, each steel plate could in principle be constructed by cutting and assembling together two 3.75 m wide and 3 cm thick plates. The total weight of a steel plate is 11 ton, giving 187 ton per magnet.

Other assembly schemes are being studied. One can envisage the use of two layers made of 1.5 cm thick plates. The plates in one layer are perpendicular to those in the other layer. This criss-cross pattern could improve the flatness and result in an easier construction while ensuring an equally good rigidity to the assembly.

Various magnet suspension methods are being considered. In the MINOS design, magnets hang on support rails by extension ears placed above their centre of gravity and stabilised in position by axial restraints. This design is attractive in terms of mechanical stability and accuracy in positioning. The suspension has to be studied in relation to anti-seismic specifications.

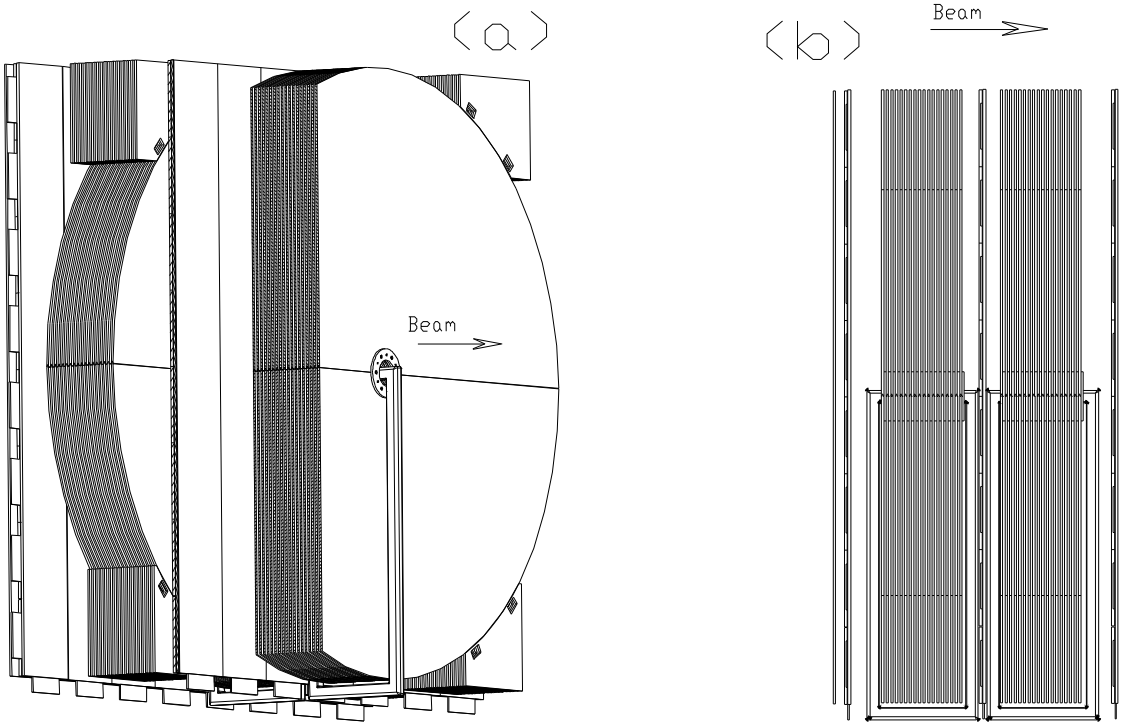

Figure 174: (a) 3D view of the spectrometer showing the two toroidal magnets (each made of 17 circular iron plates of 3 *cm* thickness) the magnet coil, the upstream and middle X and Y Precision Trackers (drift tubes) and the upstream RPC plane. For clarity, a cut is made through the middle tracker and the downstream magnet. The downstream Precision Tracker and the Inner Trackers are not shown. (b) 2D longitudinal view showing all the Precision Trackers.

Each magnet has its own coil which induces a toroidal magnetic flux density of 1.5 T averaged over the surface of each steel plate. The coil runs alongside the bottom of the magnet. Between the two magnets and their adjacent Precision Trackers, space has to be provided to host the coil legs. The coil goes through a 10 cm bore centred on the octagons. It delivers 15000 $A - turns$.

A calculation of the field map for the type of steel considered indicates that the magnetic field ranges between 1.6 T and 1.2 T. The magnetic flux density must be known with an accuracy better than 10% in order not to contribute significantly to the momentum error. The coil current is registered during data taking.

The Precision Trackers are similar to those foreseen for the dipole magnets except that the toroidal field requires layers of horizontal drift tubes, as well as vertical.

9.2 Further developments and R&D

9.2.1 Development of liquid scintillator detectors

A possible solution for the Target Trackers foresees the use of liquid scintillator as an active detection medium. Mineral oil scintillator detectors have been widely used in experiments. E734, KARMEN, LSND and MACRO are a few examples. A fully active liquid scintillator detector based on a design similar to the one described for the tracker planes, has been considered in the studies related to the I216 Letter of Intent [95] and in studies for a long baseline neutrino oscillation experiment [96].

Liquid Scintillator Trackers (LST) are made up of WLS fibres inserted in long cells filled with liquid scintillator. One LST is positioned downstream of each wall of emulsion bricks. A LST is made of two consecutive planes, with a size of about 6.5×6.5 m^2. One plane is segmented with horizontal and the other one with vertical cells. The perpendicular cell orientations allow for reconstruction in space. The design is identical for both orientations.

Each plane consists of a series of 650 parallel cells of about 1 cm^2 cross section. Planes are made of extruded, white polycarbonate profiles (panel) with dimensions of $1 \times 200 \times 650$ cm^3. These profiles include thin separators with a pitch of 1 cm, thus defining the cell structure. Polycarbonate profiles can be extruded with a high reflectivity (95%). The standard size of a panel is 2×7 m^2 and the weight is 1.7 kg/m^2. Other size panels, needed for particular detector, can be produced.

The procedure of filling and sealing has been developed and tested over several months and shows high reliability. The cell signal is extracted by means of a single WLS fibre, read out at one or both ends. Fibres have a diameter of $1-1.2$ mm, the double cladding has a thickness of about 15 μm. The emission spectrum has maximum at about 520 nm. The WLS fibres are coherently bundled, glued, cut together by a diamond saw to arrange multichannel optical connectors and coupled directly to optoelectronic chains for readout. In the case of an EBCCD readout $650-4500$ fibres can be connected to one EBCCD chain through several connectors.

Many known liquid scintillators and new scintillators based on cheap oils were tested at different conditions, temperatures, gas atmospheres, pressures to find the best one. The stability of plastic fibres in different liquid scintillators is well proven over the 5 months of tests. No degradation of fibres and liquid scintillator was measured. By choosing the appropriate scintillating mixture we obtained for a mip

9 $p.e.$ and 6.9 $p.e.$ at a distance from a photocathode of 2.5 m and 6.5 m, respectively. Attenuation lengths of 14.3 m for 1.2 mm fibres with mirrors and 9.2 m without mirrors were measured.

The optimisation of the liquid scintillators is continuing. Due to the local scintillation light capture and to the WLS conversion inside the fibre, a better performance of the liquid scintillator should be achievable, as compared to those applications in which a long attenuation length is required.

A large system of six polycarbonate panels is under construction and will soon be tested. A possible assembly scheme foresees bundles of guide fibres, connected with WLS fibres and coupled to the readout devices at the corners of the planes. This allows full access to emulsion bricks with a possible reduction of a distance between walls.

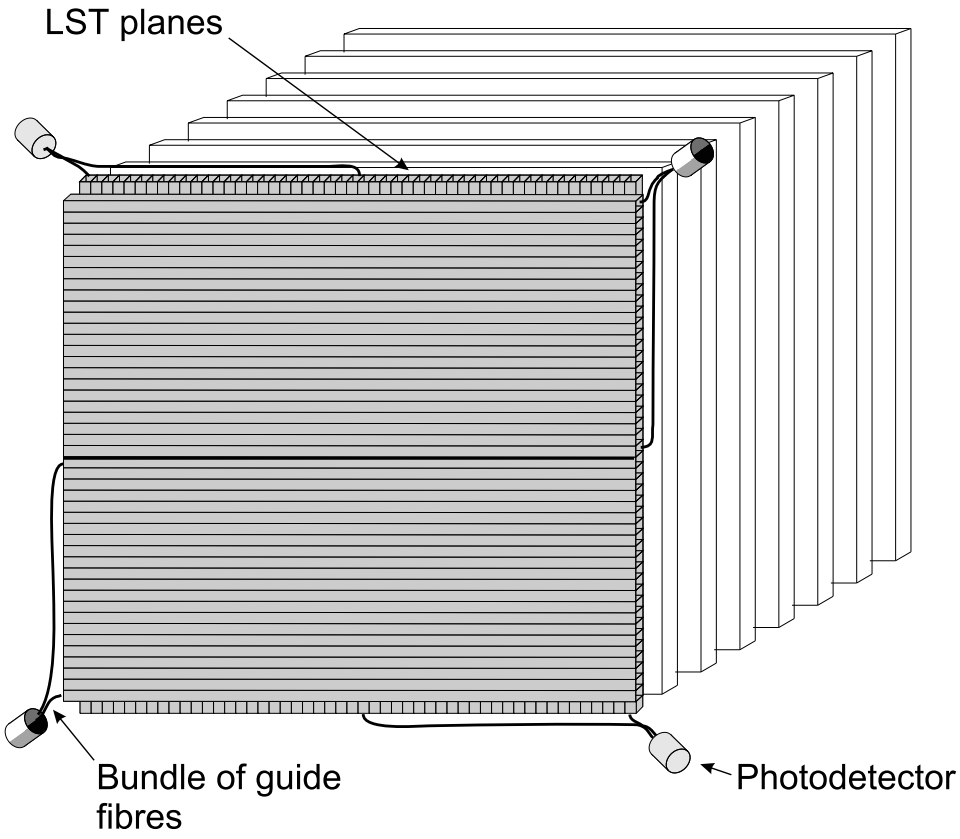

Figure 175: Layout of a possible liquid scintillator tracker (LST) detector to be used for OPERA.

9.2.2 Development of the Multi Track scanning approach

Groups of the OPERA Collaboration are following the approach of the so-called Multi-Tracking Systems (MTS). Here we briefly describe the SySal system [97] originally developed by the Salerno group. Further R&D programmes are underway in other European groups of OPERA and CHORUS, such as CERN, Münster, Naples, NIKHEF and Rome.

In SySal all tracks in each field of view are recognised regardless of their slope, provided they are within a region of angular acceptance. The detail level of the reconstruction is the single track grain, thus the highest the emulsion can yield.

The raw data are series of tomographic images of the emulsion, taken with the objective moving at regularly spaced depth levels (from 1.5 to 3.5 μm). In the present configuration, a commercial high resolution camera (1024 $\times$ 1024 pixels, 30 Hz) with an electronic shutter (0.1 to 2 ms) sends each image to a frame grabber (a Matrox Genesis with a NOA processor on board); there it is converted to a matrix of gray-scale pixels (256 levels, 8 bits per pixel).

The next step for 3D tracking in emulsion is the recognition of grains. A digital filter is used to clean each 2D image, enhancing the dark spots with the expected size and shape, and suppressing all other inhomogeneities of the image. This operation is currently performed in 12 ms by the NOA processor hosted on the frame grabber. The cluster-finding (or clustering) process, performed in parallel by the host PC CPU, takes $4 - 15$ ms depending on the number of black clusters in the image. Clusters with the expected geometrical parameters are promoted to grains.

Grains from different layers are then combined together to recognise geometrical 3D alignments. With an average number of $400 - 1000$ grains per image, and $20 - 30$ layers, it is important to reduce the combinatorial complexity. With this aim, the field of view is subdivided into cells (20 μm per each side). Local alignments of grains are detected within each cell and across boundaries of neighbouring cells. This 3D part of the track recognition process takes no longer than 0.2 s on a Pentium III running at 450 MHz.

After the tracks of one emulsion plate have been read out, the information they carry must be combined with that coming from the other plates of the same brick. Software tracking algorithms are able to perform fine alignment between films and connect track segments, thus reconstructing the complete path of a particle. This is already being done for CHORUS, in which the number of background tracks is several orders of magnitude larger than in OPERA. It is also possible to detect and reconstruct on-line trajectories with a kink, or those of neutral particles (which leave no track in the emulsion) by correlating the primary interaction point with decay/interaction vertices.

For example, Fig. 176 shows the reconstruction of a neutrino induced charm event in CHORUS. The primary interaction is well separated from the decay point of the charmed neutral particle. The 5 tracks of the event are extracted from about 300 background tracks, in turn reconstructed from nearly 8000 track segments detected on 7 consecutive emulsion plates. This corresponds to a volume with a cross sectional area of ~ 1 mm^2 and a length of 5.5 mm.

The Mega Pixel camera allows the use of low magnification (30$\times$), with the benefit of large fields of view ($190 - 220$ μm wide). Thus, with a frame rate of 30 Hz a wide area can be scanned. The current scanning speed is ~ 1 cm^2 per hour in the conditions expected for OPERA.

The Microsoft relational database SQL Server is used by the SySal system. SQL is valuable for its robustness, is easy to maintain, can be programmed with minimum effort through any programming language, and its logical scheme can be exported under different systems. It can be accessed, via ODBC, both locally and through network, from different machines and across multiple platforms, regardless of the operating system on which the client runs.

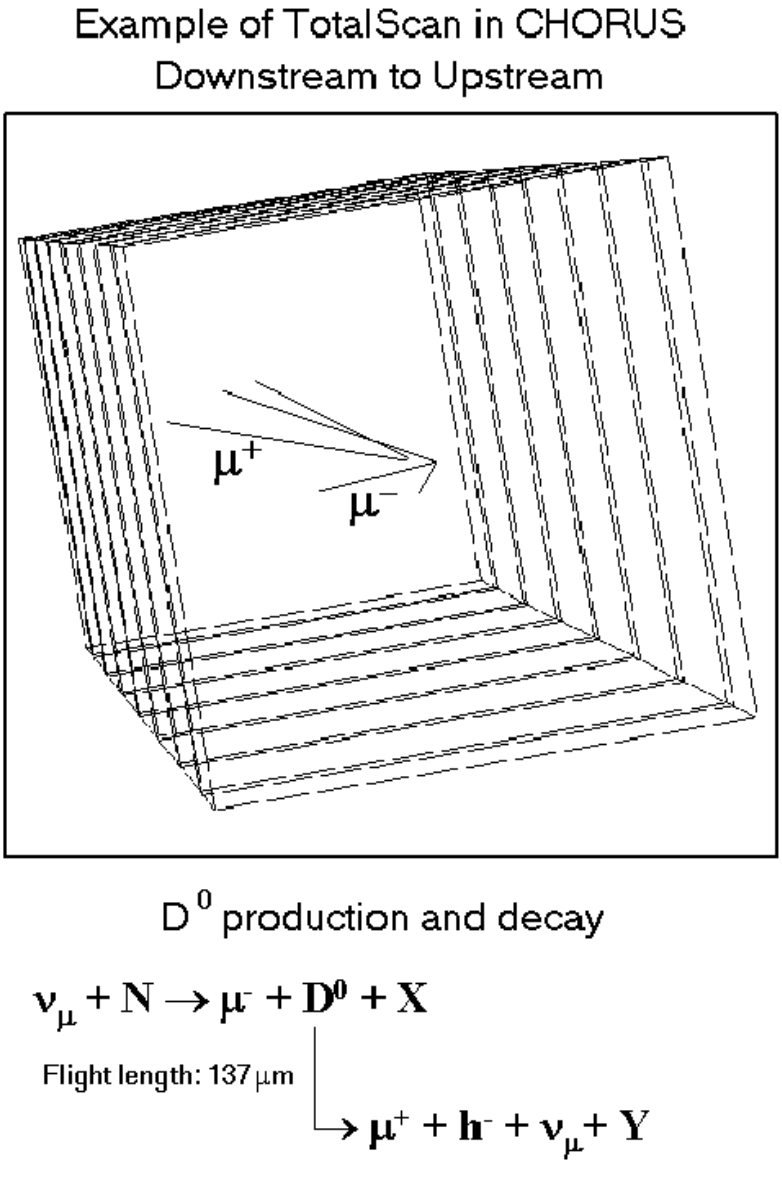

Figure 176: Neutrino induced charm event reconstructed with the SySal system in 7 consecutive emulsion plates of the CHORUS target over a surface of 1 mm^2. The primary neutrino vertex and the secondary charm decay vertex are clearly separated.

The general MTS approach is hardware-independent; therefore, it is possible to closely follow the technological evolution without changing the basic framework. The goal is to increase by one to two orders of magnitude the present scanning speed. Among the areas in which substantial upgrades can be obtained in a medium term period we quote

- a new tracking method, essentially in the two horizontal dimensions, by superposing all the fields of view of one emulsion layer; the reconstruction in space is performed at the end;
- a custom frame grabbing device, based on new commercial CMOS sensors, is being studied; it is a megapixel sensor, capable of operating at a tunable frame rate, up to 500 Hz; the amount of data (500 $Mbyte/s$) is difficult to handle by presently available frame grabbers; a dedicated electronic architecture is being studied;
- a new, specially designed stage, capable of moving and stopping without appreciable oscillations at the foreseen high scanning rates;
- a new wide field optics (for instance, a diameter of 400 μm of more) with good image quality;
- an automatic device to replace and set the emulsion films into position on the microscope stage, without the need of human intervention.

The solution of the problems related to each of the above points could lead to an increase of the overall scanning speed by a factor between two and ten with respect to the presently achieved values. Therefore the total gain between one and two orders of magnitude looks possible. Special care will be devoted to the data acquisition and handling (including a general database). In fact, due to the large quantity of data (both as input and output) any problem could have serious effects.

9.2.3 Future test beam measurements

In the coming years, the OPERA collaboration will continue to need test beams and floor space at CERN for prototype testing and studies on ECC bricks and electronic trackers.

The dimensions of the electronic detectors require a rather large floor space. The former CHARM II building seems to be suitable. The muon rates from the SPS West Area test beams are low. However, if the beam time is not limited this does not constitute a problem. In addition, a floor space in a hall of about 200 m^2 with a height of 10 m is required for assembly tests of prototypes detectors.

The experience gained with the latest test beam periods has shown that both the X5 and X7 beams are suitable for studies of the brick response to electrons and muons. The beam features are well known and excellent particle identification and rate monitoring are available. Exposures with as few as 100 particles over the whole brick surface have been achieved. These beams are well suited for several short tests distributed over the year. For test experiments in which specific trigger conditions and extensive control of the beam line are needed, we plan to use the T7 or the T9 beam in the PS East Hall.

As tentative scheme, in the forthcoming two years we will require the present setup in the CHARM II building as a permanent test facility, several short periods per year in the X5 and/or X7 beams for specific measurements of emulsion films and about one month running time per year in the PS T7 and/or T9 beam lines.

A test programme for emulsion brick components and studies of emulsion analysis techniques is underway. The outcome of the data analysis of the recent measurements may lead to other specific measurements, listed below together with their aim

- Momentum measurement by multiple scattering

  Confirm the method for inclined tracks of different momenta and angle, tested with three ECC bricks exposed to PS pions.

- Electron identification and energy measurement

  Confirm the method by using electrons with different energy ranges; one brick has been exposed at CERN and its analysis is being started.

- Detection of γ's

  Test a method to detect π^0's by reconstructing their mass, for the observation of the $\tau \rightarrow \rho\nu_\tau$ decay mode; an example of $\pi^0 \rightarrow 2\gamma$ observed in the ECC brick exposed in a test experiment has been shown in Fig. 127.

- Identification of low momentum muons

  Validate the method described in Section 6, by an exposure of a brick to a low energy beam of muons and pions.

- Alignment accuracy using low density cosmic-ray flux

  Confirm the design alignment accuracy and evaluate the minimum track density suitable for the procedure.

10 Installation of the detector

10.1 Space requirements

The space required in the underground Gran Sasso Laboratory consists of three main items

- space needed by the detector supermodules in the underground hall.

  This includes a clearance space for the devices which regularly remove the selected bricks;
- space needed for the handling and the assembly of the detector elements;
- space needed to accommodate subsidiary facilities, which do not have to be necessarily located in the same hall.

The space needed by the detector is $\sim 30\ m$ long and, transverse to the beam direction, about $10\ m$ wide and $10.7\ m$ high.

The width is determined by the $8.75\ m$ wide iron walls of the spectrometers. Additional $1.5\ m$ must be left free on each side in order to accommodate the robots for brick handling and their rails running along the detector. The width of the target is $670\ cm$. The space left on each side is adequate for brick removal and for locating the electronic trackers readout. The width of the detector is compatible with installation in the hall B or hall C of the Gran Sasso Laboratory.

The height of the supermodule is determined by the $10\ m$ height of the magnet. An extra height of about $70\ cm$ is needed for the I-beams supporting the target.

The total length of $\sim 30\ m$ is built-up as follows. For each supermodule, the target section is made of 24 modules. Each module consists of a wall of target bricks and of two layers of scintillators strips. The total module thickness is $12\ cm$ ($8.4\ cm$ for the wall and $3.6\ cm$ for the trackers and their supports). The muon spectrometer consists of three tracking stations interleaved with two magnetised iron walls. Each wall consists of a sandwich of 12 iron layers ($5\ cm$) interleaved with 11 gaps ($2\ cm$) containing the Inner Trackers.

The thickness of the three Precision Tracker stations is 70 for the external ones and $100\ cm$ for the middle one. The supermodule longitudinal dimension is thus $690\ cm$ ($290\ cm$ for the target and $400\ cm$ for the spectrometer). A $1.6\ m$ additional clearance is foreseen in front of the target of each supermodule for the access to the detector components. In front of the first target supermodule along the beam beam, an arch structure of about $2.5\ m$ length supports the longitudinal I-beams. Upstream of this structure, a tracking detector allows to veto incoming charged particles.

The largest pieces of equipment to be transported to Gran Sasso are

- the magnet iron plates $1.25 \times 8.2\ m^2$;
- modules of preassembled target-wall support structures (maximum dimension $8.0 \times 3.5\ m^2$);
- modules of preassembled target scintillator strips (maximum dimension $7.5 \times 2\ m^2$);
- modules of preassembled drift tubes (maximum dimension $8.5 \times 2.5\ m^2$);
- modules of the spectrometer inner detector RPC planes (maximum dimension $3.5 \times 1.5\ m^2$).

The space requirements in the experimental hall for the assembly of the detector elements come from

- space below the crane to receive trucks and unload the detector pieces: $12 \times 5\ m^2$;
- temporary space for the magnet building blocks: $12 \times 12\ m^2$;
- space to mount the target support structures: $4 \times 8\ m^2$;
- space to mount the scintillator planes: $10 \times 10\ m^2$;
- space to mount the Precision Trackers: $10 \times 10\ m^2$;
- space to test RPC modules: $5 \times 5\ m^2$.

In the installation schedule there could be a substantial overlap among the above requirements, because some of the mounting operations are done in series. On the contrary, given the tightness of the schedule, the assembly of the three supermodules should proceed largely in parallel. A large fraction of the above spaces has to be situated around the detector in the reach of one or two fast cranes. If this is not possible, a large fraction of the detector components would have to be unloaded in a temporary area and then transported close to the detector. This would result in considerably slowing-down the detector installation schedule, depending on the total space available in the underground hall.

Underground space is needed, but not necessarily in the experimental hall, for the

- brick assembly machine;
- brick manufacturing and storage of elements before and after fabrication;
- emulsion film erasing facility.

Space is needed for other purposes and for the operation of the detector during the run. In particular, space is required for the experimental counting rooms

- rack rooms: $100\ m^2$ ($25\ m \times 4\ m$ for 50 racks of electronics, power supplies, etc.);
- control room: $50\ m^2$ (PCs, screens, keyboards, printers, monitors, remote controls).

The rack room with the electronics racks and other heat and noise generating equipment has to be separated from the control room. One could imagine a solution on two levels with two rooms of about $100\ m^2$ on top of each other.

We foresee a total consumption of less than $400\ kW$ of electrical power, including overhead. A UPS system of about $400\ kW$ has to be installed as a backup system for short power failures (~ 10 minutes). An additional system with a diesel generator of $400\ kW$ must take over in case of a longer failures. This will not be necessary if the Gran Sasso Laboratory will be equipped with a new failure-safe electric power supply system. The controls for the distribution of the electrical power (mains, UPS, diesel, light, fuses, etc.) have to be accessible to the physicists. Special care has to be taken in designing the electric grounding system, in order to avoid loops.

Most of the $400\ kW$ heat is produced in the rack room. It can be released into the experimental hall. A water cooling system for the racks has also been considered. The control room and the surrounding rooms need air conditioning and heating.

Other services include

- computers (about 10 to 30 PCs);
- local ethernet connection and network;
- telephones (underground GSM in the tunnel for portables);
- GPS timing facility;
- gas supply and gas recovery for gaseous detectors;
- pressurised air for cleaning and possibly to drive robots;
- water supply.

10.2 Detector installation

The detector installation proceeds in three main steps: the installation of the spectrometers, of the target mechanical structure with the electronic trackers, and of the bricks.

The three spectrometers have to be installed as first, since they constitute the support for the target mechanical structure. Their mounting can proceed in series or in parallel according to a detailed schedule which has to take into account the space available around the detector in the experimental hall.

About 35 weeks are needed to complete the installation of one spectrometer. It is therefore desirable to have the possibility of installing more magnets in parallel. In the tentative installation schedule presented in this document, the mounting is conducted with a large fraction of parallelism. 6 more weeks are needed to install the $arch$ support in front of the detector and the longitudinal bars with transverse reinforcements on top of the spectrometers.

The second phase is the installation of the target section, which starts from the planes close to the spectrometer and proceeds in the upstream direction. The target wall mechanics are preassembled outside in half-wall modules. The Target Trackers are preassembled in units of 64 full-length scintillator strips packed together in a light tight metallic box, where fibres and two optical detectors (one per side) are fixed. Four of these units are necessary to form a plane.

A possible scheme foresees the installation of preassembled elements directly on the detector. First, a vertical strip plane is suspended from the top longitudinal bars and connected to the bottom structure. All strips are surveyed in their final position. The horizontal strip plane is then assembled and survey is performed. At last, the two halves of the brick support structure are attached to the top and bottom mechanical structures. With the wall in its final position, a survey is performed in order to be able to correlate particle tracks in the bricks and in the Target Trackers. If the trackers are supported by the brick support structure, the procedure has to be revised accordingly. The above operations are repeated sequentially or in parallel for each supermodule. The mounting speed depends on the space available around or near the detector.

If enough space is available, an alternative scheme consists of preassembling the detector elements in planes inside the experimental hall, as described in the following.

Whether the scintillators mechanical support is part or not of the brick wall support structure, the empty wall support frame is first assembled vertically starting from its two halves. This operation can take place on a scaffolding placed on the side along the hall. Such a support can store walls prepared in

advance. The sets of scintillator strips are mounted in the same scaffolding, either attached to the wall or just suspended from the same top and bottom beams.

A wall structure equipped with its scintillators is then rotated and placed perpendicular to the beam, as shown in Fig. 177, mounted on a temporary frame and fixed to the general support beams. Such an operation requires 1.5 m of free longitudinal space, which approximately corresponds to the space of the spectrometer Precision Trackers to be installed later. We estimate to one week the time necessary to install a full tracker plane.

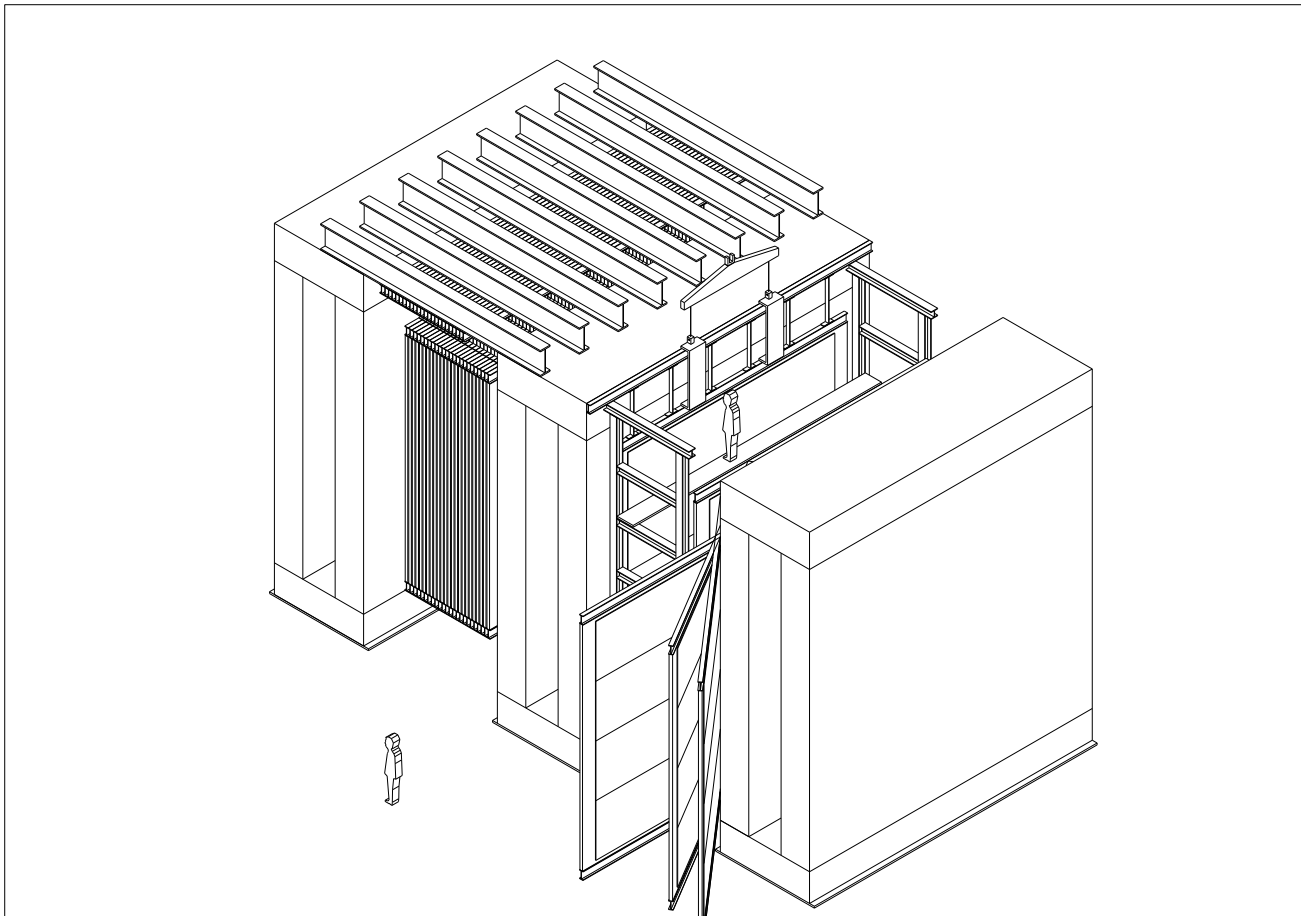

Figure 177: Installation of equipped wall structures in the target. The structures rotate to enter the temporary installation structure.

When the installation of the target section is completed, the spectrometer Precision Trackers are mounted in about two months.

The third step of the installation consists of mounting the robot for brick handling described in Section 4.3. The loading speed of the robots is expected to be about 60 bricks/hour.

10.3 General installation schedule and commissioning

The planning of the design, construction, installation and commissioning of the detector assumes that the data taking will start in May 2005, according to the CNGS beam schedule given in Fig. 178.

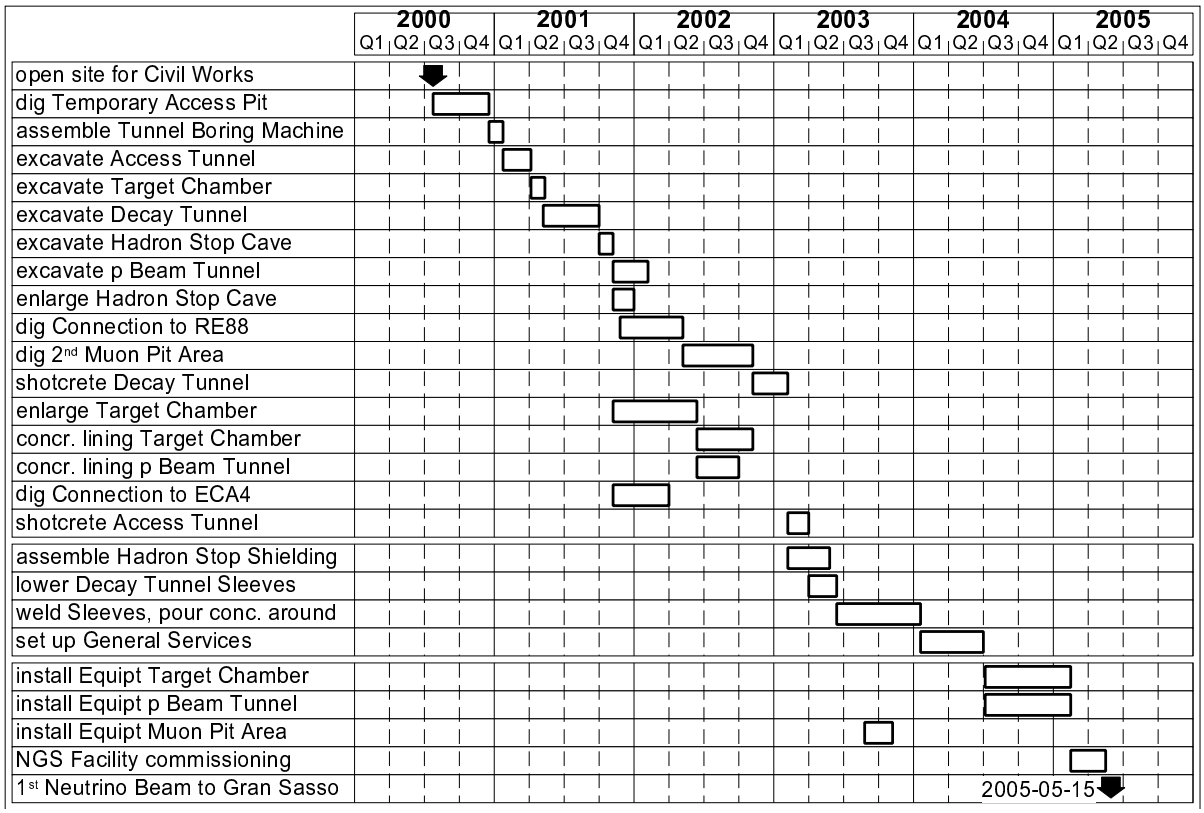

Figure 178: Planning for the realisation of the CNGS beam.

A summary of the planning for the construction of the detector is shown in Fig. 179. This tight schedule assumes a large parallelism in the mounting of the three supermodules. Once the experimental hall is assigned, the schedule will have to be revised depending on the space available for the detector and for its assembly.

A 6 months long period is necessary for the commissioning of the experiment after installation. This means that the detector must be ready for cosmic data taking by September 2004. As a consequence the assembly and installation in the Gran Sasso hall has to start in 2002. By this date, all the work for the preparation of the underground hall will have to be completed, including the installation of the infrastructure required by OPERA.

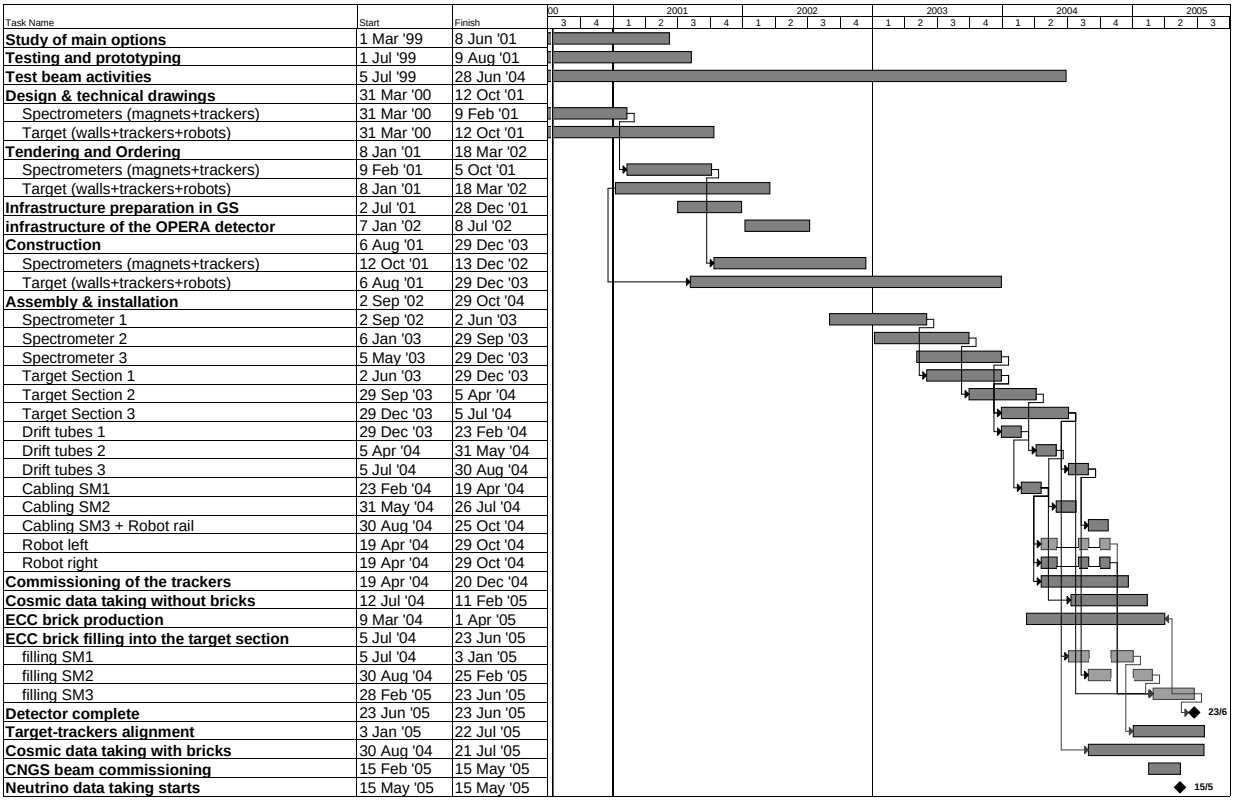

Figure 179: General planning for the construction of the OPERA detector.

As far as the decommissioning is concerned, the OPERA Collaboration is collectively responsible for the dismantling of the equipment supplied by the collaborating Institutions. The space used by the Collaboration including offices and laboratories can be made available for reallocation in about two years.

11 Experimental infrastructure

11.1 Infrastructure at Gran Sasso

Infrastructure and logistics facilities are requested to the Gran Sasso Laboratory during the OPERA test activity, installation and running phases. This includes in particular

- safety infrastructure;
- electric power supply and cabling, UPS;
- air conditioning and air exchange;
- computer network and video conference facility;
- control room and barracks;
- chemical waste management;
- special car for brick transportation and cars for laboratory access;
- mechanics and electronic workshops with technician assistance;
- administrative and secretariat assistance;
- offices in the outside laboratory.

Beside the detector and assembly areas, additional space is requested mostly underground, strictly related to the experiment characteristics. The space needed refers to

- storage of emulsion and lead plates;
- emulsion film erasing;
- automatic brick assembly;
- storage of assembled bricks;
- storage of removed bricks;
- automatic brick unpacking after removal;
- cosmic-ray emulsion station;
- development room;
- emulsion test laboratory.

Appropriate emulsion storage sites before brick assembly are needed underground. This refers to four different cases

- packages just delivered (each including 58 films, or twice as many, to be repacked into one or two bricks);
- emulsion films ready for brick assembly;
- bricks ready to be installed.

The erasing process consists of a temperature-time cycle in the range of $30 - 40^o$C for a few weeks. The procedure has to be optimised for effective background reduction with no consequences for the sensitivity and the shape of the films, after completion of the extensive tests now in progress. It is the most demanding case for emulsion storage, requiring rather large spaces and dedicated equipment for temperature control.

For emulsion storage, requiring a longer duration, radioactivity must be checked in relation to low-energy γ rays from the floor and wall concrete. The temperature, instead, should not need special and accurate settings.

For the emulsion storage, we request an underground site where bricks can be kept under controlled temperature and humidity conditions and known environmental radioactivity before installation on the detector. In a first approximation the total space is about 200 m^2. From the point of view of logistics, it would be desirable to have emulsion storage not far from the brick assembly laboratory and both sites as close as possible to the detector.

Better estimates and specifications will be given after the completion of the erasing and environmental radioactivity tests and once the exact scheduling of emulsion production, delivery, erasing, brick assembly and insertion in the apparatus are fixed. However, as a safe statement we should be prepared to store the total amount of the emulsion in the underground hall starting from end 2003.

After commissioning of the experiment, most of the emulsion storage area will be empty. However, one needs a room to temporarily store the extracted bricks before the transportation to the cosmic-ray exposure site. Therefore, an area used for the time of installation could be conveniently reshaped to host the run-time emulsion handling.

The laboratory where bricks are assembled should be controlled both in temperature and humidity. Since the emulsion films are dried at 23^oC with a relative humidity of 63%, this laboratory must be kept at the same temperature and humidity conditions. The total electric power consumption is estimated to about 5 kW. This laboratory has to be located underground, with dark room specifications and with a surface of at least 15×10 m^2 and 2.5 m height.

The number of cosmic-ray tracks which can be collected in the Gran Sasso hall is by far not sufficient for the emulsion film alignment. We estimate about 250 cosmic muons per year passing through a brick from all directions and only about 10 in a cone of $\pm 35^o$ transverse to the film surface.

Also the number of muons produced by neutrinos interactions in the rock in front of the detector is not sufficient for alignment. Before disassembly, selected bricks are therefore exposed to cosmic rays outside the underground hall to collect alignment tracks. It is necessary to find a site with a relatively small rock coverage, suitable to gather enough tracks in a few days. Candidate sites have been located in the aqueduct tunnel near the Gran Sasso Laboratory. The entrance is at about 3 km from the exit of the highway tunnel.

In the aqueduct tunnel there are two possible places. A garage of 3×16 m^2 with a coverage of about 50 m and a *niche* along the tunnel itself of about 1.5×10 m^2 with a coverage of only 20 m. Test measurements are planned to determine the cosmic flux in the two sites. Both in the garage and in the niche electric power is available. A clean and dry laboratory can only be built in the garage.

After the exposure to cosmic rays, bricks are disassembled in the different components in a dark room. Emulsions films are printed with reference marks and numbers. A printer is used with a mask with lattice pattern and a LCD shutter for numbering. Then all emulsion films are put in special racks for automatic processing. In order to keep constant the dimensions of the films, also this room has to be climatised with the same conditions as the assembly laboratory.

The emulsion films are processed by an automatic machine. This is equipped with 6 tanks for pre-soaking, developing, stopping, fixing, washing and alcohol bathing. By means of a crane, each rack filled with emulsion films is soaked in each bath continuously. In order to maintain conditions stable, a continuous replacement of the different solutions and their temperature control are necessary. Therefore, an upper level floor mixing-room and temperature controlled storage tanks are required. Processed films are dried in a cabin with mild air flowing. The expected number of processed films per day is about 1700. A large stock room of $\sim 100\ m^2$ for chemicals is needed together with at least two storage tanks for waste solutions. One is used for the fixer, for silver recovering. The expected power consumption is $10\ kW$. About 2 *ton* of water are needed.

For a long emulsion exposure, like that scheduled for OPERA, it is crucial to have the lowest possible level of background. Background grains and tracks in emulsion could mainly arise from cosmic rays (outside the hall) and from environmental radioactivity (mainly inside the hall, due to the long exposure time. This background shows up as Compton or photoelectrons from low-energy gamma rays. Tracks from particles associated to the beam, both muons and hadrons, are on the contrary too rare to constitute a problem and are not considered any further.

Although the above mentioned sources of background cannot simulate either a triggered interaction or a τ decay, they can contribute with wrong or false candidate tracks (real tracks and ghosts) and their piling-up with time may increase the scanning load and reduce the visibility through the emulsions.

Ambient radioactivity in the underground hall must be kept low. This level of activity has been measured and mapped in the past, as example by the MACRO and BOREXINO experiments, in order to identify possible hot spots. It turned out that the main source is the concrete of the floor. As the measurements were performed with electronic counters and as it is difficult to extrapolate the results to emulsion films, test exposures are being performed to assess the issue. A small dark-room has been built in the Gran Sasso underground laboratory for this purpose. Tests on radioactivity are in progress, both with counters[28] and with emulsions.

11.2 Infrastructure for the emulsion readout facilities

It is envisaged to setup two to three stations for vertex location. One can foresee a scheme in which one or two stations are located in Europe and one in Japan. The stations have to be specially organised to be fault tolerant in order to process the selected bricks.

A schematic illustration of one of these stations as planned at the Nagoya University is shown in Fig. 180. The laboratory has a surface of about $150\ m^2$ and includes several facilities in order to allow the processing rate of more than 10 bricks/day. A stock room for the emulsion films mounted on cassettes is required.

[28] Courtesy of C. Arpesella, Gran Sasso Laboratory.

Special attention has to be paid to the temperature control and to the electric power, since each S-UTS requires about 3 kW. In addition, a computer network infrastructure is required. The scanning rooms where the Track Selectors operate have to be *clean* and have controlled temperature and humidity. The floor has to be rigid to avoid vibrations while moving the microscope stages and the objective lenses. The number of the required S-UTS systems is given in Section 6. A small computer room is also needed for monitoring and controlling the station operation as well as for the online data storage.

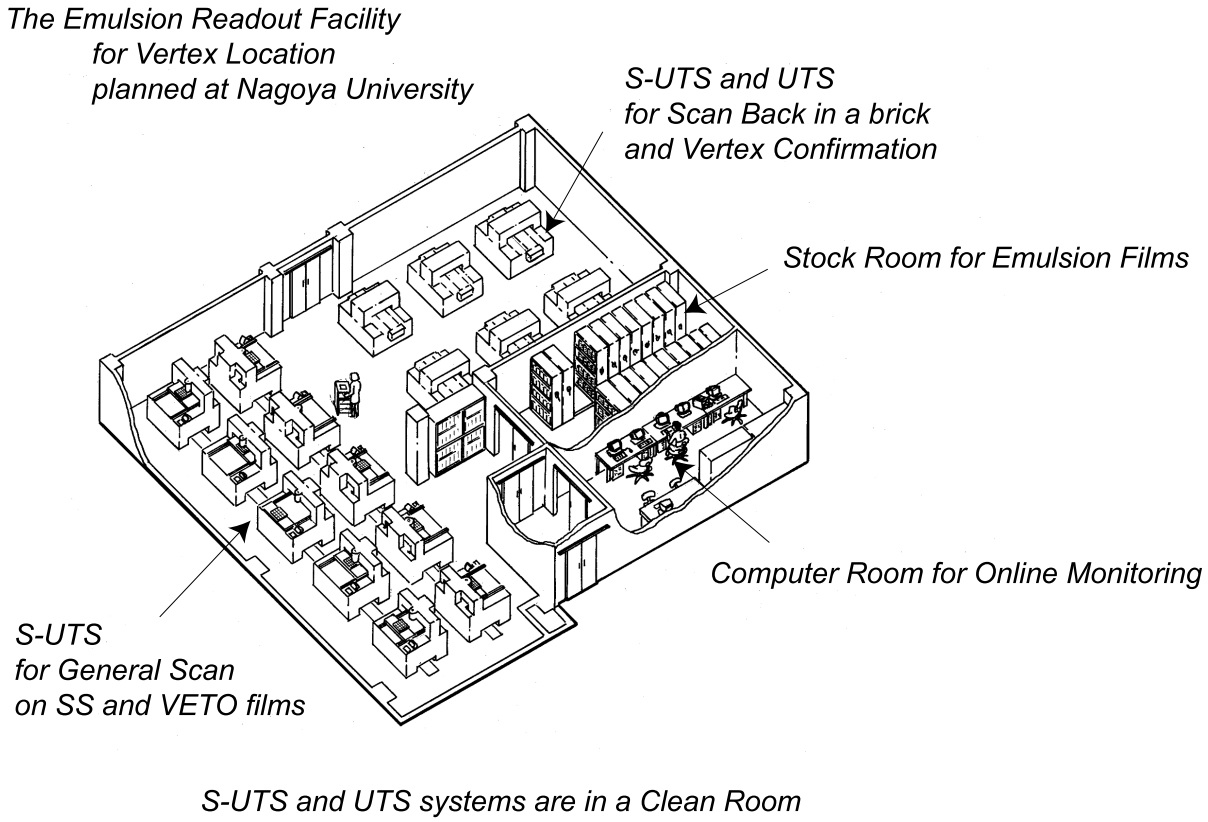

Figure 180: Illustration of a station for vertex location planned at Nagoya University. 10 S-UTS are assigned for general scan for SS and VETO films. 3 UTS are for scan back and 3 S-UTS for vertex confirmation. The S-UTS systems for vertex confirmation are used for full data taking over night.

In order to operate such a station, two 8-hours shift per day are needed each with two operators. The S-UTS systems can perform unattended scanning of VETO and SS over night (the remaining 8 hours). One physicist on shift is needed to monitor the station performance. A specific effort of coordination of the shift activities is therefore required and has to be supported by the Collaboration.

Stations for other purposes do not require such a large capability as for the vertex location. Stations for full data taking require a relatively large infrastructure, while stations for high accuracy measurements (for special events) and for cross-check analysis of candidates could be well located in several small laboratories, since they only process a small fraction of events. The required manpower obviously depends

on the size of these stations.

A communication protocol among stations and Gran Sasso must be established well before the experiment start up. It is important for two aspects. The first is for ensuring the effective collaboration among stations spread over the world in order to realise a fast data taking. The second is for the smooth share of information from the emulsion films, among the various groups to efficiently perform the physics analysis.

12 The Collaboration

12.1 Structure

The Collaboration has increased since the Progress Report [6] with groups from Beijing, Berlin, Bologna, Hagen, Padova, Rostock, Shandong, Strasbourg and Zagreb.

An organisational structure has been set up with the main aim of coordinating the work towards the realisation of the Proposal. The Collaboration Board is the decision making body of OPERA and includes one representative per Institution. A Triumvirate composed by K. Niwa, J.P. Repellin and P. Strolin acts as steering body. A. Ereditato acts as Contact Person and J.P. Fabre as Technical Coordinator. The scientific and technical activities are coordinated by Working Groups (WG) each with a few Organisers and open to all the members of the Collaboration. A Physics Coordination Group includes the WG Organisers and the members of the Triumvirate.

The organisational structure for the realisation of the experiment will be established in the forthcoming months.

12.2 Contributions to the experiment

The realisation of the experiment requires the construction of the detector and of its installation at Gran Sasso, as well as the setting-up of scanning laboratories of adequate capacity for the demanding task of quasi-online readout of the emulsion films from extracted bricks and for the precision analysis of candidate events.

The foreseen contributions from the participating groups extend to all detector elements as shown in Table 38. Some more groups may join the experiment. A more detailed sharing of the construction responsibilities among groups will be established after approval of the respective Institutions and Funding Agencies, following the approval of the experiment.

In addition, an investment is required on emulsion scanning. The readout of the extracted bricks requires the realisation of dedicated laboratories, equipped with S-UTS or equivalent scanning systems presently being developed. One of these laboratories will be situated in Japan and at least one will be in Europe. The precision scanning of candidate events will be carried out in all emulsion laboratories of the Collaboration.

Several groups of the Collaboration have already experience in readout and analysis of emulsion data and have laboratories equipped with automatic and semi-automatic scanning systems. Other groups intend or are considering to undertake such activities in the forthcoming years as a contribution to OPERA. A list of all groups is given in Table 39.

All groups of the Collaboration will participate in the global analysis of the events, including data from electronic detectors and emulsion data.

Table 38: Expected contributions to the construction of the OPERA detector.

ITEM	INSTITUTIONS
TARGET	
Lead/emulsion bricks	Ankara, Bari, Bern, CERN, Israel, Kobe, Muenster, Nagoya, Naples, Rome, Salerno, Toho.
Trackers	Bern, Brussels, CERN, Israel, LAPP, Lyon, Orsay, Strasbourg, Zagreb.
Support structure and brick handling	CERN, LAPP, LNF, Naples.
MUON SPECTROMETERS	
Magnets	Hamburg, LNF, Rostock.
Inner Trackers and XPC's	CERN, LNF, Padova.
Precision Trackers	Berlin, Hamburg, Muenster, Rostock.
Overall support structure	LNF, Naples.
TRIGGER, DAQ, SLOW CONTROL	Bern, Lyon, Strasbourg.

Table 39: Expected contributions to the readout and analysis of emulsion data.

INSTITUTIONS
Aichi, Ankara, Bari, Beijing, Bern, Bologna, CERN, Hagen, IN2P3, Israel, Kobe, LNF, Muenster, Nagoya, Naples, Rome, Salerno, Shandong, Toho and Utsunomiya.

13 Cost of the experiment

13.1 Detector cost evaluation and running cost

The detector cost has been evaluated in CHF, by applying the current exchange rate between the different currencies. Neither taxes nor custom duties have been included in the cost of materials. Manpower cost has been evaluated by considering taxes and additional charges. The results of this evaluation are summarised in Table 40 and Table 41 in which the detector cost is given for one supermodule and for the full detector, respectively.

Table 40: Cost of one supermodule.

ITEM	COST (kCHF)
TARGET	**21200**
Emulsion films	14700
Lead, mechanics, supports	4300
Target Trackers	2200
MUON SPECTROMETERS	**3100**
Magnet	1600
Inner Trackers and XPC's	550
Precision Trackers	950
TOTAL	**24300**

Table 41: Cost of the OPERA detector.

ITEM	COST (kCHF)	
Emulsion films	44100	
Other items	28800	
Supermodules		**72900**
Tooling and infrastructure		5200
External manpower		1200
Contingency (10%, excluded em. films)		3400
TOTAL		**82700**

Concerning the cost of infrastructure at the Gran Sasso Laboratory, we require the support of the LNGS for safety installations, cooling and ventilation, UPS, an additional small crane, control rooms and emulsion laboratories. The cost of the above items is evaluated to about 3 MCHF.

We have also evaluated the running cost for the OPERA detector at the Gran Sasso Laboratory. No expenditure for new bricks is foreseen, as bricks removed for analysis are replaced by other bricks installed either in the most upstream walls of each supermodule or in the edges of the walls. The main contribution to the operation cost is due to chemicals for the emulsion film development, to packing and shipping of

the developed emulsions and to standard costs for the electronic detectors (gas, electronics, etc.). The external manpower required for brick handling, film development and shipment has been considered. The overall running cost at Gran Sasso is estimated to about 1 MCHF/year.

13.2 Emulsion readout facilities and running cost

As described in the previous Sections, a possible scheme foresees one or two stations for vertex location to be operating in Europe and one in Japan, at the Nagoya University. A cost estimate is given below for a vertex location station able to process in total 30 bricks/day. The cost of other stations, such as for the full data taking, for the high accuracy measurement of special events and for the cross-check analyses, depends on the number of laboratories which will be involved and has to be defined accordingly.

In total, about 20 S-UTS systems have to be employed to process 30 bricks/day. The cost of one S-UTS is about 40 MYen (600 kCHF) and that of an UTS about 15 MYen (220 kCHF). The cost of one station able to analyse 30 events per day is then nearly 800 MYen (12 MCHF). The cost of other hardware resources, such as online computers and data storage devices amounts to 5 MYen (75 kCHF).

The operation cost to maintain a S-UTS (mechanical parts, lamp and electronics cards, etc.) and the related computer system, amounts in total to $\sim$ 1 MYen (15 kCHF)/S-UTS/year. In addition, we have to include the manpower cost of about $4-5$ operators/station. The evaluation of this cost depends on where the stations are located (Europe or Japan) and on the possible contributions from Institution manpower. In the case of the Nagoya facility, schematically shown in Fig. 180, it is estimated to be about 2 MYen/person/year, for a total of 8 MYen/year.

14 Conclusions and outlook

In this document we propose the OPERA experiment, aimed at an appearance search for $\nu_\mu \leftrightarrow \nu_\tau$ oscillation in the CNGS beam and sensitive to the parameter region indicated by the atmospheric neutrino signal. The experiment design is based on the Emulsion Cloud Chamber (ECC) detector, a modular structure made of a sandwich of passive material plates interspaced with emulsion layers. By assembling a large quantity of such modules, one can realise a $\sim 2000\ ton$ fine-grained vertex detector optimised for the study of ν_τ appearance.

Since the Progress Report of 1999 [6], further studies, tests and simulations have been performed allowing to define the design of the experiment. Baseline options have been identified for the various electronic detectors and for the target brick structure (compact bricks). In all cases the decision has been driven by the physics requirements, by consideration of cost effectiveness and by the needs of large scale production and reliable long term operation.

Progress has been made in the understanding of the features and of the basic design of the experiment as well as in the evaluation of the expected performance. An increase of the τ detection efficiency for compact bricks has been made possible by including, in particular, hadronic decay modes. The very low background confirms the merits of the emulsion for the direct observation of the τ decay. Moreover, the use of compact bricks favours the search for $\nu_\mu \leftrightarrow \nu_e$ oscillations, as anticipated in [6].

OPERA implies an unprecedented, massive use of emulsion as tracking device of extremely high precision and granularity. The industrial procurement of the vast quantity of emulsion films with adequate sensitivity is a crucial issue. R&D programmes conducted jointly with emulsion producers yielded positive results.

Automatic scanning continuously improves in speed and performance. The analyses being done for CHORUS and DONUT are furthering the understanding and stimulating improvements. An additional boost is needed for the OPERA requirement of scanning large emulsion areas. The approaches under investigation exploit the progress in the electronics and in the technology of image analysis.

The large scale of the experiment requires collaboration with industry for the electronic detectors and for the automation of the brick assembly and handling.

The layout of the experiment and other technical issues have been studied considering the requirements and the experimental conditions of the Gran Sasso Laboratory.

The OPERA sensitivity reaches $\Delta m^2 \sim 10^{-3}\ eV^2$ covering the oscillation parameter region indicated by Super-Kamiokande. A positive result on $\nu_\mu \leftrightarrow \nu_\tau$ appearance will directly identify the source of the observed effect and will constitute a milestone in the study of neutrino oscillations.

If neutrino oscillations occur at the most recent Super-Kamiokande best fit parameter values $\Delta m^2 = 3.2 \times 10^{-3}\ eV^2$ and $\sin^2 2\theta = 1$ [30] the experiment will detect 18 unambiguous τ events. 22 events would be observed at the previous best fit value $\Delta m^2 = 3.5 \times 10^{-3}\ eV^2$. The number of detected τ events will constrain the oscillation parameters, allowing to improve the determination of Δm^2 performed with atmospheric neutrinos.

As the sensitivity is not limited by background, the experiment will profit from the statistics increase through a dedicated operation of the SPS or an improved performance of the CNGS.

Acknowledgements

In addition to those already acknowledged in the text of this Proposal, several people have contributed to the design of the experiment and of the detector components, as well as to the realisation and to the tests of prototypes.

In particular, we wish to warmly acknowledge the contribution of C. de la Taille, S. Gardien, C. Girerd, B. Humbert, R. Igersheim, Y. Jacquier, T-H. Le, G. Martin-Chassard, M. Morciano, Ph. Schmitt, G. Schuster, D. Staub, S. Vanzetto and J. Wurtz for their work on the front end electronics, data acquisition and test of components; A. Franceschi, P. Mugnier, G. Passeggio and E. Vanzanella for the contribution to the technical design of the mechanical structures of the detector; B. Dulach and D. Orecchini for the design of the dipole magnet; B. D'Aquino and G. Pontoriere for the realisation of brick prototypes; J. Cailleret, E. Gamelin, B. Tischler and D. Thomas for the realisation and the test of scintillator strip detector prototypes; R. Diotallevi, P. Di Pinto and V. Di Pinto for their work on the emulsion scanning laboratory at Gran Sasso.

We are grateful to L. Durieu and J.P. Riunaud of CERN PS/AE, for their help in performing test beam measurements at the CERN PS, and L. Gatignon for the tests at the CERN SPS.

We express our gratitude to the Gran Sasso Laboratory staff and in particular to E. Scapparone for his help in the contacts with the Laboratory for the preparation of the Proposal.

The group of ITEP acknowledge the NATO Science Program (Grant PST.CLG 974889) for partial funding of a joint INFN-ITEP project "A novel Detector for Neutrino Oscillation Search".

References

[1] G. Acquistapace et al., CERN 98-02, INFN/AE-98/05, 19 May 1998.

[2] K. Niwa, Contrib. to the "Snowmass '94" Conference on Particle and Nuclear Astrophysics and Cosmology in the next Millennium, Snowmass, 1994.

[3] A. Ereditato, K. Niwa and P. Strolin, INFN/AE-97/06, Nagoya DPNU-97-07, 27 January 1997.

[4] H. Shibuya et al., LNGS-LOI 8/97.

[5] K. Kodama et al., CERN/SPSC 98-25, SPSC/M612, LNGS-LOI 8/97, Add. 1.

[6] K. Kodama et al., CERN/SPSC 99-20, SPSC/M635, LNGS-LOI 19/99.

[7] E. Eskut et al. (CHORUS Coll.), *Nucl. Instr.and Meth.* **A401** (1997) 7.

[8] S. Aoki et al., *Nucl. Instr. and Meth.* **B51** (1990) 466;

[9] T. Nakano, Ph.D. Thesis, University of Nagoya (1997);
T. Nakano, The Ultra Track Selector, Nagoya University note, in preparation.

[10] C. Weinheimer et al., to appear on the Proc. of the XIX Int. Conf. on Neutrino Physics and Astrophysics, Sudbury, 2000.

[11] V.M. Lobashev et al., to appear on the Proc. of the XIX Int. Conf. on Neutrino Physics and Astrophysics, Sudbury, 2000.

[12] B. Pontecorvo, *Zh. Eksp. Teor. Fiz.* **33** (1957) 549.

[13] B. Pontecorvo, *Zh. Eksp. Teor. Fiz.* **34** (1958) 247.

[14] Z. Maki et al., *Prog. Theor. Phys.* **28** (1962) 870.

[15] B. Pontecorvo, *J. Exptl. Theoret. Phys.* **53** (1967) 1717;
V. Gribov and B. Pontecorvo, *Phys. Lett.* **B28** (1969) 493.

[16] L. Wolfenstein, *Phys. Rev.* **D17** (1978) 2369;
S.P. Mikheyev and A. Y. Smirnov, *Sov. J. Nucl. Phys.* **42** (1986) 913;

[17] see for instance: S.M. Bilenki and B. Pontecorvo, *Phys. Reports* **C 41** (1978) 225;
V. Flaminio and B. Saitta, *La Rivista del Nuovo Cimento* **10** (1987) 1;
S.M. Bilenki et al., *Prog. Part. Nucl. Phys.* **43** (1999) 1;
A. Ereditato and P. Migliozzi, CERN-OPEN 2000-132, to appear on *La Rivista del Nuovo Cimento*;
G. Altarelli and F. Feruglio, Proc. of the VIII Int. Workshop on Neutrino Telescopes, Venezia, 1999 and references therein.

[18] A. B. MacDonald (SNO Coll.), to appear on the Proc. of the XIX Int. Conf. on Neutrino Physics and Astrophysics, Sudbury, 2000.

[19] G. Ranucci (Borexino Coll.), to appear on the Proc. of the XIX Int. Conf. on Neutrino Physics and Astrophysics, Sudbury, 2000.

[20] C. Rubbia (ICARUS Coll.), *Nucl. Phys. B (Proc. Suppl.)* **48** (1996) 172.

[21] A recent review of solar neutrino projects may be found in T. A. Kirsten, Proc. of the VIII Int. Workshop on Neutrino Telescopes, Venezia, 1999.

[22] A. Piepke (KAMLAND Coll.), to appear on the Proc. of the XIX Int. Conf. on Neutrino Physics and Astrophysics, Sudbury, 2000.

[23] G. Mills (LSND Coll.), to appear on the Proc. of the XIX Int. Conf. on Neutrino Physics and Astrophysics, Sudbury, 2000.

[24] A. Bozarko (MiniBooNE Coll.), to appear on the Proc. of the XIX Int. Conf. on Neutrino Physics and Astrophysics, Sudbury, 2000.

[25] Y. Fukuda et al., *Phys. Lett.* **B335** (1994) 237.

[26] M. Apollonio et al., *Phys. Lett.* **B420** (1998) 397;
M. Apollonio et al., *Phys. Lett.* **B466** (1999) 415.

[27] Y. Fukuda et al., *Phys. Rev. Lett.* **81** (1998) 1562;
Y. Fukuda et al., *Phys. Rev. Lett.* **82** (1999) 5194.

[28] C. Walter (Super-Kamiokande Coll.), Proc. of the Int. Conf. HEP 99, Tampere, 1999;
M. Nakahata, Proc. of the VI Int. Workshop on Topics in Astroparticle and Underground Physics, Paris, 1999.

[29] Y. Fukuda et al., *Phys. Rev. Lett.* **82** (1999) 2644.

[30] H. Sobel (Super-Kamiokande Coll.), to appear on the Proc. of the XIX Int. Conf. on Neutrino Physics and Astrophysics, Sudbury, 2000.

[31] T. Mann (Soudan 2), to appear on the Proc. of the XIX Int. Conf. on Neutrino Physics and Astrophysics, Sudbury, 2000.

[32] B. Barish (MACRO Coll.), to appear on the Proc. of the XIX Int. Conf. on Neutrino Physics and Astrophysics, Sudbury, 2000.

[33] A. Curioni et al., hep-ph/9805249;
M. Aglietta et al., CERN/SPSC 98-28, SPSC/M615;
K. Winter et al., CERN/SPSC 98-36, SPSC/M623.

[34] The K2K experiment: $http://neutrino.kek.jp/$

[35] Y. Oyama, Proc. of the YITP Workshop on Flavor Physics, Kyoto, 1998 (hep-ex/9803014).

[36] H. Noumi et al., *Nucl. Instr. and Meth.* **A398** (1997) 399.

[37] K. Nakamura (K2K Coll.), to appear on the Proc. of the XIX Int. Conf. on Neutrino Physics and Astrophysics, Sudbury, 2000.

[38] E. Ables et al., Fermilab Proposal P-875 (1995);
NuMI-L-337 (1998);
NuMI-L-375 (1998);
$http://www.hep.anl.gov/NDK/Hypertext/numi.html.$

[39] The Fermilab NuMI Group, Fermilab Report NuMI-346, October 1998.

[40] F. Arneodo et al., INFN/AE-99-17, CERN/SPSC-99-25, SPSC/P314.

[41] A. Blondel et al., CERN-EP 2000-053.

[42] M. Nakamura, *Nucl. Phys.* **B 77** (1999) 259.

[43] B. Lundberg (DONUT Coll.), to appear on the Proc. of the XIX Int. Conf. on Neutrino Physics and Astrophysics, Sudbury, 2000.

[44] K. Niwa et al., Proc. Int. Cosmic Ray Symp. on High Energy Phenomena (Cosmic Ray Lab., Univ. Tokyo, 1974) 149.

[45] J. Nishimura, *Soryusiron Kenkyu, Japan* **12** (1956) 24.

[46] C.M.G. Lattes et al. (Mt. Norikura exp.), Int. Conf. on Cosmic Rays, Jaipur, Vol. **5** (1963) 326;
M. Akashi et al., *J. Phys. Soc. Japan* **17** (1962) 427.

[47] S.L.C. Barroso et al. (Mt. Chacaltaya exp.), Proc. of the XXV ICRC, Durban, 1997.

[48] S.G. Bayburina et al. (Mt. Pamir exp.), Proc. of the XXIV ICRC, Rome, 1995.

[49] M. Akashi et al. (Mt. Fuji exp.), Proc. of the Cosmic Ray and Particle Physics Conf., Newark, 1978.

[50] J. Ren et al. (Mt. Kanbala exp.), *Phys. Rev.* **D38** (1998) 1417.

[51] K. Niu, E. Mikumo and Y. Maeda, *Progr. Theor. Phys.* **46** (1971) 1644.

[52] K. Niu, I Int. Workshop on Nuclear Emulsion, Nagoya, 12-14 June 1998.

[53] K. Hoshino et al., Contr. Paper at the XIV Int. Cosmic Ray Conf., Munich, **7** (1975) 2442.

[54] K. Hoshino et al., *Prog. Theor. Phys.* **53** (1975) 1859.

[55] N. Ushida et al., *Lett. Nuovo Cim.* **23** (1978) 577;
H. Fuchi et al., *Phys. Lett.* **85B** (1979) 135.

[56] H. Fuchi et al., *Lett. Nuovo Cim.* **31** (1981) 199.

[57] A. Ereditato et al., ICARUS-TM-98/13, OPERA 980722-01.

[58] R. Bailey et al., CERN-SL/99-034 (DI); INFN/AE-99/05.

[59] S. Buontempo et al., *Nucl. Instr. and Meth.* **A413** (1999) 255.

[60] O. Toker et al. *Nucl. Instr. and Meth.* **A340** (1994) 572;
Nucl. Instr. and Meth. **A301** (1991) 506.

[61] R. Santonico and R. Cardarelli, *Nucl. Instr. Methods* **A187** 377 (1981).

[62] R. Santonico and R. Cardarelli, *Nucl. Instr. Methods* **A263** 20 (1988).

[63] E. Petrolo et al. (WA92 Coll.), *Nucl. Instr. and Meth.* **A315** 45 (1992);
L. Antonazzi et al. (E771 Coll.), *Nucl. Instr. and Meth.* **A315** 92 (1992);
C. Bacci et al. (RD5 Coll.), *Nucl. Instr. and Meth.* **A315** 102 (1992);
A. Antonelli et al. (FENICE Coll.), *Nucl. Instr. and Meth.* **A337** 34 (1993);
A. Aloisio et al. (L3 Coll.), *Nucl. Phys. B Proceedings Supplements* Vol. **44** (1995) 417;
Anulli et al. (BABAR Coll.), *Nucl. Phys. B Proceedings Supplements* Vol. **61B** (1998) 244.

[64] F. D'Aquino et al. (MINI Coll.), *Nucl. Instr. and Meth.* **A324** 330 (1993);
M. Ambrosio et al. (Cover Plastex Coll.), *Nucl. Instr. and Meth.* **A344** 350 (1994);
B. Bartoli et al. (ARGO-YBJ Coll.), hep-ex/0002060.

[65] ATLAS Collaboration, *Nucl. Instr. and Meth.* **A340** (1994) 466;
CMS Collaboration, *Nucl. Instr. and Meth.* **A334** (1994) 98.

[66] ALICE Time of flight Technical Design Report, CERN/LHCC 2000-12, (2000).

[67] P. Paolucci, BABAR Note N.369, 1997.

[68] M. Iacovacci, Proceedings of the RPC '99 Workshop, Bari, 28-29 October 1999.

[69] E. Eskut et al. (CHORUS Coll.), *Phys. Lett.* **B434** (1998) 205.

[70] C.H. Llewellyn-Smith, *Phys. Rep.* **C 3** (1972) 271.

[71] D.Rein, L.M. Seghal, *Ann. of Phys.* **133** (1981) 79.

[72] *http* : *//wired.cern.ch.*

[73] I. Kisel et al., *Nucl. Instr. and Meth.* **A387** (1997) 433.

[74] A. Zell et al., SNNS User manual, Version 4.1, Report N 6/95. SNNS is (c) (Copyright) 1990-95 SNNS Group, Institute for Parallel and Distributed High-Performance Systems (IPVR), University of Stuttgart, Breitwiesenstrasse 20-22, 70565 Stuttgart, Germany.

[75] H. Eichinger and M. Regler,(1981) Cern Yellow Report 81-06.

[76] C.F. Powell et al., The Study of Elementary Particles by the Photograhic Method, Pergamon Press (1959).

[77] B. Van de Vyver, *Nucl. Instr. and Meth.* **A385** (1997) 91.

[78] M.C. Gonzalez-Garcia and J.J. Gomez-Cadenas, *Phys. Rev.* **D55** (1997) 1297.

[79] J.M. Conrad et al., *Rev. Mod. Phys.* **70** (1998) 1341.

[80] N. Ushida et al. (E531 Coll.), *Phys. Lett. B* **206** (1988) 375.

[81] T. Bolton, hep-ex/9708014, 1997.

[82] Particle Data Group, *Euro. Phys. J.* **1** (1998) 1.

[83] GEANT 3.21 Users's Guide, CERN writeup W5013, Routines GMOLIE, GMCOUL.

[84] P.F. Salvatore, Background Studies for the $\tau^- \to \pi^-\nu$ Channel Using the 1996 Flat-Top Muon Sample, NOMAD MEMO 98-002, 14 January, 1998.

[85] R. Hofstadter et al., High Energy Electron Scattering and Nuclear Structure Determinations, *Phys. Rev.* **92** (1953) 978.

[86] K.W. Ford and D.L. Hill, The Distribution of Charge in the Nucleus, *Ann. Rev. Nuclear Sci.* **5** (1955) 25.

[87] S.A. Akimenko et al., *Nucl. Instr. and Meth.* **A 423** (1986) 518.

[88] *http* : *//chorus*01.*cern.ch/bulte/charon* − *home.html.*

[89] $http://tosca.web.cern.ch/TOSCA/Public/TestSep97/wk.html$.

[90] G.J. Feldman and R.D. Cousins, *Phys. Rev.* **D57** (1998) 3873.

[91] T. Junk, CERN-EP/99-041.

[92] Y. Perrin et al., A toolkit for the construction of distributed, real-time, data-acquisition systems, Conf. Record of RT93, Vancouver, Canada, 1993.

[93] J. Spanggaard, CERN SL-Note-98-023 (BI);
$http://sl.web.cern.ch/SL/Publications/bi98-023.pdf$.

[94] F.C. Porter et al. (BABAR Coll.), SLAC-PUB-7951 (1998).

[95] N. Armenise et al., CERN-SPSC/97-21 (1997).

[96] M. Doucet et al., CERN-EP/2000-011.

[97] G. Rosa et al., *Nucl. Instr. and Meth.* **A394** (1997) 357.